PHOTO-IONIZATION STUDIES OF NEBULAE

Cover:
The cover shows the planetary nebula NGC 6543 (the cat's-eye nebula). The original image was taken with the Hubble Space Telescope and is distributed by STScI. This image and many others can be found on: http://oposite.stsci.edu/pubinfo/Subject.html
The spectrum shown on the cover is a synthetic *SWS* spectrum, based on the CLOUDY model of NGC 6543 presented in Chapter 6.

RIJKSUNIVERSITEIT GRONINGEN

Photo-Ionization Studies of Nebulae

Proefschrift

ter verkrijging van het doctoraat in de
Wiskunde en Natuurwetenschappen
aan de Rijksuniversiteit Groningen
op gezag van de
Rector Magnificus Dr. F. van der Woude
in het openbaar te verdedigen op
vrijdag 19 september 1997
des namiddags te 2.45 uur

door

Peter Andreas Maria van Hoof

geboren op 17 juli 1959
te Heer (Limburg)

Promotor	: Prof. Dr. S.R. Pottasch
Copromotor	: Dr. J.M. van der Hulst
Referenten	: Dr. L.B.F.M. Waters
	: Dr. M.W.M. de Graauw

Contents

Nederlandse samenvatting

1 De evolutie van sterren

Wanneer men naar de sterrenhemel kijkt ziet men jaar in, jaar uit dezelfde vertrouwde sterrenbeelden. Ze lijken niet te veranderen. In vroeger tijden ging men er dan ook van uit dat de sterrenhemel eeuwig en onvergankelijk was. Ook Griekse filosofen gingen hier van uit en zij hadden dan ook hun hele visie van de kosmos rond dit idee opgebouwd. Deze filosofen hadden zo veel gezag dat eeuwenlang niemand hun ideeën durfde aan te vechten. Pas aan het eind van de middeleeuwen durfde Copernicus het aan om aan deze denkbeelden te twijfelen en het duurde tot in deze eeuw voordat men ontdekte dat de kosmos niet onveranderlijk is en dat ook sterren geboren worden en sterven. De levensduur van een ster is echter zo lang dat men in een mensenleven geen enkele verandering kan waarnemen. Onze zon bijvoorbeeld is al vijf miljard jaar oud en het zal nog eens vijf miljard jaar duren voordat er ingrijpende veranderingen zullen plaatsvinden in het inwendige van deze ster.

Om dit proces beter te kunnen begrijpen zal men eerst moeten bekijken hoe de zon de energie produceert die het elke seconde uitstraalt. Dit gebeurt door een proces dat kernfusie heet. In het inwendige van de zon heersen enorm hoge temperaturen en dichtheden. Door deze omstandigheden kunnen twee waterstof atomen zo heftig op elkaar botsen, dat het af en toe gebeurt dat de kernen van de waterstof atomen samensmelten. Dit proces kan nog verder gaan en zo wordt uiteindelijk helium gevormd. Men zegt dan dat waterstof verbrandt wordt tot helium. Zoals bij alle verbrandingsprocessen komt hierbij energie vrij en een gedeelte daarvan zal uiteindelijk als licht worden uitgestraald. Dit is precies hetzelfde proces waarmee men ook op aarde energie probeert op te wekken in kernfusie reactoren. De zon kan dus licht uitstralen omdat in het centrum van de ster waterstof tot helium wordt verbrandt. De voorraad waterstof in de zon is enorm, maar uiteindelijk, over vijf miljard jaar, zal deze toch eens op raken. Hierdoor zal het karakter van de zon drastisch veranderen. Zij zal enorm opzwellen en afkoelen en zodoende een rode reus worden. Dit is echter nog niet het einde van het leven van de zon. In de gebieden rondom het centrum zal nog steeds waterstof aanwezig zijn en nu zal deze verbrand worden tot helium. Dit kan een tijdje doorgaan en dan is ook deze voorraad waterstof op. Ondertussen is de temperatuur en de dichtheid in het centrum de zon verder toegenomen en nu kan helium verbrand worden tot koolstof en zwaardere elementen in het centrum. De ster krimpt dan weer in. De verbranding van helium verloopt veel sneller dan de verbranding van waterstof en dit heeft tot gevolg dat de zon in deze fase veel helderder zal zijn dan ze nu is. Dit heeft uiteraard ook tot gevolg dat de voorraad helium in het centrum snel op zal zijn. In deze fase zal de zon wederom enorm opzwellen tot een rode superreus. Als laatste redmiddel kan de zon dan nog helium en waterstof verbranden in twee verschillende schillen rondom de kern. Zodoende kan ze haar enorme lichtkracht nog een tijdje handhaven. De buitenste lagen van een rode superreus zitten erg ver van de kern af en zijn nog maar heel zwak aan die kern gebonden. Door haar enorme lichtkracht kan de zon deze buitenste lagen nu makkelijk wegblazen. De zon zal dus erg veel massa verliezen en dit gaat net zo lang door tot de veel hetere kern van de ster wordt blootgelegd. De buitenste lagen van de zon worden dus steeds verder de ruimte in geblazen terwijl binnenin steeds hetere lagen van de kern worden blootgelegd. Op een bepaald moment wordt de kern zo heet dat de buitenste lagen, die nu op grote afstand van de zon zijn gekomen, worden geïoniseerd en op zullen lichten. Dit is een proces dat enigszins te vergelijken is met wat er in een spaarlamp of TL buis gebeurt. Zo'n oplichtende nevel noemt men een planetaire nevel. De zon zal in deze fase niet lang meer te leven hebben. Al snel zal alle waterstof en helium op zijn en is er niets meer over om verbrand worden. De zon zal dan af gaan koelen en uiteindelijk een witte dwerg worden. De planetaire nevel zal steeds verder uitdijen en uiteindelijk zo ijl worden dat hij onzichtbaar wordt.

2 Openstaande vragen

De evolutie van elke lage massa ster zal net zo verlopen zoals hierboven voor de zon beschreven is. Het globale schema van die evolutie is algemeen geaccepteerd. Toch blijven er nog heel wat open vragen betreffende de late stadia van deze evolutie. Met late stadia wordt hier de evolutie bedoeld vanaf het moment dat de zon voor de tweede keer opzwelt tot een rode superreus. Men noemt de ster dan een AGB ster. Dit is de fase waar het enorme massa verlies begint en het is precies dit proces dat nog niet goed begrepen wordt. Men heeft wel een globaal idee van de oorzaak, maar men is nog niet in staat om gedetailleerde berekeningen te maken die in alle opzichten realistisch zijn. Ook blijkt het erg moeilijk te zijn om waarnemingen te doen waar betrouwbare waarden voor het massa verlies uit kunnen worden afgeleid. Zodoende is nog niet goed bekend hoe groot het massa verlies in deze fase is en hoe het verandert in de tijd. Toch veranderd de ster ingrijpend door dit massa verlies en kennis op dit gebied is dan ook belangrijk om goede modellen van de evolutie van zo'n ster te kunnen maken.

In het voorgaande is ook al opgemerkt dat het enorme massa verlies van een AGB ster net zo lang doorgaat totdat alleen de kern nog over is. Op dat moment zal het massa verlies sterk verminderen. Men noemt een ster in die fase een post-AGB ster. Een post-AGB ster wordt voortdurend heter omdat het beetje massa verlies dat nog over is, steeds hetere lagen van die kern blootlegt. Dit betekent dat het tempo waarin de ster heter wordt, direct verband houdt met de snelheid waarmee ze massa verliest. Aangezien ook dat proces niet goed bekend is, is dus ook niet goed bekend hoe snel een post-AGB ster heter wordt. Toch is het belangrijk om dit te weten, want het heeft namelijk erg veel invloed op de manier waarop een planetaire nevel gevormd wordt. De post-AGB fase duurt maar heel kort en daarom zijn er nu nog maar enkele tientallen van dat soort sterren gevonden. Dit betekent dat ook uit waarnemingen nog maar weinig bekend is over deze sterren.

Wanneer een ster van de AGB fase overgaat in de post-AGB fase, zal niet alleen het massa verlies veel minder worden, de massa zal ook met een veel hogere snelheid worden uitgestoten. Dit betekent dat de lagen die tijdens deze fase worden weggeblazen uiteindelijk tegen de lagen zullen botsen die tijdens de AGB fase werden uitgestoten, en die een veel lagere snelheid hebben. Hierdoor zal de vorm van het uitgestoten materiaal geheel veranderen en ontstaat uiteindelijk de typische vorm die men bij planetaire nevels waarneemt. Dit betekent dat het massaverlies tijdens de AGB en post-AGB fase niet alleen belangrijk is voor de snelheid waarmee een ster heter wordt en naar de planetaire nevel fase evolueert, maar dat dat massa verlies tevens bepalend is voor de vorm die die nevel uiteindelijk krijgt. Dit betekent dat als men het massaverlies tijdens de AGB en post-AGB fase beter zou kennen, men ook de evolutie van post-AGB sterren en planetaire nevels veel beter zou kunnen begrijpen. Het omgekeerde is echter ook waar, namelijk dat men door het bestuderen van post-AGB sterren en planetaire nevels meer over het massa verlies tijdens de AGB en post-AGB fase kan leren.

In het voorgaande werd opgemerkt dat sterren licht kunnen uitstralen dankzij het feit dat zij in hun inwendige waterstof verbranden tot helium of helium tot nog zwaardere elementen. De onderlinge verhouding van de hoeveelheid waterstof, helium en zwaardere elementen noemt men de chemische samenstelling. Door de verbrandings processen verandert dus de chemische samenstelling in de kern van een ster. De snelheid waarmee deze processen verlopen zijn erg belangrijk om te kunnen voorspellen hoe een ster evolueert. Echter ook hier geldt dat onze kennis nog niet volledig is. Men probeert wel om theorieën op te stellen, maar het is heel moeilijk om deze met waarnemingen te toetsen omdat die verbrandings processen nou eenmaal diep verscholen in het binnenste van de ster plaatvinden. Nu is het zo dat gedurende de laatste fase van de AGB er momenten zijn waarbij de ster heel grondig gemengd wordt. Daarbij wordt materiaal uit het binnenste van de ster (waar dus die verbrandingsreacties plaatsvinden) naar de oppervlakte gebracht. Hierdoor verandert de chemische samenstelling aan de oppervlakte van de ster. Men noemt dit ook wel verrijking omdat er op deze manier meer zwaardere elementen aan de oppervlakte komen. Vervolgens wordt dit verrijkte materiaal weggeblazen en komt uiteindelijk in de planetaire nevel terecht. Dit betekent dat de chemische samenstelling van een planetaire nevel ons iets zegt over wat heel lang geleden in het binnenste van die ster is gebeurd.

In het voorgaande heeft men dus kunnen zien dat het waarnemen van post-AGB sterren en planetaire nevels om twee redenen belangrijk is: enerzijds hoopt men hierdoor meer te leren over het massa verlies tijdens de AGB en post-AGB fase en anderzijds hoopt men meer te leren over de verbrandings reacties die zich in het inwendige van de ster afspelen. Deze dingen zijn beide belangrijk om de evolutie van een ster beter te kunnen begrijpen.

3 Waarnemingen en modellen van planetaire nevels

In het voorgaande is besproken waarom het belangrijk is om planetaire nevels te bestuderen. Bij de waarnemingen van die nevels worden vaak spectra genomen. Dit is een techniek waarbij het licht dat wordt uitgezonden door de nevel, wordt uiteengerafeld in de verschillende golflengten (of kleuren) waaruit het bestaat. Dit proces kan men zelf makkelijk nabootsen door bijvoorbeeld een gloeilamp te laten schijnen op de onderkant van een CD. Wanneer men onder de juiste hoek kijkt, ziet men een regenboog van kleuren. Dit is het spectrum van het licht dat de gloeilamp uitzendt. Omdat alle kleuren die in dit spectrum voorkomen, geleidelijk in elkaar overgaan spreekt men van een continu spectrum of continuüm. Bekijkt men nu een ander soort lichtbron, zoals bijvoorbeeld een TL buis, of nog beter een spaarlamp, dan ziet men dat dit spectrum er heel anders uitziet. Men kan dit het beste zien als men een plaat karton maakt met een klein gat erin en hiermee de lamp afdekt (zodat al het licht zo veel mogelijk uit één punt komt) en verder direct zonlicht vermijdt. Als men goed kijkt ziet men dat er in dit spectrum slechts enkele kleuren voorkomen en er dus helemaal geen sprake is van een continu spectrum. Men zegt in zo'n geval dat het spectrum alleen uit emissielijnen bestaat. Bij de lamp die ik bekeek kon ik een heldere rode lijn zien, een vrij zwakke gele lijn, dan weer een heel heldere groene lijn, een heel zwakke blauwe lijn en tenslotte een zeer heldere diep violette lijn. Dit eenvoudige experiment zegt ons dus meteen dat het proces waarmee licht wordt opgewekt in een gloeilamp fundamenteel anders is dan in een spaarlamp. In de spaarlamp wordt alleen maar licht op heel nauwkeurig bepaalde golflengtes uitgezonden en die golflengtes zijn bepaald door de samenstelling van het gas binnenin de lamp.

In het voorgaande is al opgemerkt dat de processen waarmee licht wordt opgewekt in een planetaire nevel tot op zekere hoogte te vergelijken zijn met die in een spaarlamp of TL buis. Het is dan ook zo dat het licht dat door planetaire nevels wordt uitgezonden alleen uit emissielijnen bestaat. Ook hier geldt dat de preciese golflengtes van die lijnen bepaald worden door de chemische samenstelling van het gas in de nevel. Met andere woorden, door het spectrum van een planetaire nevel te bestuderen kan men de chemische samenstelling van dat gas bepalen. Het is echter ook mogelijk om andere gegevens uit het spectrum af te leiden, zoals bijvoorbeeld de temperatuur en dichtheid van de nevel maar ook de temperatuur van de centrale ster. Om deze gegevens allemaal te kunnen bepalen moet men niet alleen naar de golflengtes van de lijnen kijken, maar ook naar de onderlinge verhouding van de lichtsterkte van die lijnen (dit wordt kortweg de lijnsterkte genoemd). Het is erg ingewikkeld om deze lijnsterktes te berekenen en men heeft daarvoor dan ook grote computer programma's geschreven. Men noemt deze programma's foto-ionisatie codes.

Samenvattend kan men dus zeggen dat men planetaire nevels waarneemt door er spectra van te nemen. Deze spectra bestaan alleen uit emissielijnen en de preciese golflengtes en sterktes van die lijnen kan men gebruiken om bepaalde gegevens van de planetaire nevel af te leiden. Voorbeelden zijn de temperatuur, dichtheid en chemische samenstelling van de nevel en de temperatuur van de centrale ster. Men gebruikt een foto-ionisatie code om deze analyse uit te voeren. Men zegt dan dat men een model van de planetaire nevel maakt. De gegevens die men op deze manier vindt kan men weer gebruiken om theoretische voorspellingen over de evolutie van sterren te toetsen.

4 Inhoud van dit proefschrift

Op 17 november 1995 werd vanaf een ESA lanceerplatform in Kourou de Infrared Space Observatory (*ISO*) gelanceerd. Deze satelliet is bedoeld om waarnemingen te doen in het infrarode spectrum. Infrarood straling wordt ook wel warmtestraling genoemd en is licht met een langere golflengte dan zichtbaar licht. Ook van infrarood licht kan men een spectrum maken en er is daarin geen wezenlijk verschil met een spectrum van zichtbaar licht. Het enige verschil is dat de golflengte anders is. Daardoor is het echter mogelijk om hele andere emissielijnen te zien en dit biedt dan ook de mogelijkheid om aanvullende informatie te verkrijgen. Ook is het zo dat veel planetaire nevels stofdeeltjes bevatten en deze zenden een continu spectrum uit in het infrarood (maar niet in zichtbaar licht). Dit spectrum kan men gebruiken om informatie over het stof te verkrijgen. Omdat dit stof tijdens het massaverlies in de AGB fase werd gevormd, kan men hier dus ook weer dingen uit leren over de late evolutie stadia van sterren.

Waarnemen in het infrarood is vanaf de grond erg moeilijk. Onze atmosfeer absorbeert erg veel infrarode straling. Dit veroorzaakt het zogenaamde broeikas effect en zorgt er voor dat we een aangename temperatuur op aarde hebben. Het maakt het echter ook noodzakelijk om infrarode spectra vanuit de ruimte te maken. Dit is een van de taken die *ISO* heeft. Voor een aantal golflengten in het infrarood was het tot nu toe volledig onmogelijk om spectra te maken en *ISO* is de eerste satelliet die ons die mogelijkheid biedt. Juist omdat dit alles nog zo heel erg nieuw is, waren de bestaande foto-ionisatie codes nog niet volledig voorbereid om deze spectra te analyseren. Het was dan ook mijn eerste taak om een foto-ionisatie code uit te kiezen en die aan te passen en te testen voor dit werk. De code die gekozen werd heet CLOUDY en de veranderingen die ik hierin gemaakt heb, zijn beschreven in een appendix (hoofdstuk 8) van dit proefschrift.

Wanneer men dan op deze wijze een geschikte foto-ionisatie code heeft verkregen, kan men een model maken van een spectrum en verkrijgt men op die manier gegevens over de nevel die dit spectrum uitzond. Om nu een behoorlijke vergelijking te kunnen maken tussen deze gegevens en theoretische modellen is het echter niet alleen voldoende om zo'n model te maken, men moet ook weten hoe nauwkeurig de resultaten van dat model zijn. Dit is een vraag die niet makkelijk te beantwoorden is en waarnaar tot nu toe ook nog maar weinig onderzoek gedaan is. In hoofdstuk 2 wordt dit probleem nader onderzocht. Ik beschrijf daarin een nieuwe methode die ik heb ontwikkeld om spectra te analyseren. Deze methode is bedoeld om enerzijds de resultaten nauwkeuriger te kunnen bepalen en anderzijds om het ook mogelijk te maken om informatie over het stof af te leiden. Deze methode werd getest door haar toe te passen op een kunstmatige set waarnemingen. Dit heeft het voordeel dat men van te voren precies weet wat er uit het model moet komen. Ook kan men op deze manier allerhande waarneemfouten simuleren en onderzoeken wat de invloed daarvan is op het model. Op deze wijze wordt een gedetailleerd beeld verkregen welke gegevens van het model betrouwbaar zijn en welke niet. Vervolgens wordt de methode ook toegepast op de spectra van vijf echte planetaire nevels en worden de resultaten vergeleken met gegevens die al eerder gepubliceerd waren (en die dus met andere methodes verkregen zijn). Hieruit komt duidelijk naar voren dat de nauwkeurigheid van deze, oudere, methodes veel te wensen over laat.

Tijdens dit onderzoek kwam naar voren dat het erg belangrijk is om de diameter van een planetaire nevel goed te kunnen meten, wil men een goed model kunnen maken. In hoofdstuk 3 worden nieuwe formules afgeleid die daarbij nuttig kunnen zijn. Ook worden allerhande voorbeelden van de toepassing van die formules getoond.

De methode die in hoofdstuk 2 is beschreven, werd een aantal malen toegepast op echte nevels. Een voorbeeld hiervan is te vinden in hoofdstuk 5 waar een planetaire nevel uit de Large Magellanic Cloud (LMC) werd geanalyseerd. De LMC is een klein onregelmatig melkwegstelsel dat dicht bij ons eigen melkwegstelsel staat en tot de zogenaamde 'lokale groep' behoort. De planetaire nevel die gemodelleerd is (SMP 58), heeft als bijzonderheid dat hij de eerste planetaire nevel in de LMC is waarvan radio straling is waargenomen. Gebaseerd op dit model, en ook op andere feiten, kunnen we concluderen dat deze nevel waarschijnlijk kleiner is dan vergelijkbare nevels in ons eigen melkwegstelsel vanwege het feit dat de nevel langzamer uitdijt. Dit geeft mogelijk nieuwe inzichten over de manier waarop materie wordt uitgestoten tijdens de AGB en post-AGB fase.

In hoofstuk 6 wordt de analyse beschreven van de eerste twee spectra die met *ISO* zijn genomen. Allereerst wordt het spectrum van NGC 7027 besproken. In dit spectrum kunnen aanwijzingen worden gevonden dat de centrale ster van deze nevel in de laatste 15 jaar heter is geworden. Dit is de eerste keer dat een dergelijke aanwijzing wordt gevonden voor deze nevel. Ook voor andere nevels wordt zoiets maar zelden waargenomen. Dit betekent dat deze nevel een uitstekende kandidaat is om de evolutie van de centrale ster rechtstreeks te volgen. In het spectrum van NGC 6543 werden we verrast door het feit dat er een lijn afwezig was, die we van tevoren wel verwacht hadden. Gebaseerd op dit feit konden we concluderen dat onze oorspronkelijke aannames betreffende het spectrum van de centrale ster fout waren. We waren zelfs in staat om specifieke uitspraken te doen over de hoeveelheid extreme ultraviolet straling die deze ster uitzendt. Dit soort metingen zijn extreem moeilijk en er zijn dan ook maar heel weinig harde gegevens bekend. Dit resultaat is dan ook belangrijk om onze kennis op dit gebied te toetsen.

In hoofdstuk 4 wordt een onderzoek beschreven dat geen rechtstreeks verband met het voorgaande houdt, maar dat wel belangrijk is om de late evolutie stadia van sterren beter te begrijpen. Het betreft hier een theoretisch onderzoek, waarin de evolutie in de tijd van het spectrum van een post-AGB ster wordt onderzocht. Met name wordt hierbij aandacht besteed aan het infrarode deel van het spectrum. Zoals al eerder was opgemerkt, kan men in dit gedeelte de continue emissie van het stof vinden. Ook is al gezegd dat, om een beter begrip van de evolutie van een ster te krijgen, het belangrijk is om meer te weten te komen over het massa verlies tijdens de AGB en post-AGB fase van die evolutie. Waarnemingen aan de stofschil rond een post-AGB ster zijn een uitstekende manier om dit te doen. Uit ons onderzoek blijkt namelijk dat de evolutie van het infrarode spectrum van die stofschil erg gevoelig is voor de verschillende aannames omtrent het massa verlies, zoals die nu nog gemaakt moeten worden in evolutie berekeningen. Dit betekent dat onderzoekingen van het type zoals dat in hoofdstuk 4 wordt gepresenteerd, ons kunnen helpen om de infrarode waarnemingen van post-AGB sterren beter te begrijpen. Ze kunnen er dan uiteindelijk toe leiden, dat men meer inzicht krijgt welke aannames omtrent het massaverlies van AGB en post-AGB sterren realistisch zijn en welke niet.

Acknowledgments

First of all I would like to thank my supervisors Stuart Pottasch, Thijs van der Hulst, Rens Waters and Thijs de Graauw for making this promotion possible, for all their support in the past five years and for giving me all the freedom I could ever wish for.
I would like to thank Griet Van de Steene for her very friendly and stimulating collaboration, which I hope will continue for many years to come. Griet, your work and ideas were very important in finding my way in astronomy and I have little doubt that they will remain to do so in the future. Your intuition, which enabled you to detect any weak spot in my reasoning immediately, never ceased to amaze me.
I also wish to thank Rene Oudmaijer for his friendship and support. Rene, I always admired your thorough knowledge of the literature, something I could only wish to equal. I must mention that I have learned much from our collaboration. All of this makes it very regrettable that you switched to another line of research; nevertheless I wish you lots of success.
Furthermore I would like to thank my other co-authors Bert Zijlstra, Cecile Loup, Douwe Beintema and Fred Lahuis for their pleasant collaboration.
I would like to thank Gary Ferland for making his photo-ionization code CLOUDY available and for his help in modifying and debugging this code. Without all of this, this thesis would not have been possible.
I would like to thank the computer group for all of their support and for creating a superb computer system here in Groningen. More in particular I would like to thank Wim Zwitser and Kor Begeman which have helped me on many occasions. Their support can only be characterized as above and beyond the call of duty. Also I would like to thank Nanne Zuidema for the fact that he always had a friendly word for me.
Furthermore I would like to thank our secretaries Jantina Hoving, Gineke Alberts en Jackie Zwegers-Morris for all of their help and patience with my clumsy way of dealing with bureaucracy.
I would like to thank ASTRON, the Leids Kerkhoven Bosscha Fonds, the Kapteyn Institute, SRON Groningen, the European Union and ESO for the financial support I received in the past five years.
I thank the rest of the Kapteyn institute for the pleasant atmosphere they created and which made my work always enjoyable.
Last but not least, I would like to thank all those people which I inadvertently forgot to mention, but whose help nevertheless was very much appreciated.

1 Introduction

1.1 The late stages of stellar evolution

The evolution of low- and intermediate-mass stars (between roughly 1 $M_{\odot}$ and 8 $M_{\odot}$) has been studied for many years, but still is only partially understood. Nevertheless, a basic framework giving a qualitative description of the main events in this evolution is well established (e.g. Chiosi et al. 1992). The details of the early stages of the evolution will not be repeated here, since they are of little consequence for this discussion. The late stages of the evolution should however be recapitulated briefly. First, the asymptotic giant branch (AGB) stage must be mentioned in which the star loses large amounts of mass and eventually sheds most of its envelope. During the later stages of the AGB evolution the star will experience a series of thermal pulses (which are collectively referred to as the third dredge up) in which processed material from the interior of the star is mixed into the surface layers. At the end of the AGB evolution there is not much more left of the star than a degenerate carbon-oxygen core surrounded by a very extended, low-mass envelope. At this time the heavy mass loss decreases by several orders of magnitude and subsequently the stellar temperature starts to increase rapidly, causing the star to move to the left in the Hertzsprung-Russell (HR) diagram. This phase is called the post-AGB phase. Depending on the phase of the thermal pulse cycle, the dominant energy source at this point will either be hydrogen shell burning or helium shell burning. This dichotomy will profoundly influence the subsequent evolution the star in two ways. First, the evolutionary speed is predicted to be higher for hydrogen burning central stars than for helium burning stars. Second, helium burning central stars may experience a final thermal pulse (or helium flash) during their post-AGB evolution. These flashes are quite rare, but have been observed (see Sect. 1.1.4). During the post-AGB evolution the star will become hot enough to ionize the shell of material that was expelled during the AGB phase, causing it to be observable as a planetary nebula (PN). Not all low-mass stars necessarily go through the PN phase: if the movement to the left in the HR diagram is very slow, the AGB shell will have dispersed into the interstellar medium long before the central star is hot enough to ionize this shell. Eventually all nuclear processes will cease in the interior of the star, the nebular material will dissolve into the interstellar medium and the central star will become a white dwarf.

As already mentioned, this schematic description of the evolution is well established. However, many details still need to be filled in, both from an observational as well as from a theoretical point of view. A host of observationally defined classes of objects exists for which it is clear that they must be post-AGB objects. However, for many of these it is not fully understood how they connect with other classes or where they exactly fit into theoretical predictions of post-AGB evolution. The discussion in Sion (1996) can serve as an illustration of the complexity of this problem. The theoretical predictions give a well-ordered description with basically only two free parameters: the initial mass (or core mass) of the central star and the dichotomy of hydrogen burning versus helium burning central stars. On the other hand, the observations, when taken at face value, show a much wider variety of objects and thus suggest the presence of more free parameters. One such free parameter will undoubtedly be the binary nature of certain central stars. This yields two additional free parameters: the initial mass of the companion star and the separation between the two. Especially for close binaries mass transfer will occur, giving rise to a very complex evolution. It is not clear whether all diversity in observed post-AGB objects can be explained in this way and this is still one of the major fields of post-AGB research.

Several quantitative predictions for the post-AGB evolution of low- and intermediate-mass stars exist (e.g. Schönberner 1979, 1983; Blöcker & Schönberner 1991; Blöcker 1995a,b; Vassiliadis & Wood 1993, 1994). All of these are hampered by the fact that various gaps in the knowledge of the underlying physics exist. A few of the most important problems are listed:

- The database of nuclear reaction rates is far from complete. Some reaction rates have to be extrapolated from higher energy experimental data. For some reactions no experimental data exists at all. In such cases one has to resort to more approximate methods, or omit the data completely if the particular reaction is thought to be of lesser importance. The recent progress is described in Chiosi et al. (1992).
- The physics of turbulent layers is still only partially understood. The convection cells present in these layers are expected to move beyond the unstable layer (a process called overshooting), but no complete theory exists to describe this. Usually overshooting is modeled using heuristic fudge factors. A more detailed discussion can be found in Chiosi et al. (1992). Closely related is also the topic of hot bottom burning (e.g. Blöcker & Schönberner 1991; Herwig et al. 1997), which could explain the fact that almost all observed carbon stars have a low mass (1 $M_\odot$ to 3 $M_\odot$).
- Rotation of stars is rarely incorporated in the modeling. One attempt to do this can be found in Endal & Sofia (1981). It is well known that magnetic fields are very effective in slowing down the surface of an F or G type star (stars with an initial mass between 0.8 $M_\odot$ and 1.6 $M_\odot$). Endal & Sofia argue that dynamic friction is not sufficient to transport angular momentum from the inside of the star to the surface. Hence the star will establish itself as a differentially rotating gas sphere. It is to be expected that shearing processes will influence the stability and the turbulent motions in the interior of the star. This in turn will also influence the mixing of nuclear species. The stability criteria and the physics of turbulent motion in a (differentially) rotating medium are still far from fully understood. This explains why so few attempts to model this have been made. However, one should not infer from this that the effects of rotation are negligible.
- Mass loss processes play an important role, especially during the AGB stage of the evolution and beyond. However, the physics of the mass loss is still only partially understood. Since the observational determination of mass loss rates (especially for the post-AGB stages) is also very difficult (e.g. Oudmaijer & Bakker 1994; Oudmaijer et al. 1995), one still has to resort to heuristic mass loss laws (e.g. Blöcker 1995a).

Until recently one had to mention the incompleteness of the atomic data needed to calculate the radiative transport in the interior of the star. This influences the temperature and density structure, and the stability in the interior of the star as well. The situation has greatly improved since the start of the opacity project (Seaton 1987) and this problem can now be considered to be of lesser importance.

Hence, many questions regarding the evolutionary path in the HR diagram, the evolutionary speed and the mass loss history of post-AGB objects still remain unanswered. An obvious way to improve this situation is to test the predictions against observations, but such tests are always fraught with great difficulty. Nevertheless, there are several areas where attempts have been made to test evolutionary predictions or which show promise for doing this. We will discuss four of these areas here.

1.1.1 Nebular abundances

The first test concerns the abundance patterns found in planetary nebulae. During certain periods in the AGB and post-AGB evolution of a star, a large fraction of the envelope becomes convective and material that has undergone nuclear reactions is mixed into the surface layers (dredge-up). Later on these surface layers are shed into the nebula and the nebula can thus become a probe for the nuclear reactions that took place in the interior of the star. The models predict certain abundance patterns. These predictions are however hampered by all four problems listed in the previous section. Thus, in principle, abundance measurements could be a good way to assess the viability of the various assumptions adopted in the modeling. In practice however one is greatly hampered by problems in measuring the abundances and interpreting the results. First of all, certain elements will be depleted in dust grains. The physical processes of dust formation and dust destruction are far from fully understood. One can expect that infrared observations (e.g. with the infrared space observatory, *ISO*) will give a major impulse to this field since they will allow direct observation of the dust emission. Second, abundance gradients within nebulae may exist, but such gradients can only be observed directly for larger nebulae through spatially resolved spectroscopy. Furthermore, assumptions regarding the physics in the nebula are needed to translate observed line strengths into abundances. The method showing most promise for accurate results is photo-ionization modeling. However, there still are major uncertainties in this field as well. One of these, the lack of accurate atomic data, is now being tackled through the opacity project and the situation is improving rapidly. Another problem is that an accurate description of the stellar spectrum is needed for photo-ionization modeling. This can only be provided by non-LTE model atmospheres which include wind- and line-blanketing. In this field the situation is also rapidly improving and good models are becoming increasingly available (e.g. Sellmaier et al. 1996). One major uncertainty is that these models have hardly been tested at wavelengths shortward of the He II Lyman edge (228 Å).

The most important problem in determining abundances is the difference that can be found between the results derived from collisionally excited lines and from recombination lines (e.g. Liu et al. 1995). These differences can be very large, even more than a factor of ten! Until recently it was often assumed that these differences were caused by fluctuations in the electron temperature of the nebular plasma. Photo-ionization models however do not predict sizeable fluctuations, which is in disagreement with this assumption. This problem is often called the t^2-problem. Recent observations of the planetary nebula NGC 6153 have shown that temperature fluctuations may be present in this nebula, but that the strength of this effect is insufficient to account for the very large discrepancy between the abundances from collisionally excited and recombination lines that was found (Liu 1997). Hence the origin of this discrepancy is still unclear. Since the t^2-problem has an important impact on abundance determinations, further investigation of this problem is also needed. Infrared observations with *ISO* may prove to be of value, since the accurate measurement of certain infrared fine-structure lines can shed a new light on the t^2-problem (e.g. Dinerstein 1983; Zuckerman 1986). Various studies searching for patterns in observed nebular abundances have been published. Some report correlations, others do not (e.g. Pottasch 1990; Pottasch 1993). These results are still widely debated and one possible cause for these mixed results is that the uncertainty in the determination of abundances might be underestimated, causing possible correlations to be swamped by observational error. This might especially be the case when results from various authors, using different methods, are combined, which is often done to obtain larger sample sizes. A better understanding of the uncertainties involved in abundance determinations is one of the necessary elements to make the search for abundance patterns a fruitful one.

1.1.2 The Hertzsprung-Russell diagram

A second test for theoretical models of post-AGB evolution concerns the determination of the distribution of post-AGB objects in the HR diagram. Several predictions for the evolution of effective temperature and luminosity as a function of time exist. The speed with which hydrogen burning post-AGB stars increase their temperature is determined by the mass loss rate and the relation between the effective temperature and the envelope mass of the central star (the $M_{\rm env}$–$T_{\rm eff}$ relation; see e.g. Blöcker 1995b; van Hoof et al. 1997). The $M_{\rm env}$–$T_{\rm eff}$ relation is usually parameterized by the core mass, but actually depends on the complete evolutionary history of the star. This is why modern evolutionary calculations start on the zero age main sequence and calculate the evolution completely through to the white dwarf stage (Blöcker & Schönberner 1991; Blöcker 1995a,b; Vassiliadis & Wood 1993, 1994).

Several attempts have been made to plot observed PN in the HR diagram but until now no trustworthy conclusions could be drawn from this (e.g. Schönberner 1981; Ratag et al. 1990). The reasons for this are mainly of observational origin. The most important and most notorious problem is the determination of the distances to the nebulae. Accurate distances are only known for a handful of objects. Since the uncertainty in the distance enters quadratically into the luminosity, it is very hard to determine a reliable luminosity. A secondary problem is that it is not trivial to determine the bolometric luminosity of the central star. Especially for carbon rich nebulae, significant amounts of radiation are absorbed by the dust and re-emitted in the infrared. Usually photometry obtained with the infrared astronomical satellite (*IRAS*) is sufficient to get a good estimate of the total infrared luminosity. Furthermore, central stars of PN can be very hot and emit a significant fraction of their total luminosity at extreme ultraviolet wavelengths. This radiation is partially or completely absorbed by the nebula and re-emitted at all wavelengths: ultraviolet, optical and infrared. The most accurate way of combining all observations into a value for the bolometric luminosity is probably through photo-ionization modeling using atmosphere models. The assumed mass loss rate and the velocity structure in the wind are important for determining an accurate ultraviolet continuum of the model atmosphere (e.g. Sellmaier et al. 1996 and references therein). This is because the wind influences both the continuum level and the line blocking process. Once again we see the problem of determining the mass loss entering the discussion.

Another problem for determining the distribution of objects in the HR diagram is an accurate determination of the effective temperature of the central star. This is also a notorious problem surrounded by much discussion. Again it is probably true that the best way to determine this parameter is through photo-ionization modeling. Hence the problems surrounding the choice of the model atmosphere also pertain here. The central star temperature is best constrained by emission lines of the highest ionization stages in the plasma. An additional problem for the temperature determination is that for high temperature stars these high ionization stages have no emission lines in the optical regime. However, some of these stages do have infrared fine-structure lines, which can be observed with *ISO*. The situation is complicated further by the fact that the interaction of the central star wind with the nebula may dump mechanical energy in the plasma, raising the level of excitation. It seems reasonable however to expect that with *ISO* progress will be made in this field.

If in some future these problems would be solved to such a degree that comparison with theoretical predictions becomes meaningful, then two problems still remain in translating the calculated evolutionary tracks into a density of objects in the HR diagram. These are the distribution of initial masses of the progenitor stars (usually called the initial mass function) and the rate of evolution of the central star towards higher temperatures which is directly controlled by the mass loss. Observing the distribution of PN in the HR diagram may prove fruitful in constraining these two problems.

1.1.3 The shaping of planetary nebulae

To construct a good photo-ionization model of a nebula, detailed knowledge of the three-dimensional density structure is necessary. The processes involved in shaping the nebula are still only partially understood, although much progress has been made in the last couple of years. The shape and density structure of PN is determined by the AGB mass loss history and the hydrodynamic interaction of the fast post-AGB wind with these ejecta (e.g. Mellema 1993; Frank et al. 1993; Schönberner et al. 1997). Hence it is clear that the AGB and post-AGB mass loss history are of prime importance to understand the evolution and shaping of PN. The AGB mass loss history can best be traced in very young post-AGB stars, before the fast post-AGB wind alters the structure of the nebula. The best way to observe these young objects, which have not ionized their envelope yet, is through mid-infrared imaging of the dust emission. Attempts are now being made to model these observations in order to understand the three-dimensional structure better. First results indicate that the AGB mass loss is axially symmetric (Meixner et al. 1997). The observations of these objects should then be combined with theoretical work, in order to obtain a deeper insight into the mass loss history. Since knowledge of the current mass loss and the mass loss history plays an important role in many other fields of PN research as well, one can expect that the study of post-AGB stars and young PN may have an important impact on the whole field. However, only few genuine post-AGB stars and young PN are known to date and enlargement of this sample is certainly desirable.

1.1.4 Direct observation of central star evolution

For the highest mass central stars of planetary nebulae the expected quiescent evolutionary speed is so high that changes can be observable on timescales of several years to several decades. This phenomenon can be observed in the planetary nebula NGC 7027 where a steady decline in the 6 cm radio flux has been observed over the past couple of decades (Masson 1989; Zijlstra, private communication). This is either caused by an increase in the effective temperature of the central star, a decrease in the luminosity or a combination of both. This gives very direct information on the evolution of the central star and is in principle one of the most powerful methods for testing evolutionary predictions. Unfortunately this method is only applicable to a very small sample of the most massive central stars. The sample could be made larger by high accuracy radio flux monitoring of other nebulae. An accurate distance determination would also be necessary however to get a good estimate for the luminosity.

Another possibility for directly observing the evolution of the central star is when an explosive phenomenon like a helium shell flash occurs. Such an event can currently be observed in Sakurai's object and possibly also in the Large Magellanic Cloud (LMC) planetary nebula N66. Other examples of spectacular changes in planetary nebulae are known, but the sample of objects is very small. Furthermore, the interpretation of the observations may be difficult due to the fact that the assumption of a quasi-equilibrium state of the nebula at each moment may not be valid in such rapidly changing objects. Despite these difficulties, these objects show much promise for deepening our understanding of the central star evolution.

1.2 The Infrared Space Observatory

The importance of infrared observations for the study of planetary nebulae has been stated on several occasions in the previous discussion. For roughly three decades emission line nebulae have been observed in the infrared using various groundbased, airborne and satellite-based instruments. Much of the pioneering work in mid- and far-infrared spectroscopy of these objects has been done with balloon flights, the Lear Jet Observatory, the Kuiper Airborne Observatory (*KAO*) and the low resolution spectrometer on board of *IRAS*. The four most important reasons for doing infrared spectroscopy of emission line nebulae like planetary nebulae, but also H II regions and active galactic nuclei are to

- minimize extinction by interstellar and/or circumstellar dust,
- observe emission lines of ionization stages that can not be observed at other wavelengths,
- study the continuum and/or solid state features emitted by the dust in the nebulae,
- study molecular emission (mainly H_2 and CO) from the photo-dissociation regions (PDR's) surrounding the ionized part of the nebulae.

Infrared observations from the ground are always hampered by atmospheric absorption, mainly due to H_2O, but also due to other well-known greenhouse gases like CO_2, O_3, N_2O, CO, CH_4 and O_2. In certain wavelength regions the opacity of the atmosphere is so high that groundbased and even airborne observations are completely impossible. This is the main reason for doing infrared observations from space. Infrared satellites need to be cooled with liquid helium since otherwise the emission from the astronomical objects would be completely swamped by the background emission from the satellite itself. The amount of helium that can be carried is limited. Hence infrared satellites have a strictly limited lifetime which is typically much shorter than of comparable ultraviolet, X-ray or gamma ray missions. This explains why it is comparatively rare to have an infrared satellite available for observing.

On 17 November 1995 at 02:20 CET, *ISO* was launched from Kourou in French Guyana. This long awaited event marked the beginning of a new era in infrared astronomy, due to the unprecedented capabilities of *ISO* (Kessler et al. 1996). The payload of the satellite comprises four scientific instruments: the short-wavelength spectrometer (*SWS*) described in de Graauw et al. (1996), the long-wavelength spectrometer (*LWS*) described in Clegg et al. (1996), a camera (Cesarsky et al. 1996) and a photometer (Lemke et al.

1996). The most important improvement is that these instruments provide a coverage of wavelength regions which have never been observed before using groundbased or airborne instruments. The quality of the observations is also greatly improved since one is not hampered anymore by atmospheric absorption lines and bands which are ubiquitously present in the infrared. This not only gives the opportunity to observe emission lines and especially solid state features with greater accuracy, but should also, in principle, help to achieve a more accurate absolute flux calibration. Furthermore, the instruments give a much wider wavelength coverage and more sensitivity than could hitherto be achieved with *KAO*. The current best estimate is that the *ISO* mission will end in April 1998, i.e. after 27 months of scientific observations, which is more than 1.5 times the originally expected lifetime.

1.2.1 The ISO spectrometers

The two grating spectrometers on board *ISO* provide a wavelength coverage from 2.38 μm to 45.2 μm for *SWS* and 43 μm to 196.9 μm for *LWS*. With these instruments it is possible to obtain low to medium resolution spectra, using apertures ranging between $14'' \times 20''$ and $20'' \times 33''$ for *SWS*, and a circular aperture of approximately $80''$ for *LWS* (Swinyard et al. 1996).

The spectrometers are ideally suited for observing emission line nebulae, in particular planetary nebulae. The medium resolution and the wide wavelength coverage make it possible to simultaneously observe broad emission features from the dust and narrow atomic and molecular emission lines. The large apertures make it possible to observe, at least for smaller nebulae, the entire nebula. This makes these spectra ideally suited for analysis with photo-ionization, PDR or dust codes which also make predictions for the emission from the entire nebula. First results from the various teams already indicate that this mission will be very fruitful for the study of emission line nebulae. In particular this is the case for the following topics, many of which have already been mentioned in previous sections: the study of solid state features, the study of grain formation and grain destruction, the t^2-problem, studying the excitation processes in high excitation nebulae, obtaining accurate central star temperatures, testing model atmospheres, studying PDR chemistry and so on.

1.3 Outline

The main goal of this thesis is to make a contribution to the understanding of post-AGB evolution. From the previous discussion it has become clear that many problems have to be overcome in order to gain this understanding. It has also been argued that *ISO* can make a contribution in solving at least some of these problems. But before this can be done, first another problem needs to be tackled.

One of the basic problems in PN research is that no reliable and accurate methods are available to determine even the basic physical parameters of PN. From the previous discussion it became apparent that photo-ionization modeling of the nebulae is the most promising approach to improve on this situation. Therefore a new method has been constructed to determine the physical parameters of PN using the photo-ionization code CLOUDY (Ferland 1993). This photo-ionization code was chosen because it is widely used and has been tested for many different physical conditions. Furthermore, many important infrared emission lines were already present in the code. CLOUDY also includes a good dust model and a chemical network for the formation of molecules. This enables a fairly realistic modeling of the neutral zone of the nebula. An additional advantage of CLOUDY is that the code is fast, which is needed for our method, which is described in Chapter 2. To make the code more suitable for our purposes, including the modeling of *ISO* spectra, an extensive amount of new code was added; e.g. the code was made more user friendly, the optimizing mechanism already present was greatly extended, a calculation of the radio continuum was added, the calculation of the infrared continuum was improved to include the contribution from cold dust, many infrared emission lines and several photometric bands were added (most importantly the *IRAS* and the Johnson infrared bands), and so on. The extensions to the code are described in detail in an appendix (Chapter 8).

From the discussion in the previous sections it also became clear that it is necessary to investigate the fundamental problem of assessing the accuracy of the parameters derived using this method. Only then can one make a well-founded comparison with theoretical predictions. This is a problem which is still widely underestimated and deserves more attention. A first attempt to ascertain the accuracy of the physical parameters determined with our method is also described in Chapter 2.

In the course of this work it was found that a precise value for the angular diameter of the nebula is important for accurately determining physical parameters. The diameter is often determined using a technique called 'gaussian deconvolution'. It was found that this method was only weakly founded in theory. A theoretical investigation was therefore started to determine accurate conversion factors for a variety of surface brightness distributions. This work is described in Chapter 3.

The method for modeling nebulae has been applied several times, some of which are included in this thesis. These applications give us some first indications on how photo-ionization modeling can be helpful in solving the problems outlined above.

First, the method was used to model the LMC PN SMP 58 (Chapter 5). In this paper we could tentatively conclude that the nebulae around LMC [WR] central stars are more compact than their galactic counterparts, illustrating how modeling can give clues on radiation driven winds and the shaping of nebulae.

Second, the method has been used to model the *ISO SWS* spectra of NGC 7027 and NGC 6543 (Chapter 6). The *SWS* spectrum of NGC 7027 shows evidence for evolution, or at least variability, of the central star. The preliminary model is not successful in giving a full explanation of the observed changes in the spectrum, based on the assumption that they are only caused by an increase in the stellar temperature. Nevertheless, one can state that models of this type are needed to gain an understanding of the change in the physical conditions occuring in the central star. When this final analysis is combined with an interpretation of the reported decline of the radio flux (Sect. 1.1.4), this could result in a unique measurement of the evolutionary speed of the central star of NGC 7027. Using the model of NGC 6543, rather stringent upper limits could be placed on the He II Lyman continuum emanating from the central star. This is one of the first times that such a constraint could be derived for a stellar spectrum.

CLOUDY has also been used to conduct a parameter study of the spectral evolution of a typical post-AGB star, with particular emphasis on the evolution of the infrared colors (Chapter 4). As was already stated, several assumptions have to be made in order to calculate evolutionary tracks for post-AGB stars. A study of the type presented here is important for understanding how these assumptions affect the infrared spectrum of the post-AGB stars. The results of this study may be helpful for understanding the observations made in e.g. the *IRAS* color-color diagram. This in turn may lead to an improved understanding of mass loss processes, hydrodynamic interactions and evolutionary rates of the central star. Eventually it may lead to better evolutionary calculations. However, we are still far from this goal and our study should only be viewed as a small step towards achieving this goal. Another benefit from this study is that it may help in identifying more efficient search criteria for post-AGB stars and young PN.

The main conclusions and an outlook on future work will be given in Chapter 7.

1.4 References

Blöcker T., 1995a, A&A 297, 727

Blöcker T., 1995b, A&A 299, 755

Blöcker T., Schönberner D., 1991, A&A 244, L43

Cesarsky C.J., Abergel A., Agnèse P. et al., 1996, A&A 315, L32

Chiosi C., Bertelli G., Bressan A., 1992, ARA&A 30, 235

Clegg P.E., Ade P.A.R., Armand C. et al., 1996, A&A 315, L38

de Graauw Th., Haser L.N., Beintema D.A. et al., 1996, A&A 315, L49

Dinerstein H.L., 1983, in Flower D.R., ed., IAU Symp. 103: 'Planetary Nebulae', p. 79

Endal A.S., Sofia S., 1981, ApJ 243, 625

Ferland G.J., 1993, University of Kentucky Physics Department Internal Report

Frank A., Balick B., Icke V., Mellema G., 1993, ApJ 404, L25

Herwig F., Blöcker T., Schönberner D., El Eid M., 1997, A&A in press

Kessler M.F., Steinz J.A., Anderegg M.E. et al., 1996, A&A 315, L27

Lemke D., Klaas U., Abolins J. et al., 1996, A&A 315, L64

Liu X.-W., 1997, in 'ISO's View on Stellar Evolution', in preparation

Liu X.-W., Storey P.J., Barlow M.J., Clegg R.E.S., 1995, MNRAS 272, 369

Masson C.R., 1989, ApJ 336, 294

Meixner M., Welch W.J., Likkel L., Tafalla M., Campbell M.T., 1997, in IAU Symp. 180: 'Planetary Nebulae', in press

Mellema G., 1993, PhD thesis, University of Leiden

Oudmaijer R.D., Bakker E.J., 1994, MNRAS 271, 615

Oudmaijer R.D., Waters L.B.F.M., van der Veen W.E.C.J., Geballe T.R., 1995, A&A 299, 69

Pottasch S.R., 1990, in Mennessier M.O., Omont A., eds, 'From Miras to Planetary Nebulae: Which Path for Evolution ?', Editions Frontières, Gif sur Yvette, p. 306

Pottasch S.R., 1993, in Weinberger R., Acker A., eds, IAU Symp. 155: 'Planetary Nebulae', p. 449

Ratag M.A., Pottasch S.R., Waters L.B.F.M., 1990, in Ratag M.A., PhD thesis, University of Groningen, Chapter 4

Schönberner D., 1979, A&A 79, 108

Schönberner D., 1981, A&A 103, 119

Schönberner D., 1983, ApJ 272, 708

Schönberner D., Stahlberg J., Steffen M., Kifonidis K., Blöcker T., in IAU Symp. 180: 'Planetary Nebulae', in press

Seaton M.J., 1987, J. Phys. B 20, 6363

Sellmaier F.H., Yamamoto T., Pauldrach A.W.A., Rubin R.H., 1996, A&A 305, L37

Sion E.M., 1996, in Lundström I., Stenholm B., eds, 'Planetary Nebulas with Wolf-Rayet Type Nuclei', 1996, Ap&SS 238, 131

Swinyard B.M., Clegg P.E., Ade P.A.R. et al., 1996 A&A 315, L43

van Hoof P.A.M., Oudmaijer R.D., Waters L.B.F.M., 1997, MNRAS 289, 371 (Chapter 4)

Vassiliadis E., Wood P.R., 1993, ApJ 413, 641

Vassiliadis E., Wood P.R., 1994, ApJS 92, 125

Zuckerman B., Aller H.A., 1986, ApJ 301, 772

2 Photo-ionization modeling of planetary nebulae

P.A.M. van Hoof, G.C. Van de Steene

Abstract — The lack of accurate, generally accepted techniques to derive the physical parameters of planetary nebulae is presently one of the major limitations in the study of planetary nebula evolution. What makes the situation worse is that the magnitude of the uncertainty in the derived physical parameters is generally unknown. We wish to investigate this problem and the present paper is a first step towards this goal.

We present a new method to derive simultaneously and self-consistently all physical parameters of a planetary nebula from a set of observed quantities. A modified version of the photo-ionization code CLOUDY is used to calculate various models, searching for a best fit of the predictions to the observables in an automated way. This method uses emission line ratios, the angular diameter, the radio and the infrared flux to constrain the model. It also takes dust into account in the radiative transport. With the method we are able to determine the stellar temperature and luminosity, the inner, Strömgren and outer radius of the nebula, the density, the dust-to-gas ratio and the abundances. We investigate the accuracy of the determination of the physical parameters by applying this method to an artificial set of observables. First we prove that this method can pass a formal convergence test. Subsequently we introduce either measurement errors in the observables or change the model assumptions, and investigate how this affects the best-fit model. In this way we gain an understanding of the robustness of our method and hence of the reliability of the physical parameters. Our method is also compared with classical methods to determine the electron temperature and density and the nebular abundances. It is shown that our method suffers less from noise in the spectrum than the classical line diagnostics. However, this advantage may be lost if the model assumptions are not appropriate for the nebula being studied. The weakest points are currently the use of a blackbody approximation, the assumption that the inner dust radius coincides with the inner gas radius and the assumption of spherical symmetry.

The method has been applied to a sample of five galactic bulge planetary nebulae. Comparison of the distance independent physical parameters with published data shows good agreement between the stellar temperatures, but a large spread in the other physical parameters, especially the electron density. Large differences are also found for the electron temperature and the abundances. This confirms that the use of line diagnostics to determine these parameters is not reliable.

2.1 Introduction

Many techniques are in use to determine the physical parameters of Planetary Nebulae (PN). Some make rather simple assumptions and are only suited for a quick analysis, others are more sophisticated and can provide an in-depth study of individual PN. Most methods have in common that they are aimed at determining only one particular physical parameter. They simplify to some degree the physics in the nebula, and as a consequence their validity is still under debate. Additionally, these methods often rely on quantities which are hard to measure (e.g. weak emission lines, the stellar continuum in the *V* band, etc.), leading to large uncertainties in the derived physical parameters. The lack of accurate, generally accepted methods to determine the basic physical parameters of PN is presently the major limitation in the study of PN evolution. What makes this situation even worse is that generally the magnitude of this uncertainty is not known.

When a nebula is modeled, usually several methods are combined. This will lead to a model which is not necessarily self-consistent. For example, the adopted stellar temperature and spectrum need not be consistent with the adopted electron temperature. Furthermore, the influence of dust is often neglected. Especially for young, compact PN this is not a very good assumption. These problems result from the fact that the emission from a PN is determined by the intricate interplay between many different physical processes. This has been one of the most important motivations for the development of photo-ionization codes. The major limitation in the application of these codes has been that they require knowledge of parameters which can not be measured directly (e.g. the inner radius).

Our aim is to assess the accuracy of the determination of physical parameters. For this we have developed a method to derive simultaneously all physical parameters of a planetary nebula using as many observed quantities as possible. The method is based on photo-ionization modeling since this provides the most detailed description of the physics in the nebula. In the remainder of this introduction we will discuss the methods currently used to determine physical parameters, while simultaneously indicating the need for improvement.

Two key parameters for modeling a nebula, which are prone to measurement errors, are the electron temperature and density of the nebula. These are usually determined using line ratios of [N II] or [O III] (for the temperature) and [O II] or [S II] (for the density), as described in e.g. Osterbrock (1989). The measurement of the temperature involves the lines [N II] λ5755 or [O III] λ4363 which can be quite weak, especially in PN that suffer from large extinction. The measurement of the density involves the lines [O II] λ3726 and λ3729 which are often blended and can also by affected by extinction, or [S II] λ6716 and λ6731 which are relatively weak. An additional problem is that the density determination is not very sensitive outside the range 10^2 cm^{-3} to 5×10^3 cm^{-3}. Higher densities have been observed in young, compact PN. Due to the nature of the relation between the [S II] line ratio and the electron density, the uncertainty in the electron density will always be much greater than the measurement error in the line ratio. This is especially true outside the range mentioned above. An additional problem is that the electron temperature and density will not be constant across the nebula. In general nebulae will show ionization stratification and as a result of that the ions used for determining the electron temperature and density may reside in different regions of the nebula. Also since spectra usually do not cover the entire nebula, it is not *a priori* clear that the physical parameters deduced from the diagnostic lines can be used for modeling the entire nebula. We can circumvent some of these problems when photo-ionization models are used. One does not have to assume constant electron temperature and density since these parameters will be calculated self-consistently. However, assumptions for the hydrogen density structure in the nebula (i.e. for the mass loss history of the central star) will have to be made. To calculate a photo-ionization model, knowledge of other physical parameters of the PN is also needed. One of these is the spectral energy distribution of the incident radiation field, which is characterized by the effective stellar temperature.

The situation regarding the determination of stellar temperatures has recently been reviewed by Kaler (1989), Pottasch (1992) and Preite-Martinez (1993). The most commonly used methods are the Zanstra method, the energy balance (or Stoy) method and photo-ionization modeling. All these methods determine the stellar temperature in an indirect way, using the emission of the nebula. Both the Zanstra and the Stoy method are under discussion, and it is not clear to what extent the results can be trusted. Photo-ionization modeling of the nebula gives the most detailed treatment of the physics, but knowledge of the elemental abundances is necessary to determine the stellar temperature. The dependence on the adopted abundances is especially critical for high temperature central stars (Pottasch 1992). Thus, to determine the stellar temperature by photo-ionization modeling, this method should be combined with a simultaneous determination of the abundances.

The situation regarding abundance determinations has been reviewed by Clegg (1989, 1993). Often methods are used which assume constant electron temperature and density. The values for these constants are determined using emission line ratios, as discussed above. The derived ionic abundances then need to be transformed into elemental abundances. This requires a correction for the unobserved ionization stages, for which ionization correction factors (i.c.f.) are used (e.g. Mathis 1985). We would like to refer to the study of Alexander & Balick (1997), where a thorough discussion of the errors inherent to the use of this technique is given. Photo-ionization modeling is also in use to determine elemental abundances, and this method is the most satisfactory from a physical point of view (Perinotto 1991). It can circumvent the problematic determination of the electron temperature and density from line ratios, and can calculate the i.c.f. in an implicit way, fully consistent with physical conditions in the nebula. However, such modeling does require knowledge of distance dependent parameters, such as the stellar luminosity and the inner radius of the nebula, and thus of the distance itself.

Distance determinations of PN are still very problematic. Various methods are in use, but the range in distances obtained is often very large and no method has found general acceptance. Reviews of the current status can be found in Pottasch (1992), Terzian (1993) and Pottasch (1996). The methods can be divided into two groups. Statistical distance scales give distances which are valid on average for a statistically large sample, but they do not yield reliable results for individual objects. On the other hand, individual distance scales are considered more accurate, but most of them can only be applied to a very limited number of PN. The lack of a reliable, generally applicable method to determine distances to PN poses a key problem when using photo-ionization models.

In the previous discussion we have seen that knowledge of several physical parameters is necessary for modeling a nebula. Since these are also the parameters to be determined, we are caught in a vicious circle. With the increasing speed of present day computers, it has become feasible to use iterative schemes to determine all physical parameters of the PN simultaneously and in a self-consistent manner. The basic idea behind this approach is to find a model for the PN that gives the best overall fit to a set of observables, thus avoiding the critical dependence on a few observables, and reducing the influence of measurement errors. On the other hand it should be mentioned that the use of a photo-ionization code necessitates assumptions on the physical model of the nebula and this introduces new sources of error. We will investigate both these sources of error in this paper. Our method is an extension of most previous work in that it incorporates the radio and the infrared flux to constrain the model, and that it takes dust into account in the radiative transport.

It is only fair to say that there are also drawbacks to the use of photo-ionization models. A review of these problems, and the progress recently made, can be found in Aller (1984), Harrington (1989) and Ferland (1993a). The most important problems are the necessary simplifications that go into the geometric model of the nebula (e.g. spherical symmetry), the distribution of the gas (e.g. constant density), and the distribution of the dust (e.g. constant dust-to-gas ratio). Also the problems involved in the radiative transport in optically thick resonance lines (e.g. H I Lyα and C IV λ1549) should be mentioned.

There are also several problems which affect both photo-ionization modeling as well as classical methods to determine physical parameters. The first problem is the incompleteness of the atomic data. This problem is being tackled now through the opacity project (Seaton 1987) and the situation is improving rapidly. Another problem is the alleged presence of electron temperature fluctuations (the so called t^2-problem, e.g. Peimbert 1967; Dinerstein 1983; Zuckerman & Aller 1986; Garnett 1992). It has been proposed that temperature fluctuations are responsible for the discrepancy between abundances derived from collisionally excited lines and recombination lines, which are observed in some nebulae. Liu (1997) has shown that this discrepancy is not caused by temperature fluctuations and therefore a different mechanism must be invoked to explain this effect. Since these abundance discrepancies can be very large (a factor of 10 has been observed), this is one of the most important problems in present day PN research.

In Sect. 2.2 the method to obtain the physical parameters of a PN is described. In Sect. 2.3 the test model, used to verify the method, is described. In Sect. 2.4 the influence of measurement errors on the derived physical parameters is discussed. In Sect. 2.5 the influence of errors in the model assumptions is investigated. Subsequently the method is applied to a small sample of galactic bulge nebulae. The results are discussed in Sect. 2.6. Our conclusions are given in Sect. 2.7. All the symbols used in this paper are defined in Appendix 2.8.

2.2 The method

To model the planetary nebula, we use a modified version of the photo-ionization code CLOUDY 84.06 (Ferland 1993b). This photo-ionization code was chosen because it is widely used and has been tested for many different physical conditions. It includes a good dust model and a chemical network for the formation of molecules. This enables a fairly realistic modeling of the neutral zone of the nebula. We added a prediction for the radio continuum flux to the original code. An additional advantage of CLOUDY is that the code is fast, which is needed for our method.

The model for the PN is quite simple, and comprises the following assumptions:

1. The central star has a blackbody spectrum.
2. The nebula is spherically symmetric.
3. The density is constant inside the Strömgren radius of the nebula, and varies as $1/r^2$ outside.
4. Dust grains are intermixed with the gas at a constant dust-to-gas ratio; if no information on the composition is available they are assumed to be a mixture of graphite and silicates.
5. The filling factor, describing the small scale clumpiness of the gas, can be fixed at any value. If no information is available it is taken to be unity.
6. The distance to the nebula is fixed by an independent individual or statistical method.

The first assumption is imposed by CLOUDY. There is a grid of stellar atmosphere models present in CLOUDY, which is appropriate for PN nuclei. However, this grid only extends down to 80 000 K, which is not low enough for our purposes. Also the spacing in the grid is quite coarse, making interpolation awkward. However, when a suitable grid of atmosphere models becomes available this can easily be incorporated in our method.
The second assumption is also imposed by CLOUDY. The code is one-dimensional, and thus necessitates the assumption of spherical symmetry. Also, the computation time would be unacceptably long if non-spherically symmetric models were used in an iterative scheme. For certain nebulae (e.g. bipolar nebulae) this assumption is obviously not appropriate. However, when observables are used which are integrated over the entire nebula and one keeps in mind that the resulting model parameters are averaged values such models can still be useful. This problem will be studied in some more detail in Sect. 2.5.

The third assumption is a crude simplification inspired by the density profiles resulting from hydro-dynamical modeling of PN shells. The ionized part of the nebula is assumed to be that part of the Asymptotic Giant Branch (AGB) shell swept up by the fast wind presently coming from the central star. The density of this swept-up material is taken to be constant. Outside the ionized region we assume the presence of a neutral, undisturbed AGB shell. Taking the AGB mass-loss rate and velocity to be constant, this implies a $1/r^2$ density law for this material. A simplification of the nebular structure, where in reality often density gradients are found, is necessary to reduce the number of free parameters, because otherwise the modeling would become ill-determined. If more detailed information on the density structure of a PN exists, this can be used in our method since CLOUDY can handle arbitrary density profiles.
The fourth assumption is implied by the fact that dust is known to be present in PN. This is certainly the case for the neutral envelope, but for many nebulae dust is also present in the ionized region. Recent observations with *ISO* suggest that this is the case for all but the most evolved nebulae. This would imply that dust grains are destroyed by the stellar UV radiation, but that this process is slow. The present knowledge of dust destruction doesn't permit us to make very specific assumptions. Therefore, when no detailed information is available, we will assume that the inner radius of the dust coincides with the inner radius of the gas. If this radius is very close to the star, an alternative prescription can be used where grains only exist there where their equilibrium temperature is below a pre-described sublimation temperature. When more detailed information is available, one can also prescribe a fixed radius (e.g. the Strömgren radius) for the inner boundary of the dusty region. In all cases the dust-to-gas ratio has to be kept at a constant ratio in those regions where dust is present. If no information on the dust composition is available, a mixture of silicate and graphite grains is assumed as a compromise.
The fifth assumption is commonly made in nebular modeling. The actual value, or range of values, of the filling factor is very uncertain and is still a matter of debate (e.g. Kingsburgh & Barlow 1992).
The sixth assumption is necessary to construct a photo-ionization model, as was already discussed in Sect. 2.1. An alternative approach could be to keep the distance as a free parameter and determine it self-consistently along with the physical parameters of the nebula. This alternative method has been tested and was found to be very unstable. In most cases a distance from a good statistical distance scale or an individual method will yield more accurate answers. Hence we decided to keep the distance as a fixed parameter in all cases. More details can be found in Sect. 2.6.2.F.

The above assumptions give the following free parameters: the stellar temperature, the luminosity of the central star, the total hydrogen density in the ionized region, the inner radius of the nebula, the dust to gas ratio, and the abundances in the nebula. The outer radius of the nebula is not fixed as an input parameter, but calculated in a self-consistent manner, as described at the end of this section. Adopting certain values for the input parameters, it is possible to calculate a model for the nebula with CLOUDY, predicting the continuum and line fluxes, photometric magnitudes (including the contribution of line emission) and the Strömgren radius.

Our objective is to derive from a given set of observables the physical parameters of the PN. Therefore it is assumed that there exists a unique set of input parameters, for which the resulting model predictions give the best fit to the observables. These input parameters are then considered the best estimate for the physical properties of the PN. To compare the model predictions with the observed quantities, a goodness-of-fit estimator is calculated. This estimator is minimized by varying all the input parameters of the model, using the algorithm AMOEBA (Press et al. 1986). The full set of observed quantities necessary to do this is:

1. The emission line spectrum of the nebula. Usually this is an optical spectrum, but might also be a ultraviolet and/or infrared (IR) spectrum. The line ratios make it possible to constrain the stellar temperature, the density and the electron temperature in the nebula. They are also required to determine the abundances. For elements for which no lines are available we assume standard abundances (Aller & Czyzak 1983).
2. Since dust is included in the model we also need information on the mid- and far-infrared continuum. For this the *IRAS* fluxes are used.
3. To constrain the emission measure, either a radio continuum measurement (e.g. at 6 cm) is needed, or the absolute flux value of some hydrogen recombination line (usually Hβ). Radio fluxes are preferred, because dereddened optical line fluxes usually are more uncertain than radio measurements.
4. An accurate angular diameter of the nebula is needed, which we define as $\Theta_{\rm d} = 2r_{\rm str}/D$. Diameters determined from radio continuum observations are preferred.

Since we want to calculate the IR spectrum of the nebula, it is necessary to include the neutral region of the PN in the modeling. Especially the far-IR flux is produced predominantly in this region. Since the extent of the neutral region is unknown, we determine the outer radius from the long wavelength end of the dust emission. The longest wavelength *IRAS* flux available is best suited to do this. Usually this is the *IRAS* 60 μm flux, sometimes the *IRAS* 100 μm flux. When an individual model is calculated, the code integrates outward until the observed *IRAS* flux is reached. We define this point to be the outer boundary of the nebula. To prevent the code from integrating outward indefinitely, we use the additional criterion that the electron density should not drop below 0.1 cm^{-3}.

The goodness-of-fit estimator χ^2 is calculated using a non-standard procedure. We divided the observables into four categories: emission line ratios (lr), IR emission (e.g. *IRAS* fluxes, labeled ir), radio or Hβ fluxes (rd) and the angular diameter (ad). We will now explain how the total χ^2 of the model is calculated. First, the contribution χ_i^2 of the i-th observable to the total χ^2 is calculated as

$$\chi_i^2 = \left(\frac{O_i^{\mathrm{m}} - O_i^{\mathrm{o}}}{\min(O_i^{\mathrm{m}}, O_i^{\mathrm{o}})\, \sigma_i} \right)^2 ,$$

where O_i^{o} is the observed value for the i-th observable, O_i^{m} is the model value for this observable and σ_i is the relative error in the observed value. If the observable could only be observed as an upper limit, the following alternative formulation is used

$$\chi_i^2 = \left(\frac{\max(O_i^{\mathrm{m}}, O_i^{\mathrm{o}}) - O_i^{\mathrm{o}}}{O_i^{\mathrm{o}}\, \sigma_i} \right)^2 ,$$

where O_i^{o} now stands for the upper limit. Second, for each of the four categories the *average* χ_{c}^2 is calculated using

$$\chi_{\mathrm{c}}^2 = \frac{\sum_{i=1}^{N} \chi_i^2}{N} \quad \text{for c} = \text{lr, ir, rd, ad}.$$

Here N is the number of observables in each category. If a certain category is empty, the value for χ_{c}^2 is taken to be zero. Third, the total χ^2 of the model is calculated by adding all the averaged χ_{c}^2-values for each of the categories. We can write this as

$$\chi^2 = \chi_{\mathrm{lr}}^2 + \chi_{\mathrm{ir}}^2 + \chi_{\mathrm{rd}}^2 + \chi_{\mathrm{ad}}^2.$$

We chose this procedure because normally there are many more line ratios available than other types of observables. If a standard χ^2 would have been used, the line ratios would have completely dominated the fitting process and the other types of observables would not have gotten sufficient weight.

2.3 Testing the method

We will test the method in two stages. First we will do a formal test of the convergence of the algorithm. For this we use an ideal set of 'observables' computed with CLOUDY, using the same model assumptions as described in Sect. 2.2. The results of this test are described in Sect. 2.3.1. Second, we will test the robustness of the method. This will be done in two different ways. We will test the robustness of the results against measurement errors in the observables (Sect. 2.4) and we will test the robustness against errors in the model assumptions (Sect. 2.5). These tests give a first indication of the accuracy with which the physical parameters can be determined and are a first step towards determining error margins for the modeling results. One should however keep in mind that in principle these results are only correct for the particular model studied in this paper. Although it can be expected that these results are valid for a much wider range of models, it is also clear that they probably are not valid in all cases.

Table 2.1 — *The physical parameters for the artificial test model (the input for the method) and the resulting best-fit model obtained with the method.*

	input model	best fit
$\lg(T_*/\mathrm{K})$	4.528	4.528
$\lg(L_*/\mathrm{L}_\odot)$	3.686	3.686
$\lg(n_{\mathrm{H}}/\mathrm{cm}^{-3})$	4.179	4.179
r_{in}/mpc	20.69	20.70
r_{str}/mpc	30.12	30.12
r_{out}/mpc	142.3	142.2
$M_{\mathrm{ion}}/\mathrm{M}_\odot$	0.0394	0.0393
$M_{\mathrm{sh}}/\mathrm{M}_\odot$	0.678	0.679
$\lg \Gamma$	−2.234	−2.234
ϵ(He)	10.932	10.934
ϵ(N)	7.095	7.094
ϵ(O)	8.252	8.255
ϵ(Ne)	7.101	7.106
ϵ(S)	6.385	6.386
ϵ(Ar)	5.779	5.780
T_{e}/kK	10.063	10.058
$\lg U$	−2.086	−2.088

2.3.1 The artificial test model

In order to verify whether the method could reproduce the physical parameters correctly, we constructed an artificial set of 'observables' for which the physical parameters were known in advance. We used CLOUDY to calculate this test model. The model is more or less typical of a young PN, with a small, high density shell of low excitation. The metallicity of the nebula was low: $\lg Z \approx -0.65$. The parameters of the test model are given in Table 2.1.

We calculated several sequences of models (runs) using different initial estimates for the model parameters. These sequences were terminated when a prescribed accuracy was reached for all model parameters. We did several runs for each set of input data to assure that AMOEBA found the correct minimum of the χ^2-function. Sometimes AMOEBA would stop before the correct minimum was reached and this procedure is necessary to circumvent this problem. This is a well known problem of all numerical algorithms searching for the minimum in a multi-dimensional space (e.g. Press et al. 1986).

When the computed observables of the test model were used as input for the method, we could reproduce all physical parameters with good accuracy. The smallest discrepancy was approximately 0.02 % for the stellar temperature and luminosity; the largest discrepancy was less than 1.2 % for the neon abundance. These small differences can be attributed to the fact that for the weakest lines in the input file (e.g. the neon lines), round-off errors in the printed values for the line flux ratios were non-negligible. The values of the physical parameters for the best-fit model are given in Table 2.1. The computed observables of the original test model and the best-fit model are shown in Table 2.2. The

Table 2.2 — *Comparison between the 'observables' from the test model (the input for the method) and the results from the best-fit model obtained with the method. The strength of the emission lines are given relative to* Hβ *= 100. The entry [O II] λ3727 stands for both lines in the doublet.*

ion	λ Å	input model	best fit
[O II]	3727	122.11	122.62
[Ne III]	3869	2.10	2.11
[Ne III]	3969	0.65	0.65
Hδ	4102	30.01	30.02
Hγ	4340	50.72	50.73
[O III]	4363	0.60	0.60
He I	4472	2.84	2.84
He II	4686	<0.50	0.00
Hβ	4861	100.00	100.00
[O III]	4959	30.48	30.45
[O III]	5007	91.45	91.35
He I	5876	8.95	8.95
[O I]	6300	0.92	0.92
[S III]	6312	0.99	0.99
[O I]	6364	0.31	0.31
[N II]	6548	12.49	12.48
Hα	6563	270.85	270.84
[N II]	6584	37.47	37.45
[S II]	6716	1.79	1.80
[S II]	6731	3.76	3.76
He I	7065	4.60	4.60
[Ar III]	7136	3.25	3.25
[O II]	7319	14.47	14.54
[O II]	7330	11.74	11.79
[Ar III]	7751	0.76	0.76
[S III]	9069	15.87	15.86
[S III]	9532	41.35	41.32
obs.	unit		
F_ν(12 μm)	Jy	2.137	2.139
F_ν(25 μm)	Jy	33.19	33.19
F_ν(60 μm)	Jy	35.00	35.00
F_ν(100 μm)	Jy	10.04	10.04
F_ν(2 cm)	mJy	93.23	93.22
F_ν(6 cm)	mJy	103.97	103.96
Θ_d	arcsec	3.154	3.155
χ^2			9.5×10^{-4}

value of χ^2 was calculated assuming an uncertainty of 10 % in all 'observables'. The χ^2 is very low due to the fact that this is a perfect test model, i.e. the input data contain no measurement errors.

We conclude that the method is capable of reproducing the physical parameters of this ideal test model.

2.4 The influence of measurement errors

In this section we investigate what consequences 'measurement' errors in the observables of our ideal test model have for the determination of the physical parameters. Two different approaches to this problem were used, depending on the type of observable. In the case of the emission lines we chose to investigate the influence of measurement errors in all lines simultaneously (Sect. 2.4.1). For the *IRAS* fluxes, the angular diameter, and the radio flux we investigated the effect of measurement errors in each observable separately (Sect. 2.4.2).

2.4.1 The emission lines

In order to assess the influence of measurement errors in the emission line ratios, we have calculated twelve artificial spectra, ranging from 3500 Å to 10 000 Å, based on our test model described in Sect. 2.3. We have tried to make these spectra as realistic as possible. We assumed that the spectra suffered from interstellar reddening with $E(B-V) = 0.50$. The reddening law given by Pottasch (1984) was adopted. Then we assumed that the spectra were taken on a CCD with a response curve given by

$$R_\lambda = 0.05 + 0.45 \exp\left[-4\ln 2\left(\frac{(\lambda/\text{Å}) - 6500}{3000}\right)^2\right].$$

The resulting spectra had approximately 40 000 counts in Hα. The resolution was 5.75 Å and there were 2.5 pixels per resolution element. Subsequently Poisson noise was added to each of the spectra, assuming an additional read-out-noise of 6.0 counts. Finally the spectra were corrected back for the CCD response (i.e. were 'flux calibrated'). One of the resulting (still reddened) spectra is shown in Fig. 2.1. All twelve spectra are essentially identical, apart from the fact that a different seed for the random generator was used in each case. This is analogous to an astronomical object from which twelve separate spectra were taken using the same instrument and settings for each spectrum.

The line intensities in these spectra were determined using the following procedure. First, the line fluxes were measured using gaussian fits. Subsequently, a first attempt was made to deredden these fluxes, using the following estimate for the interstellar extinction:

$$E(B-V) = 2.251 \times \lg\left[\frac{F(\text{H}\alpha)}{R \times F(\text{H}\beta)}\right], \qquad (1)$$

where $F(\text{H}\alpha)$ and $F(\text{H}\beta)$ stand for the observed fluxes of both lines, and R stands for the intrinsic (i.e. unreddened) ratio $F(\text{H}\alpha)/F(\text{H}\beta)$. In our first attempt, the canonical value R = 2.85 would be assumed. Next, the dereddened line fluxes were used to make a first estimate for the electron temperature and density using the package NEBULAR in IRAF (Shaw & Dufour 1995). These values were then used as model input for CLOUDY to determine a better estimate for R. The resulting value was substituted in eq. (1), and in this way a more accurate measurement for the interstellar extinction could be obtained. Subsequently, the final dereddening of the spectrum could be done, using the extinction law from Pottasch (1984).

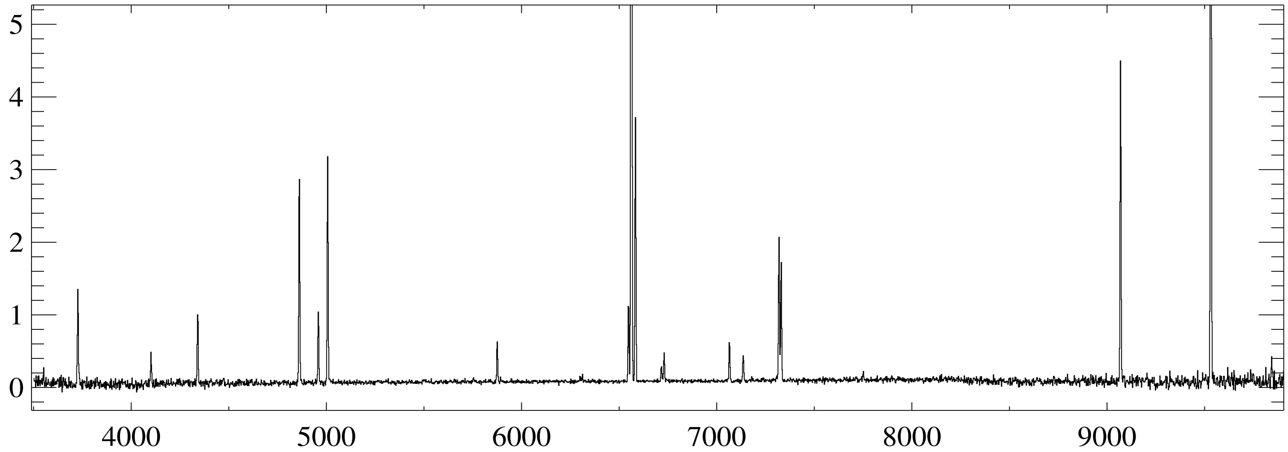

Figure 2.1 — *Artificial spectrum of the test model. This spectrum was calculated using a realistic detector response function and an interstellar extinction of $E(B-V) = 0.5$. The resolution is 5.75 Å. The x-axis gives the wavelength in Å, the y-axis the flux, normalized at the inner radius of the nebula, in 10^{-16} W m^{-2} Hz^{-1}.*

A. Error estimates

We used two different methods to obtain error estimates for the line fluxes. The first step for both methods is to make a gaussian fit to the observed line profile, assuming a constant 1 σ error in the spectrum. For one method the error estimate for the line flux was calculated by integrating the absolute value of the residuals (i.e. the difference between the fitted gaussian and the actual spectrum) over the range of the fit (approximately -2.5 to $+2.5 \times$ FWHM from the center of the line). This error estimate will be denoted by e_2. We will refer to this method as the residual estimate.

For the other method we use the residuals to get an estimate for the 1 σ errors in the original spectrum. For this we assume that the residuals originate from noise only and that the noise can be described by Poisson statistics. We can write

$$F_\lambda = K_\lambda \times N_\lambda$$

$$\sigma_\lambda = K_\lambda \times \sqrt{N_\lambda}.$$

Our assumptions assure that the residuals r_λ^2 will, on average, be equal to the error in the original spectrum σ_λ^2. Therefore we can replace σ_λ by r_λ and get the following equation

$$K_\lambda = r_\lambda^2 / F_\lambda$$

which will on average be true. Subsequently we assume that K_λ is constant over the entire width of the profile. Hence we can average K_λ over all pixels used in the fit ($\overline{K_\lambda}$). This should give a good approximation to the actual value of K_λ. The average $\overline{K_\lambda}$ is subsequently used to calculate the 1 σ errors in the original spectrum

$$\sigma_\lambda = \sqrt{\overline{K_\lambda} \times F_\lambda}.$$

Using these new 1 σ errors, the gaussian fit was repeated and a covariance matrix was calculated. We could subsequently calculate the 1 σ error in the line flux using standard error propagation theory. These errors will be denoted by e_1. We will refer to this method as the K-method.

It was found that for the spectra studied here, the residual estimates were substantially higher for weak lines than the results of the K-method. For strong lines however, both methods give almost identical results. The line fluxes that were measured in the spectrum have to be converted to intensities (i.e. scaled relative to Hβ) and dereddened. Both steps introduce additional uncertainties in the result. These uncertainties were quadratically summed, assuming that the adopted intrinsic flux ratio $F(\mathrm{H}\alpha)/F(\mathrm{H}\beta)$ had a relative error of 5 % and $E(B-V)$ had a relative error of 10 %.

B. Results and discussion

The line intensities we had measured were used to determine the electron temperature, electron density and nebular abundances for each of the twelve spectra. This was done in three different ways. First, classical line diagnostics were applied. To this end the NEBULAR package in IRAF was used (Shaw & Dufour 1995), which we assume to be a state of the art implementation of these techniques. We determined the electron temperature using [O II], [N II] or [S III] lines and we determined the electron density using [S II] lines. The [O III] temperature could not be determined since the [O III] λ4363 line could not be detected in any of the twelve spectra. Once the electron temperature and density were known, we could determine the ionic abundances for N^+, O^0, O^+, O^{2+}, S^+, S^{2+} and Ar^{2+}. We could not determine the Ne^{2+} abundance, since in none of the spectra the neon lines were detectable. The abundances were determined assuming a constant electron temperature in all zones. For this the value from the [S III] diagnostic was used, which is the most accurate. The ionic abundances were converted to elemental abundances using the following four expressions.

$$\frac{N(\mathrm{O})}{N(\mathrm{H})} = \frac{N(\mathrm{O}^0) + N(\mathrm{O}^+) + N(\mathrm{O}^{2+})}{N(\mathrm{H}^+)}$$

$$\frac{N(\mathrm{N})}{N(\mathrm{H})} = \frac{N(\mathrm{N}^+)}{N(\mathrm{H}^+)} \left[\frac{N(\mathrm{O})}{N(\mathrm{O}^+)}\right]$$

$$\frac{N(\mathrm{S})}{N(\mathrm{H})} = \frac{N(\mathrm{S}^+) + N(\mathrm{S}^{2+})}{N(\mathrm{H}^+)}$$

$$\frac{N(\mathrm{Ar})}{N(\mathrm{H})} = 1.73\,\frac{N(\mathrm{Ar}^{2+})}{N(\mathrm{H}^+)}$$

The first and the third expression are only valid for a low excitation nebula, as is studied here. The second expression was taken from Henry (1990), the fourth from Ratag & Pottasch (1990). The He^+ abundance was computed using the expressions given in Brocklehurst (1971, 1972) and Clegg (1987). No attempt has been made to correct this result for the presence of neutral helium, which is very difficult to do. All results are listed in the first section of Table 2.3. We consider these values the most accurate that can be achieved with line diagnostics, given the quality of the spectra.

Second, we have used the measured line intensities, combined with either the error estimates from the K-method or the residual method, as input for our photo-ionization modeling. The values and error estimates for the other observables that are needed (i.e. the *IRAS* fluxes, the radio fluxes and the angular diameter) were kept at the values listed in Table 2.2. The model parameters for the best-fit models are listed in the last two section of Table 2.3.

The results shown in Table 2.3 suffer from two types of error. There is a systematic error due to the fact that the method will not give the exact result, even for perfectly measured data, and there is a random error due to fact that the noise affects the line fluxes. For the data we are studying here, the systematic error is much smaller than the random error. Hence, the random error is a good measure for the accuracy of each method. Therefore we have determined, for each of the rows in Table 2.3, the 1 σ standard deviation of the twelve individual determinations in that row. The results are shown in the last column. Note that the electron temperature and density with their respective standard deviations are given as linear quantities, while all other parameters with their standard deviations are given logarithmically.

When one compares the determination of the electron density using the [S II] lines with the determination by our photo-ionization method, one can see that the determination using the line diagnostic is far more unreliable. This can be understood when one realizes that the density in the nebula is high. This makes the [S II] method very sensitive to measurement errors because the [S II] line ratio is only a very shallow function of density in this regime. The photo-ionization method obviously does not suffer from such problems and yields far more accurate results. When one compares the determination of the electron temperature using the [S III] lines with the determination using the [N II] lines, one can see that [S III] diagnostic is more reliable. This is caused by the fact that the [N II] λ5755 line is very close to the detection limit in the spectra, while the [S III] λ6312 line is more easily detected and hence suffers less from noise in the spectrum. The [S III] method is also somewhat more stable against measurement errors. The temperature determined with the [O II] method is shown to be very unreliable. This method uses both the [O II] doublets at λ3727 and λ7325. The poor results for the [O II] method are not caused by noise in the spectrum: all the lines in these doublets are reasonably strong. However, due to the fact that the doublets are spaced far apart in the spectrum, the method does suffer from uncertainties in the dereddening. The method is also intrinsically more sensitive to errors in the line ratio. The combination of these two effects explains the poor results for the [O II] method. Again one can see that the results from the photo-ionization modeling give more accurate results, although the differences are somewhat less striking than in the case of the electron density. The fact that photo-ionization modeling yields more accurate values for the electron density and temperature can be understood in a qualitative sense when one realizes that this method uses the entire spectrum and also other information like the radio flux and the angular diameter to make a self-consistent model of the entire ionized region. This makes the method less sensitive to measurement errors in one individual line. The effects of the measurement errors in each of the lines tend to cancel each other. From this it also apparent that the accuracy of photo-ionization modeling relies on the fact that many lines of different ionization stages should be present in the spectrum.

When one compares the abundance determinations for the elements heavier than helium, one can see that the determination using photo-ionization modeling again is more accurate. This is caused by the fact that the electron temperature and density are more accurately determined in the photo-ionization models. It is especially worth noticing the uncertainty of almost a factor of two in the determination of the oxygen abundance using line diagnostics. This is caused by the fact that the [O III] λ5007 line is an important cooling line of the plasma. This implies that the strength of this line, the oxygen abundance and the electron temperature in the plasma are very closely linked. Raising the oxygen abundance will result in a stronger λ5007 line. This in turn will result in more efficient cooling and hence in a lower electron temperature. This effect will make the λ5007 line weaker, thus reducing the effect of the rising abundance. The net result is that the O^{2+} abundance is a very sensitive function of the electron temperature given the strength of the λ5007 line. Since O^{2+} is an important ionization stage, this will also affect the total oxygen abundance.

In all honesty it should be mentioned that the results in Table 2.3 are somewhat biased towards more accurate

Table 2.3 — *The physical parameters determined using the test spectra with noise added. First the results are given using classical line ratio methods, determined using the package* NEBULAR *in* IRAF. *An entry 'und.' indicates that the measured line ratio was outside the theoretically allowed range. In 7 out of 12 spectra only upper limits could be determined for the [N II] λ5755 line, these were converted into upper limits for the electron temperature. Second, the results from* CLOUDY *are given, using both the e_1 and e_2 error estimates. The first 12 columns give the results for each of the individual spectra, the last column gives the 1σ standard deviation of the results in that row and is a measure for the accuracy of the determination of that particular physical parameter.*

using classical methods	sp. 1	sp. 2	sp. 3	sp. 4	sp. 5	sp. 6	sp. 7	sp. 8	sp. 9	sp. 10	sp. 11	sp. 12	σ
$\epsilon(He^+)$	10.815	10.821	10.740	10.791	10.806	10.777	10.787	10.809	10.782	10.772	10.809	10.802	0.022
ϵ(N)	7.131	7.081	6.960	7.065	7.185	6.909	7.047	7.035	7.130	7.063	7.261	6.962	0.095
ϵ(O)	8.314	8.356	8.002	8.292	8.472	7.904	8.448	8.261	8.706	8.516	8.803	8.104	0.254
ϵ(S)	6.437	6.383	6.307	6.412	6.502	6.262	6.448	6.391	6.535	6.469	6.630	6.336	0.098
ϵ(Ar)	5.827	5.768	5.648	5.814	5.842	5.594	5.714	5.731	5.711	5.700	5.893	5.660	0.085
T_e/kK [O II]	16.838	11.869	15.678	12.714	13.458	16.538	6.836	11.200	5.551	6.458	7.189	11.288	3.847
T_e/kK [N II]	< 11.129	12.483	< 11.090	11.358	< 11.192	16.258	< 9.097	< 10.898	< 8.246	10.772	< 9.387	12.261	1.918†
T_e/kK [S III]	9.089	9.389	10.809	9.568	8.629	11.432	10.300	9.855	9.944	10.224	8.482	10.803	0.862
n_e/cm^{-3} [S II]	8000	und.	und.	8800	und.	8700	37900	13900	57400	43700	33000	15100	17200

CLOUDY, using error estimate e_1	sp. 1	sp. 2	sp. 3	sp. 4	sp. 5	sp. 6	sp. 7	sp. 8	sp. 9	sp. 10	sp. 11	sp. 12	σ
$\lg(T_*/K)$	4.530	4.528	4.525	4.525	4.529	4.532	4.528	4.524	4.527	4.528	4.527	4.529	0.002
$\lg(L_*/L_\odot)$	3.683	3.686	3.687	3.692	3.685	3.677	3.684	3.689	3.688	3.683	3.687	3.682	0.004
$\lg(n_H/cm^{-3})$	4.165	4.170	4.210	4.166	4.165	4.198	4.182	4.207	4.168	4.205	4.172	4.197	0.017
$\lg(r_{in}/cm)$	16.798	16.802	16.821	16.803	16.798	16.813	16.806	16.823	16.799	16.818	16.802	16.815	0.009
$\lg(r_{str}/cm)$	16.972	16.970	16.962	16.973	16.972	16.963	16.967	16.963	16.971	16.962	16.970	16.963	0.004
$\lg(r_{out}/cm)$	17.652	17.648	17.606	17.659	17.656	17.600	17.639	17.602	17.660	17.603	17.651	17.610	0.024
$\lg(M_{ion}/M_\odot)$	−1.391	−1.397	−1.437	−1.396	−1.391	−1.424	−1.408	−1.434	−1.395	−1.431	−1.399	−1.424	0.017
$\lg(M_{sh}/M_\odot)$	−0.156	−0.150	−0.208	−0.153	−0.159	−0.206	−0.175	−0.197	−0.164	−0.199	−0.159	−0.190	0.021
$\lg\Gamma$	−2.235	−2.248	−2.225	−2.243	−2.232	−2.220	−2.229	−2.242	−2.228	−2.231	−2.238	−2.233	0.008
$\epsilon(He^+)$	10.804	10.810	10.740	10.774	10.788	10.796	10.775	10.767	10.760	10.779	10.784	10.790	0.019
ϵ(He)	10.962	10.994	10.881	10.931	10.934	10.956	10.919	10.950	10.886	10.949	10.940	10.966	0.031
ϵ(N)	7.089	7.108	7.106	7.106	7.097	7.196	7.102	7.087	7.106	7.121	7.094	7.114	0.027
ϵ(O)	8.219	8.284	8.307	8.297	8.229	8.236	8.252	8.351	8.223	8.302	8.243	8.300	0.040
ϵ(Ne)	7.101‡	7.101‡	7.101‡	7.101‡	7.101‡	7.101‡	7.101‡	7.101‡	7.101‡	7.101‡	7.101‡	7.101‡	
ϵ(S)	6.361	6.344	6.386	6.408	6.337	6.437	6.387	6.389	6.369	6.403	6.385	6.424	0.029
ϵ(Ar)	5.742	5.754	5.795	5.832	5.699	5.793	5.801	5.855	5.742	5.776	5.758	5.841	0.044
T_e/kK	10.121	10.020	9.985	9.974	10.118	10.061	10.067	9.905	10.115	9.984	10.069	9.979	0.066
n_e/cm^{-3}	15400	15600	17000	15400	15400	16600	16000	16900	15500	16900	15600	16600	640
$\lg U$	−2.055	−2.070	−2.155	−2.069	−2.056	−2.121	−2.092	−2.156	−2.063	−2.142	−2.074	−2.125	0.038
χ^2	0.594	0.418	0.762	0.163	0.614	1.633	0.159	1.173	0.422	0.760	0.191	0.501	

CLOUDY, using error estimate e_2	sp. 1	sp. 2	sp. 3	sp. 4	sp. 5	sp. 6	sp. 7	sp. 8	sp. 9	sp. 10	sp. 11	sp. 12	σ
$\lg(T_*/K)$	4.530	4.531	4.524	4.525	4.530	4.530	4.529	4.523	4.527	4.528	4.528	4.528	0.002
$\lg(L_*/L_\odot)$	3.683	3.682	3.690	3.691	3.683	3.683	3.684	3.692	3.688	3.686	3.686	3.684	0.003
$\lg(n_H/cm^{-3})$	4.175	4.170	4.188	4.171	4.174	4.181	4.180	4.189	4.175	4.182	4.177	4.185	0.006
$\lg(r_{in}/cm)$	16.803	16.800	16.811	16.804	16.802	16.806	16.805	16.814	16.804	16.808	16.805	16.809	0.004
$\lg(r_{str}/cm)$	16.969	16.970	16.967	16.971	16.969	16.967	16.968	16.967	16.970	16.967	16.969	16.966	0.001
$\lg(r_{out}/cm)$	17.642	17.643	17.640	17.656	17.644	17.634	17.639	17.636	17.650	17.636	17.644	17.632	0.007
$\lg(M_{ion}/M_\odot)$	−1.401	−1.397	−1.415	−1.400	−1.401	−1.407	−1.407	−1.416	−1.402	−1.409	−1.403	−1.411	0.006
$\lg(M_{sh}/M_\odot)$	−0.164	−0.147	−0.182	−0.157	−0.167	−0.172	−0.177	−0.164	−0.168	−0.167	−0.166	−0.173	0.009
$\lg\Gamma$	−2.236	−2.250	−2.228	−2.241	−2.231	−2.234	−2.227	−2.250	−2.231	−2.240	−2.236	−2.236	0.007
$\epsilon(He^+)$	10.799	10.833	10.738	10.770	10.789	10.795	10.774	10.773	10.763	10.791	10.783	10.788	0.022
ϵ(He)	10.962	11.034	10.866	10.923	10.940	10.959	10.916	10.955	10.899	10.963	10.940	10.955	0.039
ϵ(N)	7.091	7.081	7.108	7.099	7.096	7.130	7.105	7.084	7.104	7.090	7.094	7.102	0.012
ϵ(O)	8.244	8.282	8.261	8.290	8.244	8.244	8.246	8.328	8.250	8.275	8.248	8.271	0.025
ϵ(Ne)	7.101‡	7.101‡	7.101‡	7.101‡	7.101‡	7.101‡	7.101‡	7.101‡	7.101‡	7.101‡	7.101‡	7.101‡	
ϵ(S)	6.383	6.357	6.382	6.410	6.372	6.419	6.383	6.392	6.371	6.394	6.399	6.414	0.018
ϵ(Ar)	5.777	5.786	5.769	5.828	5.725	5.799	5.793	5.838	5.753	5.787	5.768	5.821	0.031
T_e/kK	10.078	10.030	10.049	9.987	10.087	10.055	10.078	9.930	10.071	10.022	10.060	10.022	0.043
n_e/cm^{-3}	15800	15700	16200	15600	15800	16000	15900	16200	15700	16000	15800	16100	190
$\lg U$	−2.076	−2.065	−2.111	−2.078	−2.075	−2.089	−2.088	−2.118	−2.082	−2.095	−2.084	−2.100	0.015
χ^2	0.114	0.341	0.163	0.076	0.171	0.364	0.046	0.419	0.118	0.168	0.037	0.123	

† The standard deviation was calculated excluding the upper limits.
‡ The neon abundance was held constant since only upper limits were available for the neon lines.

results for the photo-ionization modeling. The results for these models do not only depend on the emission line spectrum, but also on other observables like the *IRAS* and radio fluxes and the angular diameter which are assumed to be perfectly measured. Also the results depend on the model assumptions, which in this case are a perfect match with the assumptions used to compute the artificial spectrum. In reality this will of course not be the case, and this will have a negative effect on the accuracy of photo-ionization models. These effects will be discussed in more detail in the following sections. Since line diagnostics do not suffer, or at least suffer less from these uncertainties, it is not *a priori* clear that photo-ionization modeling yields more accurate results. Probably the most important factor for accurate abundance determinations with photo-ionization models is the choice of the central star spectrum.

The situation concerning the determination of the helium abundance is different from other elements. This is because the helium lines are recombination lines and the relative strength of these lines is much less sensitive to the electron temperature and density. Hence the accuracy of the abundance determination is mainly determined by the measurement error in the line flux. This explains why the accuracy of the classical method and the photo-ionization method is much the same. One can also see that the determination of the total helium abundance is less accurate than the determination of the He^+ abundance. This indicates the difficulty of correcting for the neutral helium fraction, even when using photo-ionization models which in principle give the most accurate correction.

The photo-ionization models do not only give the electron temperature, density and the abundances, but also yield values for other physical parameters. One can see that these parameters are determined with high precision. Most accuracies are within a few percent. Hence we conclude that noise in the spectrum has little influence on the determination of these parameters. One can see that the photo-ionization models using the residual error estimates are more accurate that the models using the error estimates from the K-method. This can be made plausible in the following way. The noise in the spectrum mainly affects weak lines. Therefore the measured flux for these lines will deviate most from the intrinsic flux. Hence it can be expected that these lines will have the most negative influence on the model. Since the residual method gives larger error estimates for weak lines, less weight will be given to them in the modeling. Hence their overall influence will be less and the resulting models will be better. From this we can conclude that that the error estimates are important for the accuracy of the resulting models and also that care should be taken not to give too much weight to weak lines since they can have a negative effect on the quality of the models.

From the results in this section we can draw the conclusion that in principle it is possible to achieve a higher accuracy with photo-ionization models, when compared to classical line diagnostics, given that sufficient lines of different ionization stages are present in the spectrum and also that sufficient other observational material of good quality is present. Care should be taken in using realistic model assumptions and appropriate error estimates.

2.4.2 The angular diameter, radio flux and the IRAS fluxes

We investigated the effect of observational errors in the angular diameter, the radio flux and the *IRAS* fluxes by changing the values of the observables one by one. These observables were taken from our test model described in Sect. 2.3. We used observational errors amounting to -0.10, -0.05, $+0.05$, and $+0.10$ dex of the nominal value for each observable, and calculated the best-fit model for each case.

We will use the quantity ζ to express the effect of observational errors on the best-fit model. First we will give a definition of ζ. We will denote the physical parameters of the model (i.e. the stellar temperature, luminosity etc.) with the generic symbol P and the observables (i.e. the angular diameter, radio flux etc.) with the generic symbol O. For all the observables and physical parameters belonging to the models with observational errors we will use the subscript m, for the observables and physical parameters belonging to the true model without observational errors we will use the subscript t. The effect of the measurement error on the physical parameter is represented by:

$$\zeta \equiv \Delta \lg P / \Delta \lg O, \tag{2}$$

where we have used the definitions

$$\Delta \lg O = \lg O_\mathrm{m} - \lg O_\mathrm{t} = \lg(O_\mathrm{m}/O_\mathrm{t}),$$

$$\Delta \lg P = \lg P_\mathrm{m} - \lg P_\mathrm{t} = \lg(P_\mathrm{m}/P_\mathrm{t}).$$

Hence from the previous discussion it is clear that $\Delta \lg O$ will only take the values -0.10, -0.05, $+0.05$, and $+0.10$ dex. The values for ζ are given in Table 2.4. To obtain the actual logarithmic difference in the physical parameter P (in dex), the value of ζ simply needs to be multiplied with the value of $\Delta \lg O$ given in the header of the column.

The meaning of ζ can be viewed in the following way. A measurement error in each of the observables will result in an error in the determination of each of the physical parameters of the best-fit model. To first order one can say that the relative error in the determination of the physical parameter is equal to the relative error in the observable times the absolute value of ζ. Hence, the smaller the absolute value of ζ is, the more stable the determination of the particular physical parameter is against the observational error that is being considered. One can roughly say that for $|\zeta| \leq 1$ the physical parameter is well determined or robust, for $1 < |\zeta| \leq 2.5$ the physical parameter is less reliable but still useful, and for $|\zeta| > 2.5$ the parameter is unreliable.

One should bear in mind that for a different set of observables (i.e. for a different PN), the coefficients ζ may differ. This is especially true if the model is less constrained

Table 2.4 — *The influence of measurement errors in the observables on the derived physical parameters. The measurement error was introduced in the observable (O) indicated in the first line of each header. The amount of the error in dex is indicated in the second line. The entries ζ in the table give the ratio of the logarithmic difference in the derived physical parameter P and the measurement error (i.e. $\Delta \lg P / \Delta \lg O$, both in dex).*

obs.	Θ_d				F_ν(6 cm)				F_ν(12 μm)			
$\Delta \lg O$/dex	−0.10	−0.05	+0.05	+0.10	−0.10	−0.05	+0.05	+0.10	−0.10	−0.05	+0.05	+0.10
T_*	−0.08	−0.09	−0.08	−0.07	+0.10	+0.11	+0.11	+0.11	−0.10	−0.09	−0.10	−0.09
L_*	+0.44	+0.47	+0.45	+0.41	+0.29	+0.28	+0.29	+0.30	+0.34	+0.35	+0.35	+0.33
n_H	−1.70	−1.78	−1.82	−1.77	+0.71	+0.75	+0.82	+0.81	−0.32	−0.33	−0.32	−0.28
r_{in}	+0.14	+0.05	−0.18	−0.29	+0.61	+0.62	+0.64	+0.62	−0.49	−0.51	−0.57	−0.59
r_{str}	+0.75	+0.78	+0.84	+0.85	+0.06	+0.06	+0.08	+0.10	−0.05	−0.04	−0.02	−0.02
r_{out}	+0.07	+0.29	+0.52	+0.50	+0.20	+0.14	+0.09	+0.11	+1.19	+1.22	+1.27	+1.19
M_{ion}	+1.49	+1.63	+1.69	+1.66	+0.35	+0.29	+0.25	+0.26	+0.42	+0.41	+0.43	+0.37
M_{sh}	−0.17	+0.12	+0.50	+0.54	+1.00	+0.96	+1.00	+1.04	+1.21	+1.24	+1.26	+1.19
Γ	−0.38	−0.48	−0.59	−0.58	−1.06	−1.03	−1.08	−1.10	−0.69	−0.68	−0.63	−0.58
ϵ(He)	+0.09	+0.29	+0.39	+0.40	−0.07	−0.12	−0.17	−0.15	+0.36	+0.38	+0.29	+0.35
ϵ(N)	−0.18	−0.21	−0.19	−0.19	+0.15	+0.14	+0.12	+0.14	−0.03	−0.02	−0.04	−0.05
ϵ(O)	−0.03	+0.07	+0.05	+0.00	+0.16	+0.10	+0.05	+0.02	+0.29	+0.28	+0.23	+0.22
ϵ(Ne)	−0.03	+0.08	+0.03	−0.13	+0.01	−0.10	−0.14	−0.19	+0.50	+0.51	+0.40	+0.36
ϵ(S)	−0.40	−0.40	−0.38	−0.40	+0.26	+0.23	+0.25	+0.21	+0.06	+0.07	+0.06	+0.05
ϵ(Ar)	+0.14	+0.29	+0.31	+0.27	+0.05	−0.02	−0.08	−0.11	+0.43	+0.46	+0.38	+0.37
T_e	−0.02	−0.04	−0.04	−0.03	−0.02	−0.01	−0.01	+0.00	−0.04	−0.04	−0.03	−0.03
$\lg U$	+1.69	+1.98	+2.46	+2.62	−1.41	−1.48	−1.57	−1.52	+1.44	+1.50	+1.61	+1.62

obs.	F_ν(25 μm)				F_ν(60 μm)				F_ν(100 μm)			
$\Delta \lg O$/dex	−0.10	−0.05	+0.05	+0.10	−0.10	−0.05	+0.05	+0.10	−0.10	−0.05	+0.05	+0.10
T_*	+0.01	+0.05	−0.01	+0.00	+0.03	+0.05	−0.08	−0.04	+0.06	−0.02	−0.02	−0.01
L_*	+0.13	+0.09	+0.13	+0.14	+0.06	+0.03	+0.10	+0.08	−0.06	−0.04	−0.02	−0.03
n_H	+0.16	+0.48	+0.02	+0.06	+0.41	+0.52	−0.53	−0.25	+0.43	−0.26	−0.24	−0.14
r_{in}	+0.33	+0.83	+0.07	+0.14	+0.92	+0.95	−0.76	−0.30	+0.83	−0.38	−0.38	−0.25
r_{str}	+0.02	+0.01	+0.02	+0.02	+0.02	+0.02	+0.03	+0.03	−0.01	−0.02	−0.01	−0.01
r_{out}	−3.61	−7.17	−1.83	−2.10	−3.48	−3.98	+7.18	+3.61	−3.50	+3.17	+4.29	+3.62
M_{ion}	−0.80	−1.69	−0.25	−0.29	−0.89	−0.99	+1.71	+0.84	−0.91	+0.59	+0.87	+0.80
M_{sh}	−3.92	−7.72	−2.22	−2.62	−3.62	−4.20	+7.72	+3.89	−3.62	+3.80	+4.74	+3.97
Γ	+1.26	+2.33	+0.54	+0.75	+2.06	+2.35	−1.67	−0.58	+1.70	−1.16	−0.98	−0.70
ϵ(He)	−0.16	−0.45	−0.03	−0.08	−0.55	−0.58	+0.40	+0.11	−0.35	+0.33	+0.24	+0.21
ϵ(N)	−0.02	−0.01	−0.03	−0.02	−0.01	+0.03	−0.05	−0.01	+0.00	+0.01	−0.01	−0.01
ϵ(O)	−0.19	−0.39	−0.07	−0.11	−0.29	−0.36	+0.35	+0.13	−0.31	+0.19	+0.16	+0.11
ϵ(Ne)	−0.21	−0.37	−0.05	−0.12	−0.13	−0.33	+0.47	+0.22	−0.32	+0.15	+0.13	+0.09
ϵ(S)	−0.06	−0.13	−0.03	−0.04	−0.11	−0.11	+0.06	+0.01	−0.08	+0.04	+0.04	+0.04
ϵ(Ar)	−0.26	−0.61	−0.09	−0.15	−0.54	−0.65	+0.52	+0.22	−0.50	+0.34	+0.26	+0.18
T_e	+0.04	+0.07	+0.01	+0.02	+0.06	+0.07	−0.06	−0.02	+0.06	−0.04	−0.03	−0.02
$\lg U$	−0.68	−1.95	−0.05	−0.22	−2.11	−2.28	+1.98	+0.85	−2.01	+0.94	+0.92	+0.60

by observables, but also models of PNe with a high temperature central star or of PNe which are optically thin in the Lyman continuum may show a different behavior. We will now give a more detailed discussion of the results in Table 2.4. Please note that this discussion pertains *only* to the influence of the measurement errors studied in this section. The results in Sect. 2.4.1 and Sect. 2.5 should also be considered to get a more complete overview of all the uncertainties involved in the modeling process.

A. The stellar temperature

From the table we can see that the stellar temperature remains almost uninfluenced by any measurement error. This result stems from the fact that many spectral lines of different ionization stages are used. All these lines already constrain the ionization structure and thus the stellar temperature. This means that the determination of the stellar temperature is very robust, provided that a reasonable number of spectral lines are present in the spectrum, ranging over different ionization stages. This can be a problem for obscured PN, since then many lines at shorter wavelengths will be undetectable due to extinction.

B. The stellar luminosity

We see that the determination of the stellar luminosity also is very robust. This result might be somewhat surprising. However, one should realize that the main uncertainty in the luminosity is caused by the uncertainty in the distance determination. In our models the distance was fixed at the correct value. Furthermore, the nebula we are studying is young and compact. Hence a large fraction of the stellar luminosity is absorbed by the dust (approximately 55 %).

Since we use the *IRAS* fluxes to constrain the model, this already gives a good constraint for the stellar luminosity.

C. The hydrogen density

The remarks in this section apply to the hydrogen density, but are equally valid for the average electron density. Many observables are considered by our method which influence the determination of the density: the radio emission, the angular diameter, the IR emission, and also the ionization structure in the nebula. From the results in Table 2.4 we can see that the determination of the density is mainly affected by measurement errors in the Strömgren diameter. This is not surprising; if for instance the measured Strömgren radius would be too large, then also the ionized volume in the model will be too large. In order to match the measured radio flux, the only thing the model can do is lower the nebular density. The second largest influence on the determination of the density are measurement errors in the radio flux itself, which can be understood using the same argument. The determination of the density is fairly robust against other measurement errors.

D. The inner, Strömgren and outer radius

The inner radius of the nebula is determined by two factors: the dust temperature, which is constrained by the *IRAS* colors, especially the 12 μm over 25 μm flux ratio, and the ionization structure of the nebula. Due to this double constraint the inner radius is reasonably well determined, although measurement errors in the radio flux and the various *IRAS* fluxes will influence the value to some degree.

The Strömgren radius of the nebula is determined by the angular diameter, which is defined as $\Theta_{\rm d} = 2r_{\rm str}/D$. Since one of the observables we try to fit is the angular diameter, this quantity should remain more or less constant in the best-fit model. Therefore the Strömgren radius is well determined except when there are measurement errors in the angular diameter itself.

For the outer radius the largest coefficients occur when the long wavelength end of the IR radiation (i.e. the *IRAS* 25 μm, 60 μm or 100 μm flux) is affected by measurement error. This could be expected, since the *IRAS* flux is used to define the outer radius of the nebula. The behavior of the outer radius can be quite different from the other two radii. This is caused by the fact that the amount of neutral material can vary, without having any effect on the radio emission or the emission line ratios (except for certain neutral lines like e.g. [O I] λ6300; however these lines have only limited influence on our models). The fact that the outer radius is unreliable is caused to some degree by the fact that we are trying to model a young, partially ionized nebula where the outer radius is only determined by the far-IR flux. For an older, completely ionized nebula one might expect the situation to be better since then the radio flux and the angular diameter can also give a constraint on the outer radius.

E. The (ionized) shell mass

Both the ionized shell mass and the total shell mass are completely determined by the hydrogen density and the inner, Strömgren and outer radius. Hence the remarks made in Sect. 2.4.2.C and Sect. 2.4.2.D pertain here as well. The coefficients for the ionized shell mass indicate that the value is less reliable but still useful. However, one should bear in mind that the value also heavily depends on the accuracy of the assumed distance and this will be the main source of uncertainty. The total shell mass should be considered unreliable even when an accurate distance is available.

F. The dust-to-gas ratio

The determination of the dust-to-gas ratio is mainly influenced by the uncertainty in the 25 μm, 60 μm and 100 μm *IRAS* fluxes and the radio flux. This latter result may seem surprising, but can be understood when we consider the change in the density caused by the measurement error in the radio flux. If the dust-to-gas ratio would have remained unchanged, the *IRAS* fluxes would have changed in the same way as the radio flux. Since there are no measurement errors in the *IRAS* fluxes in this particular model, this effect needs to be countered by changing the dust-to-gas ratio in the opposite sense as the hydrogen density. The coefficients listed in Table 2.4 can become fairly large and hence the dust-to-gas ratio should be considered less reliable but still useful.

G. The abundances

All the coefficients for the abundances are small, hence the determination of the abundances is robust (provided that at least two lines, preferably of different ionization stages, of that element are present in the spectrum). Problems in the abundance determination might arise if line optical depth effects and/or (inter)-stellar contamination play a role. Also the well-known discrepancy between the abundances determined using collisionally excited lines and recombination lines indicates that there is a fundamental problem in the determination of abundances that is not yet understood.

H. The electron temperature

One can see that the coefficients for the electron temperature are all very small, so that the determination of this temperature is very robust. This result is no surprise. The shape of the stellar spectrum (which is determined by the effective temperature), the ionization structure and the electron temperature of the plasma are very intimately linked. The ionization structure is well constrained by the spectrum and hence also the effective temperature and the electron temperature can be accurately determined using our method.

I. The ionization parameter

The ionization parameter is determined by the effective temperature and luminosity of the central star and the inner radius and hydrogen density of the plasma. Hence the remarks made in the corresponding sections pertain here as well. With so many parameters influencing the ionization parameter, we can see that this parameter is less reliably determined, but still useful. This result may be somewhat surprising, since it is often claimed that the ionization structure in the nebula can be parameterized by the ionization parameter. The ionization structure is well constrained by the spectrum, hence one might expect that the ionization parameter would be well constrained as well. This is not the case and hence this line of reasoning must be too simplistic. Closer inspection of the results in Table 2.4 reveals that the coefficients for the ionization parameter and the dust-to-gas ratio often have opposite signs. Especially when measurement errors are introduced in the longer wavelength *IRAS* fluxes, the correlation is quite striking. This result can be understood when one realizes that the dust grains influence the ionization structure as well. These grains preferentially absorb UV photons and help to soften the radiation field, thereby reducing the level of excitation in the nebula. This explains why measurement errors in the *IRAS* fluxes have such a big impact on the ionization parameter.

2.5 Different model assumptions

We described the assumptions for our simple PN model in Sect. 2.2. The model has been chosen such that on the one hand the number of free parameters was kept to a minimum and on the other hand the model still was sufficiently realistic for the resulting physical parameters to be meaningful. The number of free parameters must be kept to a minimum because otherwise there is not enough information in the observables to constrain them. This would result in an ill-determined best-fit model and the physical parameters would be very sensitive to observational error. We have investigated this effect in the previous section and found that our simple model passed this test reasonably well. In this section we would like to investigate the other side of the balance: is our simple model realistic enough or is it too simplistic? In other words: how accurate are the physical parameters from our best-fit model when we try to model a PN for which our simple model assumptions are not fully appropriate?

2.5.1 The distance and the filling factor

In this section we use the observables from our test model again (see Sect. 2.3) and we investigate the influence of the distance and the filling factor on the best-fit model. Both parameters are notoriously hard to measure and there still is a lot of discussion about them. For a review of the status of distance determinations we refer to Pottasch (1992), Terzian (1993) and Pottasch (1996). The situation regarding the measurement of filling factors is for instance described in Kingsburgh & Barlow (1992). Both these parameters are represented by a single number in our models and we can investigate the influence of an error in the assumed value in a straightforward manner. The influence of the distance was tested by making four best-fit models using a distance which differed -0.10, -0.05, $+0.05$ and $+0.10$ dex from the true value. The influence of the filling factor was tested by making two best-fit models using a filling factor of $\lg\epsilon = -0.20$ and -0.10. In other words, in this section the set of observables is *not* changed. What is changed is the value for the distance or the filling factor used in the best-fit model. The results are represented using the parameter ζ again, which now is defined as

$$\zeta \equiv \Delta \lg P / \Delta \lg M, \tag{3}$$

where M is a generic symbol for a model parameter (i.e. the distance and the filling factor). To make the best-fit models, no measurement errors were assumed in the observables and all other model assumptions remained unchanged (i.e. only the distance or the filling factor were changed in any model). The results are shown in Table 2.5.

Table 2.5 — *The influence of the distance and the filling factor on the derived physical parameters. The amount of the change in the model parameter used in the best-fit model (w.r.t. the standard value) in dex is indicated in the second row. The entries ζ in the table give the ratio of the logarithmic difference in the derived physical parameter P and the amount of change in the model parameter M (i.e. $\Delta \lg P / \Delta \lg M$, both in dex).*

model par.	D				ϵ	
$\Delta \lg M$/dex	-0.10	-0.05	$+0.05$	$+0.10$	-0.20	-0.10
T_*	-0.02	-0.02	-0.02	-0.02	-0.02	-0.02
L_*	$+2.02$	$+2.02$	$+2.02$	$+2.02$	$+0.02$	$+0.02$
$n_{\rm H}$	-0.38	-0.37	-0.37	-0.36	-0.38	-0.38
$r_{\rm in}$	$+1.07$	$+1.07$	$+1.07$	$+1.07$	$+0.07$	$+0.07$
$r_{\rm str}$	$+0.97$	$+0.96$	$+0.97$	$+0.96$	-0.04	-0.03
$r_{\rm out}$	$+0.83$	$+0.84$	$+0.81$	$+0.84$	-0.15	-0.16
$M_{\rm ion}$	$+2.37$	$+2.37$	$+2.37$	$+2.36$	$+0.37$	$+0.37$
$M_{\rm sh}$	$+2.39$	$+2.40$	$+2.38$	$+2.41$	$+0.41$	$+0.40$
Γ	-0.55	-0.56	-0.56	-0.55	-0.56	-0.55
ϵ(He)	$+0.17$	$+0.16$	$+0.20$	$+0.13$	$+0.17$	$+0.14$
ϵ(N)	-0.02	-0.03	-0.01	-0.01	-0.01	-0.02
ϵ(O)	$+0.20$	$+0.21$	$+0.23$	$+0.21$	$+0.19$	$+0.19$
ϵ(Ne)	$+0.23$	$+0.25$	$+0.29$	$+0.23$	$+0.23$	$+0.21$
ϵ(S)	$+0.01$	$+0.00$	$+0.01$	$+0.02$	$+0.01$	$+0.01$
ϵ(Ar)	$+0.22$	$+0.22$	$+0.25$	$+0.21$	$+0.21$	$+0.19$
$T_{\rm e}$	-0.03	-0.03	-0.03	-0.03	-0.03	-0.03
$\lg U$	$+0.22$	$+0.20$	$+0.21$	$+0.19$	$+0.21$	$+0.22$

A. The distance

When the coefficients in Table 2.5 are inspected one only finds large values for ζ for the distance dependent parameters. These values can be understood quite easily. Using simple arguments one would expect $L_* \propto D^2$, which is almost exactly what we find. Using a similar argument one would expect the inner, Strömgren and outer radius to vary proportional to D, and the ionized and total shell mass proportional to D^3. This is almost what we find, but not completely. This is caused by the fact that the absolute flux values (the radio flux and the *IRAS* fluxes) change as D^2, not D^3 like the emitting volume does. Hence the model has to make a compromise between the two effects and we see that the shell volume and especially the shell mass change slower than D^3. This effect also causes the hydrogen density and the dust-to-gas ratio to change, although they are not distance dependent parameters. The changes are quite small though and these parameters can still be considered well determined. All other distance independent parameters are robust against errors in the assumed distance.

We can conclude that the uncertainty in the distance is one of the larger contributors to the uncertainties in the final model, especially for the distance dependent parameters. Unfortunately there is no way around this problem and it can only be resolved by improving the accuracy of the distance.

B. The filling factor

When the coefficients in Table 2.5 are inspected one sees that none of them are big. Hence we can say that the model is robust against errors in the assumed value of the filling factor. The largest effects are on the density, the dust-to-gas ratio and the (ionized) shell mass. These effects can be understood fairly easy when one realises that when the filling factor varies, the absolute flux values (the radio flux and the *IRAS* fluxes) change proportional to ϵ, while the emitting volume remains unchanged. Since the emitting volume is well constrained by the observables, the best-fit model (which assumes a wrong value for the filling factor) can only adjust the density and the dust-to-gas ratio in order to fit the flux values. This effect also causes the (ionized) shell mass to be off. All other parameters are robust against errors in the filling factor.

We can conclude that the modeling results are not very sensitive to the assumed value for the filling factor. However, one should realize that some authors claim very low values for ϵ for certain nebulae. If such low values are appropriate, then modeling with our default value $\epsilon = 1$ could introduce sizeable errors in the model. On the other hand, one can always choose a different value for the filling factor in the best-fit model, if this is considered more realistic.

2.5.2 Modeling more realistic nebulae

In this section we will look more closely at the model assumptions which we have not considered in the previous section. These can not be tested by simply changing a number, so we have used a different approach here. We have made six different test models, in which we changed one model assumption at a time. Then we extracted the usual set of observables from these six models (i.e. the same set we have used in our previous discussions). No measurement errors were assumed for the observables. Next we applied our method and determined a best-fit model using standard model assumptions. Finally we compared the best-fit model with the original model and in this way we could assess how realistic the physical parameters from the best-fit model were. The results are presented as the straight difference between the logarithms of the parameters of both models. They are shown in Table 2.6. Below we will discuss each model in more detail.

Table 2.6 — *The influence of errors in the model assumptions on the derived physical parameters. The different models that where used are indicated in the header of each column. The entries in the table give the error in the physical parameter P in dex, and are defined as* $\lg P_{\rm best-fit} - \lg P_{\rm true}$. *The χ^2 for each of the models is also indicated.*

model	Kurucz	Dens1	Dens2	Dens3	Dust1	Dust2
T_*	−0.026	+0.000	+0.001	+0.011	−0.003	+0.021
L_*	−0.028	+0.003	+0.012	−0.169	+0.020	−0.033
$n_{\rm H}$	+0.019	+0.091	+0.018	−0.091	+0.000	+0.082
$r_{\rm in}$	−0.008	+0.028	+0.025	−0.066	−0.005	+0.120
$r_{\rm str}$	−0.012	−0.006	+0.002	−0.012	−0.002	+0.020
$r_{\rm out}$	−0.089	−0.010	+0.125	+0.054	+0.119	+0.001
$M_{\rm ion}$	−0.030	+0.004	−0.014	−0.710	+0.009	−0.058
$M_{\rm sh}$	−0.081	−0.007	−0.033	+0.033	+0.165	+0.096
Γ	+0.068	+0.000	+0.083	+0.083	+0.054	−0.056
ϵ(He)	+0.120	−0.008	−0.017	−0.079	+0.007	−0.044
ϵ(N)	−0.111	−0.019	−0.001	−0.024	−0.002	−0.023
ϵ(O)	+0.097	−0.007	−0.016	−0.076	+0.008	−0.090
ϵ(Ne)	−0.440	+0.003	−0.011	−0.103	+0.023	−0.144
ϵ(S)	+0.030	−0.016	−0.004	−0.046	+0.002	−0.029
ϵ(Ar)	+0.186	−0.004	−0.022	−0.061	+0.012	−0.090
$T_{\rm e}$	−0.026	+0.001	+0.003	+0.011	−0.001	+0.017
$\lg U$	+0.053	−0.144	−0.054	+0.077	+0.023	−0.313
χ^2	0.902	0.072	0.035	0.464	1.510	0.924

A. Case 1: Kurucz

In the first model we have replaced the blackbody spectrum by a Kurucz (1991) model atmosphere with $T_{\rm eff} = 40\,000$ K and $\lg[g/({\rm cm\,s^{-2}})] = 4.50$. All the remaining model parameters and assumptions were left unaltered. This model has roughly the same level of excitation as our original model presented in Table 2.2. From the results in Table 2.6 one can see that in the best-fit model mainly the abundances are affected. Especially the neon and argon abundances are quite bad. This can be understood as follows. The ionization structure strongly depends on how much ionizing photons are emitted and this number is different for each ion because each has a different ionization threshold. Hence the ionization structure strongly depends on the shape of the stellar spectrum. When the strength of emission lines is modeled by our method, knowledge of the ionization structure is implicitly used to account for ionization stages which are not observed. Hence one can expect that the error in the abundances is largest for those elements where the dominant ionization stage is not observed (i.e. for neon and to a lesser extent argon). Other parameters like the extent of the ionized region and the electron temperature are determined by integrals over the Lyman continuum and are therefore less sensitive to the precise shape of the spectrum. We can see that in our best-fit model these parameters are reasonably determined. This is even the case for the stellar temperature. This can be understood when one realizes that in the temperature regime studied here, the number of hydrogen ionizing photons is a very steep function of effective temperature. Hence only a small adjustment in the temperature is sufficient to get the same ratio of ionizing flux to total flux as in the Kurucz model.

Hence we can conclude that modeling a realistic nebula using a blackbody spectrum can lead to substantial errors in the abundances. However, it should be noted that the magnitude of the effect depends very much on which lines are present in the spectrum (most importantly if the dominant ionization stages are observed) and how big the difference is between the real and the blackbody spectrum at the ionization edges of the dominant ionization stages. It should be noted that for higher temperatures, the difference between a blackbody spectrum and a model atmosphere becomes less. Also for wind-blanketed non-LTE models the difference with a blackbody spectrum usually is less than for Kurucz models (Gabler et al. 1989; Sellmaier et al. 1996). Further discussion can be found in Beintema et al. (1996). We conclude that our blackbody assumption is not a good one, however we are forced to use it since no suitable grid of model atmospheres is present in the code. As soon as such a grid becomes available, it can easily replace the blackbody spectra.

B. Case 2: Dens1

In the second test case we have looked at the influence of non-constant density distributions inside the Strömgren sphere. We made a model which had very large sinusoidal density fluctuations inside the Strömgren sphere and a $1/r^2$ density law outside. The density was defined by

$$\lg(n_{\rm H}/{\rm cm}^{-3}) = 4.1785 + 0.5 \sin\left(\frac{r/{\rm cm} - r_{\rm in}/{\rm cm}}{2.29234\times 10^{14}}\right)$$

inside the Strömgren sphere with $\lg(r_{\rm in}/{\rm cm}) = 16.80516$ and $\lg(r_{\rm str}/{\rm cm}) = 16.8943$. This density law changes continuously into a $1/r^2$ density law outside the Strömgren sphere. This distribution was chosen such that the best-fit model would be able to reproduce the density distribution in the neutral region very well. Hence mismatches in the neutral region did not influence the modeling. These effects will be studied in the next test case. To compare the density of the best-fit model with the original density distribution we calculated the average value of $n_{\rm H}^2$ over the Strömgren sphere and took the square root. This yielded $\lg(n_{\rm ave}/{\rm cm}^{-3}) = 4.4022$; this value was also used to calculate the ionization parameter.

When we view the results in Table 2.6 we see that the best-fit resembles the original model surprisingly well. This can be understood when we consider that the density fluctuations only have a very small influence on the electron temperature and limited influence on the dominant ionization stage. The best-fit model is still able to reproduce the ionization structure in an average sense and hence the ionized region can be modeled very well by a constant density. The largest differences between both models are for the density itself and the ionization parameter. This is not surprising since we used only a crude estimate for both numbers, which obviously is not fully appropriate. Hence we conclude that density fluctuations are no problem for our method and that the best-fit model will yield some kind of average of the density inside the Strömgren sphere.

C. Case 3: Dens2

In the third test case we have looked at the influence of a density distribution which does not behave as $1/r^2$ in the neutral zone. For this we made a model where the density distribution still was constant in the inner parts and which behaved as $1/r^2$ in the outer parts, but where the constant density part would reach deep into the neutral zone (out to $\lg(r/{\rm cm}) = 17.12$). All the other model assumptions would remain unaltered. With this particular density distribution, our method could in principle make a perfect fit to the density distribution inside the Strömgren sphere, but not outside.

When we view the results in Table 2.6 we see that the best-fit resembles the original model very well. This is not surprising, the change in the density distribution only influences the neutral lines and the *IRAS* fluxes. We can see that the largest discrepancies between both models are for the outer radius and the dust-to-gas ratio. The amount of material in the neutral zone of the best-fit model is much less than in the original model and the method tries to compensate this by increasing the outer radius. The *IRAS* fluxes can be further boosted by increasing the dust-to-gas ratio. We conclude that incorrect assumptions on the density distribution in the neutral zone have little consequence for the best-fit model. They mainly influence the dust-to-gas ratio, the ionization parameter and the outer radius (which can not be considered accurate anyway).

D. Case 4: Dens3

In the fourth test case we have made a crude model for a bipolar nebula, consisting of two superimposed spherically symmetric models. For the equatorial regions of the nebula we have used the standard model presented in Sect. 2.3, hence the nebula is optically thick in the Lyman continuum in this direction. For the polar regions we have used a different model with a larger inner and outer radius and a lower density. All these parameters were chosen such that the ionization parameters is higher in the polar direction than in the equatorial direction. The polar model is fully ionized and therefore optically thin in the Lyman continuum. The observables from both models were added using appropriate weighting factors, representing the solid angle which was occupied by both regions. Subsequently a spherically symmetric best-fit model was made using standard assumptions. Since for a bipolar nebula it is not possible to assign a single number to the hydrogen density, the inner, Strömgren and outer radius and the ionization parameter, we have used the values from the equatorial model as a reference. The electron temperature was the average of both models, weighted by the total Hβ flux emanating from both regions (this gave $T_e = 10\,012$ K).

When we view the results in Table 2.6 we see that the best-fit model has a moderately lower luminosity and a much lower ionized mass than the original model. The best-fit model is optically thick in the Lyman continuum, which could be expected since the radiation from the equatorial region dominates the total emission from the nebula. Hence no Lyman photons escape the nebula in the best-fit model and all are reprocessed into other forms of radiation. On the other hand, the original model is not fully optically thick and hence in this case Lyman continuum photons do escape the nebula. Therefore, if the reprocessed radiation is used as a measure for the total luminosity of the central star, and the nebula is assumed to be optically thick (as is indicated by the best-fit model), then this would lead to a value for the luminosity which is too low. This line of reasoning also leads to an explanation for the fact that the ionized mass is far too low. Most of the ionized mass is contained in the polar regions, which on the other hand emit only a small fraction of the total emission from the nebula. Hence the polar regions get little weight in the modeling and the total ionized mass can not be expected to be modeled accurately. Since the polar regions have a different level of excitation as the equatorial regions, the optical spectra from both regions are different as well. This leads to the fact that the combined spectrum can not be modeled accurately and this influences the abundances in the best-fit model. Also other parameters are affected, most importantly the dust-to-gas ratio. We can see that modeling a bipolar nebula with our standard assumptions can lead to moderate errors in important parameters, most importantly the luminosity and the abundances. Less important parameters like the ionized mass are totally unreliable.

E. Case 5: Dust1

If the composition of the grains in a nebula is not known, our method uses a mixture of silicate and graphite grains. However, the presence of both oxygen-rich and carbon-rich grains is only rarely observed in real nebulae. Hence this model assumption might introduce errors in the best-fit model. In this section we will investigate the magnitude of these errors. In this test case we will make a model which contains pure graphite dust with the same dust-to-gas ratio as our original model. We will try to model the resulting observables using a standard mixture of silicates and graphite.

When we view the results in Table 2.6 we can see that the error in the dust composition introduces only minor errors in the best-fit model. The largest influence is on the outer radius and the total shell mass of the best-fit model. This is no surprise. The different dust composition causes a different run of the grain emissivity as a function of radius. This will cause the shape of the infrared spectrum to change and hence also the ratio of the various *IRAS* fluxes. Since the outer radius (and thus also the total shell mass) is completely determined by the *IRAS* fluxes, it can be expected that it is seriously affected by an error in the dust composition. Since both these quantities could not be considered reliable anyway, this introduces no new problems. One can see that also the dust-to-gas ratio of the best-fit model is affected. This could be expected as well. In general the absorption efficiency of silicates and graphite is not equal (van Hoof et al. 1997), so different amounts are needed to absorb the same amount of flux. Hence we conclude that the assumption of a mixture of graphite and silicates has only little influence on the best-fit model, although the dust-to-gas ratio should be viewed with caution when the dust composition of the nebula is not known. We would like to point out that different assumptions on the dust composition in the best-fit model can easily be made when more detailed information is available.

F. Case 6: Dust2

In our standard model assumptions we assume that the inner radius of the gas and the dust are equal. However it is not *a priori* clear that this should be the case. In this test case we will make a model with a different inner radius of the dust ($\lg(r/\mathrm{cm}) = 16.88$). The resulting observables will be modeled using the standard model assumptions.

When we view the results in Table 2.6 we can see that the largest discrepancy between the two models is for the inner radius of the nebula. This can be understood since the *IRAS* 12 μm over 25 μm flux ratio is sensitive to the hottest dust, i.e. to the emission from the dust at the inner edge of the nebula. Since the *IRAS* fluxes have a rather large weight in the optimizing process, the *IRAS* 12 μm over 25 μm flux ratio is an important factor in determining the inner radius of the nebula. Since in our test model the inner radius of the gas is smaller than the inner radius of the dust, also the inner radius which follows from the optical spectrum (especially the highest ionization stages) and from the *IRAS* 12 μm over 25 μm flux ratio are not equal. Since in the best-fit model both values have to be equal, one could expect that the inner radius would be forced somewhere in between both values. However, we actually find that the inner radius is pushed even further out than the inner radius of the dust in the original test model. This indicates that our method is to some degree unstable against this kind of error. This is a consequence of the fact that changing the inner radius causes many other parameters to change as well. The pattern of changes is complicated and we will not try to give a full explanation. Several important parameters are affected by this problem, most importantly the hydrogen density, the abundances, and to a lesser degree also the stellar temperature and luminosity. Also other parameters like the ionization parameter and the dust-to-gas ratio are affected.

Since the *IRAS* 12 μm over 25 μm flux ratio is important for determining the inner radius one should realize that the following problems can influence the determination. First, the composition of the grains is usually not known. In these cases a mixture of silicate and graphite grains is assumed. Different emissivities for the grains will give a different *IRAS* 12 μm over 25 μm flux ratio. Second, the density is assumed to be constant within the Strömgren sphere. If a density gradient would exist near the inner radius, this would alter the *IRAS* 12 μm over 25 μm flux ratio. Third, the grain size distribution is not known. The absorption coefficients used in CLOUDY are based on the grain size distribution of Mathis et al. (1977). Especially the presence of very small grains, such as PAH grains, might also change the *IRAS* 12 μm over 25 μm flux ratio (Zijlstra et al. 1994). Fourth, because the detectors of *IRAS* are large, the fluxes might suffer from confusion. This can affect all colors.

We can conclude that the problems discussed in this section can have a rather serious impact on the quality of the best-fit models. A solution to this problem is not apparent to us at this stage, but future research will be directed at improving this situation.

2.6 Modeling of some galactic bulge PN

To test the method, including the determination of the distance, on real data, we selected a small sample of galactic bulge nebulae from Ratag et al. (1990, hereafter RPDM). Galactic bulge nebulae can be assumed to be at a distance of approximately 7.8 kpc (Feast 1987). We chose the nebulae from RPDM since they publish good quality spectra and also carried out their own photo-ionization analysis of the data which we can use for comparison. The radio observations for these PN are described in Gathier et al. (1983). The following selection criteria were used:

1. The PN should have a quality 2 or 3 *IRAS* 12 μm flux and quality 3 *IRAS* 25 μm and 60 μm fluxes.
2. The absolute value for the radial velocity should be larger than 100 km s^{-1}.
3. The excitation class should not be labeled peculiar.

The resulting five PN are presented in Table 2.7. All nebulae except M 2−4 are indicated by Acker et al. (1992) as likely bulge PN. In view of the large radial velocity of M 2−4, $v_{\rm LSR} = -175.8$ km s^{-1} (Gathier et al. 1983) it is unlikely to be a foreground object. In Table 2.8 we give the input values for the observables used for the modeling, together with the resulting model predictions. As can be seen from this table, not all the lines present in the spectra are predicted by CLOUDY, most notably the higher Balmer lines of hydrogen and several helium lines. Also the element Chlorine is not included in the code. The resulting physical parameters for the nebulae are given in Table 2.9.

Table 2.7 — *Our sample of PN selected from Ratag et al. (1990).*

name	PN G	α(1950) h m s	δ(1950) ° ′ ″
H 1−40	359.7−02.6	17 52 22.9	−30 33 06
M 1−20	006.1+08.3	17 26 00.7	−19 13 32
M 2−4	349.8+04.4	16 57 47.7	−34 45 17
M 2−23	002.2−02.7	17 58 32.7	−28 25 45
M 3−15	006.8+04.1	17 42 32.4	−20 56 52

The hydrogen density mentioned is the constant density inside the Strömgren sphere.

2.6.1 Individual remarks

The PN in our sample all have nearly the same medium excitation class. This probably is partially a result of our selection criterion that the nebulae should have been detected by *IRAS* in the 12 μm band (criterion 1). Old bulge PN, having a high excitation class and cool dust, might have insufficient 12 μm flux to be detected by *IRAS*.

In the rest of this section each of the PN in our sample will be discussed individually, with special emphasis on the problems encountered during the modeling.

A. H 1−40

Two lines were omitted from the list of observables because of the following reasons. First the He II λ4686 line was omitted, because the flux ratio given by RPDM is quite high, indicative of a high stellar temperature. However, the rest of the observational data are not consistent with such a high stellar temperature. Also, this line is listed in Table 3 of RPDM, but is not present in their Table 1. Webster (1988, hereafter W88) took a spectrum of this PN, and she didn't report the detection of this line. She should however have detected a line of the strength mentioned by RPDM. In view of these uncertainties we decided to omit this line. Since RPDM included this line in their modeling, this probably explains the higher stellar temperature they obtain.

The fitting of the [O III] λ4363 line was also problematic. The observed flux was far too low to be consistent with the electron temperature predicted by our model. Since the electron temperature derived from the [N II] lines is much higher (and more consistent with the value determined by our model), and also because the [O III] λ4363 line is much stronger in the spectrum of W88 (however not as strong as predicted by our model), we decided that its value was too uncertain and omitted it from the input.

B. M 1−20

The intensity of the Hα line seems quite high, and is not fitted well. The discrepancy is too large to be attributed to measurement errors, hence this might indicate that the spectrum has not been sufficiently dereddened. There is

Table 2.8 — *Comparison of the observed quantities (mostly taken from Ratag et al. 1990) and the model fit for our sample of PN. The strength of the emission lines is given relative to Hβ = 100. The measured line fluxes have been dereddened. The entries [O II] λ3727, λ7325 and [S II] λ4071 all stand for the entire multiplet. All observables for which entries in both columns obs. and model are present, have been weighted in the goodness-of-fit estimator, except where indicated.*

ion	λ	H 1−40		M 1−20		M 2−4		M 2−23		M 3−15	
	Å	obs.	model	obs.	model	obs.	model	obs.	model	obs.	model
[O II]	3727	32.4:	38.5	55.5	83.1	97.1	125.2	14.2	20.4	48.6	101.5
H 12	3750							3.4			
H 11,O III	3771							4.2			
H 10	3798			5.5		4.0		5.1			
H 9	3835			6.7		7.1		6.5			
[Ne III]	3869	79.1	79.4	69.1	67.6	64.7	67.6	82.4	80.0	89.9	90.1
H 8,He I	3889	12.9		18.1		17.4		13.9		16.6	
[Ne III],Hϵ	3969	19.9		25.5		33.6		38.3		25.4	
He I	4026			2.7		2.7		1.82			
[S II]	4071	3.3	2.5		2.3	3.6	3.0	2.5	3.8		1.8
Hδ,N III	4102	25.8	29.4	25.6	30.3	24.7	30.5	24.0	30.2	26.1	29.5
C II	4267										
Hγ	4340	47.1	50.2	49.1	51.0	45.9	51.2	48.2	50.9	49.0	50.2
[O III]	4363	4.6‡	12.0	7.5	5.4	2.9	2.1	13.9	9.9	3.3:	7.5
He I	4472	6.5	4.4	5.8	5.2		4.5	5.1	5.5	5.0	5.1
N III	4641									20.3	
He II	4686	17.1?‡	1.9		0.7		0.2		1.0	4.1	3.5
[Ar IV],He I	4712			1.33		0.91		1.09		1.94	
[Ar IV]	4740	4.45	4.70	0.71	1.16	0.33:	0.70	0.80	1.42		6.67
Hβ	4861	100.	100.	100.	100.	100.	100.	100.	100.	100.	100.
He I	4922	1.36:				1.42		0.87			
[O III]	4959	307.	276.	336.†	315.	272.†	213.	304.	350.	328.†	219.
[O III]	5007	915.	827.	1009.†	946.	815.†	640.	1006.	1051.	983.†	658.
[N I]	5201		0.20		0.07		0.22		0.00		0.59
[Cl III]	5517							0.21			
[Cl III]	5538			0.47				0.25			
[N II]	5755	1.92:	2.16	0.92	1.05	1.39	1.52	1.19	1.06	1.0:	1.4
He I	5876	15.5	15.9	15.7	16.0	13.8	13.8	17.2	17.8	16.3	16.3
[O I]	6300	2.8	2.7	4.7	4.1	2.9	3.7	4.2	3.3	2.8	3.6
[S III]	6312	1.70	1.48	0.79:	1.12	1.59	1.33	2.4	2.3	1.24	1.00
[O I]	6364	0.88	0.88	1.46	1.35	1.00	1.23	1.42	1.09	0.79	1.19
[N II]	6548		19.9		14.6		32.1		6.4		18.8
Hα	6563	280.	278.	303.	269.	275.	268.	283.	269.	305.	278.
[N II]	6584	61.4	59.7	45.4	43.8	85.6	96.1	18.9	19.2	57.6	56.3
He I	6678	3.8		4.0		3.2		4.7		4.6	
[S II]	6716	0.99	0.96	1.17	1.45	2.72	3.16	0.78	0.47	2.65	3.38
[S II]	6731	1.71	1.99	2.32	2.91	5.0	6.0	1.55	1.05	5.4	5.2
He I	7065	7.9	11.4	10.5	9.7	5.6	7.1	14.4	12.0	7.5	9.2
[Ar III]	7136	13.6	13.3	9.1	7.5	15.2	13.0	14.0	11.2	19.2	19.3
He I	7281			0.83		0.3:		0.94		0.59	
[O II]	7325	9.2	14.2	14.9	17.1	8.3	14.0	19.3	21.4	6.6	8.7
obs.	unit										
F_ν(12 μm)	Jy	2.38	2.38	1.13	1.00	0.56	0.53	1.93	2.10	$<$ 0.53	0.19
F_ν(25 μm)	Jy	18.45	19.11	3.94	4.44	5.00	5.83	9.31	6.54	5.66	6.02
F_ν(60 μm)	Jy	11.91	11.42	2.38	2.30	5.77	5.18	1.64	1.64	8.02	7.77
F_ν(100 μm)	Jy	$<$ 73.48	3.22	$<$ 4.59	0.66	$<$ 12.59	1.73	$<$ 126.70	0.24	$<$ 10.39	2.72
F_ν(6 cm)	mJy	31.	31.0	47.	47.7	32.	32.2	41.	41.4	65.	65.4
Θ_d	arcsec	1.26	1.27	1.98	1.81	2.16	2.13	0.72	0.67	5.4	5.19
χ^2			0.63		1.68		2.28		4.17		2.75

: A colon indicates that the value is uncertain.
† The sum of the intensities of the doublet was split using the ratio 3:1.
‡ This line was not weighted in the goodness-of-fit estimator χ^2, see also Sect. 2.6.1.

Table 2.9 — *The physical parameters of the galactic bulge PN in our sample determined with* CLOUDY. *Abundances of elements for which only one line was observed are marked uncertain.*

	H 1−40	M 1−20	M 2−4	M 2−23	M 3−15
$\lg(T_*/\mathrm{K})$	4.800	4.774	4.705	4.782	4.916
$\lg(L_*/\mathrm{L}_\odot)$	3.798	3.607	3.555	3.639	3.663
$\lg(n_\mathrm{H}/\mathrm{cm}^{-3})$	4.321	4.124	3.923	4.855	3.527
r_in/mpc	13	0.21	11	9	33
r_str/mpc	24	34	40	13	98
r_out/mpc	279	363	351	13	519
$M_\mathrm{ion}/\mathrm{M}_\odot$	0.042	0.092	0.088	0.015	0.47
$M_\mathrm{sh}/\mathrm{M}_\odot$	1.34	2.34	1.89	0.015	6.5
$\lg\Gamma$	−1.70	−3.11	−2.50	−2.46	−2.60
ϵ(He)	10.96	11.02	10.96	11.05	11.03
ϵ(N)	7.78	7.81	8.13	7.67	7.60
ϵ(O)	8.23	8.72	8.84	8.67	8.22
ϵ(Ne)	7.39:	7.82:	8.15:	7.75:	7.53:
ϵ(S)	6.37	6.66	6.90	6.79	6.31
ϵ(Ar)	5.98	5.99	6.36	6.08	6.20:
T_e/kK	12.7	9.5	8.3	10.2	12.0
$\lg U$	−1.40	+2.14	−1.16	−1.80	−1.58

however no evidence from the fits to the other lines to support this suspicion.

Our model gives a very small inner radius, also resulting in a very high ionization parameter. This is caused by the high *IRAS* 12 μm over 25 μm flux ratio, which might indicate the presence of hot dust. See also the discussion in Sect. 2.5.2.F.

C. M 2−4

The spectrum is fitted quite well, be it that there is slight discrepancy for the [O III] λ4959 and λ5007 lines. This is caused by the [O II] λ3727 line, which usually has a larger uncertainty due to extinction and detector insensitivity.

D. M 2−23

This PN has the highest χ^2 of all PN in our sample. This is mainly caused by the weak lines, which might indicate that this spectrum has a lower signal-to-noise when compared to the other spectra. RPDM do not list error margins for their line flux ratios, so we had to assume reasonable values.

The model is not able to fit the *IRAS* 25 μm flux, which is very high compared both to the 12 μm and 60 μm flux. A possible explanation could be the presence of a 30 μm dust feature in the spectrum (Hoare 1990). This would imply that the nebula is carbon-rich, since this feature has only been observed in carbon-rich nebulae. The central star has spectral type Of (Aller & Keyes 1987, hereafter AK87).

The large difference between the optical diameter of 8.5″ (Acker et al. 1992) and the radio diameter of 0.72″ (Gathier et al. 1983) suggests that this nebula might be a core-halo nebula. All other evidence gathered in this paper also is consistent with this assumption and we will adopt it throughout the paper. Since we used the radio diameter for the modeling, our model is only valid for the core region. The fact that our model is density bounded and gives a low ionized mass is consistent with the fact that we are only modeling the core region.

E. M 3−15

There is a suggestion of a systematic trend when comparing the observed and the modeled line flux as a function of wavelength. Also the observed intensity of the Hα line seems quite high. This might indicate that the spectrum has not been sufficiently dereddened.

This PN has a [WC]-type central star (AK87). The central star temperature, the excitation class 5.5 (taken from RPDM) and the low *IRAS* 12 μm to 25 μm flux ratio all are consistent with an early spectral type: [WC3-4] (cf. Kaler 1989, Méndez & Niemela 1982 and Zijlstra et al. 1994 respectively).

The *IRAS* 12 μm flux is not listed as an upper limit in the Point Source Catalogue. However, when we used this value for the modeling, the resulting model was unrealistic. We therefore assume that the 12 μm flux suffers from confusion and took the quoted value to be an upper limit. See also the discussion in Sect. 2.5.2.F.

2.6.2 Discussion

In this section the modeling results are discussed by comparing them with results from other studies in the literature. Since distance dependent parameters are usually not given by other authors, we will restrict ourselves to the distance independent parameters of PN.

A. Stellar temperatures

In Table 2.10 we present a comparison with the stellar temperatures given in the literature. These temperatures were derived using the Zanstra method and photo-ionization modeling. Results using the energy balance or Stoy method are not listed since we consider this method, or at least the data for the nebulae being studied here, to be unreliable. One can see that the derived values agree quite well with only few outliers.

The temperatures determined by our method agree well with the hydrogen Zanstra temperatures, with the single exception of the temperature for M 2−23 given by Tylenda et al. (1991a). Since the other three determinations using the Zanstra method agree quite well, we assume the value given by Tylenda et al. to be erroneous.

To derive stellar temperatures for photo-ionization modeling, sometimes certain line-ratios are used as temperature indicators (e.g. He II λ4686 over Hβ). Especially for cooler central stars, where few temperature sensitive lines are available, this makes the determination dependent on one or two lines. Nevertheless, the results from the photo-ionization models usually are in good agreement. Exceptions are the temperature for H 1−40 derived

Table 2.10 — *Comparison of the stellar temperatures for the PN in our sample. The temperatures are given in kilokelvin. The abbreviations for the methods have the following meaning: H I – hydrogen Zanstra method, AM – photo-ionization modeling using atmosphere models, BB – photo-ionization modeling using blackbody approximation.*

H 1−40	M 1−20	M 2−4	M 2−23	M 3−15	ref.	meth.
		55.	64.		3	H I
	53.		56.		4	H I
		51.5	65.0		5	H I
	65.		85.		7	H I
			50.	62.5	1	AM
80.0?	50.0	50.0	57.5	72.5	6	AM
64.					2	BB
63.1	59.4	50.7	60.5	82.4	8	BB

References – 1) Aller & Keyes (1987) using atmosphere models by Husfeld et al. (1984). 2) Dopita et al. (1990). 3) Gleizes et al. (1989). 4) Kaler & Jacoby (1991). 5) Pottasch & Acker (1989). 6) Ratag et al. (1990) using atmosphere models by Clegg & Middlemass (1987) and Husfeld et al. (1984). 7) Tylenda et al. (1991a). 8) This work.

by RPDM, and the temperatures for M 3−15. The deviating value given by RPDM can probably be attributed to the He II λ4686 line, which they used as a temperature indicator. We refer to the discussion in Sect. 2.6.1.A. For M 3−15 we find a higher stellar temperature than other authors. The largest discrepancy is with the value from AK87. An explanation for this is not apparent to us, since all the other physical parameters determined by AK87 agree quite well with our results.

We conclude that the temperature determination for the central stars in this sample is fairly reliable, although the situation for M 3−15 is not completely clear. This confirms our results from the previous sections where we found the temperature determination to be very robust.

B. Electron temperatures

In Table 2.11 the electron temperatures derived by different authors are compared. The electron temperature determined by CLOUDY is a weighted mean of the temperature in the nebula (see Sect. 2.8). The observational material shows a large spread in most cases, even when the same method is used. This indicates that the electron temperature determination, at least in those cases where diagnostic lines have been used, is not very reliable. This is in agreement with our results in Sect. 2.4.1. Note the large difference between the [N II] and [O III] temperatures in the case of M 2−23. This difference is not caused by measurement error. For this particular object, the temperature derived from the [N II] lines has no physical meaning (Liu, private communication).

The electron temperatures derived from our method are in most cases just outside the range of values found with line diagnostics; three times at the low end and twice at the high end. The results from the previous sections indicate that the electron temperature determination with

Table 2.11 — *Various determinations of the electron temperature for the nebulae in our sample. The temperatures are given in kilokelvin. The abbreviations for the methods have the following meaning: ave. – average of [N II] and [O III], model – average temperature defined in Sect. 2.8.*

H 1−40	M 1−20	M 2−4	M 2−23	M 3−15	ref.	meth.
			18.0		1	[N II]
	17.1				2	[N II]
	12.5	12.5			4	[N II]
		10.2			7	[N II]
	10.4				8	[N II]
13.1	10.2	9.7	19.2	9.4:	9	[N II]
10.1					11	[N II]
			11.0		1	[O III]
	10.8				2	[O III]
	13.1	11.6			4	[O III]
		8.7			5	[O III]
			12.9		6	[O III]
	9.9				8	[O III]
9.3	10.4	8.5	13.0	8.4:	9	[O III]
9.7					11	[O III]
			12.6	11.2:	3	ave.
		11.1			10	ave.
12.7	9.5	8.3	10.2	12.0	12	model

References – 1) Acker et al. (1989). 2) Acker et al. (1991). 3) Aller & Keyes (1987). 4) Costa et al. (1996). 5) Cuisinier et al. (1996). 6) Kaler (1979). 7) Kaler et al. (1993). 8) Kaler et al. (1996). 9) Ratag et al. (1990). 10) Tylenda et al. (1991b). 11) Webster (1988). 12) This work.

our method should be very robust. It is not apparent to us why the average values of the electron temperature derived from line diagnostics do not coincide with our results. This might indicate a problem, although the fact that we find both higher and lower results is not indicative of a systematic effect. Nevertheless, this should be investigated further in future research, using a larger sample.

C. Electron densities

In Table 2.12 the electron densities derived by different authors are compared. The electron density determined by CLOUDY is a weighted mean of the density in the nebula (see Sect. 2.8). There exist enormous differences between the various determinations in the literature, even when the same method has been applied. This indicates that the determination of densities with line diagnostics is very unreliable, which confirms our results in Sect. 2.4.1. Note the enormous differences between the [S II], [Cl III] and [Ar IV] densities for M 1−20 derived by Kaler et al. (1996).

Our values differ substantially from the values given by RPDM, although they are based on the same observational data. This is because we use a completely different method to determine the density and this is also consistent with our result that line diagnostics are unreliable. For three out of five nebulae we find results which are within the range of values found with other methods. For M 2−4 we find a value which is slightly outside this range. The results

Table 2.12 — *Various determinations of the electron density for the nebulae in our sample. The densities are given in 10^3 cm^{-3}. The abbreviations for the methods have the following meaning: radio – density determined from the radio flux, model – average density defined in Sect. 2.8.*

H 1−40	M 1−20	M 2−4	M 2−23	M 3−15	ref.	meth.
			13.6		1	[S II]
10.9	4.7			24.3	2	[S II]
			3.0	2.5	3	[S II]
	17.8	4.5			5	[S II]
		7.0			6	[S II]
15.0					7	[S II]
		4.2			9	[S II]
	85.				10	[S II]
4.4	9.2	5.6	11.5	10.6	11	[S II]
				4.2	13	[S II]
		3.6			14	[S II]
35.1					16	[S II]
		5.7			9	[Cl III]
	7.8				10	[Cl III]
			79.		4	[Ar IV]
	1.0				10	[Ar IV]
			63.		15	[Ar IV]
13.5					7	radio
			20.		8	radio
	10.				12	radio
22.7	14.6	9.1	79.3	3.7	17	model

References – 1) Acker et al. (1989). 2) Acker et al. (1991). 3) Aller & Keyes (1987). 4) Boffi & Stanghellini (1994). 5) Costa et al. (1996). 6) Cuisinier et al. (1996). 7) Dopita et al. (1990). 8) Kaler (1979). 9) Kaler et al. (1993). 10) Kaler et al. (1996). 11) Ratag et al. (1990). 12) Shaw & Kaler (1989). 13) Stanghellini & Kaler (1989). 14) Tylenda et al. (1991b). 15) Webster (1976). 16) Webster (1988). 17) This work.

in the previous sections indicate that our determination of the density is somewhat susceptible to measurement errors and errors in the model assumptions. This might provide an explanation for the discrepancy. The fact that we only model the core region of M 2−23 provides an explanation for the very high density we find for this nebula. Webster (1976) and Boffi & Stanghellini (1994, using the same spectrum) also find a high value using the [Ar IV] line ratio. The [Ar IV] lines are expected to be formed predominantly in the core region and hence this would confirm our results. On the other hand, the excitation in the core region is too high to form large amounts of S^+. Hence the [S II] lines can be expected to originate from the halo and should therefore indicate lower densities. This of course also depends on the exact position of the slit over the nebula. All of this might be an explanation for the extremely large spread of values found for this nebula.

The quality of the data in Table 2.12 makes a comparison with our results meaningless. However, the data are at least consistent with the assumption that our results are more accurate than the results from line diagnostics.

D. Nebular abundances

In Table 2.13 we give a comparison of the abundances we determined with other literature values. We did not include the nitrogen abundance from Henry (1990). After a discussion with Dr. Henry it was established that this abundance was flawed by an error in the analysis (as is also the case for the nitrogen abundances of M 4−3 and H 1−23 listed in the same paper; all other results are not affected). We also did not include the abundances for M 2−23 listed in Köppen et al. (1991). It was established that this analysis was flawed by an error as well, and Dr. Köppen kindly provided us with a re-analysis of his data. The higher nitrogen abundance given by Walton et al. (1993) for M 2−23 might be a result of the inclusion of *IUE* data in their analysis. On average they find a higher nitrogen abundance for bulge PN than other authors.

One can see that large differences can be found between the various abundance determinations in the literature. If we exclude our own results, we can find the following statistics. For elements heavier than helium, we find a difference between the lowest and highest abundance determination larger than or equal to 0.3 dex in 12 out of 22 cases, and larger than or equal to 0.5 dex in 4 out of 22 cases. For the helium abundances we find a spread larger than 0.1 dex in 2 out of 5 cases. Especially the abundances for M 2−23 show a large spread and should be considered uncertain. From this we draw the conclusion that, at least for the sample studied here, abundance determinations can not be considered very accurate. Uncertainties exceeding 0.2 dex to 0.3 dex are not uncommon. This situation is even worse than what we predicted in Sect. 2.4.1.

When one compares the abundances for the individual PN with the values from RPDM, one can see that for the two objects where the electron temperature is in good agreement (M 1−20 and M 2−4), the abundances also agree very well. For the other objects the abundance determinations differ. We attribute this to the difference in the determination of the electron temperature. When we compare our abundance determinations with the other values found in the literature, we see that our results often are slightly outside the range of values found by other authors. This behavior is well correlated: either all outliers are at the low end or at the high end. This behavior is also well correlated with our electron temperature determination. When our electron temperature determination is at the low end, our abundances are at the high end, and the reverse is also true (see also Sect. 2.6.2.B). This indicates that the main source of uncertainty in the abundance determination is the electron temperature. Hence the discussion given in Sect. 2.6.2.B applies here as well.

E. Stellar broadband fluxes

Since CLOUDY calculates the attenuation of the stellar continuum separately from the transport of the diffuse nebular continuum, we are able to predict broadband photometric

Table 2.13 — *Comparison of the abundance determinations of the PN in our sample.*

	H 1−40				M 1−20				M 2−4			
ref:	4	9	12	13	2	7	9	13	2	3	9	13
ϵ(He)	11.03	11.06	11.04	10.96	11.07	10.94	11.02	11.02	11.11	10.96:	10.99	10.96
ϵ(N)	7.72	8.08		7.78	7.39	7.80	7.75	7.81	7.65	8.17	8.09	8.13
ϵ(O)	8.52	8.70	8.53	8.23	8.30	8.65	8.62	8.72	8.30	8.77	8.80	8.84
ϵ(Ne)	7.89	7.69		7.39:			7.79	7.82:			7.90	8.15:
ϵ(S)	6.88	6.77		6.37	6.43:		6.52	6.66	6.64	7.03	6.96	6.90
ϵ(Ar)	6.6	6.43		5.98			6.05	5.99	6.31	6.36	6.25	6.36

	M 2−23								M 3−15			
ref:	1	5	6	8	9	10	11	13	1	5	9	13
ϵ(He)	11.00	10.93		10.88:	10.98	10.92	10.96	11.05	11.03	11.01	11.03	11.03
ϵ(N)	7.68	8.20	7.70	7.55	7.40	8.13		7.67	8.08		8.14	7.60
ϵ(O)	8.40	8.42	8.18	8.34	8.22	8.47	8.11	8.67	8.41	8.51	8.74	8.22
ϵ(Ne)	7.60	7.62		6.46:	7.15	7.65		7.75:	7.48	7.62	7.86	7.53:
ϵ(S)	6.6			6.29	6.30			6.79	6.7:		6.86	6.31
ϵ(Ar)	5.75:			5.86	5.81			6.08	6.5		6.53	6.20:

References – 1) Aller & Keyes (1987). 2) Costa et al. (1996). 3) Cuisinier et al. (1996). 4) Dopita et al. (1990). 5) Henry (1990). 6) Kaler (1980). 7) Kaler et al. (1996). 8) Köppen (private communication). 9) Ratag et al. (1990). 10) Walton et al. (1993). 11) Webster (1976). 12) Webster (1988). 13) This work.

fluxes for the central star as they would appear through the nebula. In this way we could calculate a prediction for the Johnson B and V magnitudes. However, observed stellar magnitudes will be reddened due to interstellar extinction as well, and we have to take this into account in our predictions. To calculate the total extinction towards the nebula, we averaged all the measurements we could find in the literature. Since the continuum fluxes predicted by CLOUDY already take the internal extinction into account, we only have to correct the stellar magnitudes for the external extinction. Hence we used the internal extinction from our model, and subtracted it from the total extinction. Then we used this value for the external extinction to predict the reddened B and V magnitudes of the central star. Where necessary, we applied the interstellar reddening law given by Pottasch (1984). A comparison of the calculated values with the literature values taken from Acker et al. (1992) is given in Table 2.14.

The predicted magnitudes are slightly higher than observed, but still in remarkable good agreement, considering the fact that we use a blackbody approximation to determine these values. Given the fact that a blackbody of a given temperature has more ionizing photons than a realistic spectrum with the same effective temperature, one can expect that in the best-fit model the total luminosity will be underestimated to compensate for this effect. However, we find that this effect is only very modest and this can be understood from the fact that we include the dust emission in the modeling. Grains can be heated very efficiently by Balmer continuum photons, as well as by Lyman continuum photons. Therefore, the *IRAS* fluxes give a good constraint on the Balmer continuum flux. This counteracts the previously mentioned underestimation of the total luminosity and explains the remarkable accuracy of our stellar broadband fluxes.

Table 2.14 — *For the PN in our sample we give in column 2 and 3 the Johnson B and V magnitudes resp. predicted by our model, in column 4 the internal extinction derived from our model, in column 5 the average total extinction derived from the Balmer decrement and the absolute* Hβ *flux, in columns 6 and 7 the predicted reddened values for the Johnson B and V magnitudes and in column 8 and 9 the measured magnitudes given in Acker et al. (1992).*

name	$B_{\rm mod}$ mag	$V_{\rm mod}$ mag	$A_V^{\rm int}$ mag	$A_V^{\rm tot}$ mag	$B_{\rm pred}$ mag	$V_{\rm pred}$ mag	B mag	V mag
H 1−40	15.7	15.7	1.11	5.03	20.8	19.6		
M 1−20	14.6	14.9	0.06	2.45	17.8	17.3	17.7	17.1
M 2−4	14.4	14.6	0.14	2.66	17.7	17.2	17.6	17.0
M 2−23	14.6	14.9	0.08	1.64	16.7	16.5	16.7	
M 3−15	15.5	15.8	0.10	4.39	21.1	20.1		

F. Distance

In our model assumptions we assume the distance to be a fixed number. However, our method can easily be changed in such a way that the distance would be maintained as a free parameter. When this is done, the best-fit model would also give an estimate for the distance. We have investigated the possibility to use our method this way. We found that this method works in principle, but that the spread in the resulting distance determinations is large. The results are vulnerable to all kinds of observational errors, especially to the error in the determination of the angular diameter. Since the angular diameter is notoriously hard to measure, this makes the results very uncertain. We have determined the distances to the bulge nebulae in our sample this way and found a very large spread in the results (van Hoof & Van de Steene 1996). The spread is larger than what is expected from a statistical method (Van de Steene & Zijlstra 1995).

Closer investigation reveals that this method of determining distances is in essence identical to the method described in Phillips & Pottasch (1984). They already concluded that this method is unreliable. The use of a wrong value for the distance not only influences the distance dependent parameters but also some distance independent parameters, as was already discussed in Sect. 2.5.1.A. We therefore do not recommend this method, and advise the use of separately determined distances.

2.7 Conclusions and future research

1. We presented a method which enables a fully self-consistent determination of the physical parameters of a PN. The method uses the spectrum, the *IRAS* and radio fluxes and the angular diameter of the nebula. The method is tested on an artificial set of 'observations' and it is shown that it is capable of reproducing all the physical parameters of the PN.
2. We studied the effect of observational errors on the derived physical parameters. The errors have little effect on the stellar temperature and luminosity, the electron temperature and the abundances. They have some effect on the hydrogen density, the inner and the Strömgren radius and the ionized mass. Observational errors have a larger, though limited, effect on the dust-to-gas ratio and the ionization parameter. The outer radius and the total shell mass are very vulnerable to measurement errors and should be considered unreliable.
3. The best-fit models are mainly influenced by measurement errors in the weak lines, and therefore care should be taken not to give too much weight to these lines in the modeling process.
4. The influence of errors in the model assumptions on the resulting best-fit model was also tested. The errors that had the largest effect where: the use of a blackbody spectrum instead of a realistic model atmosphere, the assumption that the inner radius of the gas coincides with the inner radius of the dust, and the attempt to model a non-spherically symmetric nebula with a spherically symmetric model. Also the use of a wrong value for the distance has a large effect, although mainly on the distance dependent parameters. The presence of large density fluctuations or other spherically symmetric deviations from the assumed density distribution have surprisingly little influence on the resulting model. Also the precise value for the filling factor is not critical. The only two physical parameters which appear to be robust against all these errors are the stellar temperature and the electron temperature. All other parameters are affected to some degree.
5. We applied the method to a sample of five galactic bulge PN. Comparison of the distance independent physical parameters with published data shows that the stellar temperatures generally are in good agreement and can be considered reliable. The literature data for the electron temperature, electron density and also for the abundances show a large spread, indicating that the use of line diagnostics is not reliable. Comparison of the various abundance determinations indicates that the uncertainty in the electron temperature is the main source of uncertainty in the abundance determination. The large spread in the literature data makes a comparison with our results meaningless.
6. Our conclusion is that our method for making photo-ionization models works, provided that ample observational data of good quality are available and that sufficient emission lines of various ionization stages are observed in the spectrum. Where possible, particular care should be taken to make the model assumptions as realistic as possible.
7. Future research will be aimed at improving the stability of our method and finding new and easier ways of assessing the accuracy of modeling results. In the near future, our aims will be directed at improving the critical dependence of the modeling results on the *IRAS* 12 μm over 25 μm ratio. Also the discrepancy between our electron temperature determinations and the values from other methods should be investigated. In future modeling we also want to test other model assumptions which may better describe the PN structure and might improve our ability to model bipolar nebulae. Finally we wish to include the use of model atmospheres in our method as soon as a suitable grid becomes available.

Acknowledgments. We wish to thank Drs. J. Köppen and R.B.C. Henry for extensive discussions of their results. We thank Drs. S.R. Pottasch, L.B.F.M. Waters and J.M. van der Hulst for helpful comments. Drs. R.D. Oudmaijer, T. de Jong and the anonymous referee are thanked for critically reading the manuscript. The authors acknowledge support from the Netherlands Foundation for Research in Astronomy (ASTRON) under grant no. 782–372–033 and 782–372–035. PvH wishes to thank ESO for their hospitality and financial support during his stay in Santiago where part of this paper was written. The photo-ionization code CLOUDY was used, written by Gary Ferland and obtained from the University of Kentucky, USA. We thank Gary Ferland for his invaluable help in debugging and modifying the code.

2.8 Appendix: Symbols

The following definitions for the symbols have been used.

A_V	– The extinction at the central wavelength of the Johnson *V* band (5553 Å) in magnitudes.
B	– The magnitude of a star in the Johnson *B* band.
c	– The speed of light.
D	– The distance to the nebula.
$e_{1,2}$	– Error estimate for the line flux ratios.

$E(B-V)$ – Measure for the interstellar extinction, $A_V = 3.066 \times E(B-V)$
F – The flux. A subscript λ or ν indicates the flux density per unit wavelength or frequency.
g – The gravitational acceleration.
K_λ – Calibration of a raw spectrum in absolute flux units per count as a function of wavelength.
L_* – The luminosity of the central star.
M – Generic symbol for a model parameter of a PN.
$M_{\rm ion}$ – The mass of the ionized material in the nebula.
$M_{\rm sh}$ – The total mass of the nebula.
$n_{\rm e}$ – The electron density.
$\overline{n_{\rm e}}$ – Average electron density, defined as $\overline{n_{\rm e}} = \int n_{\rm e}^3 {\rm d}V / \int n_{\rm e}^2 {\rm d}V$.
$n_{\rm H}$ – The total number density of hydrogen.
N_λ – The number of counts as a function of wavelength in a raw spectrum.
O – Generic symbol for an observable of a PN.
P – Generic symbol for a physical parameter of a PN.
$Q_{\rm H}$ – The number of hydrogen ionizing photons emitted by the central star.
r – Distance from the central star.
$r_{\rm in}$ – The inner radius of the nebula.
$r_{\rm out}$ – The outer radius of the nebula.
$r_{\rm str}$ – The Strömgren radius of the nebula.
r_λ – The residual of the fit as a function of wavelength.
R – The intrinsic ratio of $F({\rm H}\alpha)/F({\rm H}\beta)$.
R_λ – Relative detector response, the number of counts per flux unit as a function of wavelength.
t^2 – The r.m.s. of the fluctuations in the electron temperature.
T_* – The effective temperature of the central star.
$T_{\rm e}$ – The electron temperature in the nebula.
$\overline{T_{\rm e}}$ – Average electron temperature computed by CLOUDY, $\overline{T_{\rm e}} = \int n_{\rm e}^2 T_{\rm e} {\rm d}V / \int n_{\rm e}^2 {\rm d}V$.
U – The ionization parameter, $U = Q_{\rm H}/4\pi r_{\rm in}^2 n_{\rm H} c$.
$v_{\rm LSR}$ – The radial velocity w.r.t. the Local Standard of Rest
V – The magnitude of a star in the Johnson V band.
Z – The number density of metals in the star w.r.t. the solar value.
α – Right Ascension.
Γ – The dust-to-gas mass ratio.
δ – Declination.
Δ – The absolute error in a certain quantity.
ϵ – The filling factor, describing the small scale clumpiness of the gas in the nebula.
$\epsilon(\ldots)$ – The logarithmic number density of an element. $\epsilon({\rm H}) \equiv 12$.
ζ – Coefficient describing the accuracy of a model parameter, defined in eqs. (2) and (3).
$\Theta_{\rm d}$ – The angular diameter of the nebula.
λ – The wavelength.
ν – The frequency.
σ – The standard deviation. A subscript λ indicates the standard deviation as a function of wavelength.
χ^2 – Goodness-of-fit estimator.

2.9 References

Acker A., Köppen J., Stenholm B., Jasniewicz G., 1989, A&AS 80, 201
Acker A., Köppen J., Stenholm B., Raychev B., 1991, A&AS 89, 237
Acker A., Ochsenbein F., Stenholm B. et al., 1992, Strasbourg-ESO Catalogue of Galactic Planetary Nebulae, ESO, Garching bei München
Alexander J., Balick B., 1997, AJ, in press
Aller L.H., 1984, Physics of Thermal Gaseous Nebulae, Reidel, Dordrecht, p. 256
Aller L.H., Czyzak S.J., 1983, ApJS 51, 211
Aller L.H., Keyes C.D., 1987, ApJS 65, 405 (AK87)
Beintema D.A., van Hoof P.A.M., Lahuis F. et al., 1996, A&A 315, L253 (Chapter 6)
Boffi F.R., Stanghellini L., 1994, A&A 284, 248
Brocklehurst M., 1971, MNRAS 153, 471
Brocklehurst M., 1972, MNRAS 157, 211
Clegg R.E.S., 1987, MNRAS 229, 31P
Clegg R.E.S., 1989, Proc. IAU Symp. 131: Planetary Nebulae, Torres-Peimbert S. (ed.), Kluwer, Dordrecht, p. 139
Clegg R.E.S., 1993, Proc. IAU Symp. 155: Planetary Nebulae, Weinberger R., Acker A. (eds.), Kluwer, Dordrecht, p. 549
Clegg R.E.S., Middlemass D., 1987, MNRAS 228, 759
Costa R.D.D., Chiappini C., Maciel W.J., de Freitas Pacheco J.A., 1996, A&AS 116, 249
Cuisinier F., Acker A., Köppen J., 1996, A&A 307, 215
Dinerstein H.L., 1983, in Flower D.R., ed., IAU Symp. 103: 'Planetary Nebulae', p. 79
Dopita M.A., Henry J.P., Tuohy I.R. et al., 1990, ApJ 365, 640
Feast M.W., 1987, The Galaxy, Gilmore G., Carswell B. (eds.), Reidel, Dordrecht, p. 1
Ferland G.J., 1993a, Proc. IAU Symp. 155: Planetary Nebulae, Weinberger R., Acker A. (eds.), Kluwer, Dordrecht, p. 123
Ferland G.J., 1993b, University of Kentucky Physics Department Internal Report
Gabler R., Gabler A., Kudritzki R.P., Puls J., Pauldrach A., 1989, A&A 226, 162
Garnett D.R., 1992, AJ 103, 1330
Gathier R., Pottasch S.R., Goss W.M., van Gorkom J.H., 1983, A&A 128, 325
Gleizes F., Acker A., Stenholm B., 1989, A&A 222, 237
Harrington J.P., 1989, Proc. IAU Symp. 131: Planetary Nebulae, Torres-Peimbert S. (ed.), Kluwer, Dordrecht, p. 157
Henry R.B.C., 1990, ApJ 356, 229
Hoare M.G., 1990, MNRAS 244, 193
Husfeld D., Kudritzki R.P., Simon K.P., Clegg R.E.S., 1984, A&A 134, 139
Kaler J.B., 1976, ApJ 210, 843
Kaler J.B., 1979, ApJ 228, 163
Kaler J.B., 1980, ApJ 239, 78
Kaler J.B., 1986, ApJ 308, 322

Kaler J.B., 1989, Proc. IAU Symp. 131: Planetary Nebulae, Torres-Peimbert S. (ed.), Kluwer, Dordrecht, p. 229
Kaler J.B., Jacoby G.H., 1991, ApJ 372, 215
Kaler J.B., Bell D., Hayes J., Stanghellini L., 1993, PASP 105, 599
Kaler J.B., Kwitter K.B., Shaw R.A., Browning L., 1996, PASP 108, 980
Kingsburgh R.L., Barlow M.J., 1992, MNRAS 257, 317
Köppen J., Acker A., Stenholm B., 1991, A&A 248, 197
Kurucz R.L., 1991, Rev. Mex. Astron. Astrofís. 23, 181
Liu X.-W., 1997, in 'ISO's View on Stellar Evolution', in preparation
Mathis J.S., 1985, ApJ 291, 247
Mathis J.S., Rumpl W., Nordsieck K.H., 1977, ApJ 217, 425
Méndez R.H., Niemela V.S., 1982, Proc. IAU Symp. 99: Wolf-Rayet Stars: Observations, Physics, Evolution, de Loore C.W.H., Willis A.J. (eds.), Reidel, Dordrecht, p. 457
Osterbrock D.E., 1989, Astrophysics of Gaseous Nebulae and Active Galactic Nuclei, University Science Books, Mill Valley, pp. 119 and 132
Peimbert M., 1967, ApJ 150, 825
Perinotto M., 1991, ApJS 76, 687
Phillips J.P., Pottasch S.R., 1984, A&A 130, 91
Pottasch S.R., 1984, Planetary Nebulae, Reidel, Dordrecht, p. 95
Pottasch S.R., 1992, A&AR 4, 215
Pottasch S.R., 1996, A&A 307, 561
Pottasch S.R., Acker A., 1989, A&A 221, 123
Preite-Martinez A., 1993, Proc. IAU Symp. 155: Planetary Nebulae, Weinberger R., Acker A. (eds.), Kluwer, Dordrecht, p. 65
Press W.H., Flannery B.P., Teukolsky S.A., Vetterling W.T., 1986, Numerical Recipes, Cambridge University Press, p. 289
Ratag M.A., Pottasch S.R., 1990, A&A 227, 207
Ratag M.A., Pottasch S.R., Dennefeld M., Menzies J.W., 1990, PhD thesis, Groningen, Chapter 2 (RPDM)
Robbins R.R., 1968, ApJ 151, 511
Samland M., Köppen J., Acker A., Stenholm B., 1992, A&A 264, 184
Seaton M.J., 1987, J. Phys. B 20, 6363
Sellmaier F.H., Yamamoto T., Pauldrach A.W.A., Rubin R.H., 1996, A&A 305, L37
Shaw R.A., Dufour R.J., 1995, PASP 107, 896
Shaw R.A., Kaler J.B., 1989, ApJS 69, 495
Stanghellini L., Kaler J.B., 1989, ApJ 343, 811
Terzian Y., 1993, Proc. IAU Symp. 155: Planetary Nebulae, Weinberger R., Acker A. (eds.), Kluwer, Dordrecht, p. 109
Tylenda R., Stasińska G., Acker A., Stenholm B., 1991a, A&A 246, 221
Tylenda R., Acker A., Stenholm B., Gleizes F., Raychev B., 1991b, A&AS 89, 77
Van de Steene G.C., Zijlstra A.A., 1995, A&A 293, 541
van Hoof P.A.M., Van de Steene G.C., 1996, Planetary Nebulas with Wolf-Rayet Type Nuclei, Lundström I., Stenholm B. (eds.), Ap&SS 238, 83
van Hoof P.A.M., Oudmaijer R.D., Waters L.B.F.M., 1997, MNRAS 289, 371 (Chapter 4)
Walton N.A., Barlow M.J., Clegg R.E.S., 1993, Proc. IAU Symp. 155: Planetary Nebulae, Weinberger R., Acker A. (eds.), Kluwer, Dordrecht, p. 581
Webster B.L., 1976, MNRAS 174, 513
Webster B.L., 1988, MNRAS 230, 377 (W88)
Zuckerman B., Aller H.A., 1986, ApJ 301, 772
Zijlstra A.A., van Hoof P.A.M., Chapman J.M., Loup C., 1994, A&A 290, 228 (Chapter 5)

3 Measuring angular diameters of nebulae

P.A.M. van Hoof

Abstract — When measuring diameters of partially resolved sources, often a technique called 'gaussian deconvolution' is used. This technique is applicable to both optical and radio observations and can be used for planetary nebulae, H II regions, galaxies or any other extended source. This technique yields a gaussian diameter which subsequently has to be multiplied with a conversion factor to obtain the true angular diameter of the source. This conversion factor is a function of the Full Width at Half Maximum (FWHM) of the beam (in the case of radio observations) or the point spread function (in the case of optical observations). It also depends on the intrinsic surface brightness distribution (geometry) of the source. Usually the FWHM of the source and beam are measured using gaussian fits, but they can also be determined using second moments. This alternative technique is studied here for the first time and it is found that in this case the conversion factor has a different value which is *independent* of the beam size, but which still depends on the geometry. However, in the limit for infinitely large beam sizes, the values of the conversion factors for both techniques are equal. Hence all subsequent conclusions are equally valid for both techniques. In this paper conversion factors are presented for a number of simple geometries: a circular constant surface brightness disk and a spherical constant emissivity shell, using a range of values for the inner radius. Also more realistic geometries are studied, based on a spherically symmetric photo-ionization model of a planetary nebula. This enabled a study of optical depth effects, a comparison between images in various emission lines and the use of power law density distributions. It is found that the conversion factor can be very sensitive to the assumed geometry and to optical depth effects. Differences of several tens of percent have been found. For optical observations, the conversion factor depends on which emission line is chosen to observe the source. This is partly caused by excitation effects. Again differences of several tens of percent are possible. Hence care should be taken when comparing optical and/or radio measurements. Nebulae which have a power law drop-off in their density distribution usually have a 'fuzzy' edge and the Strömgren radius of the nebula will be situated somewhere in the faint surface brightness regions. For such nebulae the conversion factors can become very large and are very sensitive to the assumed geometry, both in the case of optical and radio observations. In such cases the use of gaussian deconvolution is not appropriate.

3.1 Introduction

The accurate measurement of angular diameters is a long standing problem. This problem is pertinent to the study of planetary nebulae, H II regions, galaxies or any other extended sources. Nevertheless, only few papers dedicated to this problem can be found in the literature (e.g. Mezger & Henderson 1967; Panagia & Walmsley 1978; Bedding & Zijlstra 1994; Schneider & Buckley 1996; Wellman et al. 1997). In this paper, the emphasis will be on nebular research. However, most results are also valid in a more general context.

Three methods are in general use to determine angular diameters. Method 1 determines the Full Width at Half Maximum (FWHM) of the nebula by making a least-squares fit of a two-dimensional gaussian to the measured surface brightness profile. This method is sometimes called 'gaussian deconvolution.' Method 2 is basically identical to method 1 except that it determines the FWHM using the second moment of the profile instead of a gaussian fit. Method 3 directly measures the radius at which a prescribed value of the surface brightness is reached, often a certain fraction of the peak surface brightness (e.g. 10 %). The last method is in general use for good quality observations of well resolved sources. In all other cases, i.e. when the source is only partially resolved, either method 1 or 2 is used, depending mainly on the preference of the observer. These methods have the disadvantage that they yield a result that has no well-defined physical meaning. Hence, a conversion factor is needed to translate the result into something which does have a well-defined meaning. In nebular research this usually is the Strömgren radius. This conversion factor depends on the method being used, the intrinsic surface brightness profile of the source and the resolution of the observation. In this paper the intrinsic surface brightness profile will be defined as the surface brightness profile that would be observed with a perfect instrument (i.e. an instrument with infinite resolving power). For brevity it will be referred to as the geometry of the source.

For nebulae with a sharp outer radius, i.e. a steep drop-off to zero surface brightness at a certain radius, it is easy to measure this radius using method 3, provided that observations of sufficient resolution and quality are available. This way no assumptions have to be made on the geometry of the source and this explains the popularity of the third method. It should however be stressed that in *all* other cases assumptions have to be made on the intrinsic surface brightness profile in order to interpret the results.

In general observations do not always have the resolution required for the use of method 3. If the size of a resolution element is not negligible compared to the angular diameter, the image will be broadened and needs to be deconvolved. This can be done by using method 1 or 2 and subsequently multiplying the result with a conversion factor. As was already mentioned, this conversion factor depends on the assumed geometry.

Another problem is that not all nebulae have a sharp outer radius. Often, when deeper images are made, more emission is detected at lower surface brightness levels. Such nebulae will be referred to as having a fuzzy outer radius. For optical observations, the interpretation of the low level emission is uncertain. It may originate from a tenuous plasma but may also be emission from the inner parts of the nebula reflected by dust particles in the neutral zone. Radio observations do not suffer from this ambivalence. However, they usually lack the sensitivity to pick up emission at these low surface brightness levels. Hence this problem still leads to a lot of controversy about what the real radius of the nebula is. The definitive answer can probably only be given when the next generation of highly sensitive radio arrays with large collecting area become available. This paper however, will not deal with this problem. Nevertheless, it can be stated that for fuzzy nebulae the 10 % radius (or a radius at any other percentage level) does not have a physical meaning and does not represent the nebular size very well. It is often found that the radius becomes increasingly larger when deeper images are taken. Hence, the size of such nebulae can not be represented by a single number. The possible application of method 1 or 2 to such nebulae will be discussed in Sect. 3.7.

This article will have the following structure: in Sect. 3.2 some basic assumptions and definitions will be given. Also, the methods used to determine the conversion factors will be discussed. In Sect. 3.3 conversion factors will be given for various simple geometries: a circular constant surface brightness disk and a spherical constant emissivity shell, using a range of values for the inner radius. In Sect. 3.4 these results will be compared to previous studies found in the literature and a discussion will be given. Next, the conversion factors will be studied using more realistic geometries based on a photo-ionization model of a planetary nebula. In Sect. 3.5 the influence of optical depth effects on the observed surface brightness profile and on the conversion factor will be studied. In Sect. 3.6 images made in several optical emission lines will be compared and the influence on the conversion factor will be discussed. In Sect. 3.7 the effect of non-constant density laws on the conversion factor will be studied. These density laws allow a discussion of the appropriateness of methods 1 and 2 for fuzzy nebulae. Finally, in Sect. 3.8 the main conclusions will be presented. The theory used to derive the conversion factors is presented in several appendices. In Sect. 3.10 the full analytical theory for deriving a deconvolved FWHM of a radially symmetric function by fitting two-dimensional gaussians will be given. In Sect. 3.11 the same will be done using the second moments method. In Sect. 3.12 some additional proofs will be presented and finally in Sect. 3.13 all the symbols that have been used will be defined.

3.2 Assumptions and computational methods

The methods discussed in this article are valid for observations at any wavelength. More in particular, they are valid for radio, optical and infrared observations. The resolution of these observations is usually characterized by the size of the beam profile for radio data and by the size of the point spread function for optical or infrared data. Throughout the paper the term 'beam' will be used and it will be implicitly understood that it can also mean 'point spread function' were appropriate. It will be assumed that the beam can be approximated by a gaussian. This is a reasonable assumption, both for radio and for optical observations. First, in the reduction of radio observations, the (possibly complicated) antenna pattern of the telescope is replaced by a perfect gaussian of the same resolution in the CLEAN procedure. Second, for optical observations the point spread function is normally determined by the seeing which can be approximated by a gaussian. This approximation is however only valid for the core region of the point spread function, further out it is better represented by an inverse square law (e.g. King 1971). This implies that care should be taken when interpreting low level emissions surrounding barely resolved nebulae, accurate knowledge of the point spread function is then required (Falomo 1996). For simplicity it will be assumed throughout this paper that both the geometry of the nebula and the beam are radially symmetric. This is a rather severe restriction; nebulae rarely are circular and also, for radio observations, the beam usually is elliptical. However, the general case was deemed to complicated and no attempt will be made to solve it.

As was already remarked, a conversion factor is needed to translate the FWHM diameter yielded by method 1 or 2 into a Strömgren diameter. In this paper the Strömgren radius of the nebula will be denoted by r_s. In the rest of this paper it will be assumed that the true diameter of the nebula is $\Theta_d = 2r_s$. The measured FWHM of the nebula will be denoted by Φ and the FWHM of the beam by Φ_b. Throughout the paper the 'deconvolved' FWHM diameter Φ_d will be used, which is defined by

$$\Phi_d = \sqrt{\Phi^2 - \Phi_b^2}. \tag{4}$$

This quantity is also commonly called the 'gaussian' diameter. The conversion factor to obtain the the true angular diameter from the deconvolved FWHM can now be defined as

$$\Theta_d = \gamma\Phi_d \quad \Rightarrow \quad \gamma = \Theta_d/\Phi_d = 2r_s/\Phi_d. \tag{5}$$

This conversion factor is a function of the resolution of the observation, or to be more precise, of the ratio of the source diameter and the beam size. Hence an independent parameter β is chosen, which is defined as

$$\beta = \Phi_d/\Phi_b. \tag{6}$$

In the following sections more details will be given of the techniques that have been used to calculate the conversion factors, both for the gaussian fit method and the second moments method.

3.2.1 Method 1: gaussian fits

First we will discuss the technique that has been used to calculate the conversion factors for the gaussian fit method. This technique is based on an implicit equation from which the value of $\gamma(\beta)$ can be solved for arbitrary β. The derivation of this expression will not be given here, but can be found in Sect. 3.10. The actual formula that has been used is given in eq. (35). To use this technique, first the radial moments (defined in eq. 10) of the surface brightness profile have to be computed. This is done using either an analytic expression (if available) or a numerical integration scheme. Next these radial moments and also the value for β are substituted in eq. (35). Finally the value for the conversion factor γ is solved from this equation using a Newton-Raphson scheme. This procedure is repeated for a range of values for β and thus the behavior of the conversion factor $\gamma(\beta)$ as a function of β can be found.

In order to represent the results efficiently, a simple analytic function will be fitted to the conversion factors. Tests have shown that $\gamma(\beta)$ can be approximated extremely well by the following function

$$\gamma_f(\beta) = \frac{a_1}{1 + a_2\beta^2} + a_3 \tag{7}$$

which will be used throughout this paper. The fit is determined by minimizing the reduced χ^2 which is defined as

$$\chi^2 = \frac{1}{N}\sum_{n=1}^{N} \left[\gamma(\beta_n) - \gamma_f(\beta_n)\right]^2. \tag{8}$$

Here N is the total number of points at which the conversion factor has been evaluated (usually 251, with $\beta_n = 0\,(0.02)\,5$).

3.2.2 Method 2: second moments

The second moment method is widely used to calculate the FWHM of an arbitrary profile. In general however, the result of this method will not be identical to the FWHM derived from a gaussian fit. Hence, also the value for the conversion factor will be different. To distinguish the results of the two methods, a subscript 2 will be used on all quantities derived with the second moments method. In Sect. 3.11 it will be proven that when the second moments method is used to derive the deconvolved FWHM, the conversion factor is constant (i.e. *independent* of beam size). Furthermore, this constant value is equal to the value of the conversion factor for the gaussian fit method in the limit for infinitely large beams. In other words, the conversion factor for the second moment method is given by

$$\gamma_2(\beta) = \gamma(0) \quad \text{for all } \beta \in [0, \infty).$$

Due to this relation it is not strictly necessary to give separate results. The value for the conversion factor when second moments are used can always be calculated using the following expression

$$\gamma_2 \approx \gamma_f(0) = a_1 + a_3. \tag{9}$$

Given the quality of the fitting function γ_f, this yields results with more than sufficient accuracy (a few times 10^{-3} down to a few times 10^{-4}).

3.3 The conversion factor for simple geometries

The methods which have been discussed in the previous section are usually applied to images which are only partly

Table 3.1 — *The parameters for calculating the conversion factors. Results are given for a constant surface brightness disk and for a constant emissivity shell with various ratios of the inner to outer radius (as indicated in column 1). The conversion factors for the gaussian fit method can be calculated using eq. (7), the conversion factors for the second moment method are given separately in the last column. The latter values can also be calculated using eqs. (42), (46) or (48) substituting $\beta = 0$ where necessary.*

case	a_1	a_2	a_3	χ^2	γ_2
disk	0.3512	0.7874	1.3469	5.4(–8)†	1.6986
shell 0.0	0.3358	0.7907	1.5629	4.1(–8)	1.8991
shell 0.1	0.3368	0.7896	1.5609	4.3(–8)	1.8982
shell 0.2	0.3431	0.7835	1.5482	5.1(–8)	1.8918
shell 0.3	0.3563	0.7745	1.5187	6.3(–8)	1.8756
shell 0.4	0.3729	0.7694	1.4733	6.8(–8)	1.8468
shell 0.5	0.3875	0.7715	1.4168	6.5(–8)	1.8049
shell 0.6	0.3959	0.7786	1.3546	6.1(–8)	1.7510
shell 0.7	0.3963	0.7871	1.2909	5.9(–8)	1.6877
shell 0.8	0.3893	0.7940	1.2281	5.7(–8)	1.6180
shell 0.9	0.3766	0.7981	1.1678	5.4(–8)	1.5449
limit 1.0	0.3600	0.7994	1.1106	5.0(–8)	1.4711

† 5.4(–8) stands for 5.4×10^{-8}.

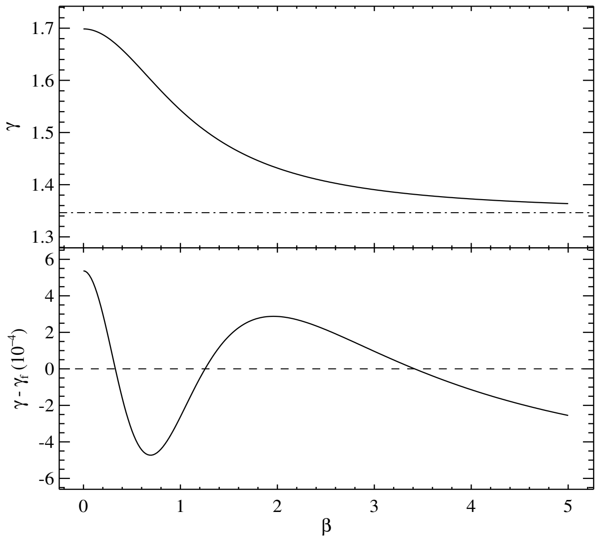

Figure 3.1 — *The conversion factors for a constant surface brightness disk (upper panel) and the residuals of the fit to these conversion factors (lower panel). The dash-dotted line in the upper panel indicates the value for $\gamma(\infty)$.*

resolved. Hence they contain little direct information on the intrinsic surface brightness profile. If no other information is available, the intrinsic surface brightness profile has to be assumed in order to calculate the conversion factors. In such cases, the choice is usually a very simple geometry. In this section, the conversion factors for these cases will be determined. The work in this section will be based on the geometries that were treated in Bedding & Zijlstra (1994). These are the constant surface brightness disk (the limiting case of a spherically symmetric nebula which is completely optically thick, or alternatively a nebula with cylindrical symmetry viewed along the axis), and the constant volume emissivity shell and sphere (the limiting case of a spherically symmetric nebula with zero optical thickness). These cases will be treated in more detail here, and also shells with an arbitrary inner radius will be treated. The sphere can be viewed as the limiting case of a shell with zero inner radius.

3.3.1 The constant surface brightness disk

The conversion factors for the gaussian fit method are shown in Fig. 3.1 and the parameters for the fit are given in Table 3.1. The limiting values of this fit agree very well with the predicted values (eqs. 42 and 19). The residuals of the fit are shown in Fig. 3.1. The conversion factor for the second moment method is also given in Table 3.1.

3.3.2 The constant emissivity shell

Conversion factors for the gaussian fit method were also computed for the case of a constant emissivity shell with a range of values for the ratio of the inner to outer radius: r_i/r_s = 0.0 (0.1) 1.0. The results are shown in Fig. 3.2 and the fit parameters are given in Table 3.1. Again the quality of the fits is very good. It can be seen that the shape of the curve doesn't change very much as a function r_i/r_s, but that the height of the curve does. This means that the correct value for the conversion factor does depend quite critically on the assumed value for the inner radius. The conversion factors for the second moment method are also given in Table 3.1.

3.4 Comparison of the results

In this section the results from Sect. 3.3 will be compared with other results. First, the conversion factors will be compared to the results from a completely different technique applied by the author. This is done to verify the correctness of the procedure used in this paper. This comparison will be limited to the geometries that were already studied in the literature: the constant surface brightness disk, the constant emissivity sphere and the constant emissivity shell with r_i/r_s = 0.8. Next, the results from this paper will be compared to other data that have been published.

3.4.1 Comparison with a different technique

In order to verify the procedure described in Sect. 3.2.1 for calculating conversion factors using gaussian fits, a completely different technique was also used to calculate the conversion factors. This technique essentially mimics the procedure used in real observations: a given surface brightness profile first is convolved with a gaussian of prescribed

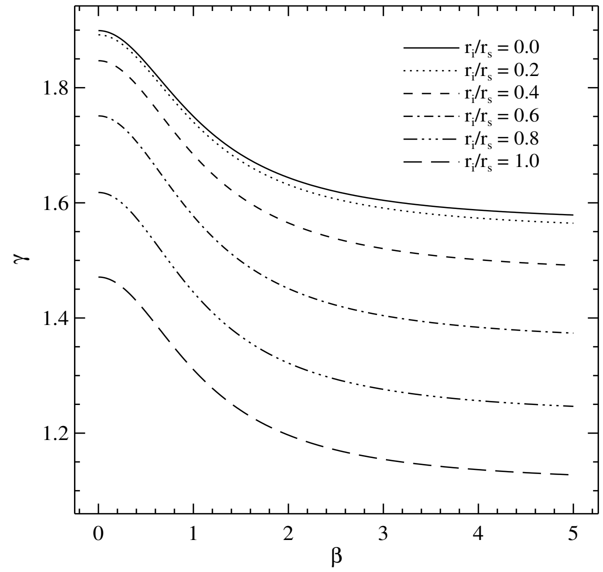

Figure 3.2 — *The conversion factor for constant emissivity shells for various ratios of the inner to outer radius ($r_\mathrm{i}/r_\mathrm{s}$).*

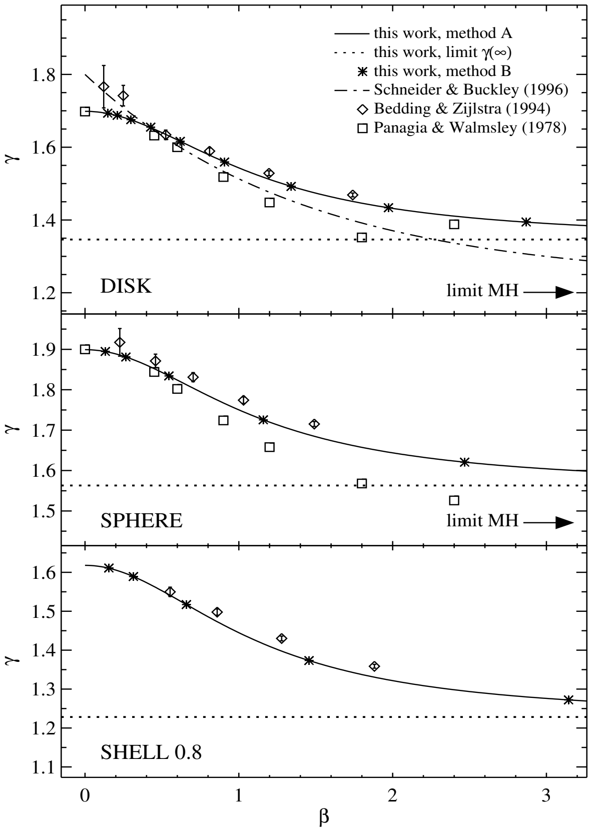

Figure 3.3 — *Comparison of this work with previous results. Methods A and B are explained in the text. The arrows 'limit MH' indicate the value for $\gamma(\infty)$ obtained by Mezger & Henderson (1967).*

width and then a gaussian is fitted to the resulting convolved surface brightness profile. Subsequently the deconvolved width of this gaussian is compared to the Strömgren diameter of the unconvolved profile and the conversion factor is calculated. In order to distinguish the two techniques, the procedure described in Sect. 3.2.1 will be called method A, and the procedure described here will be called method B. The reason that method A was adopted throughout the paper, and not method B, is that it is by far the fastest and most accurate method.

For the three geometries that have been mentioned above, the results of method A were compared to the results of method B. They were found to be in excellent agreement. For the disk case it was found that $\chi^2 = 4.6\times10^{-7}$, for the shell case $\chi^2 = 7.4\times10^{-8}$ and for the sphere case $\chi^2 = 3.0\times10^{-8}$ (see eq. 8). This proves the correctness of method A. The comparison is also visualized in Fig. 3.3.

Since the calculation of the conversion factors using the second moments method is closely linked to the calculation of the conversion factors for the gaussian fit method (see Sect. 3.2.2), this also proves the correctness of our results for the second moment method.

3.4.2 Comparison with published results

Four papers have been previously published which were (at least in part) dedicated to calculating conversion factors. These are Mezger & Henderson (1967, hereafter MH), Panagia & Walmsley (1978, hereafter PW), Bedding & Zijlstra (1994, hereafter BZ) and Schneider & Buckley (1996, hereafter SB). A comparison of all the results is shown in Fig. 3.3. A cross-reference of the symbols used in the various papers is given in Table 3.2. It should be noted that in all these papers the gaussian fit method was used. The second moment method has never been studied before in the literature and hence no comparison can be given for the results of this method.

Mezger & Henderson (1967) assumed that conversion factors are independent of the beam size. They derived the conversion factors by comparing the diameter of an unconvolved disk or sphere to a gaussian with the same peak surface brightness and total flux. Hence one could say that they assumed $\beta = \infty$. However their method is clearly not appropriate, since fitting a gaussian to a given profile is not flux-conservative. The gaussian will in general have a different total flux than the original profile. It can be seen that their results are substantially lower than the results from this study.

Panagia & Walmsley (1978) re-examined the conversion factors for both geometries. They concluded that the conversion factors depend on the beam size and that adopting the results of MH will generally lead to an underestimation of the nebular diameter. The value of the conversion factor for $\beta = 0$ was calculated using an analytic expression, for the other points they probably used a method which is essentially identical to method B. It can be seen that for

Table 3.2 — *Cross-reference for the symbols used in this paper and the previous publications.*

this work	MH	PW	BZ	SB
Φ_b		Θ_A	Θ_{PSF}	Θ_{beam}
Φ_d	Θ_G	Θ_G	Θ_{gauss}	Θ_{gauss}
r_s	$\frac{1}{2}\Theta_{sph,cyl}$	Θ_R	$\frac{1}{2}\Theta_{true}$	$\frac{1}{2}\Theta_{PN}$
β		$\frac{\Theta_G}{\Theta_A}$	$\frac{\Theta_{gauss}}{\Theta_{PSF}}$	$\frac{\Theta_{gauss}}{\Theta_{beam}}$
$\gamma(\beta)$	$\frac{\Theta_{sph,cyl}}{\Theta_G}$	$2\frac{\Theta_R}{\Theta_G}$	$\frac{\Theta_{true}}{\Theta_{gauss}}$	$\frac{\Theta_{PN}}{\Theta_{gauss}}$

$\beta = 0$ their results coincide with the results of this paper. However, for larger β an increasing discrepancy between the results becomes apparent. In the disk case they even find a minimum in $\gamma(\beta)$ which is not reproduced in this work. These discrepancies will be discussed together with the results of SB.

Bedding & Zijlstra (1994) re-examined the conversion factors for the disk and the sphere case and also added the case of a shell geometry. The method they used was essentially identical to method B. Unfortunately their results are only given in graphical form, making it hard to read off the values of $\gamma(\beta)$. The error bars in Fig. 3.3 represent the uncertainty involved in this process. Their results are clearly the most accurate of all previous studies. It seems they systematically make a slight overestimate of the conversion factor. An explanation for this is not apparent to the author.

Schneider & Buckley (1996) studied only the disk geometry. They were the first to use an analytic fit to the conversion factor as a function of β. The method they used was essentially identical to method B. In their results it can be seen that the conversion factor is progressively underestimated for larger β. The most likely explanation for this result (and also for the results of PW) is as follows. The gaussian fit to the (convolved) surface brightness profile is determined by minimizing the quadratic residuals, which is defined as an integral over an infinite region (see eq. 11). In a numerical code this integral is replaced by an integral over a finite region, where the upper limit of this region should be large enough not to influence the result. If the upper limit is chosen too low, the fit will not be 'punished' for the tails of the gaussian outside the integration region. In the case of a disk geometry this will lead to an overestimation of the FWHM as is shown in Fig. 3.4. In view of this result, it is recommended to use a *diameter* for the fitting region which is at least 3 times the FWHM diameter of the fit, irrespective of the fact if the nebula has a non-zero surface brightness in the whole of this region or not. For nebulae with extended faint emission the integration region should encompass the whole of the nebula of course. In the case where the surface brightness profile is a perfect gaussian (which is the case in the limit for infinitely large beam sizes, $\beta = 0$), the mentioned effect does not exist. The residuals will be zero everywhere and the upper limit of the integration region is irrelevant. The bigger the discrepancy between the actual profile and a perfect gaussian is (i.e. the larger β is), the stronger the fit will be affected by the effect. This is exactly what can be seen in the results from PW and SB. The local minimum that was found by PW for the disk case may have been caused by the fact that they used a larger integration region for the last point.

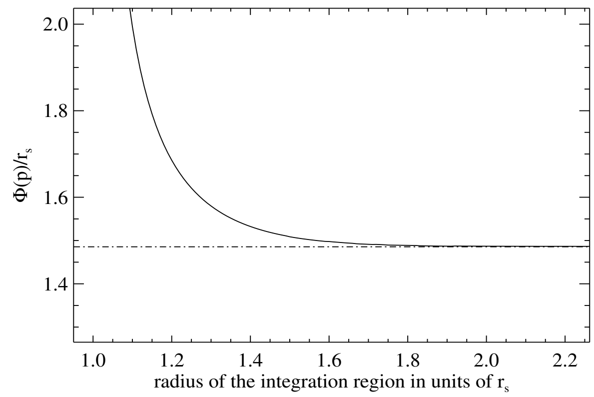

Figure 3.4 — *The* FWHM *resulting from a gaussian fit to a constant surface brightness disk as a function of the radius of the fitting region. The dash-dotted line indicates the value of the* FWHM *for an infinitely large fitting region, i.e. the correct value given by eq. (19).*

For very small values of β, SB find higher values for the conversion factor than this study. This is probably an artifact of the fitting function adopted by SB. It was found to give lower quality fits than the fitting function adopted in this paper, while it has the same number of free parameters. This can be illustrated by applying both fitting functions to the conversion factors for a constant surface brightness disk. The fitting function given in eq. (7) yields $\chi^2 = 5.4\times10^{-8}$ (see eq. 8), while the fitting function of SB result in $\chi^2 = 7.2\times10^{-5}$. This result can be understood in a qualitative sense by looking at the analytic form of both fitting functions. The conversion factor $\gamma(\beta)$ has a first derivative which is zero at $\beta = 0$, as is also the case for the fitting function adopted in this paper. This is however not the case for the fitting function adopted by SB. Hence the fitting function adopted by SB will result in first order deviations for small β, while the fitting function in eq. (7) only results in second order deviations. Since it is impossible to compute the conversion factor for very small β using method B (as was done by SB), their fit will not be constrained there and thus their choice of fitting function will result in too high values for the conversion factor close to $\beta = 0$.

When the results of PW are viewed for large beam sizes it can be seen that the conversion factor is roughly 1.7 in the disk case, and roughly 1.9 in the sphere case. This had led to the popular notion that the deconvolved FWHM should be multiplied by 1.8 to obtain the correct diameter, inde-

Table 3.3 — *The parameters for calculating the conversion factors in different observing modes. The conversion factors for the gaussian fit method can calculated using eq. (7), the conversion factors for the second moment method can calculated using eq. (9).*

case	a_1	a_2	a_3	$\tau^\dagger$
radio 2 cm	0.3428	0.7853	1.6222	2.88(–2)
radio 6 cm	0.3429	0.7860	1.6067	2.91(–1)
radio 20 cm	0.3462	0.7892	1.4767	3.63(+0)
radio 60 cm	0.3529	0.7870	1.3708	3.58(+1)
radio 200 cm	0.3433	0.7854	1.3753	4.37(+2)
Hα	0.3605	0.7822	1.4937	9.06(–1)
Hα+[N II]	0.3569	0.7867	1.3656	9.06(–1)
Hβ	0.3644	0.7817	1.4842	1.26(+0)
[O III]	0.4083	0.7892	1.3176	1.22(+0)

† The optical depth is measured from the center of the nebula to the outer edge.

pendent of beam size and geometry. The popularity of this assumption should in all probability be attributed to its simplicity. However, from the previous discussion it becomes clear that quite substantial errors can be made this way, as was already pointed out by PW. The magnitude of this error can easily be greater than the observational uncertainties in the measurement itself. Hence this simplification can not be justified. This implies that assumptions about the intrinsic surface brightness profile are unavoidable. Since there obviously is room for discussion about these assumptions, the author would like to urge all observers to publish besides the derived angular diameter (which depends on this assumption) also *both* the deconvolved FWHM (which does not depend on this assumption) and the beam size. This allows other scientists to make their own assumptions and compare the results.

3.5 Optical depth effects

In the previous sections several simple geometries have been studied where an analytic expression for the intrinsic surface brightness profile can be assumed. However, in the following section more realistic geometries will be studied. These will be based on a photo-ionization model of a planetary nebula. The procedure to calculate the conversion factors in this case is as follows. A table with the emissivity and the absorption coefficient as a function of distance to the star is calculated with a modified version of the photo-ionization code CLOUDY 84.12a (Ferland 1993). When the emissivities and the absorption coefficients are known, the radiative transport equation can be integrated numerically, assuming spherical symmetry and neglecting scattering processes. This is done by a separate code which yields an intrinsic surface brightness profile. This profile can then be used to determine the conversion factors using the procedure already described in Sect. 3.2.1.

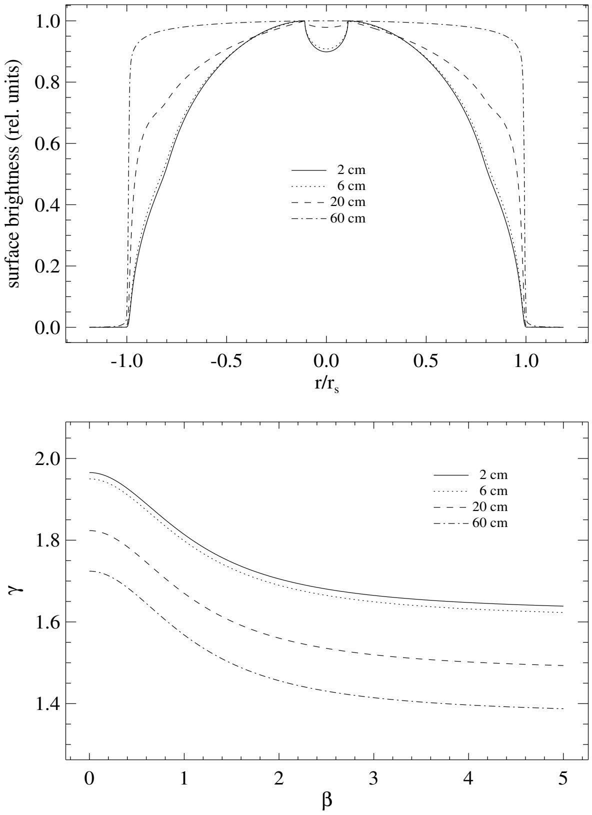

Figure 3.5 — *The surface brightness profiles (upper panel) and the conversion factors (lower panel) computed at wavelengths of 2 cm, 6 cm, 20 cm and 60 cm. The maximum surface brightness has been normalized to unity.*

To study the effect of varying optical depth with wavelength, the results of the planetary nebula model have been used at various wavelengths in the radio regime. The physical process responsible for the emission and absorption at these wavelengths are free-free interactions between protons and electrons. It is a well known fact that the optical depth τ due to free-free absorption increases towards longer wavelengths as $\tau \propto \lambda^{2.1}$ (e.g. Pottasch 1984: p. 88). The input parameters used for the model are the ones for the NGC 7027 model discussed in Beintema et al. (1996). This nebula was chosen solely for the purpose of getting a realistic model. The fact that NGC 7027 is quite large and thus well resolved in most observations is of no importance. One could assume that another nebula is modeled here which is very similar to NGC 7027, but at a much larger distance. Using this model, the shape of the surface brightness profile at various wavelengths could be determined. It turns out that the surface brightness profile is very sensitive to optical depth effects. To illustrate this, various profiles are shown in Fig. 3.5. The conversion factors to obtain the true angular diameter at the various wavelengths are shown in Fig. 3.5. The nebula is only marginally optically thick at 6 cm, but this already has a noticeable effect on the conversion factor. At 20 cm the nebula is mildly optically thick, and this has a strong effect on the conversion factor.

It should be remarked that the geometry for the nebula favors a big effect on the conversion factor for increasing optical depth. For large optical depths the surface brightness profile of any nebula resembles that of a constant surface brightness disk, as was discussed in Sect. 3.3. Thus the conversion factors in this case will also be much the same. Since for the model discussed here the conversion factors at optically thin wavelengths are much higher than this, they must change quite drastically once optical depth effects set in. If on the other hand the conversion factor in the optically thin case would be more or less similar to that of a disk, then optical depth effects are expected to have a lesser effect. However, in general this can not be assumed *a priori*, and thus care should be taken when comparing measurements taken at different wavelengths. This is not only true because of the effects described above, but also because at different wavelengths the beam size will be different, hence β will be different and this will influence the conversion factor as well if the gaussian fit method is used.

3.6 Imaging in emission lines

Since optical images are also often used to determine the radius of a nebula, the conversion factors for these images will be investigated as well. For this the same model was used as discussed in the previous section. The emissivity was assumed to be the volume emissivity of the following emission lines: Hα, Hβ, [N II] λ6548, λ6584 and [O III] λ5007. The contribution of continuum emission in the images was neglected. When solving the radiative transport equations, continuum optical depth effects were included, but not line optical depth effects. Next, the surface brightness profiles were computed for images taken in pure Hα light, in Hα+[N II] $\lambda\lambda$6548, 6584, in Hβ and in [O III] λ5007. The results are shown in the upper panel of Fig. 3.6. Finally, the conversion factors were computed for these profiles. The parameters for the fits are given in Table 3.3, the curves are shown in the lower panel of Fig. 3.6.

The first thing that can be noticed is that the surface brightness profiles in the various emission lines look completely different and that they also differ from the radio surface brightness profiles shown in Fig. 3.5. Also the positions for the peak surface brightness are completely different. This implies that even in well resolved images, the measured diameter can be different depending on which line is used. This is caused by excitation effects. Given this, it can already be expected that the conversion factors should be different for the various images as well, which is indeed confirmed. The conversion factors for images in pure Hα and Hβ light are nearly identical, which can be expected from the fact that the relative level populations depend only mildly on electron temperature and density. However, this situation completely changes when the [N II] lines are included in the passband of the Hα filter (as is

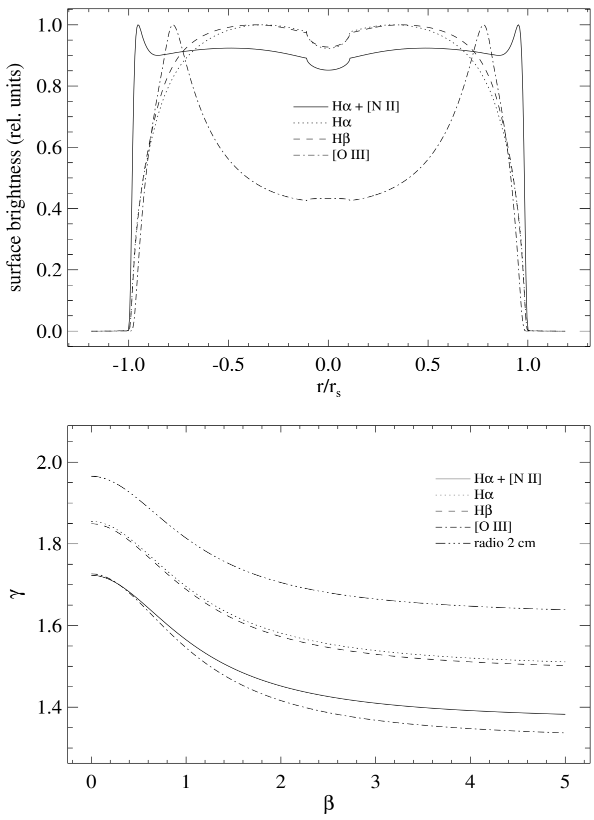

Figure 3.6 — *The intrinsic surface brightness profiles (upper panel) and the conversion factors (lower panel) in various emission lines. The maximum surface brightness has been normalized to unity. Note the different position of the peak surface brightness in the [O III] and the Hα+[N II] image. The conversion factors for the 2 cm radio image have also been shown for reference.*

usually the case). This has a considerable effect on the conversion factor. Also the conversion factors for the [O III] image are quite different from the Hβ case, but, by chance, nearly coincide with the values for the Hα+[N II] image. It can be seen that all conversion factors for the optical images are considerably smaller than the values for the (optically thin) 2 cm radio image.

From this the conclusion can be drawn that angular diameters measured using different techniques can *not* be compared directly, even in well resolved images. In general the conversion factors for the various images will be different, depending on the intrinsic surface brightness profile and the beam size of the observation. For the case that has been studied above, differences exceeding 30 % are possible.

3.7 Non-constant density geometries

The nebular model that has been discussed so far assumes a constant hydrogen density inside the Strömgren sphere. This automatically leads to a sharp boundary of the nebula.

Table 3.4 — *The parameters for calculating the conversion factors for various density profiles. The conversion factors for the gaussian fit method can calculated using eq. (7), the conversion factors for the second moment method can calculated using eq. (9).*

α	Θ_d arcsec	a_1	a_2	a_3	Kurt
0.00	11.37	0.3428	0.7853	1.6222	–0.560
-0.50	12.61	0.3188	0.7911	1.7573	–0.496
-1.00	15.04	0.2418	0.8397	2.0415	–0.363
-1.25	17.47	0.1253	1.1091	2.3545	–0.222
-1.35	18.98	0.0391	3.8565	2.5602	–0.131
-1.40	19.94	–0.078	0.078	2.740	–0.073
-1.50	22.50	–0.252	0.476	3.103	+0.083

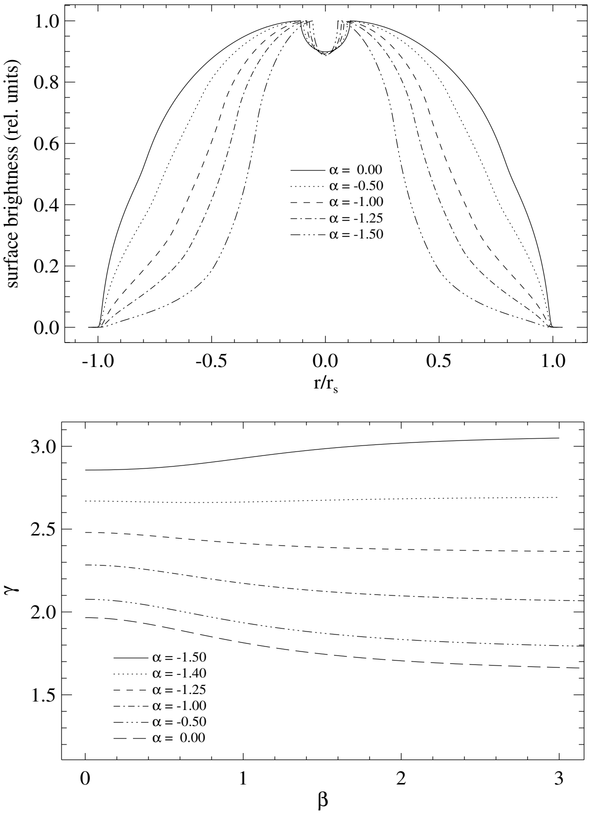

Figure 3.7 — *The intrinsic surface brightness profiles (upper panel) and the conversion factors (lower panel) for different density distributions. The maximum surface brightness has been normalized to unity.*

To investigate how the conversion factors behave for nebulae with fuzzy boundaries, the density law was changed in the following way. For the inner parts of the nebula ($\lg(r/\text{cm}) < 16.6$) the density law remained unchanged (i.e. constant), but for the outer parts an r^α law was assumed. This roughly models a nebula where the inner parts have undergone hydrodynamic interactions with the fast post-AGB wind, but where the outer parts are not yet disturbed. Values of α were used ranging from 0.0 down to -1.5. All the other parameters of the model were kept unaltered. For all models a radio image was calculated at a wavelength of 2 cm. The surface brightness profiles and conversion factors are shown in Fig. 3.7. In Table 3.4 the parameters for the fits to the conversion factors together with the true angular diameters of the nebulae can be found.

The first thing that can be noticed is that the conversion factors become increasingly larger as α becomes more negative. This is of course no surprise. The FWHM of an image is mainly determined by the high surface brightness core. Hence, the more centrally peaked the image becomes, the smaller the FWHM will be with respect to the Strömgren radius. Thus the conversion factor will become larger. The second thing that can be noticed is that the behavior of the conversion factor as a function of β changes when α is varied. When α is lowered, the conversion factor gradually changes from a monotonically decreasing function to a monotonically increasing function. This behavior is also reflected by the fact that the sign of a_1 changes from positive to negative. For a certain range of values around $\alpha \approx -1.38$, the conversion factor is neither monotonically decreasing or increasing, but displays a local minimum (see Fig. 3.8). It is the first time that this kind of behavior is reported for the conversion factor. This behavior can be roughly parameterized by the kurtosis of the surface brightness profile which is defined by

$$\text{Kurt}\left[f(r)\right] = \frac{c_0 c_4}{c_2^2} - 2$$

where the term -2 makes the expression zero for a gaussian profile. Profiles with negative kurtosis (which can be considered 'broader' than a gaussian) result in a negative second derivative of $\gamma(\beta)$ at $\beta = 0$. Hence this function bends downward and generally this will result in a monotonically decreasing behavior. Conversely, profiles with positive kurtosis will result in a positive second derivative of $\gamma(\beta)$, which will generally result in a monotonically increasing behavior. There are exceptions to this rule, when the kurtosis is close to zero. This is illustrated in Fig. 3.8.

From the previous discussion it can be seen that the conversion factor is a very strong function of α. This can be easily understood when the nature of the changes to the density profile is viewed. Since a large part of the constant density regime inside the Strömgren sphere remains unaltered when α is changed, also the high surface brightness core of the nebula remains more or less unaltered. Since both method 1 and 2 are most sensitive to this part, the deconvolved FWHM will not change much as a function of α. However, the Strömgren radius is very sensitive to α, as can be seen in Table 3.4. This implies that the conversion factor must also be a sensitive function of α. If the Strömgren is chosen as a physically meaningful radius, this makes it almost impossible to measure this radius from low resolution observations if density distributions similar to the ones discussed here are suspected. It is the authors opinion that in such a case the only meaningful thing to do is to publish

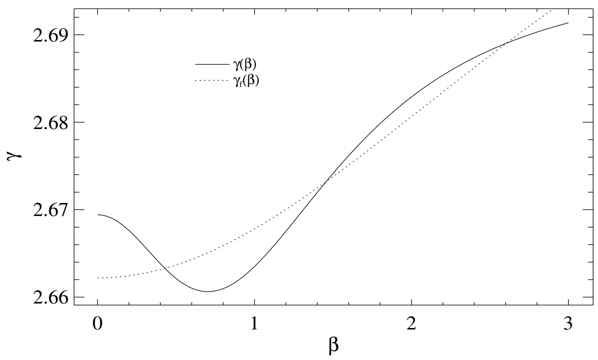

Figure 3.8 — *The conversion factors for the density distribution with* $\alpha = -1.40$.

the deconvolved FWHM and the beam size and not to make an attempt to calculate the Strömgren radius.

3.8 Conclusions

In this work conversion factors have been determined to convert the deconvolved FWHM of a partially resolved nebula to its true diameter. It was already found by Mezger & Henderson (1967) that this conversion factor depends on the (assumed) intrinsic surface brightness profile of the nebula. In a subsequent study by Panagia & Walmsley (1978) it was found that the conversion factor also depends on the beam size of the observation when gaussian fits are used. This can lead to differences of several tens of percent. In this paper an alternative method to measure the FWHM, using second moments, is studied for the first time. Also the influence of the intrinsic surface brightness profile on the conversion factor is studied in much more detail. The following recommendations and conclusions were reached. Unless explicitly noted otherwise, they are valid both for the gaussian fit and the second moments method and also for observations at arbitrary wavelengths.

1. When making a gaussian fit to a surface brightness profile, it is recommended to use a diameter for the fitting region which is at least 3 times the FWHM diameter of the fit in *all* cases. If the fitting region is chosen too small, it will influence the fit. A larger fitting region should be used if extended faint emission is present.
2. The deconvolved FWHM derived using gaussian fits is in general not equal to the deconvolved FWHM derived using the second moment method. Hence the conversion factors will also be different in both cases. For the second moment method, the conversion factor is *independent* of the beam size. Its value is in all cases equal to the conversion factor for the gaussian fit method in the limit for infinitely large beams. The conversion factor for the second moment method does depend on the assumed surface brightness profile.
3. The conversion factor is very sensitive to the adopted intrinsic surface brightness profile. Differences up to 40 % can be found for constant emissivity shells with different inner radii. Hence, great care should be taken when making a choice for the intrinsic geometry.
4. Because of this, observers are urged to publish, besides the Strömgren diameter of the nebula, the deconvolved FWHM, the method used (i.e. gaussian fit or second moments) and the *beam size*.
5. The conversion factor is very sensitive to optical depth effects, so care should be taken when comparing observations made at different wavelengths. This is especially the case for radio observations. Differences of several tens of percent are possible.
6. For optical observations the conversion factor depends on which emission line is chosen. This is partly due to excitation effects and this results in the fact that even well resolved images in different emission lines can yield different diameters. It is also caused by the fact that the intrinsic surface brightness profile is different in different emission lines. Again differences of several tens of percent are possible. Hence care should be taken when comparing optical and radio measurements.
7. Nebulae which have a power law drop-off in their density distribution usually have a fuzzy edge and the Strömgren radius will be situated in the faint surface brightness regions of the nebula. For such nebulae the conversion factors can become very large and are very sensitive to the assumed geometry of the nebula. Since this geometry can in general not be assessed accurately, it is not meaningful to apply a conversion factor and only the deconvolved FWHM and the beam size should be published. Also direct measurement of the radius at a certain fraction of the peak surface brightness is meaningless for such nebulae.
8. For all geometries studied previously, the conversion factor for gaussian fits becomes larger for larger beam sizes. In general however, this is *not* always the case. This behavior is roughly controlled by the kurtosis of the intrinsic surface brightness profile.

Acknowledgments. The photo-ionization code CLOUDY has been used, written by Gary Ferland and obtained from the University of Kentucky, USA. The author would like to thank G.C. Van de Steene for inspiring this research. PvH was supported by NFRA grant 782–372–033.

3.9 References

Bedding T.R., Zijlstra A.A., 1994, A&A 283, 955 (BZ)
Beintema D.A., van Hoof P.A.M., Lahuis F. et al., 1996, A&A 315, L253 (Chapter 6)
Falomo R., 1996, ESO Messenger 86, 37
Ferland G.J., 1993, University of Kentucky, Physics Department, Internal Report
King I.R., PASP 83, 199
Mezger P.G., Henderson A.P., 1967, ApJ 147, 471 (MH)
Panagia N., Walmsley C.M., 1978, A&A 70, 411 (PW)
Pottasch S.R., 1984, Planetary Nebulae. Reidel, Dordrecht
Schneider S.E., Buckley D., 1996, ApJ 459, 606 (SB)
Wellman G.F., Daly R.A., Wan L., 1997, ApJ 480, 79

3.10 Appendix: Determining diameters using gaussian fits

In this section the conversion factor will be studied for the case where the FWHM of the observed surface brightness profile is determined using gaussian fits. An implicit equation will be derived from which the value of $\gamma(\beta)$ can be solved for arbitrary β. This equation will also be used to derive the first terms of a Taylor series expansion of $\gamma(\beta)$ around $\beta = 0$. This implicit equation is derived in three stages. First it will be shown how to derive the width of a gaussian fitted to an arbitrary function in Sect. 3.10.1. Next an expression for a surface brightness profile convolved with a gaussian of arbitrary size in Sect. 3.10.2 will be derived. Finally in Sect. 3.10.3 these results will be combined to determine the conversion factor. In this process various lemma's will be used which can be found in Sect. 3.12.

Note 1: in the remainder of this paper all functions are implicitly assumed to be radially symmetric.

Note 2: in the remainder of this paper the following constraint will be imposed on the surface brightness profile $f(r)$:

(1) $0 \leq f(r) \leq F$ for all $r \in [0, \infty)$

When c_n is defined as

$$c_n = \int_0^\infty f(r) r^{n+1} \mathrm{d}r \tag{10}$$

the following additional constraint can be formulated

(2a) c_{2n} exists for $n = 0, 1$ with $c_0 > 0$

In Sect. 3.10.2 and 3.10.3 a more severe constraint has to be imposed

(2b) c_{2n} exists for all $n \in \mathbb{N}_0$ with $c_0 > 0$

It should be noted that the fact that c_n exists automatically implies that all c_i exist with $i \leq n$, as is shown in lemma 3.1.

Note 3: in the remainder of this paper it will be assumed that $r_\mathrm{s} = 1$.

3.10.1 Fitting a gaussian to a surface brightness profile

In this section the formulae to approximate a surface brightness profile $f(r)$ with a two dimensional gaussian in a least-squares sense will be derived. The gaussian will be written as

$$g(r; a, p) = a\,\mathrm{e}^{-pr^2} \quad \text{with } a > 0,\ p > 0$$

In order to determine a least squares fit to the surface brightness profile, the integral over the quadratic residuals χ^2 needs to be minimized. Hence the following two equations need to be solved:

$$\frac{\partial \chi^2}{\partial p} = \frac{\partial}{\partial p} \int_0^{2\pi} \int_0^\infty \left[f(r) - g(r; a, p) \right]^2 r \mathrm{d}r \mathrm{d}\varphi = 0 \tag{11}$$

and

$$\frac{\partial \chi^2}{\partial a} = \frac{\partial}{\partial a} \int_0^{2\pi} \int_0^\infty \left[f(r) - g(r; a, p) \right]^2 r \mathrm{d}r \mathrm{d}\varphi = 0 \tag{12}$$

Eq. (11) will be evaluated first. After integration over φ and reversal of the order of differentiation and integration one gets

$$-4\pi \int_0^\infty \left[f(r) - g(r; a, p) \right] \frac{\partial g(r; a, p)}{\partial p} r \mathrm{d}r = 0$$

One can easily prove that this is allowed, provided c_0 and c_2 exist, using lemma 3.3 and 3.4. Since

$$\frac{\partial g(r; a, p)}{\partial p} = -ar^2 \mathrm{e}^{-pr^2}$$

one finds, after division by the constants,

$$\int_0^\infty \left[f(r) - a\mathrm{e}^{-pr^2} \right] r^2 \mathrm{e}^{-pr^2} r \mathrm{d}r = 0$$

and thus

$$\int_0^\infty f(r)\, r^3\, \mathrm{e}^{-pr^2} \mathrm{d}r = a \int_0^\infty r^3\, \mathrm{e}^{-2pr^2} \mathrm{d}r = \frac{a}{8p^2} \tag{13}$$

For eq. (12) one finds after a similar derivation that

$$\int_0^\infty f(r)\, r\, \mathrm{e}^{-pr^2} \mathrm{d}r = \frac{a}{4p} \tag{14}$$

Hence

$$\int_0^\infty f(r)\, r\, \mathrm{e}^{-pr^2} \mathrm{d}r = 2p \int_0^\infty f(r)\, r^3\, \mathrm{e}^{-pr^2} \mathrm{d}r$$

and thus the width of the gaussian fitted to the surface brightness profile can be found by solving eq. (15).

$$I(p) = \int_0^\infty f(r)\,(1 - 2pr^2)\, r\, \mathrm{e}^{-pr^2} \mathrm{d}r = 0 \tag{15}$$

If the substitution $s = pr^2$ is used, one can write

$$I(p) = \frac{1}{2p} \int_0^\infty f\left(\sqrt{s/p}\,\right)\, (1 - 2s)\, \mathrm{e}^{-s} \mathrm{d}s = 0 \tag{16}$$

Once the width has been determined, the height of the gaussian can be solved from either eq. (13) or eq. (14). Using eq. (15) one can easily see that

$$\lim_{p \to 0} I(p) = c_0 \ > \ 0$$

Substituting a Taylor series expansion of f in eq. (16) one can prove that

$$\lim_{p \to \infty} I(p) = -\, f^{(n)}(0)\ p^{-\frac{n}{2}-1} \frac{(n+1)\,\Gamma\!\left(\frac{n}{2}+1\right)}{2\,n!} + \mathcal{O}\left(p^{-\frac{n}{2}-\frac{3}{2}}\right) \ < \ 0$$

Where $f^{(n)}(0)$ with $n \in \mathbb{N}_0$ denotes the first non-zero derivative of f. Its value must be positive due to constraint (1). Since I is a continuous function in p, its limiting behavior assures that at least one solution of eq. (16) must exist. Since

$$\frac{\partial^2 \chi^2}{\partial a^2} = \frac{\pi}{p} \ > \ 0$$

this solution can either be a saddle point or a minimum depending on the sign of

$$\frac{\partial^2 \chi^2}{\partial p^2} = -2\pi \frac{a}{p} \int_0^\infty \frac{\mathrm{d}f}{\mathrm{d}r}\, r^4\, \mathrm{e}^{-pr^2} \mathrm{d}r \tag{17}$$

From this equation it is clear that for monotonically decreasing $f(r)$ all solutions of eq. (16) must be minima. Given the fact that χ^2 and its derivatives are continuous functions in both a and p, this implies that only one minimum can exist and thus the solution of eq. (16) must be unique. In general however, this is not the case.

A. The constant surface brightness disk

Eq. (16) usually gives rise to very nasty implicit equations which can only be solved numerically. Since this result is not of prime interest anyway (gaussian fits are usually not applied to well-resolved images), the equation will not be solved for the geometries treated in this paper. However, one exception will be made. For a constant surface brightness disk the intrinsic surface brightness profile is very simple

$$f(r) = \begin{cases} f_0 & r \le r_\mathrm{s} \\ 0 & r > r_\mathrm{s} \end{cases} \tag{18}$$

Without loss of generality it can be assumed that $f_0 = 1/\pi$ and $r_s = 1$. One can easily see that this profile satisfies constraints (1) and (2b). Substituting eq. (18) in eq. (17) one can also prove that a unique fit must exist. Hence, to determine the width of the gaussian fitted to the unconvolved profile, one may substitute eq. (18) in eq. (16):

$$\int_0^p f_0\,(1-2s)\,\mathrm{e}^{-s}\mathrm{d}s = 0$$

Evaluation of this integral results in

$$\frac{1}{\pi}\left[(2p+1)\,\mathrm{e}^{-p} - 1\right] = 0$$

Multiplying this equation by π and taking the natural logarithm yields the following implicit equation for p

$$p = \ln(2p+1) = 1.2564312\ldots \quad\Rightarrow\quad \Phi(p) = 1.4855024\ldots \quad\Rightarrow\quad \gamma(\infty) = 1.3463458\ldots \tag{19}$$

3.10.2 An expression for the convolved surface brightness profile

In this section an expression for an intrinsic surface brightness profile convolved with a gaussian of arbitrary size will be derived. This way a relation between the intrinsic and the observed profile will be found. The intrinsic (unconvolved) surface brightness profile will be written as $f(r)$ and the convolved profile as $f_c(r)$. Hence

$$f_c(x,y) = \int_{-\infty}^{\infty}\int_{-\infty}^{\infty} f(x',y')\,g(x-x',y-y';a,p)\,\mathrm{d}x'\mathrm{d}y' = a\int_{-\infty}^{\infty}\int_{-\infty}^{\infty} f(x',y')\,\mathrm{e}^{-p(x-x')^2}\mathrm{e}^{-p(y-y')^2}\mathrm{d}x'\mathrm{d}y' \tag{20}$$

In order to evaluate eq. (20) the exponential functions will be replaced by their Taylor series in the following way:

$$\mathrm{e}^{-p(x-x')^2} = \mathrm{e}^{-px^2}\mathrm{e}^{-px'^2}\mathrm{e}^{2pxx'} = \mathrm{e}^{-px^2}\mathrm{e}^{-px'^2}\sum_{n=0}^{\infty}\frac{(2pxx')^n}{n!} \tag{21}$$

Since it can easily be proved that eq. (21) has an infinite radius of convergence it is allowed to substitute eq. (21) in eq. (20), hence

$$f_c(x,y) = a\int_{-\infty}^{\infty}\int_{-\infty}^{\infty} f(x',y')\,\mathrm{e}^{-px^2}\mathrm{e}^{-px'^2}\mathrm{e}^{-py^2}\mathrm{e}^{-py'^2}\left[\sum_{n=0}^{\infty}\frac{(2pxx')^n}{n!}\right]\left[\sum_{n=0}^{\infty}\frac{(2pyy')^n}{n!}\right]\mathrm{d}x'\mathrm{d}y' =$$

$$= a\,\mathrm{e}^{-p(x^2+y^2)}\int_{-\infty}^{\infty}\int_{-\infty}^{\infty} f(x',y')\,\mathrm{e}^{-p(x'^2+y'^2)}\sum_{n=0}^{\infty}(2p)^n\sum_{i=0}^{n}\frac{(xx')^{n-i}(yy')^i}{(n-i)!\,i!}\mathrm{d}x'\mathrm{d}y'$$

When x', y' are changed to radial coordinates this equation can be rewritten as

$$f_c(x,y) = a\,\mathrm{e}^{-p(x^2+y^2)}\int_0^{\infty}\int_0^{2\pi} f(r')\,\mathrm{e}^{-pr'^2}\sum_{n=0}^{\infty}(2p)^n\sum_{i=0}^{n}\frac{x^{n-i}y^i}{(n-i)!\,i!}\,r'^n\cos^{n-i}\varphi'\,\sin^i\varphi'\,r'\,\mathrm{d}\varphi'\,\mathrm{d}r'$$

When the order of the integration and summation is reversed one finds (lemma 3.5 proves that this is allowed)

$$f_c(x,y) = a\,\mathrm{e}^{-p(x^2+y^2)}\int_0^{\infty} f(r')\,\mathrm{e}^{-pr'^2}\sum_{n=0}^{\infty}(2p)^n r'^{n+1}\sum_{i=0}^{n}\frac{x^{n-i}y^i}{(n-i)!\,i!}\int_0^{2\pi}\cos^{n-i}\varphi'\,\sin^i\varphi'\,\mathrm{d}\varphi'\,\mathrm{d}r' \tag{22}$$

The inner integral is well known and yields a non-zero result only when both $n-i$ and i are even. In this case the result is

$$\int_0^{2\pi}\cos^{2n-2i}\varphi\,\sin^{2i}\varphi\,\mathrm{d}\varphi = 2\pi\,\frac{(2n-2i)!\,(2i)!}{2^{2n}\,n!\,(n-i)!\,i!} \tag{23}$$

When eq. (23) is substituted in eq. (22) and all the odd terms in n and i are omitted one finds

$$f_c(x,y) = a\,\mathrm{e}^{-p(x^2+y^2)}\int_0^{\infty} f(r')\,\mathrm{e}^{-pr'^2}\sum_{n=0}^{\infty}(2p)^{2n}r'^{2n+1}\sum_{i=0}^{n}\frac{x^{2n-2i}y^{2i}}{(2n-2i)!\,(2i)!}\,2\pi\,\frac{(2n-2i)!\,(2i)!}{2^{2n}\,n!\,(n-i)!\,i!}\,\mathrm{d}r' =$$

$$= 2\pi\, a\, \mathrm{e}^{-p(x^2+y^2)} \int_0^\infty f(r')\, \mathrm{e}^{-pr'^2} \sum_{n=0}^{\infty} (2p)^{2n} r'^{2n+1} \frac{1}{2^{2n}\, n!} \sum_{i=0}^{n} \frac{x^{2n-2i} y^{2i}}{(n-i)!\, i!}\, \mathrm{d}r' =$$

$$= 2\pi\, a\, \mathrm{e}^{-p(x^2+y^2)} \int_0^\infty f(r')\, \mathrm{e}^{-pr'^2} \sum_{n=0}^{\infty} \frac{p^{2n}}{n!^2}\, r'^{2n+1} \sum_{i=0}^{n} \binom{n}{i}\, x^{2(n-i)} y^{2i}\, \mathrm{d}r' =$$

$$= 2\pi\, a\, \mathrm{e}^{-p(x^2+y^2)} \int_0^\infty f(r')\, \mathrm{e}^{-pr'^2} \sum_{n=0}^{\infty} \frac{p^{2n}}{n!^2}\, r'^{2n+1} (x^2+y^2)^n\, \mathrm{d}r'$$

When x, y are changed to radial coordinates and the order of integration and summation are reversed one gets (lemma 3.5 proves that this is allowed)

$$f_\mathrm{c}(r) = 2\pi\, a\, \mathrm{e}^{-pr^2} \sum_{n=0}^{\infty} \frac{p^{2n}}{n!^2}\, r^{2n} \int_0^\infty f(r')\, r'^{2n+1} \mathrm{e}^{-pr'^2} \mathrm{d}r' \tag{24}$$

When the generalized n-th moment of $f(r)$ is defined as

$$c_n(p) = 2\pi \int_0^\infty f(r)\, r^{n+1} \mathrm{e}^{-pr^2} \mathrm{d}r \tag{25}$$

eq. (24) can be rewritten to the following expression for the convolved surface brightness profile

$$f_\mathrm{c}(r) = a\, \mathrm{e}^{-pr^2} \sum_{n=0}^{\infty} \frac{c_{2n}(p)\, p^{2n}}{n!^2}\, r^{2n} \tag{26}$$

Given the fact that $c_{2n}(p)$ is finite for all $p \in (\,0, \infty\,)$ (lemma 3.2) one can easily prove that this series has an infinite radius of convergence. An alternative formulation for eq. (26) can be derived which will be used further on. When the exponential in eq. (25) is expanded in a Taylor series in p (which can easily be shown to have an infinite radius of convergence) one finds

$$c_n(p) = 2\pi \int_0^\infty f(r)\, r^{n+1} \sum_{k=0}^{\infty} (-1)^k \frac{(pr^2)^k}{k!} \mathrm{d}r$$

The order of integration and summation may be reversed (lemma 3.6), hence

$$c_n(p) = \sum_{k=0}^{\infty} (-1)^k \frac{p^k}{k!}\, 2\pi \int_0^\infty f(r)\, r^{n+2k+1} \mathrm{d}r$$

When eq. (10) is used one can write

$$c_n(p) = \sum_{k=0}^{\infty} (-1)^k \frac{p^k}{k!}\, c_{n+2k} \tag{27}$$

When eq. (27) is substituted in eq. (26) one gets

$$f_\mathrm{c}(r) = a\, \mathrm{e}^{-pr^2} \sum_{n=0}^{\infty} \frac{r^{2n}}{n!^2} \sum_{k=0}^{\infty} (-1)^k \frac{p^{2n+k}}{k!}\, c_{2n+2k} \tag{28}$$

3.10.3 The width of the convolved surface brightness profile

Now an expression for the convolved profile has been found, the next task is to determine the width p' of a gaussian fitted to this profile. This is equivalent to measuring the FWHM of an observed profile. The result can be found by substituting eq. (28) in eq. (16). This gives

$$\int_0^\infty (1-2s)\, \mathrm{e}^{-s} f_\mathrm{c}\left(\sqrt{s/p'}\right) \mathrm{d}s = 0 \quad \Rightarrow \quad \int_0^\infty (1-2s)\, \mathrm{e}^{-s} a\, \mathrm{e}^{-s\frac{p}{p'}} \sum_{n=0}^{\infty} \frac{s^n}{p'^n n!^2} \sum_{k=0}^{\infty} (-1)^k \frac{p^{2n+k}}{k!}\, c_{2n+2k}\, \mathrm{d}s = 0 \quad \Rightarrow$$

$$\int_0^\infty (1-2s)\, a\, \mathrm{e}^{-s\left(\frac{p}{p'}+1\right)} \sum_{n=0}^\infty \left(\frac{p}{p'}\right)^n \frac{s^n}{n!^2} \sum_{k=0}^\infty (-1)^k \, \frac{p^{n+k}}{k!}\, c_{2n+2k}\, \mathrm{d}s = 0$$

When one abbreviates $\zeta = \frac{p}{p'} + 1$ and divides by a one can write

$$\int_0^\infty (1-2s)\, \mathrm{e}^{-\zeta s} \sum_{n=0}^\infty (\zeta-1)^n \frac{s^n}{n!^2} \sum_{k=0}^\infty (-1)^k \, \frac{p^{n+k}}{k!}\, c_{2n+2k}\, \mathrm{d}s = 0$$

When the order of summation and integration is reversed (lemma 3.7 proves that this is allowed) one finds

$$\sum_{n=0}^\infty \frac{(\zeta-1)^n}{n!^2} \sum_{k=0}^\infty (-1)^k \, \frac{p^{n+k}}{k!}\, c_{2n+2k} \int_0^\infty (1-2s)\, s^n \mathrm{e}^{-\zeta s} \mathrm{d}s = 0$$

It is well known that

$$\int_0^\infty x^n\, \mathrm{e}^{-px} \mathrm{d}x = \frac{n!}{p^{n+1}}$$

Hence

$$\sum_{n=0}^\infty \frac{(\zeta-1)^n}{n!^2} \sum_{k=0}^\infty (-1)^k \, \frac{p^{n+k}}{k!}\, c_{2n+2k} \left[\frac{n!}{\zeta^{n+1}} - 2\frac{(n+1)!}{\zeta^{n+2}}\right] = 0 \quad \Rightarrow$$

$$\sum_{n=0}^\infty \frac{1}{n!} \frac{(\zeta-1)^n}{\zeta^{n+2}} \sum_{k=0}^\infty (-1)^k \, \left[\, \zeta - 2(n+1)\,\right] \, \frac{p^{n+k}}{k!}\, c_{2n+2k} = 0$$

When this summation is regrouped into terms with equal powers of p one finds

$$\sum_{n=0}^\infty c_{2n} p^n \sum_{k=0}^n (-1)^{n-k} \, \frac{1}{(n-k)!\, k!} \left[\, \zeta - 2(k+1)\,\right] \frac{(\zeta-1)^k}{\zeta^{k+2}} = 0 \quad \Rightarrow$$

$$\sum_{n=0}^\infty \frac{c_{2n} p^n}{n!} \sum_{k=0}^n (-1)^{n-k} \binom{n}{k} \left[\, \zeta - 2(k+1)\,\right] \frac{(\zeta-1)^k}{\zeta^{k+2}} = 0 \tag{29}$$

Usually the width of a gaussian is given as the Full Width at Half Maximum (FWHM) value Φ. One can easily see that the FWHM for the beam Φ_b is given by

$$\Phi_\mathrm{b}(p) = 2\sqrt{\frac{\ln 2}{p}} \tag{30}$$

The deconvolved FWHM Φ_d of a fitted gaussian can be defined as

$$\Phi_\mathrm{d}(p', p) = \sqrt{\Phi^2(p') - \Phi_\mathrm{b}^2(p)} \tag{31}$$

Substituting eq. (30) in eq. (31) gives

$$\Phi_\mathrm{d}(p', p) = 2\sqrt{\frac{\ln 2}{p'} - \frac{\ln 2}{p}} = 2\sqrt{\frac{\ln 2}{p}(\frac{p}{p'} - 1)} = 2\sqrt{\frac{\ln 2}{p}(\zeta - 2)} \tag{32}$$

When one recalls the definition for β in eq. (6) a relation between ζ and β can be obtained

$$\beta = \frac{\Phi_\mathrm{d}(p', p)}{\Phi_\mathrm{b}(p)} = 2\sqrt{\frac{\ln 2}{p}(\zeta - 2)} \Big/ 2\sqrt{\frac{\ln 2}{p}} = \sqrt{\zeta - 2} \quad \Rightarrow \quad \zeta = \beta^2 + 2 \tag{33}$$

When eq. (5) and eq. (32) are combined, a relation between p and γ can be found

$$\gamma(\beta) = \frac{2}{\Phi_\mathrm{d}(p', p)} = \sqrt{\frac{p(\beta)}{(\zeta-2)\ln 2}} = \sqrt{\frac{p(\beta)}{\beta^2 \ln 2}} \quad \Rightarrow \quad p(\beta) = \gamma^2(\beta)\, \beta^2 \ln 2 \tag{34}$$

When eqs. (33) and (34) are substituted in eq. (29) one finds

$$\sum_{n=0}^{\infty} \frac{c_{2n}\,\gamma^{2n}(\beta)\,\beta^{2n}\ln^n 2}{n!} \sum_{k=0}^{n} (-1)^{n-k} \binom{n}{k} (\beta^2 - 2k) \frac{(\beta^2+1)^k}{(\beta^2+2)^{k+2}} = 0$$

If it is assumed that $\beta > 0$ this equation can be multiplied by $(\beta^2+2)^2/\beta^2$. This yields the generating equation for $\gamma(\beta)$

$$\sum_{n=0}^{\infty} \frac{c_{2n}\gamma^{2n}(\beta)\ln^n 2}{n!} \sum_{k=0}^{n} (-1)^{n-k} \binom{n}{k} (\beta^2 - 2k)\,\beta^{2n-2} \left(\frac{\beta^2+1}{\beta^2+2}\right)^k = 0 \tag{35}$$

Now one can determine $\gamma(0)$ by taking the limit $\beta \to 0$ of the left-hand side of eq. (35). This yields

$$c_0 - c_2\gamma^2(0)\ln 2 = 0 \quad \Rightarrow \quad \gamma(0) = \sqrt{\frac{c_0}{c_2 \ln 2}} \tag{36}$$

This yields the following expression for the deconvolved FWHM.

$$\Phi_{\rm d}(0,0) = 2\sqrt{\frac{c_2 \ln 2}{c_0}} \tag{37}$$

So it can be seen that the deconvolved FWHM of the source in the limit for very large beams is fully determined by two simple integrals over the intrinsic surface brightness profile. When eq. (37) is compared with eq. (49) one can see that this limiting value simply is the FWHM derived from the second moment of the unconvolved profile. In the next section it will be shown that this is also the deconvolved FWHM derived from the second moment of a profile convolved with a beam of arbitrary width.

Eq. (35) can also be used to determine a value for $\gamma(\beta)$ for arbitrary β. It can easily be solved numerically using a Newton-Raphson scheme. Without proof the following result will be given for the limit $\beta \to \infty$

$$\sum_{n=0}^{\infty} (-1)^n\,(2n+1) \frac{c_{2n}\,\gamma^{2n}(\infty)\,\ln^n 2}{n!} = 0 \tag{38}$$

Which can be used to determine the limiting value of the conversion factor for the unconvolved profile. It can be shown that the Taylor series of $\gamma(\beta)$ contains only even powers of β. Hence one may write

$$\gamma(\beta) = \sum_{l=0}^{\infty} g_{2l}\beta^{2l}$$

It should be noted that in general this expansion need not have an infinite radius of convergence, hence this expression is only valid sufficiently close to $\beta = 0$. Now the $2n$-th power of this series can be calculated, which will have the same radius of convergence as the original series

$$\gamma^{2n}(\beta) = \sum_{l=0}^{\infty} g_{2l}^{(2n)}\beta^{2l} \quad \text{with} \quad g_0^{(2n)} = g_0^{2n} \quad \text{and} \quad g_{2l}^{(2n)} = \frac{1}{2l\,g_0} \sum_{k=1}^{l} \left[\,2k\,(2n+1) - 2l\,\right] g_{2k}\, g_{2l-2k}^{(2n)} \tag{39}$$

When eq. (39) is substituted in eq. (35) one finds

$$\sum_{n=0}^{\infty} \frac{c_{2n}\ln^n 2}{n!} \sum_{l=0}^{\infty} g_{2l}^{(2n)} \sum_{k=0}^{n} (-1)^{n-k} \binom{n}{k} (\beta^2 - 2k)\,\beta^{2n+2l-2} \left(\frac{\beta^2+1}{\beta^2+2}\right)^k = 0 \tag{40}$$

Taking the 2nd derivative, the 4th derivative, etc… to β of eq. (40) and subsequently take the limit $\beta \to 0$, new equations are obtained from which g_2, g_4, etc… can be solved. Without proof the following result will be given

$$\gamma(\beta) = \sqrt{\frac{c_0}{c_2 \ln 2}} \left(1 - \frac{2c_2^2 - c_0c_4}{4c_2^2}\beta^2 + \frac{20c_2^4 - 18c_0c_2^2c_4 + 7c_0^2c_4^2 - 2c_0^2c_2c_6}{32c_2^4}\beta^4\right) + \mathcal{O}(\beta^6)\,(\beta \to 0) \tag{41}$$

Again it is noted that this series expansion in general need not have an infinite radius of convergence, hence it is only valid sufficiently close to $\beta = 0$.

A. Two worked-out examples

The constant surface brightness disk

The coefficients c_{2n} for the constant surface brightness disk can be calculated by substituting eq. (18) in eq. (10). This gives

$$c_{2n} = 2\pi \int_0^1 \frac{1}{\pi} r^{2n+1} \mathrm{d}r = \frac{2}{2n+2}$$

Substituting this result in eq. (41) yields (where additional terms are given without proof)

$$\gamma(\beta) = \sqrt{\frac{2}{\ln 2}} \left(1 - \frac{1}{6}\beta^2 + \frac{5}{36}\beta^4 - \frac{43}{360}\beta^6 + \frac{1367}{12960}\beta^8 - \frac{51817}{544320}\beta^{10} + \frac{57119}{653184}\beta^{12} \right) + \mathcal{O}(\beta^{14})\ (\beta \to 0) \quad (42)$$

The constant volume emissivity shell

The geometry for the constant volume emissivity shell is shown in Fig. 3.9. Using this figure one can easily understand that the surface brightness for any given line of sight is proportional to the length of that part of the line that actually passes through the nebula. Hence for a constant emissivity shell the surface brightness profile is given by

$$f(r) = \begin{cases} 2j_\nu \left(\sqrt{r_\mathrm{s}^2 - r^2} - \sqrt{r_\mathrm{i}^2 - r^2} \right) & r \le r_\mathrm{i} < r_\mathrm{s} \\ 2j_\nu \sqrt{r_\mathrm{s}^2 - r^2} & r_\mathrm{i} < r \le r_\mathrm{s} \\ 0 & r_\mathrm{i} < r_\mathrm{s} < r \end{cases} \quad (43)$$

Without loss of generality it can be assumed that $j_\nu = \frac{1}{4\pi}$ and $r_\mathrm{s} = 1$. First an analytic expression for c_{2n} will be deduced by substituting eq. (43) in eq. (10)

$$c_{2n} = \left(\int_0^1 r^{2n+1} \sqrt{1 - r^2} \mathrm{d}r - \int_0^{r_\mathrm{i}} r^{2n+1} \sqrt{r_\mathrm{i}^2 - r^2} \mathrm{d}r \right)$$

These integrals can be solved easily by using the substitution $t = r^2$ and give

$$c_{2n} = \sum_{k=0}^{n} (-1)^{k+n} \binom{n}{k} \frac{1 - r_\mathrm{i}^{2n+3}}{2n + 3 - 2k} \quad (44)$$

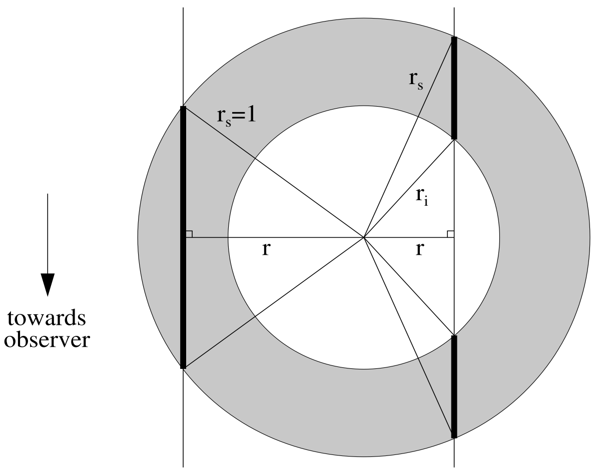

Figure 3.9 — *The geometry for a constant volume emissivity shell is shown. Two lines of sight through the shell are also shown. The surface brightness for these lines of sight is proportional to the length of the thick parts of the lines.*

The coefficients in the limiting case for an infinitely thin shell can also be calculated. After normalization to $c_0 = 1$ one finds

$$c_{2n} = \sum_{k=0}^{n} (-1)^{k+n} \binom{n}{k} \frac{2n + 3}{2n + 3 - 2k} \quad (45)$$

Substituting eq. (44) in eq. (36) gives

$$\gamma(0) = \sqrt{\frac{5(1 - r_\mathrm{i}^3)}{2(1 - r_\mathrm{i}^5) \ln 2}} \quad (46)$$

When eq. (44) is substituted in eq. (41) the following expression for the spherical case $r_\mathrm{i} = 0$ is found (again giving additional terms without proof):

$$\gamma(\beta) = \sqrt{\frac{5}{2\ln 2}} \left(1 - \frac{1}{7}\beta^2 + \frac{5}{42}\beta^4 - \frac{1157}{11319}\beta^6 + \frac{2226013}{24720696}\beta^8 - \frac{42074119}{519134616}\beta^{10} \right) + \mathcal{O}(\beta^{12})\ (\beta \to 0) \quad (47)$$

When eq. (45) is substituted in eq. (41) one finds for the limiting case $r_\mathrm{i} \to 1$

$$\gamma(\beta) = \sqrt{\frac{3}{2\ln 2}} \left(1 - \frac{1}{5}\beta^2 + \frac{59}{350}\beta^4 - \frac{128}{875}\beta^6 + \frac{70117}{539000}\beta^8 - \frac{20675393}{175175000}\beta^{10} \right) + \mathcal{O}(\beta^{12})\ (\beta \to 0) \quad (48)$$

3.11 Appendix: Determining diameters using second moments

It is well known that the FWHM of a gaussian is related to the second moment of the gaussian profile through:

$$\Phi_2 = 2\sqrt{\frac{c_2 \ln 2}{c_0}} \tag{49}$$

This formula is widely used to calculate the FWHM of an arbitrary profile. In general however, the result will not be identical to the FWHM derived from a gaussian fit. To distinguish the two values a subscript 2 has been used. Since the definition of the FWHM is not identical, also the value for the conversion factor will be different. One can define (using eq. 30)

$$\Phi_{\rm d} = \sqrt{\Phi_2^2 - \Phi_{\rm b}^2(p)} \quad \Rightarrow \quad \gamma_2(\beta) = \frac{2}{\Phi_{\rm d}} = \left[\ln 2 \left(\frac{c_2}{c_0} - \frac{1}{p}\right)\right]^{-\frac{1}{2}} \tag{50}$$

Now an expression for the radial moments of the convolved profile will be derived. To distinguish between the values of the radial moments for the unconvolved and the convolved profile, a prime will be used in the latter case. Substituting eq. (28) in eq. (10) one finds

$$c_0{}' = 2\pi\, a \sum_{n=0}^{\infty}\sum_{k=0}^{\infty} (-1)^k \frac{p^{2n+k}}{n!^2\, k!}\, c_{2n+2k} \int_0^{\infty} r^{2n+1}\, {\rm e}^{-pr^2}\, {\rm d}r$$

Here the order of summation and integration has been reversed; in lemma 3.8 it is proven that this is allowed. The integral can evaluated easily using the substitution $s = r^2$ and yields

$$c_0{}' = \pi a \sum_{n=0}^{\infty}\sum_{k=0}^{\infty} (-1)^k \frac{p^{2n+k}}{n!^2\, k!}\, c_{2n+2k} \frac{n!}{p^{n+1}} = \pi \frac{a}{p} \sum_{n=0}^{\infty}\sum_{k=0}^{\infty} (-1)^k \frac{p^{n+k}}{n!\, k!}\, c_{2n+2k}$$

It will be used that the gaussian $g(r; a, p)$ should be normalized to 1; this implies $a = p/\pi$. When the summation is reordered one finds

$$c_0{}' = \sum_{n=0}^{\infty}\sum_{k=0}^{n} (-1)^k \frac{p^n}{(n-k)!\, k!}\, c_{2n} = \sum_{n=0}^{\infty} \frac{p^n}{n!}\, c_{2n} \sum_{k=0}^{n} (-1)^k \binom{n}{k} = \sum_{n=0}^{\infty} \frac{p^n}{n!}\, c_{2n}\, \delta_{n0} = c_0 \tag{51}$$

Where the well known result

$$\sum_{k=0}^{n} (-1)^k \binom{n}{k} = \delta_{n0} \quad \text{for all } n \in \mathbb{N}_0$$

has been used. After a similar derivation one can find

$$c_2{}' = \pi a \sum_{n=0}^{\infty}\sum_{k=0}^{\infty} (-1)^k \frac{p^{2n+k}}{n!^2\, k!}\, c_{2n+2k} \frac{(n+1)!}{p^{n+2}} = p\frac{1}{p^2} \sum_{n=0}^{\infty}\sum_{k=0}^{\infty} (-1)^k\, (n+1)\, \frac{p^{n+k}}{n!\, k!}\, c_{2n+2k} =$$

$$= \frac{1}{p} \sum_{n=0}^{\infty}\sum_{k=0}^{\infty} (-1)^k\, 1\, \frac{p^{n+k}}{n!\, k!}\, c_{2n+2k} + \frac{1}{p} \sum_{n=0}^{\infty}\sum_{k=0}^{\infty} (-1)^k\, n\, \frac{p^{n+k}}{n!\, k!}\, c_{2n+2k} = \frac{c_0}{p} + \sum_{n=1}^{\infty}\sum_{k=0}^{\infty} (-1)^k \frac{p^{n-1+k}}{(n-1)!\, k!}\, c_{2n+2k}$$

If the summation is reordered again, one gets

$$c_2{}' = \frac{c_0}{p} + \sum_{n=1}^{\infty}\sum_{k=0}^{n-1} (-1)^k \frac{p^{n-1}}{(n-k-1)!\, k!}\, c_{2n} = \frac{c_0}{p} + \sum_{n=1}^{\infty} \frac{p^{n-1}}{(n-1)!}\, c_{2n} \sum_{k=0}^{n-1} (-1)^k \binom{n-1}{k} =$$

$$= \frac{c_0}{p} + \sum_{n=1}^{\infty} \frac{p^{n-1}}{(n-1)!}\, c_{2n}\, \delta_{n1} = \frac{c_0}{p} + c_2 \tag{52}$$

Substituting eqs. (51) and (52) in eq. (50) one finds

$$\gamma_2(\beta) = \left[\ln 2 \left(\frac{c_2{}'}{c_0{}'} - \frac{1}{p}\right)\right]^{-\frac{1}{2}} = \left[\ln 2 \left(\frac{1}{p} + \frac{c_2}{c_0} - \frac{1}{p}\right)\right]^{-\frac{1}{2}} = \sqrt{\frac{c_0}{c_2 \ln 2}} = \gamma(0) \tag{53}$$

Thus it has been proven that the conversion factor for second moments is independent of beam size and equal to the conversion factor for gaussian fits in the limit for infinitely large beams. Without proof the following more general result will be given

$$c_{2n}{}' = \sum_{k=0}^{n} a_{nk} \frac{c_{2k}}{p^{n-k}} \quad \text{where } a_{nk} \text{ are defined by} \quad a_{00} \equiv 1; \quad \sum_{k=0}^{n} a_{nk} x^k \equiv (x+n)\ldots(x+2)(x+1) \quad \text{for } n > 0$$

3.12 Appendix: Additional proofs

In this section additional proofs for the existence and convergence of certain integrals and series will be presented.

Lemma 3.1

It will be proven that when c_n exists, then also all c_i exist with $i < n$

$$c_i = 2\pi \int_0^\infty f(r) r^{i+1} \mathrm{d}r = 2\pi \int_0^1 f(r) r^{i+1} \mathrm{d}r + 2\pi \int_1^\infty f(r) r^{i+1} \mathrm{d}r \leq \pi F + 2\pi \int_1^\infty f(r) r^{n+1} \mathrm{d}r \quad \Rightarrow$$

$$c_i \leq \pi F + c_n - \int_0^1 f(r) r^{n+1} \mathrm{d}r \leq \pi F + c_n$$

Since $f(r) r^{n+1}$ is positive everywhere. Hence the integral c_i exists for all $i < n$.

Lemma 3.2

It will be proven that $c_n(p)$ exists for all $n \in \mathbb{N}_0$ and all $p \in [\,0, \infty\,)$, if it is assumed that c_n is exists. The assumption implies by definition that $c_n(p)$ exists for $p = 0$, hence in the remainder it will be assumed that $p > 0$. One can write

$$c_n(p) = 2\pi \int_0^\infty f(r)\, r^{n+1} \mathrm{e}^{-pr^2} \mathrm{d}r \leq 2\pi\, F \int_0^\infty r^{n+1} \mathrm{e}^{-pr^2} \mathrm{d}r = \pi\, F \int_0^\infty s^{\frac{n}{2}} \mathrm{e}^{-ps} \mathrm{d}s = \frac{\pi\, F\, \Gamma\!\left(\frac{n}{2}+1\right)}{p^{\frac{n}{2}+1}}$$

Here the substitution $s = r^2$ has been used. This proves the lemma.

Lemma 3.3

It will be proven that the integral I_{nkl} exists for all $n, k, l \in \mathbb{N}_0$ with $k + l > 0$ provided that c_n exists.

$$I_{nkl} = \int_0^\infty f^k(r) g^l(r; a, p) r^{n+1} \mathrm{d}r$$

For $k > 0$ one can use

$$I_{nkl} \leq a^l \int_0^\infty f^k(r) r^{n+1} \mathrm{d}r \leq a^l F^{k-1} \int_0^\infty f(r) r^{n+1} \mathrm{d}r = a^l F^{k-1} c_n$$

and hence the integral exists if c_n exists. For $k = 0$ one can write

$$I_{n0l} = a^l \int_0^\infty \mathrm{e}^{-lpr^2} r^{n+1} \mathrm{d}r$$

This integral is well known and exists for all $l > 0$.

Lemma 3.4

It will be proven that the integral I_{nkl} is uniformly convergent for all $a, p \in (0, \infty)$ and all $\varphi \in [\,0, 2\pi\,]$ for any $n, k \in \mathbb{N}_0$ and any $l \in \mathbb{N}$ provided that c_{2n} exists. One can use

$$I'_{nkl} = \int_X^Y f^k(r) g^l(r; a, p) r^{2n+1} \mathrm{d}r \leq a^l F^k \int_X^Y \mathrm{e}^{-lpr^2} r^{2n+1} \mathrm{d}r$$

If the substitution $s = r^2$ is used, one find

$$I'_{nkl} \leq \frac{a^l F^k}{2} \int_{X^2}^{Y^2} \mathrm{e}^{-lps} s^n \mathrm{d}s = \frac{a^l F^k}{2(lp)^{n+1}} \sum_{i=0}^{n} \frac{n!}{(n-i)!} \left[(lpX^2)^{n-i}\, \mathrm{e}^{-lpX^2} - (lpY^2)^{n-i}\, \mathrm{e}^{-lpY^2} \right]$$

Since $lpY^2 > 0$ one may write

$$I'_{nkl} \leq \frac{a^l F^k}{2(lp)^{n+1}} \sum_{i=0}^{n} \frac{n!}{(n-i)!} (lpX^2)^{n-i}\, \mathrm{e}^{-lpX^2}$$

Since $n!/(n-i)! \leq n!$ and $(lpX^2)^{n-i} \leq (lpX^2)^n$ for $X > (lp)^{-\frac{1}{2}}$, one may write

$$I'_{nkl} \leq \frac{a^l F^k}{2(lp)^{n+1}} (n+1)\, n!\, (lpX^2)^n\, \mathrm{e}^{-lpX^2} = \frac{(n+1)!\, a^l F^k}{2lp} X^{2n}\, \mathrm{e}^{-lpX^2}$$

One can see that $\lim_{X\to\infty} |I'_{nkl}| = 0$, hence one can always find an X such that $|I'_{nkl}| < \epsilon$ for all $\epsilon > 0$. Since c_{2n} exists, also the integral I_{nkl} exists (lemma 3.3) and this proves that I_{nkl} is uniformly convergent.

Lemma 3.5

It will be proven that the series

$$\sum_{n=0}^{\infty}\sum_{i=0}^{n} a_{ni} = \sum_{n=0}^{\infty}\sum_{i=0}^{n} a\, \mathrm{e}^{-p(x^2+y^2)} f(r')\, \mathrm{e}^{-pr'^2}\, (2p)^n \frac{x^{n-i}y^i}{(n-i)!\,i!}\, r'^n \cos^{n-i}\varphi' \,\sin^i\varphi'$$

is uniformly convergent on the interval $r' \in [0, R]$ for arbitrary large R and $\varphi' \in [0, 2\pi]$ provided c_{2n} exists for all $n \in \mathbb{N}_0$. The last criterion implies that c_n exists for all $n \in \mathbb{N}_0$ (lemma 3.1). One can see that the integral

$$\left| \int_0^{\infty}\int_0^{2\pi} a_{ni}\, r'\mathrm{d}\varphi'\mathrm{d}r' \right| \le \int_0^{\infty}\int_0^{2\pi} |a_{ni}|\; r'\mathrm{d}\varphi'\mathrm{d}r' \le 2\pi a\, \mathrm{e}^{-p(x^2+y^2)}\, (2p)^n \frac{x^{n-i}y^i}{(n-i)!\,i!} \int_0^{\infty} f(r')\, \mathrm{e}^{-pr'^2} r'^{n+1}\mathrm{d}r'$$

exists, provided c_n exists (lemma 3.3). Hence all terms a_{ni} are integrable. Furthermore one can write

$$|a_{ni}| \le aF(2p)^n \frac{x^{n-i}y^i}{(n-i)!\,i!} r'^n \le aF(2p)^n \frac{r^n}{(n-i)!\,i!} r'^n$$

where x, y have been changed to radial coordinates. Hence

$$\left|\sum_{i=0}^{n} a_{ni}\right| \le \sum_{i=0}^{n} |a_{ni}| \le aF(2p)^n r'^n \frac{r^n}{n!} \sum_{i=0}^{n} \binom{n}{i} = aF(2p)^n \frac{r^n\, r'^n}{n!} 2^n < aF(4p\mathrm{e})^n \frac{r^n\, r'^n}{n^n}$$

since $n! > n^n \mathrm{e}^{-n}$. Hence

$$\left|\sum_{i=0}^{n} a_{ni}\right| < aF(4p\mathrm{e})^n \frac{r^n\, R_m^n}{n^n} \equiv b_n \quad \text{with} \quad R_m = \max(\, R, 1\,)$$

Now one can write

$$\lim_{n\to\infty} |b_n|^{1/n} = \lim_{n\to\infty} (aF)^{1/n} \frac{4p\mathrm{e}r R_m}{n} = \lim_{n\to\infty} \frac{4p\mathrm{e}r R_m}{n} = 0$$

for arbitrary large R. Hence the series $\sum b_n$ is absolutely convergent (Cauchy) and therefore the series $\sum\sum a_{ni}$ is uniformly convergent (Weierstrass).

Lemma 3.6

It will be proven that the series

$$\sum_{k=0}^{\infty} a_k = \sum_{k=0}^{\infty} 2\pi\, (-1)^k\, \frac{p^k}{k!}\, r^{n+2k+1} f(r)$$

is uniformly convergent on the interval $r \in [0, R]$ for arbitrary large R and all $n \in \mathbb{N}_0$ provided that c_{2i} exists for all $i \in \mathbb{N}_0$. The last criterion implies that c_i exists for all $i \in \mathbb{N}_0$ (lemma 3.1) and thus one can easily see that all terms a_k are integrable over the interval $[\,0, \infty\,)$ for all $n \in \mathbb{N}_0$. Furthermore one can write

$$|a_k| = 2\pi \frac{p^k}{k!}\, f(r)\, r^{n+2k+1} \le \frac{2\pi F R_m^{n+1}}{k!} p^k R_m^{2k} < 2\pi F R_m^{n+1} \frac{\mathrm{e}^k p^k R_m^{2k}}{k^k} \equiv b_k \quad \text{with} \quad R_m = \max(\, R, 1\,)$$

since $k! > k^k \mathrm{e}^{-k}$ for $k > 0$. One can write

$$\lim_{k\to\infty} |b_k|^{1/k} = \lim_{k\to\infty} \left(2\pi F R_m^{n+1}\right)^{1/k} \frac{\mathrm{e}pR_m^2}{k} = \lim_{k\to\infty} \frac{\mathrm{e}pR_m^2}{k} = 0$$

for arbitrary large R and all $n \in \mathbb{N}_0$. Hence the series $\sum b_k$ is absolutely convergent (Cauchy) and therefore the series $\sum a_k$ is uniformly convergent (Weierstrass).

Lemma 3.7

It will be proven that the series

$$\sum_{n=0}^{\infty}\sum_{k=0}^{\infty} a_{nk} = \sum_{n=0}^{\infty}\sum_{k=0}^{\infty} \frac{(\zeta-1)^n}{n!^2}(-1)^k \frac{p^{n+k}}{k!}\, c_{2n+2k}(1-2s)\, s^n \mathrm{e}^{-\zeta s}$$

is uniformly convergent on the interval $s \in [\,0, S\,]$ for arbitrary large S and for all $p \in (\,0, \infty\,)$ and $\zeta \in [\,2, \infty\,)$, provided that c_{2i} exists for all $i \in \mathbb{N}_0$. First the summation will be reordered, this yields

$$\sum_{n=0}^{\infty}\sum_{k=0}^{n} a_{nk} = \sum_{n=0}^{\infty}\sum_{k=0}^{n} \frac{(\zeta-1)^{n-k}}{(n-k)!^2}(-1)^k \frac{p^n}{k!}\, c_{2n}(1-2s)\, s^{n-k} \mathrm{e}^{-\zeta s}$$

Given the fact that $\zeta \geq 2$ and all c_{2n} are finite one can easily see that all terms are integrable. Since either $k \geq n/2$ or $(n-k) \geq n/2$, it follows that $(n-k)!^2\, k! \geq \Gamma\big(\frac{n}{2}+1\big)$ and one can write

$$|a_{nk}| = \frac{(\zeta-1)^{n-k} p^n}{(n-k)!^2\, k!}\, c_{2n}(1-2s)\, s^{n-k} \mathrm{e}^{-\zeta s} \leq 2c_{2n} \frac{(\zeta-1)^n p^n}{\Gamma\big(\frac{n}{2}+1\big)} S_m^{n+1} \quad \text{with } S_m = \max(\,S, 1\,)$$

Hence

$$\left|\sum_{k=0}^{n} a_{nk}\right| \leq \sum_{k=0}^{n} |a_{nk}| \leq 2c_{2n}\,(n+1)\,\frac{(\zeta-1)^n p^n}{\Gamma\big(\frac{n}{2}+1\big)} S_m^{n+1} < 2c_{2n}\,(n+1)\, S_m \frac{(2\mathrm{e})^{n/2}(\zeta-1)^n p^n S_m^n}{n^{n/2}} \equiv b_n$$

since $\Gamma\big(\frac{n}{2}+1\big) > \big(\frac{n}{2}\big)^{n/2} \mathrm{e}^{-n/2}$ for $n > 0$. Now one can write

$$\lim_{n\to\infty} |b_n|^{1/n} = \lim_{n\to\infty} \big[2c_{2n}\,(n+1)\, S_m\big]^{1/n} (\zeta-1)pS_m\sqrt{\frac{2\mathrm{e}}{n}} = \lim_{n\to\infty} (\zeta-1)pS_m\sqrt{\frac{2\mathrm{e}}{n}} = 0$$

for arbitrary large S, all $p \in (\,0, \infty\,)$ and all $\zeta \in [\,2, \infty\,)$. Hence the series $\sum b_n$ is absolutely convergent (Cauchy) and therefore the series $\sum\sum a_{nk}$ is uniformly convergent (Weierstrass).

Lemma 3.8

It will be proven that the series

$$\sum_{k=0}^{\infty}\sum_{l=0}^{\infty} a_{nkl} = \sum_{k=0}^{\infty}\sum_{l=0}^{\infty} 2\pi\, a\,(-1)^l\, \frac{p^{2k+l}}{k!^2\, l!}\, c_{2k+2l} r^{2k+n+1}\, \mathrm{e}^{-pr^2}$$

is uniformly convergent on the interval $r \in [\,0, R\,]$ for arbitrary large R, with $p \in (\,0, \infty\,)$ and for all $n \in \mathbb{N}_0$, provided that c_{2i} exists for all $i \in \mathbb{N}_0$. After reordering the summation of the series, one finds

$$\sum_{k=0}^{\infty}\sum_{l=0}^{k} a_{nkl} = \sum_{k=0}^{\infty}\sum_{l=0}^{k} 2\pi\, a\,(-1)^l\, \frac{p^{2k-l}}{(k-l)!^2\, l!}\, c_{2k} r^{2k-2l+n+1}\, \mathrm{e}^{-pr^2}$$

One can easily see that all terms are integrable since $p > 0$ and all c_{2k} are finite. Since either $l \geq k/2$ or $(k-l) \geq k/2$, it follows that $(k-l)!^2\, l! \geq \Gamma\big(\frac{k}{2}+1\big)$ and one can write

$$|a_{nkl}| = 2\pi\, a\, \frac{p^{2k-l}}{(k-l)!^2\, l!}\, c_{2k} r^{2k-2l+n+1}\, \mathrm{e}^{-pr^2} \leq 2\pi\, a\, c_{2k}\, \frac{P_m^{2k} R_m^{2k+n+1}}{\Gamma\big(\frac{k}{2}+1\big)} \quad \text{with } P_m = \max(\,p, 1\,) \text{ and } R_m = \max(\,R, 1\,)$$

Hence

$$\left|\sum_{l=0}^{k} a_{nkl}\right| \leq \sum_{l=0}^{k} |a_{nkl}| \leq 2\pi\, a\,(k+1)\, c_{2k}\, \frac{P_m^{2k} R_m^{2k+n+1}}{\Gamma\big(\frac{k}{2}+1\big)} < 2\pi\, a\,(k+1)\, c_{2k}\, R_m^{n+1}\, \frac{(2\mathrm{e})^{k/2} P_m^{2k} R_m^{2k}}{k^{k/2}} \equiv b_{nk}$$

since $\Gamma\big(\frac{k}{2}+1\big) > \big(\frac{k}{2}\big)^{k/2} \mathrm{e}^{-k/2}$ for $k > 0$. Now one can write

$$\lim_{k\to\infty} |b_{nk}|^{1/k} = \lim_{k\to\infty} \big[2\pi\, a\,(k+1)\, c_{2k}\, R_m^{n+1}\big]^{1/k} P_m^2 R_m^2 \left(\frac{2\mathrm{e}}{k}\right)^{\frac{1}{2}} = \lim_{k\to\infty} P_m^2 R_m^2 \left(\frac{2\mathrm{e}}{k}\right)^{\frac{1}{2}} = 0$$

for arbitrary large R, all $p \in (\,0, \infty\,)$ and all $n \in \mathbb{N}_0$. Hence the series $\sum b_{nk}$ is absolutely convergent (Cauchy) and therefore the series $\sum\sum a_{nkl}$ is uniformly convergent (Weierstrass).

3.13 Appendix: Symbols

The following definitions for the symbols have been used.

a – Measure for the height of the gaussian.
$a_{1,2,3}$ – Parameters for the fit to the conversion factor. Defined in eq. (7).
c_n – Radial moments of the surface brightness profile. Defined in eq. (10).
$c_n(p)$ – Generalized radial moments of the surface brightness profile. Defined in eq. (25).
$f(r)$ – The surface brightness profile of the nebula.
F_ν – The flux density per unit frequency.
$g(r; a, p)$ – Two-dimensional gaussian profile.
j_ν – The emissivity per unit frequency.
p – Measure for the width of a gaussian. Related to the FWHM through eq. (30).
r – Polar coordinate on the sky. Subscripts have the following meaning:
  i – the inner radius of the nebula,
  s – the Strömgren or outer radius of the nebula.
x,y – Cartesian coordinates on the sky.
α – Parameter used in an r^α density law.
β – Ratio of the deconvolved FWHM diameter of the nebula to the FWHM of the beam.
γ – Factor to convert the deconvolved FWHM to the true angular diameter. Subscripts have the following meaning:
  <none> – gaussian fits were used to determine the FWHM
  2 – second moments were used to determine the FWHM (eq. 50).
  f – indicates the fitting function used to approximate $\gamma(\beta)$.
Γ – The gamma function.
δ – Kronecker delta symbol.
ζ – Auxiliary variable, related to β through eq. (33).
Θ_d – True angular diameter of the nebula ($\Theta_\mathrm{d} \equiv 2r_\mathrm{s}$).
λ – Wavelength.
τ – Optical depth.
φ – Polar coordinate on the sky.
Φ – The FWHM diameter of a profile. Subscripts have the following meaning:
  <none> – indicates the FWHM of a gaussian profile,
  b – indicates the FWHM of the beam,
  d – indicates the deconvolved FWHM of a profile (defined in eq. 31 or eq. 50),
  2 – indicates the FWHM of a profile obtained using second moments (eq. 49).

4 The spectral evolution of post-AGB stars†

P.A.M. van Hoof, R.D. Oudmaijer, L.B.F.M. Waters

Abstract — A parameter study of the spectral evolution of a typical post-AGB star, with particular emphasis on the evolution of the infrared colors, is presented. The models are based on the latest evolutionary tracks for hydrogen burning post-AGB stars. For such tracks the evolutionary rate is very dependent on the assumed mass loss rate as a function of time. We investigate this effect by modifying the mass loss prescription. The newly calculated evolutionary rates and density distributions are used to model the spectral evolution of a post-AGB star with the photo-ionization code CLOUDY, including dust in the radiative transfer. Different assumptions for the dust properties and dust formation are considered. It is shown that by varying these parameters in a reasonable way, entirely different paths are followed in the *IRAS* color-color diagram. First of all, the effects of the evolution of the central star on the expanding dust shell can not be neglected. Also the dust properties and the definition of the end of the AGB phase have an important effect. The model tracks show that objects occupying the same location in the *IRAS* color-color diagram can have a different evolutionary past, and therefore the position in the *IRAS* color-color diagram alone can not *a priori* give a unique determination of the evolutionary status of an object. An alternative color-color diagram, the *K*–[12] vs. [12]–[25] diagram, is presented. The tracks in this diagram seem less affected by particulars of the grain emission. This diagram may be a valuable additional tool for studying post-AGB evolution.

4.1 Introduction

The transition phase between the Asymptotic Giant Branch (AGB) and planetary nebulae (PNe) has gained much attention over the last decade. AGB stars lose mass fast and get obscured by their circumstellar dust. As the star leaves the AGB, its mass loss rate decreases significantly and the star may become sufficiently hot to ionize its circumstellar material and be observable as a PN. During the transition from the AGB to the PN phase (the post-AGB or proto-planetary nebula phase) the dust shell created during the AGB moves away from the central star and becomes optically thin after a few hundred years; the obscured star becomes observable. The transition time from the AGB to the PN phase is estimated to be a few thousand years (e.g. Pottasch 1984).

Whereas PNe are relatively easy to find because of their rich optical emission line spectra, post-AGB stars have more inconspicuous spectra and are therefore much harder to find. The number of post-AGB stars only started to become large after the *IRAS* mission, that was successful in detecting objects surrounded by circumstellar dust.

Several samples of post-AGB stars are presented in the literature (e.g. Volk & Kwok 1989; Hrivnak et al. 1989; van der Veen et al. 1989; Trams et al. 1991; Oudmaijer et al. 1992; Slijkhuis 1992). Most of these objects are stars with supergiant-type spectra, surrounded by dust shells. These samples of post-AGB stars have in common that the original criteria which were employed to find them implicitly made assumptions on the spectral energy distribution (SED) of post-AGB stars. Some authors used criteria on the *IRAS* colors, because post-AGB stars were expected to be located in a region in the *IRAS* color-color diagram between AGB

† Published in MNRAS 289, 371.

stars and PNe (e.g. Volk & Kwok 1989; Hrivnak et al. 1989; van der Veen et al. 1989; Slijkhuis 1992). Other authors loosened this criterion and searched for objects in the entire color-color diagram, but with an additional criterion that the central star should be optically visible (e.g. Trams et al. 1991; Oudmaijer et al. 1992; Oudmaijer 1996).

Such samples are subject to selection effects, so the objects that have been selected do not have to be representative for the entire population of post-AGB stars. In order to understand these selection effects and to obtain a handle on the kinds of objects that could have been missed, it is useful to investigate the spectral energy distribution from a theoretical point of view by following the spectral evolution of a post-AGB star with an expanding circumstellar shell. Moreover, this type of study allows one to investigate and understand the processes that occur in the circumstellar shell during the transition.

Several such studies have been published. Most of these studies focus on the expanding dust shell with a dust radiative transfer model. Authors like e.g. Siebenmorgen et al. (1994), Szczerba & Marten (1993), Loup (1991), Slijkhuis & Groenewegen (1992) and Volk & Kwok (1989) performed calculations describing the evolution of the circumstellar dust shell. Work concerning the evolution of a star with an expanding shell has also been performed with photo-ionization codes (Volk 1992), and hydrodynamical models (Frank et al. 1993; Mellema 1993; Marten & Schönberner 1991). None of these models include dust, except for Volk (1992) who used the output of the photo-ionization code CLOUDY (Ferland 1993) as input for a dust model.

Our objective is to investigate the spectral evolution of a hydrogen burning post-AGB star with a photo-ionization model containing a dust code. The aim of this work is twofold:

Firstly we investigate the processes in the circumstellar envelope. The emphasis in this paper will be on the infrared properties of this shell. For this, both the expansion of the shell and the evolution of the central star have to be taken into account.

Secondly, we investigate the influence of certain assumptions on the evolutionary timescales. Only few post-AGB evolutionary grids have been published, never giving a fine grid for the coolest part of the evolution. The original Schönberner tracks (1979, 1983) presented only a limited number of time points of the evolution, while Vassiliadis & Wood (1994) omit the phase between 5000 K and 10 000 K altogether. The predicted timescales that are available are calculated with a pre-defined end of the AGB and assumed post-AGB mass loss rates. These choices can influence the post-AGB evolutionary timescales considerably, as was already demonstrated by Trams et al. (1989) and Górny et al. (1994). The situation has changed now with the results of Blöcker (1995a,b), who calculated new evolutionary sequences, and made extensive tables available describing certain key parameters during the post-AGB phase. The published relation between the envelope mass and effective temperature allows one to construct detailed timescales using one's own mass loss prescriptions during the (post-) AGB evolution, which makes the model results less dependent on the mass loss formulation that was used by Schönberner (1979, 1981, 1983).

In this paper first we describe the method to calculate evolutionary timescales and the adopted mass loss prescriptions. The results of Blöcker (1995a,b) are used as a basis to create synthetic evolutionary tracks, and some aspects of the evolutionary timescales that are predicted are discussed. Next we describe the photo-ionization code CLOUDY that was used and the assumptions that were made to conduct the study of the spectral evolution of post-AGB stars. We then present the first results of a parameter study of a typical post-AGB object, based on the 0.605 $M_{\odot}$ track from Blöcker (1995b).

4.2 The central star evolution

Many stellar evolutionary models are presented in the recent literature, but only two groups calculate the AGB quantitatively including mass loss. These are Vassiliadis & Wood (1993, 1994) and Blöcker & Schönberner (1991) and Blöcker (1995a,b). Both groups calculate the evolution of a star from the main sequence through the red giant phase to the white dwarf stage. There are slight differences in the core mass – luminosity relations and the use of a different initial – final mass relation, but their results show qualitatively the same behavior in the evolution of stars in the HR diagram. The main differences between the models are the mass loss prescriptions on the AGB.

The AGB mass loss rates in the formulation of Vassiliadis & Wood are derived from the mass loss – pulsation period ($\dot{M}$–P) relation given by Wood (1990). For periods longer than 500 d for low mass stars, and larger pulsation periods for higher mass objects, a maximum value of the AGB mass loss rate is invoked (of the order of 10^{-5} $M_{\odot}$ yr^{-1}). Blöcker used a mass loss rate which is dependent on the luminosity of the star. He fitted the results of Bowen's (1988) theoretical study of mass loss in Mira variables. Basically this is the Reimers mass loss (Reimers 1975) multiplied by a luminosity dependent factor. These mass loss rates are not limited by a maximum value. Since the adopted AGB mass loss rates by the above authors differ, some striking differences between the results of their calculations exist. The $\dot{M}$–P relation of Wood (1990) is questioned by Groenewegen & de Jong (1994). Using the synthetic evolutionary model of Groenewegen & de Jong (1993), they were able to fit the luminosity function of carbon stars in the LMC with the Bowen mass loss adopted by Blöcker (1995a), but not with the Vassiliadis & Wood mass loss rates.

The mass loss rates do not only govern the evolution on the AGB. During the post-AGB phase, the mass loss rates also have a drastic influence on the timescales of the AGB –

PN transition. Since the temperature of the star for a given core mass is determined by the mass of the stellar envelope, larger mass loss rates will cause the star to evolve to higher temperatures more quickly and can therefore decrease the timescale of the transition strongly. Trams et al. (1989) showed that when the adopted post-AGB mass loss rates of a 0.546 $M_\odot$ star are raised by a factor of 5 to 10 to a value of 10^{-7} $M_\odot$ yr^{-1}, the transition time from the AGB to the PN phase is shortened from 100 000 yr to only 5000 yr. This would make a low mass star readily observable as a PN, while the (longer) predicted timescales prevent such objects to become an observable PN since the circumstellar shell would have moved far away from the star and would have dispersed into the interstellar medium long before the star emits a sufficient amount of ionizing photons. In order to study the evolutionary timescales of post-AGB stars, it is important to understand post-AGB mass loss better.

4.2.1 Determination of the evolutionary timescales

The evolutionary timescales of hydrogen burning post-AGB stars are determined by the core mass and the mass loss rates of the star. In this section we present the computational details of this procedure, compute the evolutionary timescales and investigate several aspects of these timescales. We use the tracks by Blöcker (1995a,b) to determine the evolutionary timescales. Blöcker calculated several tracks for his investigation of the evolution of stars on the AGB and beyond. The tracks include a complete calculation of a 3 $M_\odot$ object that ends as a 0.605 $M_\odot$ white dwarf and a 4 $M_\odot$ (0.696 $M_\odot$) sequence. To these sequences, the 1.0 $M_\odot$ (0.565 $M_\odot$) track of Schönberner (1983) was added. We start with a recapitulation of the mass loss laws we have used (see also Blöcker 1995b).

A. The mass loss laws

During the red giant branch, the mass loss is parameterized by the Reimers mass loss rate $\dot{M}_{\rm R}$ given in eq. (54), where the scaling parameter η is set to 1 for all tracks.

$$\dot{M}_{\rm R}/({\rm M_\odot\,yr^{-1}}) = 4\times10^{-13}\,\eta\,\frac{(L/{\rm L_\odot})(R/{\rm R_\odot})}{(M/{\rm M_\odot})} \qquad (54)$$

With L, R and M the luminosity, radius and mass of the star. Since AGB stars lose mass at a faster rate than red giants, a different formulation is adopted for the AGB mass loss rates. To this end, Blöcker fitted the numerical results of Bowen, as given in eq. (55).

$$\dot{M}_{\rm B1}/({\rm M_\odot\,yr^{-1}}) = \qquad (55)$$
$$4.83\times10^{-9}\,(M_{\rm ZAMS}/{\rm M_\odot})^{-2.1}(L/{\rm L_\odot})^{2.7}\dot{M}_{\rm R}$$
$$\dot{M}_{\rm B2}/({\rm M_\odot\,yr^{-1}}) =$$
$$4.83\times10^{-9}\,(M/{\rm M_\odot})^{-2.1}(L/{\rm L_\odot})^{2.7}\dot{M}_{\rm R}$$

The difference between $\dot{M}_{\rm B1}$ and $\dot{M}_{\rm B2}$ is the division by the current mass of the star instead of the initial mass of the star. The timescales for the 0.565 $M_\odot$ track of Schönberner were recalculated by us using the $M_{\rm env}$–$T_{\rm eff}$ relation given by Schönberner but with the mass loss prescriptions of Blöcker. For all tracks the $\dot{M}_{\rm B1}$ prescription was used, except for the 0.605 $M_\odot$ track where $\dot{M}_{\rm B2}$ was used, which results in larger AGB mass loss rates.

The mass loss rates can reach values of the order of 10^{-4} $M_\odot$ yr^{-1} to 10^{-3} $M_\odot$ yr^{-1} and it is clear that if this mass loss would last for a long time, the star would evaporate. Thus, an end to the AGB (-wind) has to be invoked. Blöcker used the pulsation period to define the end of the high mass loss phase; he assumed that AGB stars pulsate in the fundamental mode, where the period can be calculated using eq. (56) taken from Ostlie & Cox (1986).

$$\lg(P_0/{\rm d}) = \qquad (56)$$
$$-1.92 - 0.73\lg(M/{\rm M_\odot}) + 1.86\lg(R/{\rm R_\odot})$$

When the central star has reached an inferred pulsation period of $P_{\rm a}$ = 100 d (which occurs when the star has a surface temperature somewhere between roughly 4500 K and 6000 K) the Bowen mass loss stops. When the star has subsequently reached an inferred pulsation period of $P_{\rm b}$ = 50 d the post-AGB mass loss starts; in between the mass loss rates are connected by a smooth transition. Hence the following definitions will be used in the remainder of the paper: the AGB phase is that part of the evolution where the pulsation period is greater than $P_{\rm b}$, the (AGB) transition phase is that part of the evolution where the pulsation period is in between $P_{\rm a}$ and $P_{\rm b}$, and finally the post-AGB phase is that part of the evolution where the pulsation period is smaller than $P_{\rm b}$.

One should realize that post-AGB stars with pulsation periods larger than 50 d exist (e.g. HD 52961 with a period of 72 d; Waelkens et al. 1991; Fernie 1995). Thus the pulsation period recipe used by Blöcker should only be regarded as an approximate parameterization of the end of the AGB.

For lower temperatures the post-AGB mass loss is given by the Reimers law (54). Since the Reimers mass loss is proportional to ${T_{\rm eff}}^{-2}$ for a constant luminosity and stellar mass, the post-AGB mass loss rates decrease during the evolution of the object. A radiation driven wind will take over when the star has reached temperatures above approximately 20 000 K. The mass loss rate for this wind, based on Pauldrach et al. (1988), is given by eq. (57). Hence at any stage of the post-AGB evolution either eq. (54) or eq. (57) is used, whichever of the two yields the biggest mass loss.

$$\dot{M}_{\rm CPN}/({\rm M_\odot\,yr^{-1}}) = 1.29\times10^{-15}\,(L/{\rm L_\odot})^{1.86} \qquad (57)$$

During the evolution on the AGB and beyond, the envelope mass is reduced due to two processes. In the outer parts of the envelope, mass is lost through a wind, and at the bottom of the envelope, mass is diminished by hydrogen burning. From Trams et al. (1989) we find the mass loss due to hydrogen burning:

$$\dot{M}_{\rm H}/({\rm M_\odot\ yr^{-1}}) = 1.012 \times 10^{-11}\,(L/{\rm L_\odot})X_{\rm e}^{-1} \qquad (58)$$

With $X_{\rm e}$ the hydrogen mass fraction in the envelope (70 %).

B. The evolutionary timescales

The evolutionary timescales for hydrogen burning post-AGB stars depend firstly on the core mass and secondly on the mass loss rates. The evolutionary timescales can be calculated relatively easy by making use of the fact that there exists a unique relation between the envelope mass and the stellar temperature for every core mass. One can calculate the evolutionary timescales by combining this relation with the mass loss prescriptions given in the previous section. Dr. Blöcker kindly provided us with tables from which the $M_{\rm env}$–$T_{\rm eff}$ relation could be reproduced.

The timescale for the envelope depletion is given by:

$$\frac{\Delta M_{\rm env}}{\Delta t} = \dot{M}_{\rm wind} + \dot{M}_{\rm H} \qquad (59)$$

Using the $M_{\rm env}$–$T_{\rm eff}$ relation this expression can be transformed into an expression for the evolutionary rate $\Delta T_{\rm eff}/\Delta t$ of the central star

$$\frac{\Delta T_{\rm eff}}{\Delta t} = \frac{\Delta T_{\rm eff}}{\Delta M_{\rm env}} \times \frac{\Delta M_{\rm env}}{\Delta t} = \frac{\dot{M}_{\rm wind} + \dot{M}_{\rm H}}{\frac{{\rm d}M_{\rm env}}{{\rm d}T_{\rm eff}}} \qquad (60)$$

Integrating this expression yields the actual timescales for the evolution of the central star.

In Fig. 4.1 some relations for the 0.565 $\rm M_\odot$, 0.605 $\rm M_\odot$ and 0.696 $\rm M_\odot$ tracks are presented. The upper panel shows the envelope mass as function of photospheric temperature. The second panel presents the mass loss rates as function of temperature, and the third panel shows the evolutionary rate in kelvin per year as function of temperature. In the second panel it is visible that the transition phase occurs at higher temperatures for larger core masses with the recipes described above.

The evolutionary rate, mass loss rate and envelope mass are related to each other in the following way. The evolutionary rate in terms of increase in temperature per year is slow on the steep part of the $M_{\rm env}$–$T_{\rm eff}$ relation, and more rapid on the shallow part. Larger mass loss rates imply of course more rapid changes in the stellar temperature. These effects are visible in Fig. 4.1: at low temperatures in the post-AGB phase the evolutionary rates are smallest, while for higher temperatures the evolutionary rate increases. The minima around $\lg(T_{\rm eff}/{\rm K}) \approx 3.7$ to 3.9 correspond to the onset of the smaller post-AGB mass loss, slowing down the evolution which accelerates later on the shallow part of the $M_{\rm env}$–$T_{\rm eff}$ relation.

Interestingly, the minimum in the evolutionary rate occurs right after the end of the AGB transition phase. The net increase in effective temperature in kelvin per year is

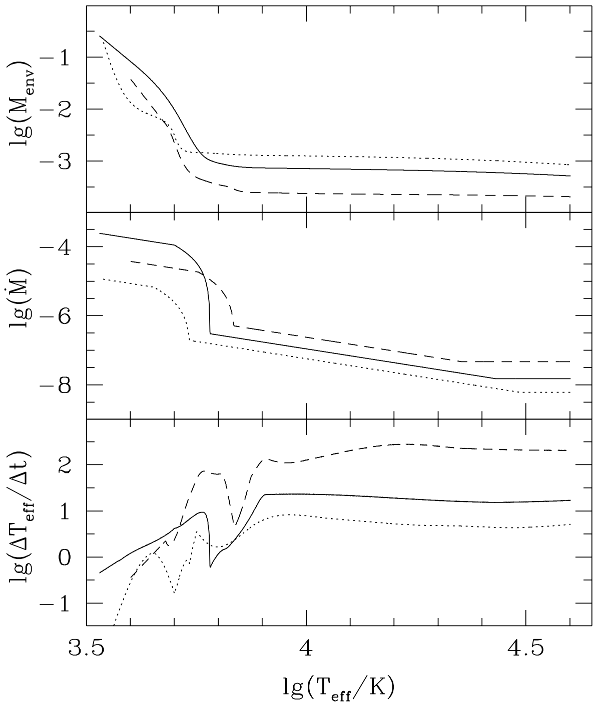

Figure 4.1 — *The $M_{\rm env}$–$T_{\rm eff}$ relations, mass loss rates and resulting evolutionary rates for the 0.565 $\rm M_\odot$ (dotted line), 0.605 $\rm M_\odot$ (solid line) and 0.696 $\rm M_\odot$ (dashed line) tracks. The envelope mass is given in solar masses, the mass loss rate in solar masses per year and the evolutionary rate in kelvin per year. Note that the 0.605 $\rm M_\odot$ track has a larger AGB mass loss rate. For this particular track, the B2 mass loss rate was used.*

the slowest for all tracks just after the start of the post-AGB evolution, which is when the temperature of the objects correspond to G or F spectral types. The increase in temperature is less than 1 $\rm K\,yr^{-1}$ for the 0.565 $\rm M_\odot$ and 0.605 $\rm M_\odot$ tracks. How does this evolutionary rate compare with the observations? Fernie & Sasselov (1989) calculated the possible increase in temperature for UU Her stars. From the absence of a change in pulsation period of UU Her, 89 Her and HD 161796, they place an upper limit of 0.5 $\rm K\,yr^{-1}$ on the temperature increase. Their conclusion was that these objects can not be post-AGB stars because the evolutionary rates should be much higher. However, this may be the case when one averages over the entire post-AGB temperature span, but the observed lack of temperature increase is consistent with the predictions for this temperature range, as was already shown by Schönberner & Blöcker (1993). Therefore a post-AGB nature for the UU Her stars can not be excluded on this basis.

4.2.2 The influence of mass loss on the evolutionary timescales

It is evident from the above that the value of the post-AGB mass loss rate has an important effect on the evolutionary timescales. However, the mass loss rate is not known observationally for cool post-AGB stars. The usual tracer of mass loss, Hα emission, which is often observed in the spectra of post-AGB objects is likely to be the result of stellar pulsations (see the discussion by Oudmaijer & Bakker 1994 and Lèbre et al. 1996). A possible tracer of mass loss in cool post-AGB stars is the CO first-overtone emission at 2.3 μm (Oudmaijer et al. 1995), but, given this is true, the mass loss rates still have to be determined.

The lack of theoretical and observational values for post-AGB mass loss rates forced Schönberner and Blöcker to resort to the heuristic Reimers law for the cool part of the post-AGB evolution. As an illustration of the effect of the post-AGB mass loss rates on the evolutionary timescales, we have calculated these timescales for three core masses with the post-AGB mass loss rate at 0, 1, 5 and 10 times the standard post-AGB value (indicated as 0×pAGB etc.). The results for the 0.565 $M_\odot$, 0.605 $M_\odot$ and 0.696 $M_\odot$ tracks are presented in Table 4.1, where the timescales since the end of the transition mass loss phase are given. The increase of the post-AGB mass loss rates indeed decreases the timescales of the evolution, confirming the results of Trams et al. (1989) and Górny et al. (1994). The 0×pAGB mass loss rate effectively determines the slowest possible evolutionary speed, since the only mass loss is through hydrogen burning. On average, the difference in speed between 0×pAGB and 1×pAGB is roughly a factor of two to three.

Table 4.1 — *Evolutionary timescales for different values of post-AGB mass loss rates; the post-AGB phase starts at P_b = 50 d.*

$\dot{M}_{\rm PAGB}$ / $T_{\rm eff}$ (K)	0×pAGB	1×pAGB	5×pAGB	10×pAGB
$M_{\rm core}$ = 0.565 $M_\odot$, L = 3891 $L_\odot$				
5 426	0	0	0	0
5 500	312	76	18	9
6 000	1113	286	70	36
7 000	2810	815	207	107
10 000	3974	1306	349	182
15 000	5172	2092	651	353
20 000	6383	3089	1141	653
25 000	7544	4156	1768	1068
30 000	8709	5292	2526	1604
$M_{\rm core}$ = 0.605 $M_\odot$, L = 6310 $L_\odot$				
6 042	0	0	0	0
6 500	1671	458	113	58
7 000	2510	715	178	92
10 000	3122	948	241	125
15 000	3487	1181	325	171
20 000	3822	1458	452	248
25 000	4154	1769	625	358
30 000	4481	2093	832	501
$M_{\rm core}$ = 0.696 $M_\odot$, L = 11 610 $L_\odot$				
6 846	0	0	0	0
7 000	94	29	7	4
7 500	192	62	15	8
10 000	245	84	22	11
15 000	287	111	30	16
20 000	309	129	38	21
25 000	331	151	50	28
30 000	354	174	65	38

4.2.3 Distribution over spectral type

The availability of the evolutionary rates allows us to investigate the predicted distribution over spectral type. Oudmaijer et al. (1993) and Oudmaijer (1996) used the coarse grid of the Schönberner (1979, 1983) tracks and found that a star spends by far most of the time as a B-type star. Only for the 0.644 $M_\odot$ track half of the time is spent in the G phase, and somewhat less as a B star, while almost no time is spent as an F or A star.

One might not expect that an object would spend a large fraction of the time as a B star, because the evolutionary rates are largest for B spectral type (Fig. 4.1). This can be understood however when we consider the large range of temperatures that corresponds to spectral type B: roughly between 10 000 K and 30 000 K. In contrast, A stars only have a temperature range between approximately 7500 K and 10 000 K. The large evolutionary rates multiplied by the temperature range then result in a longer time spent as a B star during the post-AGB evolution. The large fraction of time that is spent as a G star in the 0.644 $M_\odot$ track is explained by the steep $M_{\rm env}$–$T_{\rm eff}$ relation for temperatures less than approximately 6000 K, as can be deduced from eq. (60). The distribution over spectral type for the tracks presented here with 1×pAGB mass loss is calculated using the conversion from effective temperature to spectral type listed by Straižys & Kuriliene (1981). These are $T_{\rm eff}$(A0I) = 9800 K, $T_{\rm eff}$(F0I) = 7400 K and $T_{\rm eff}$(G0I) = 5700 K.

To allow for a comparison with the distributions presented by Oudmaijer et al. (1993) we will assume in this section that the post-AGB phase starts when $T_{\rm eff}$ = 5000 K and ends when $T_{\rm eff}$ = 25 000 K. The distributions can be easily obtained by calculating the time spent as a G star (5000 K – G0), F star (G0 – F0) etc., and subsequently dividing these numbers by the total time spent as a post-AGB star. The resulting distributions are plotted in Fig. 4.2. For comparison the distribution over spectral type of the sample of 21 post-AGB objects in the list of Oudmaijer et al. (1992) is given. The observed distribution peaks at F, while no B stars are found at all.[1]

One should realize that planetary nebula central stars with temperatures below 25 000 K are observed: e.g. IRAS19336–0400 with $T_{\rm eff}$ = 23 000 K (Van de Steene et al. 1996; Van de Steene & van Hoof 1995). Hence one could

[1] The few B type objects in the sample of Oudmaijer et al. (1992) appear to have low effective temperatures. HR 4049 and HD 44179 (the central star of the Red Rectangle) are listed in the literature as a B star, but abundance analyses showed that the effective temperature is lower than typical for a B star: about 7500 K (late A or early F type; van Hoof et al. 1991; Waelkens et al. 1992). The reason that these objects were classified as B, instead of late A stars, is the extreme metal deficiency of these stars, so that few metallic lines are present in the spectra. Thus the observed spectra mimic the spectra of hot objects.

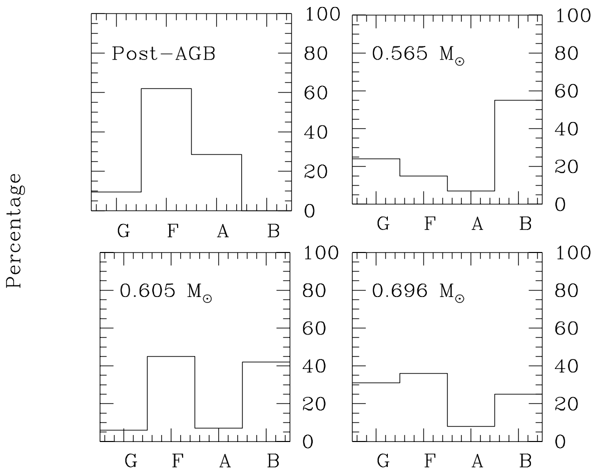

Figure 4.2 — *Distribution over spectral type. Upper left panel; the post-AGB candidate stars in the sample of Oudmaijer et al. (1992), the other panels show the predicted distribution for the 0.565 $M_\odot$, 0.605 $M_\odot$ and 0.696 $M_\odot$ tracks.*

also assume an upper limit of 20 000 K for the post-AGB regime. However, the distribution over spectral type is not very different in this case, the fraction of B-type stars will be lower by approximately 10 %.

The 0.605 $M_\odot$ distribution is different from the results presented by Oudmaijer et al. (1993) for the 0.598 $M_\odot$ Schönberner track. In the present plot, the distribution peaks at F, while the 0.598 $M_\odot$ distribution peaks at G. The distribution for the same track is different in Oudmaijer (1996), since there the evolutionary timescales were shortened by 1000 yr 'in order to make the old 0.598 $M_\odot$ track consistent with the new calculations' (Marten & Schönberner 1991). This resulted in a distribution that strongly peaks at spectral type B.

The main differences between the old 0.598 $M_\odot$ and new 0.605 $M_\odot$ calculations are the progenitor mass of the star (1 $M_\odot$ and 3 $M_\odot$ respectively), the mass loss prescriptions and the definition of the end of the AGB. In the Schönberner calculations, no transition wind was assumed: the AGB mass loss would abruptly change into a post-AGB wind at 5000 K. In the Blöcker calculations, a transition wind is assumed between 5000 K and 6000 K for the 0.605 $M_\odot$ track. This implies *shorter* timescales for the G type phase of the 0.605 $M_\odot$ track with respect to the older calculations, but does not affect the time spent as F, A or B stars, where for both tracks a Reimers post-AGB mass loss is assumed. The only explanation we can find for the apparent difference in evolutionary speed is that the dependence of the temperature on the envelope mass of the 0.605 $M_\odot$ track is different from the 0.598 $M_\odot$ track. Apparently, the slope of the $M_{\rm env}$–$T_{\rm eff}$ relation can differ significantly for stars with a different evolutionary past, even when the resulting core masses are nearly identical.

The predicted distributions in Fig. 4.2 show large differences. For the smallest core mass, most of the time is spent as a B star. For the 0.605 $M_\odot$ case the lifetime is distributed evenly over the F and B phase. The fastest track with a core mass of 0.696 $M_\odot$ shows a minimum at A, while the rest of the lifetime is spread evenly over G, F and B. The 0.605 $M_\odot$ distribution nicely reproduces the observed peak at F. However, all tracks predict many more B stars than observed.

In order to compare the observed and predicted distributions more quantitatively, we have performed a Kolmogorov-Smirnov test using both an upper limit of 20 000 K and 25 000 K for the post-AGB regime. The resulting probabilities are given in Table 4.2. From these tests it appears that the 0.565 $M_\odot$ track is an unlikely model for the observed post-AGB sample. On the other hand, the 0.605 $M_\odot$ and the 0.696 $M_\odot$ tracks can not be excluded. Given the fact that stars on the 0.696 $M_\odot$ track evolve much faster than on the 0.605 $M_\odot$ track, they would constitute only a small fraction of the total number of observable post-AGB stars. We will adopt the 0.605 $M_\odot$ track to describe the post-AGB evolution in the remainder of this paper.

Table 4.2 — *The results of the Kolmogorov-Smirnov test comparing various evolutionary tracks with the observed post-AGB sample. The tests have been performed using a range of temperatures for the post-AGB regime of 5000 K to 20 000 K (second column) or alternatively 5000 K to 25 000 K (third column).*

track $M_\odot$	probability 20 000 K	probability 25 000 K
0.565	4.5×10^{-4}	2.8×10^{-6}
0.605	2.4×10^{-2}	6.4×10^{-4}
0.696	6.7×10^{-2}	1.3×10^{-1}

This exercise shows that the predictions of the distribution over spectral type are subject to large uncertainties, depending both on the $M_{\rm env}$–$T_{\rm eff}$ relation and the assumed mass loss prescription. However, regardless what assumptions are made, one would expect a fair number of B-type post-AGB stars, which are not observed in the sample depicted in Fig. 4.2. Hence this discrepancy remains unresolved. Reversely it can be stated that when a larger sample of post-AGB stars with reliable temperature determinations becomes available, the procedure described here can be a very effective means for testing evolutionary tracks.

4.3 The model

In order to calculate the spectral evolution of post-AGB stars, we used the photo-ionization code CLOUDY version 84.12a (Ferland 1993). Some modifications have been made to the code to facilitate the computations. The most important change was the introduction of several broadband photometric filters, including the Johnson and the *IRAS* filters. The in-band fluxes for these filters were calculated by folding both the spectral energy distribution and the emission line contribution with the filter passband. Internal extinction due to continuum opacities was included both in the continuum and the line contribution.

A dust model written by P.G. Martin was already included in the original code. For our modeling we used the grain species labeled 'ISM Silicate' and 'ISM Graphite'. The optical constants were taken from Martin & Rouleau (1991). The absorption and scattering cross sections were calculated assuming a standard ISM grain size distribution (Mathis et al. 1977). All calculations were done assuming a dust-to-gas mass ratio of 1/150. For the chemical composition of the gas we assumed the abundances given in Aller & Czyzak (1983), supplemented with educated guesses for elements not listed therein (as given in CLOUDY).

The original code only allowed for the computation of a model with a constant dust-to-gas ratio throughout the entire nebula. However, the density profiles we calculate extend from the stellar surface outward. It is not realistic to assume that dust is present near the stellar surface and therefore we introduced new code in CLOUDY to solve this problem. This enabled the dust to exist only outside a prescribed radius or, alternatively, only in those regions where the equilibrium temperature of the dust would be below a prescribed sublimation temperature. These prescriptions work as a binary switch: at a certain radius either no dust or the full amount is present. In those regions where dust exists, the dust-to-gas ratio is assumed to be constant.

Two models for the dust formation are adopted. In the first model it is assumed that dust is only formed in the AGB wind, hence in material that was ejected before the stellar pulsation period reached P_b. We will call this the AGB-only dust formation model. In the second model it is assumed that the dust formation continues in the post-AGB wind. We will call this the post-AGB dust formation model. Due to limitations of the code, which we discuss below, we will only investigate the spectral evolution after the post-AGB phase has started. This implies that for the AGB-only dust formation model, the inner dust radius is already at a distance from the central star and the equilibrium temperature of the grains is always below the sublimation temperature. In the post-AGB dust formation model we assume that dust only exists in those parts of the nebula where the equilibrium temperature of the grains is below the sublimation temperature. The assumed values for the sublimation temperature are 1500 K for graphite and 1000 K for silicates.

It should be noted that we only try to model dust *formation* and not the *destruction* of grains by the stellar UV field or shocks. Especially in the AGB-only dust formation model the grains at the inner dust radius are always exposed and it is expected that they eventually will be destroyed. However, little is known about grain destruction, and the rate at which this destruction occurs is very uncertain. In the case of continuing dust formation in the post-AGB wind this problem can be expected to be of lesser importance since there is a constant supply of new grains shielding the older grains.

The radiative transport in CLOUDY is treated in one dimension only, i.e. the equations are solved radially outwards. This assumption makes the code unsuitable to compute models of nebulae with significant amounts of scattered light and/or diffuse emission when the nebula has a moderate to high absorption optical depth. For low optical depths re-absorption of diffuse emission in the nebula is negligible and the assumptions in CLOUDY work very well. However, for moderate to high optical depths the re-absorption of diffuse emission that is produced in the outer parts of the nebula and is radiated inwards becomes important. The assumptions made in CLOUDY make it impossible to account for this energy source, nor for the amount of flux absorbed in these regions. Since the circumstellar envelope is optically thick in the AGB phase, our calculations always start shortly after the transition from the AGB to the post-AGB phase is complete.

For low temperature models the only source of diffuse light at optical and UV wavelengths is scattering of central star light by dust grains; for the highest temperature models bound-free emission also plays a role. Since for the highest temperatures the models have a low absorption optical depth, the bound-free emission causes only minor problems and we can judge the quality of the models primarily by investigating the (wavelength-averaged) scattering optical depth. An example of this approach will be shown in Sect. 4.4.

In the calculations, the central star was assumed to emit as a blackbody. All the models were calculated for a distance of 1 kpc.

4.3.1 Density profiles of the circumstellar shell

The density profiles of the expanding shell are calculated for the homogeneous and spherical case. Using the mass loss prescriptions described above and assuming an outflow velocity they can be calculated for any moment in time t.

$$\rho(r,t) = \frac{\dot{M}_{\rm wind}(t_{\rm ej})}{4\pi r^2(t,t_{\rm ej}) v_{\rm exp}(t_{\rm ej})} \tag{61}$$

with

$$r(t,t_{\rm ej}) = R_*(t_{\rm ej}) + (t - t_{\rm ej}) v_{\rm exp}(t_{\rm ej})$$

the distance from the center of the star, R_* the stellar radius; $t_{\rm ej}$ stands for the time when a certain layer was ejected, $v_{\rm exp}$ is the expansion velocity of the wind at the moment of ejection. It is assumed to be constant thereafter and hydrodynamical effects are neglected (see also Sect. 4.3.3). In particular, the post-AGB wind has a higher velocity than the AGB shell and will eventually overtake it. That part of the post-AGB wind which has done so contains little mass and is simply discarded.

4.3.2 The AGB circumstellar shell

The AGB shell is the principal contributor to the *IRAS* fluxes, and it is necessary to have a good description of the stellar temperature as function of the time during the AGB, in order to compute the mass loss history using eq. (55). The M_{env}–T_{eff} relation discussed in Sect. 4.2.1.B starts at temperatures roughly between 3000 K and 4000 K (the relations we received from Blöcker extend to lower temperatures than given in his paper). A description of the AGB evolution for lower temperatures is lacking. Unfortunately, the evolution of T_{eff} and L on the AGB is not shown in the Blöcker papers. We therefore simply extrapolate the M_{env}–T_{eff} relation logarithmically to lower temperatures. The 'AGB' star then evolves according to the extended relation. The M_{env}–T_{eff} relation rises rather steeply at the low temperature end so that only a limited amount of extrapolation is necessary. In this way we find reasonable start temperatures for the AGB. Since our method implicitly assumes that the luminosity remains constant during the AGB, the Bowen mass loss rates decrease with temperature. We investigate two different cases of AGB mass loss in the extrapolated part of the M_{env}–T_{eff} relation: the normal Bowen mass loss and a constant mass loss held at the value of the Bowen mass loss rate at the first point of the M_{env}–T_{eff} relation as given by Blöcker. These choices do not have implications for the post-AGB evolution.

4.3.3 Expansion velocities

The observed mean expansion velocity of AGB winds is 15 km s^{-1} (Olofsson 1993), and this will be used as the typical AGB outflow velocity. During the post-AGB phase the situation is different. Slijkhuis & Groenewegen (1992) assumed that the post-AGB wind has the same outflow velocity (15 km s^{-1}) as the AGB wind. The escape velocity (and hence also the outflow velocity) increases with temperature however. The increasing radiation pressure from the hotter star on the less dense post-AGB wind accelerates the dust and will decrease the densities in the post-AGB wind. The escape velocity for a 10 000 K star is already of the order of 100 km s^{-1} to 150 km s^{-1}. In addition, Szczerba & Marten (1993) found that dust was accelerated to 150 km s^{-1} during the post-AGB phase. We therefore assume an expansion velocity of 150 km s^{-1} in the post-AGB phase.

One should realize that the scenario of a fast wind that follows a slow wind results in a collision between the two winds (as shown by e.g. Mellema 1993 and Frank et al. 1993). When inspecting the plots of Mellema (1993) we find that the effects of the colliding winds only start to become significant when the radiation driven wind ($\dot{M}_{\mathrm{CPN}}$) with velocities in excess of thousands of kilometers per second has developed. The effect of colliding winds will be neglected in the further calculations in this paper.

4.4 The model runs

In this section we will investigate the spectral evolution of a post-AGB star by varying certain parameters that influence the mass loss rate, wind velocity and the evolutionary speed of the central star. We restrict ourselves to the 0.605 M$_\odot$ track and the emphasis will be on the infrared properties of the dust shell around the star. We calculated a total of seven runs. Every individual run consists of four different series of models. These individual models represent post-AGB shells with carbon-rich or oxygen-rich dust, both with and without dust formation in the post-AGB wind. We assumed the total mass of the AGB and post-AGB shell to be 2 M$_\odot$. With the extrapolated M_{env}–T_{eff} relation this implies a start temperature of the AGB of 2543 K. The different run parameters are outlined in Table 4.3.

Table 4.3 — *The calculated runs for the 0.605 M$_\odot$ track, with an initial envelope mass of 2 M$_\odot$, and an AGB expansion velocity of 15 km s^{-1}.*

Run	v_{PAGB} (km s^{-1})	P_{a} (d)	P_{b} (d)	Constant mass loss
1	15	100	50	no
2	15	100	50	yes
3	150	100	50	yes
4	150	100	50	no
5	150	125	75	no
6	1500	100	50	no
7	150	125	75	yes

The main differences between the runs are threefold. Firstly, as stated above, the post-AGB wind velocity is subject to uncertainty. In order to assess the influence of this velocity we used three different values: 15 km s^{-1}, 150 km s^{-1} and 1500 km s^{-1}. Secondly, the differences between a decreasing AGB mass loss rate and a constant mass loss rate are investigated. In the second case the constant mass loss is kept at the value of the Bowen mass loss rate at the first point of the M_{env}–T_{eff} relation as given by Blöcker. This value for the mass loss of $\dot{M} = 1.99 \times 10^{-4}$ M$_\odot$ yr^{-1} will then be adopted throughout the extrapolated part of the M_{env}–T_{eff} relation, i.e. for temperatures between 2543 K and 3743 K. Approximately 85 % of the total shell mass is ejected in this phase. Thirdly, the definition of the end of the AGB is adjusted. As an alternative the pulsation periods that define the start of the transition wind and the start of the post-AGB phase are set to 125 d and 75 d respectively, which corresponds to a transition phase occurring between 4723 K and 5418 K. For these runs the start of the transition period (defined by P_{a}) will be reached earlier, however the transition period itself will take much longer due to the fact that the M_{env}–T_{eff} relation is much steeper now in the transition region, making the evolutionary speed much slower. This gives the paradoxical result that an earlier start of the transition phase gives rise to a later start of the post-AGB phase. Also the smaller mass loss rates result in a slower

Table 4.4 — *The ages of the different models since the end of the AGB transition phase. The age of the AGB shell, in the case of the (P_a,P_b) = (100d,50d) models (= normal end), is 6465 yr in the case of a decreasing mass loss and 10 326 yr in the case of a constant mass loss. For the (P_a,P_b) = (125d,75d) models (=early end), these ages are 6741 yr and 10 603 yr respectively.*

$T_{\rm eff}$ (K)	t(normal) (yr)	t(early) (yr)	$T_{\rm eff}$ (K)	t(normal) (yr)	t(early) (yr)
5 450		553	9 000	904†	5510
5 500		1308	9 500	926†	5532
5 550		1950	10 000	948	5553
5 600		2492	11 000	991†	5597
5 700		3328	12 000	1036	5642
5 800		3904	13 000	1082†	5688
6 000		4528	14 000	1131	5736
6 050	13	4619‡	15 000	1180†	5786
6 100	89	4695‡	16 000	1232	5838
6 150	154	4760‡	17 000	1286†	5892
6 200	211	4817‡	18 000	1342	5947
6 250	262	4867	19 000	1399†	6004
6 500	457	5063	20 000	1457	6063
7 000	715	5320	25 000	1768	6374
7 500	823	5429	30 000	2093†	6699
8 000	860	5466	35 000	2409	7014
8 500	883†	5488			

† These models are not shown in the graphite tracks in Figs. 4.4 and 4.7.

‡ These models are not shown in the tracks in Fig. 4.10.

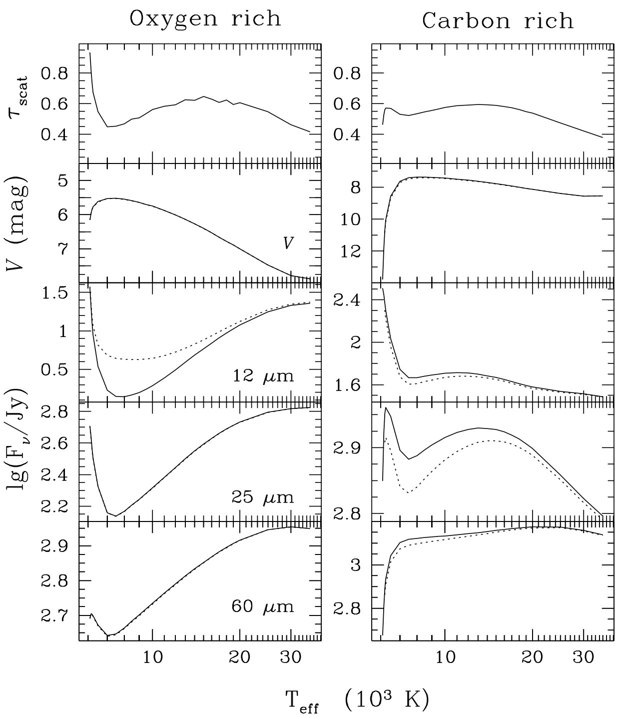

Figure 4.3 — *The V magnitude and the 12 μm, 25 μm and 60 μm flux densities as function of temperature during the post-AGB evolution for the 0.605 $M_\odot$ run 4 models. The solid lines represent the models without dust formation in the post-AGB outflow. The dashed lines indicate the models with dust formation in the post-AGB wind. In the panels where no dashed lines are visible, the values are indistinguishable. All curves start at $T_{\rm eff}$ = 6100 K, except the curves for graphite with post-AGB dust formation which start at 6200 K.*

evolution between 5418 K to 6042 K (the start of the post-AGB phase in the (P_a,P_b) = (100d,50d) runs). After the star has reached $T_{\rm eff}$ = 6042 K, the post-AGB mass loss rates are the same, and consequently the evolutionary speed in terms of kelvin per year is identical.

The models are calculated at the temperatures listed in Table 4.4. The second and third entries in this table reflect the time that has passed since the end of the transition wind for the (P_a,P_b) = (100d,50d) and (P_a,P_b) = (125d,75d) case respectively.

We will start with the results of run 4, which we will use as a reference since we consider the parameters for this run the most realistic. Subsequently we discuss the main differences between this model run and the other runs. The main results of run 4 are visualized in Fig. 4.4, where the tracks in the *IRAS* color-color diagram are plotted, in Fig. 4.3 where certain fluxes are plotted, and in Figs. 4.5 and 4.6 where a selection of spectral energy distributions is presented. In these figures a distance of 1 kpc to the object is assumed. We will discuss the results for the oxygen-rich and carbon-rich dust separately.

For this run we have made an estimate for the wavelength-averaged scattering optical depth (see also the discussion in Sect. 4.3). For the models without post-AGB dust formation the results are shown in Fig. 4.3. The results for the models with post-AGB dust formation are not shown, but they are almost identical. It can be seen that the scattering optical depths for the silicate and graphite models are very similar, while on the other hand the absorption optical depth is much higher for the graphite models when compared to the silicate models (this can be judged by comparing the V magnitudes). This is caused by a combination of two effects. Firstly, graphite is a very efficient absorber at optical wavelengths and a relatively less efficient scatterer. The reverse is the case for silicates. This tends to level out the differences. Secondly, in the averaging process the optical depths are weighted by the output spectrum. This spectrum peaks much more towards the red for the graphite models due to the higher internal extinction. The scattering optical depth is lower at longer wavelengths and this tends to level out the differences even further. The latter effect also explains why the scattering optical depth drops off so slowly, or even rises towards higher temperatures. The peak of the energy distribution shifts towards the blue, where the scattering efficiency is much higher, thus countering the effects of the dilution of the circumstellar envelope.

Using these results we were able to obtain a worst case estimate for the amount of energy that could have been missed in the dust emission due to the fact that the scat-

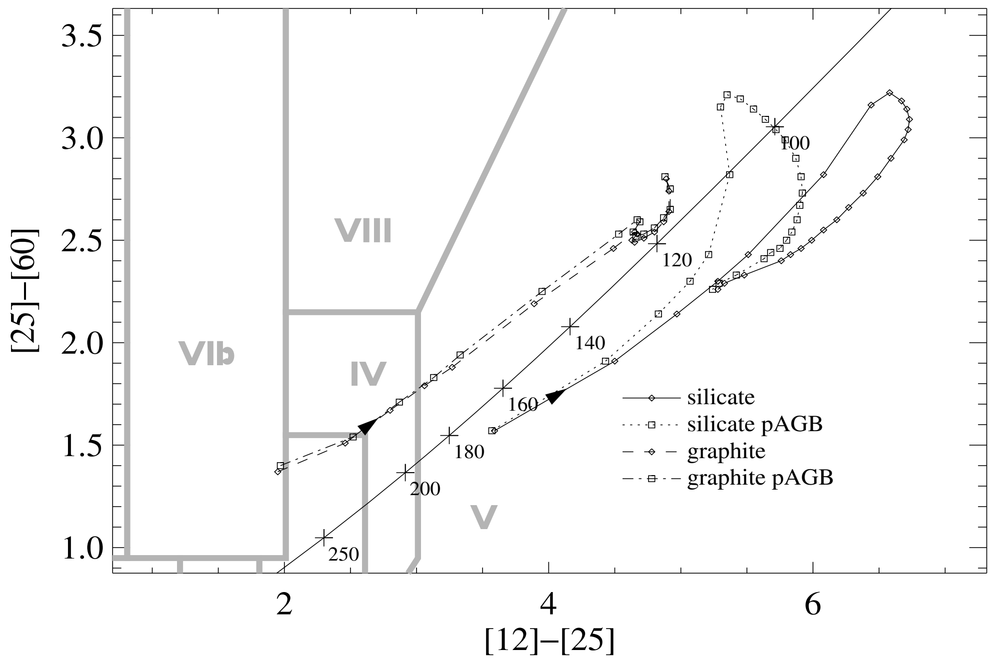

Figure 4.4 — *IRAS color-color diagram – run 4. The arrows indicate the evolution of the IRAS color with time. The definitions for the IRAS colors are as presented in Oudmaijer et al. (1992). With these definitions the Rayleigh-Jeans point, where objects hotter than approximately 2000 K are found, is located at (0,0). The boxes as defined by van der Veen & Habing (1988) are drawn in. The straight line represents the blackbody line. Selected temperatures are indicated. The first data point for all tracks is the $T_{\rm eff}$ = 6050 K model.*

tering processes were not properly treated in our models. The amounts for the models shown in Fig. 4.3 are typically 10 % to 20 % of the total far-IR flux for the silicate models, and 5 % to 10 % for the graphite models. The worst case estimates for the models not shown in Fig. 4.3, i.e. the lowest temperature models, are all below 40 %. These estimates reflect on the accuracy of the absolute fluxes and magnitudes predicted by our models. However, they are expected to cancel in a first order approximation when colors are calculated. Therefore we decided to omit the lowest temperature models whenever absolute fluxes are shown, but to include them when colors are shown.

Scattering processes will not only influence the total amount of energy absorbed, but also the run of the dust temperature with radius. This can influence the shape of the spectrum and hence also the colors. It is impossible to make an estimate for the magnitude of this effect and we will assume it to be negligible.

4.4.1 Silicate dust

We will start with a description of the silicate tracks in the *IRAS* color-color diagram (Fig. 4.4). At first the [12]–[25] and [25]–[60] colors both increase. At some point the [25]–[60] color remains constant, while [12]–[25] still increases. This is followed by a decrease in both the [12]–[25] and [25]–[60] colors. Hence the track makes a clockwise loop in the color-color diagram.

The first part of the track represents the cooling of the dust shell due to its expansion. From Table 4.4 one sees the inner radius of the shell has increased by a factor of 4 between $T_{\rm eff}$ = 6200 K and $T_{\rm eff}$ = 8000 K, which leads to a cooling and a decrease of the *IRAS* fluxes (Fig. 4.3). The following evolution in the *IRAS* color-color diagram is rather counter-intuitive. Normally one would expect that the shell would make the familiar counter-clockwise loop in the color-color diagram as found by Loup (1991), Volk & Kwok (1989) and Slijkhuis & Groenewegen (1992). In such a loop, the shell continues to cool, until the photospheric radiation begins to dominate the emission, first at the 12 μm band. At this time, the 25 μm flux and the [12]–[25] color decrease strongly due to the expansion and cooling of the shell. The [25]–[60] color will continue to increase slowly. Later, as the star starts to dominate at 25 μm, the [12]–[25] color will remain constant and the [25]–[60] color will start to decrease. When the star is the dominant contributor in all three *IRAS* bands, the loop will end in the Rayleigh-Jeans point. However, the above authors assumed a constant temperature of the central star, while the effects of an evolving star on the *IRAS* colors can not be neglected; in the 0.605 $M_\odot$ track the star rapidly evolves toward higher effective temperatures. For example, the kinematic age of the shell, and thus its outer (or inner) radius, has increased by only 25 % between $T_{\rm eff}$ = 8000 K and $T_{\rm eff}$ = 12 000 K. One can regard the circumstellar shell as essentially stationary around the evolving star. An evolving star embedded in a

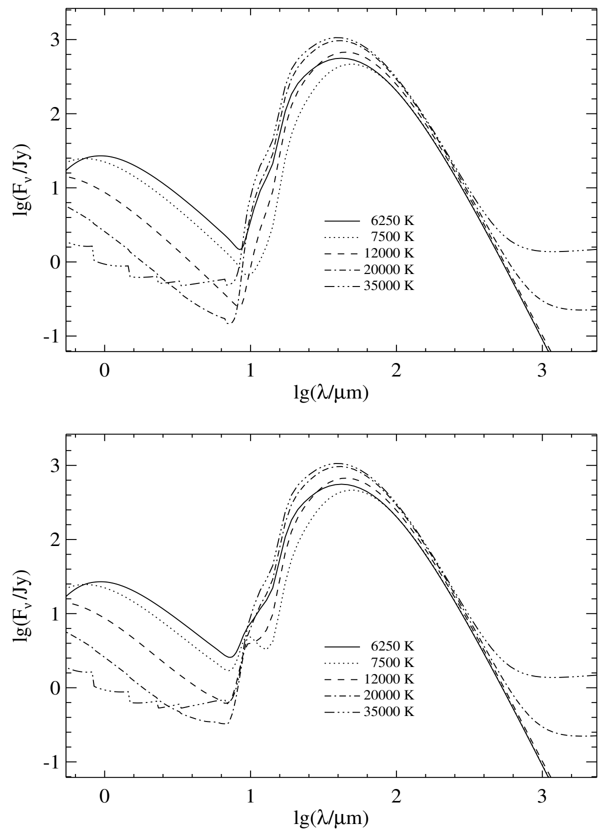

Figure 4.5 — *The spectral energy distribution at several stages during the post-AGB evolution. The upper panel shows the SED for silicate dust without post-AGB dust formation, the lower panel with dust formation, both for run 4. The flux densities are calibrated for an assumed distance of 1 kpc. The temperatures are indicated. Note the presence of the silicate emission feature at 10 μm in the post-AGB dust models.*

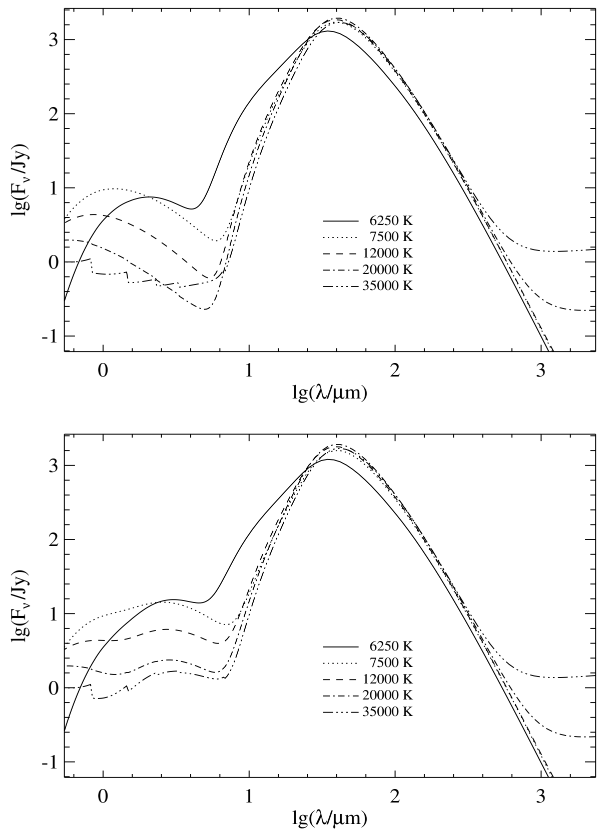

Figure 4.6 — *As the previous figure, but now for graphite with and without post-AGB dust formation (lower panel, respectively upper panel). Note the hot dust that emits strongly in the near-infrared, but hardly contributes to the 12 μm flux density.*

stationary shell results in a heating of the dust and an increase of the *IRAS* fluxes (Fig. 4.3). The effect of re-heating of the circumstellar envelope was already found by Marten et al. (1993) in their calculations. The re-heating continues even beyond the last data point, hence in the color-color diagram the track keeps evolving to higher color temperatures in both colors. Around the turning point the 12 μm flux is partly due to the photosphere. The photospheric flux decreases for higher temperatures so that the 12 μm flux reacts later to the rising dust flux than the 25 μm and 60 μm flux. Therefore the [12]–[25] color starts decreasing later than the [25]–[60] color. The result is a clockwise loop in the color-color diagram.

One should note the behavior of the *IRAS* flux densities in Fig. 4.3. The flux densities reach a minimum during the slow evolution of the star. The minimum is followed by gradual increase in the total infrared output due to the heating of the shell resulting from the increasing absorbing efficiency of the dust (see also the discussion in Sect. 4.4.2). A model star like this (i.e. with silicate dust) would have a larger chance of being detected in an infrared survey like *IRAS* when it has evolved to higher temperatures. This fact, combined with the predicted distribution over spectral type implies that hot post-AGB stars, or young PNe should be expected to be more abundant in samples of evolved stars with infrared excess.

A. Dust formation in the post-AGB wind

The addition of dust formation in the post-AGB wind changes the spectral energy distribution. From Fig. 4.3 it is visible that the 25 μm and 60 μm flux densities have the same values as in the AGB-only dust formation case. The 12 μm band is strongly affected by the addition of the hot dust. This is due to the presence of the 10 μm silicate emission feature which causes the emissivity of the hot silicate dust to peak strongly at 10 μm. The larger 12 μm flux density is immediately reflected in the color-color diagram. It puts the starting point at a slightly higher color temperature than before. As the feature increases in strength, the track bends toward higher [12]–[25] color temperatures. Then, when the star is evolving more rapidly than the shell expands, the cool AGB shell is heating up, and the track

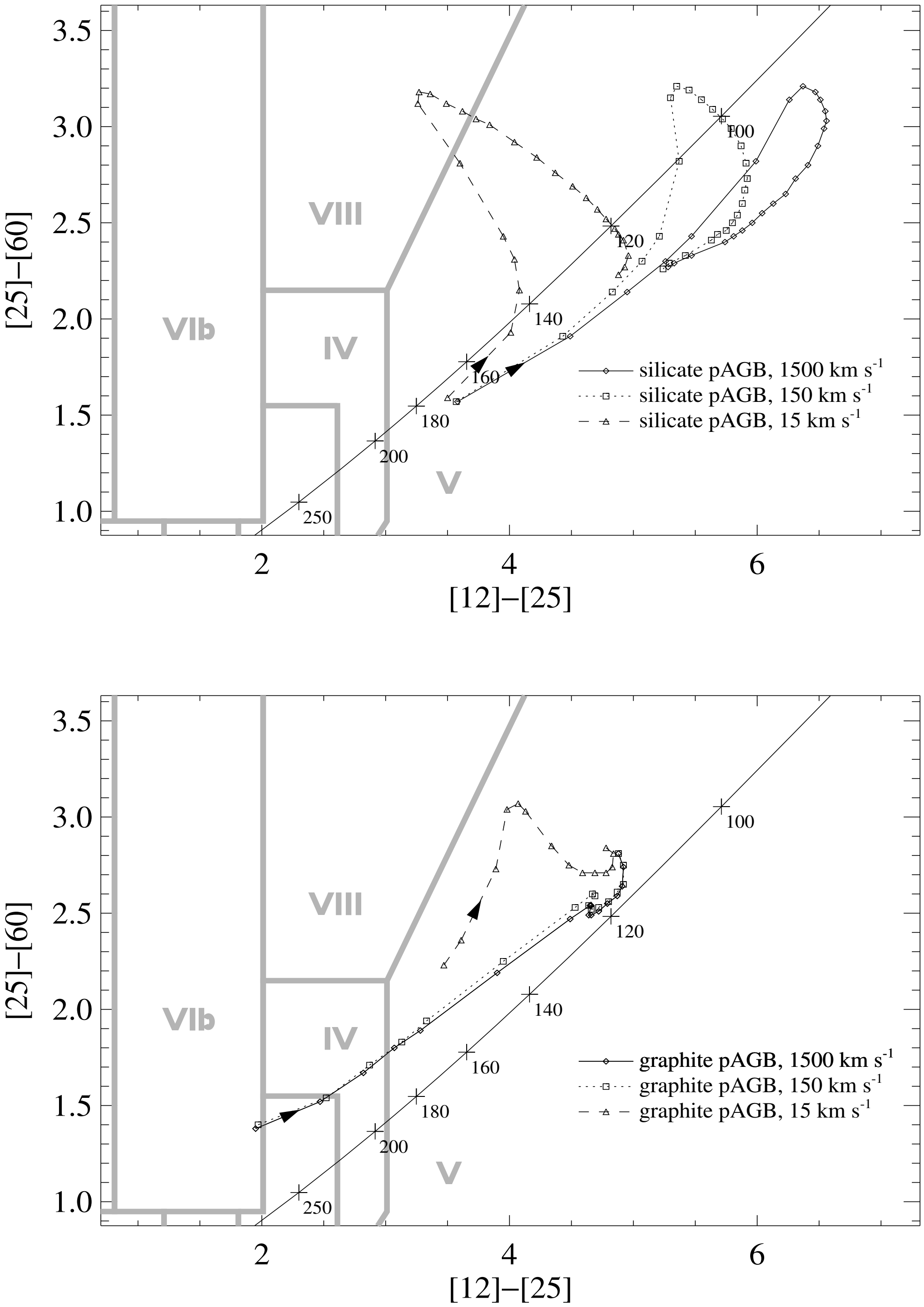

Figure 4.7 — *In these IRAS color-color diagrams, the effect of different velocities of the post-AGB wind with dust formation is presented. The 15 km s^{-1}, 150 km s^{-1} and 1500 km s^{-1} models are calculated in runs 1, 4 and 6. The upper diagram shows the silicate models, the lower diagram the graphite models. The graphite 15 km s^{-1} track starts at 6200 K, all others at 6050 K.*

moves down. At the same time, the [12]–[25] color temperature decreases, reflecting a weakening of the silicate feature relative to the 25 μm flux. This effect is caused by the circumstances under which dust in the post-AGB wind is formed. As the star becomes hotter, also the distance increases at which the equilibrium temperature of the dust goes below 1000 K. Therefore the dust formation will take place at larger distances from the star, in a diluted local radiation field where the dust density will be lower. Consequently, the silicate feature weakens and the track moves to lower [12]–[25] color temperatures. Eventually the contribution of the 10 μm feature will become negligible and the track will move asymptotically to the track without post-AGB dust formation.

B. Different post-AGB wind velocities

In Fig. 4.7 the effect of a different post-AGB wind velocity is shown for silicate dust in the upper panel. The models have been calculated for velocities of 15 km s^{-1}, 150 km s^{-1} and 1500 km s^{-1}. The 1500 km s^{-1} tracks resemble the AGB-only dust formation models, because the amount of dust in the post-AGB wind is not large enough to yield an observable effect. The low outflow velocity model shows all the effects outlined for the 150 km s^{-1} models even stronger because the amount of hot dust has increased.

4.4.2 Carbon-rich dust

Let us now turn to the models with carbon-rich dust. This type of dust is a more efficient absorber than silicate dust as can be seen in Fig. 4.3. The visual magnitude is larger than for the oxygen rich models, reflecting a larger circumstellar extinction in the Johnson *V* band. One can also see that the infrared energy output is larger.

The beginning of the track of the carbon-dust models in the color-color diagram (Fig. 4.4) is located at a higher color temperature than for the oxygen-rich models because more energy is absorbed by the dust. At first, the track moves to lower temperatures, and as the star begins to evolve more rapidly, the curve makes a slight backward loop in the diagram due to the heating of the shell. Then, contrary to the silicate model, the shell cools again.

This somewhat unexpected result can be explained by the properties of the absorbing material. It is instructive to investigate the effective cross section Q_0 of the two grain species as a function of the effective temperature of the central star spectrum (i.e. a blackbody). Q_0 is defined as

$$Q_0 = \frac{\int_0^\infty B_\nu(T_{\rm eff})\alpha_\nu {\rm d}\nu}{\int_0^\infty B_\nu(T_{\rm eff}){\rm d}\nu} \quad (62)$$

With B_ν the blackbody intensity distribution and α_ν the absorption cross section of the grains. The formula is chosen in such a way that the total energy absorbed by the grains is proportional to $L \times Q_0$. Note that L is constant during the evolution. The absorption coefficients have been

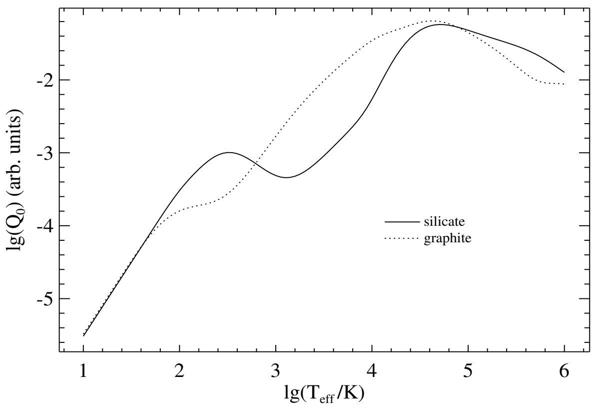

Figure 4.8 — *The effective cross section for the grain species used in our study as a function of the effective temperature of a blackbody. The total luminosity of the central source remains constant and the dust-to-gas mass ratio for both grain species is equal.*

chosen such that both grain species have the same dust-to-gas mass ratio. The resulting curves are shown in Fig. 4.8

For temperatures between approximately 1000 K and 50 000 K silicates absorb less energy than graphite. It can be a factor of 10 lower in the temperature range for cool post-AGB stars. This is caused by the fact that silicates are inefficient absorbers at optical wavelengths. From these results we can expect that for temperatures between 10 000 K and 50 000 K the total IR emission of silicates will rise much more drastically than for graphite. For temperatures above 50 000 K the peak of the energy distribution shifts into the EUV. At these wavelengths silicates are more efficient absorbers and we can see that for these temperatures the total amount of energy absorbed by the silicates is higher than for graphite.

Thus, in the last data points of the track in the *IRAS* color-color diagram, the absorption efficiency of graphite does increase less strongly with rising effective temperature. In this case, the interplay between the evolving star (now heating up the shell less rapidly) and the expanding shell (giving rise to cooling) has as a result that the expanding shell becomes the more dominant factor and consequently the shell cools. In Fig. 4.3 these two effects are illustrated by the decreasing *IRAS* fluxes.

A. Dust formation in the post-AGB wind

In contrast to oxygen-rich dust, graphite has no feature in the *IRAS* 12 μm pass band. Also the shape for the emissivity law of graphite is such that the hot dust peaks at near-infrared wavelengths, contributing negligibly to the 12 μm band (Figs. 4.3 and 4.6). Therefore one does not expect a large effect of the hot dust on the *IRAS* 12 μm flux. However, the 12 μm, 25 μm and 60 μm flux densities of these models are lower than for the corresponding AGB-only dust formation models (Fig. 4.3). This stems from the

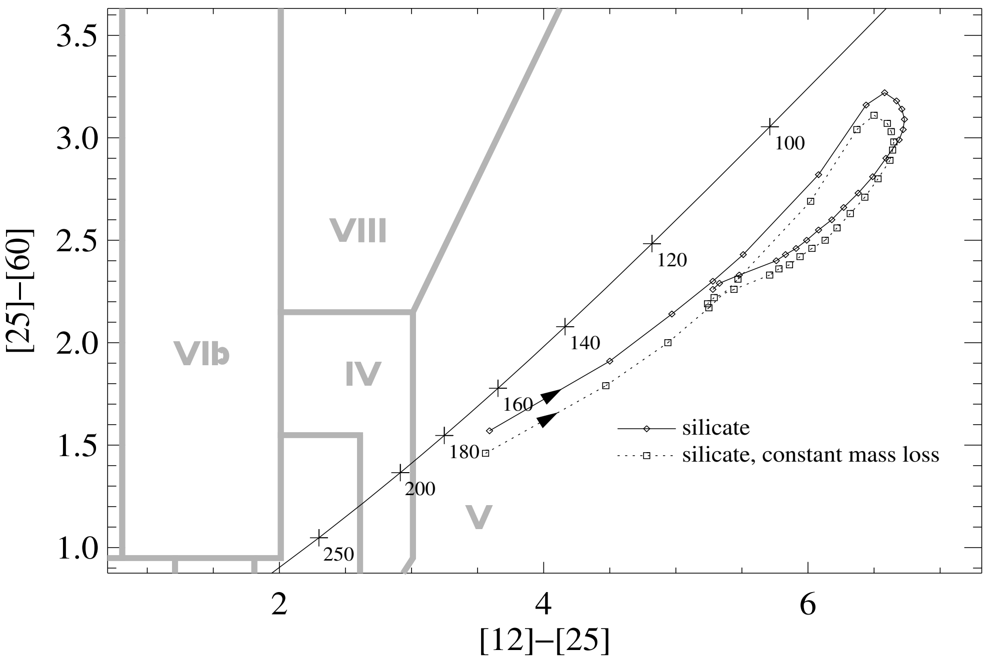

Figure 4.9 — *IRAS color-color diagram in which the difference between the decreasing and constant mass loss (runs 4 and 3) are shown for the silicate tracks. The first data point for both tracks is the $T_{\rm eff}$ = 6050 K model.*

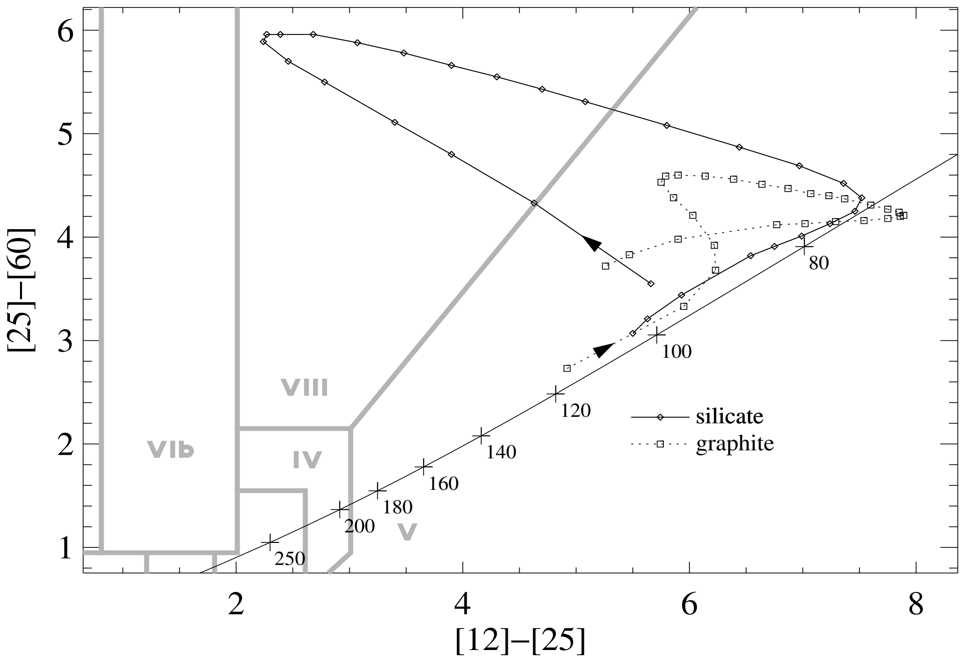

Figure 4.10 — *IRAS color-color diagram for the models without post-AGB dust formation in run 5, the case with an earlier start of the transition phase than in run 4. The first data point for both tracks is the $T_{\rm eff}$ = 5450 K model.*

fact that the hot dust absorbs a large fraction of the stellar energy, yielding a cooler AGB shell.

B. Different post-AGB wind velocities

The effect of the post-AGB outflow velocity on the graphite models is presented in the lower panel of Fig. 4.7. The 1500 km s^{-1} track behaves almost the same as the 150 km s^{-1} track and the track without post-AGB dust. The 15 km s^{-1} track however is different, first it moves upward, then bends downward and finally makes the counter-clockwise loop. The initial increase in the [25]–[60] color is caused by the fact that the large amount of hot dust now shields the AGB shell more efficiently, making the AGB shell even cooler than previously. As the star becomes hotter, the dust condensation radius moves rapidly outward, making shielding less efficient. The AGB shell now obtains more energy from the central star and heats up, resulting in higher [25]–[60] temperatures. The tracks evolve asymptotically towards each other and finally the counter-clockwise loop sets in, as was already explained.

4.4.3 Constant mass loss

In Fig. 4.9 the silicate tracks for run 4 (decreasing AGB mass loss) and run 3 (constant mass loss) in the *IRAS* color-color diagram are shown. Both the [12]–[25] and the [25]–[60] color temperature of the constant mass loss track are slightly higher than for the decreasing mass loss track.

The constant mass loss creates relatively more cool dust further from the star. This cooler dust emits less radiation and therefore the hotter dust at the inner parts of the AGB shell (where the mass loss rates for both tracks are the same) will dominate the spectrum more. This gives the result that the integrated spectrum of all dust appears hotter. This effect is strongest at 60 μm, less at 25 μm and absent at 12 μm. As a whole, the effect of different AGB mass loss rates is small. The effect on the graphite tracks is basically the same and is not shown.

4.4.4 Different end of the AGB

For all the models that have been discussed so far, it was assumed that the transition mass loss starts at P_a = 100 d, and that the Reimers mass loss starts at P_b = 50 d. However, the evolutionary behavior of the calculated models strongly depends on the exact moment of 'superwind' cessation (Szczerba 1993). In this section, we will present an investigation into the effect of changing this unknown parameter.

As stated before, the evolution of the central star in the (P_a,P_b) = (100d,50d) and the (P_a,P_b) = (125d,75d) models is identical after T_{eff} = 6042 K. However, the density structure of the circumstellar shell is entirely different when the star has reached this temperature. Whereas the (P_a,P_b) = (100d,50d) model then barely has a detached shell, the (P_a,P_b) = (125d,75d) model already has a shell with a kinematic age in excess of 4500 yr, which has much cooler dust.

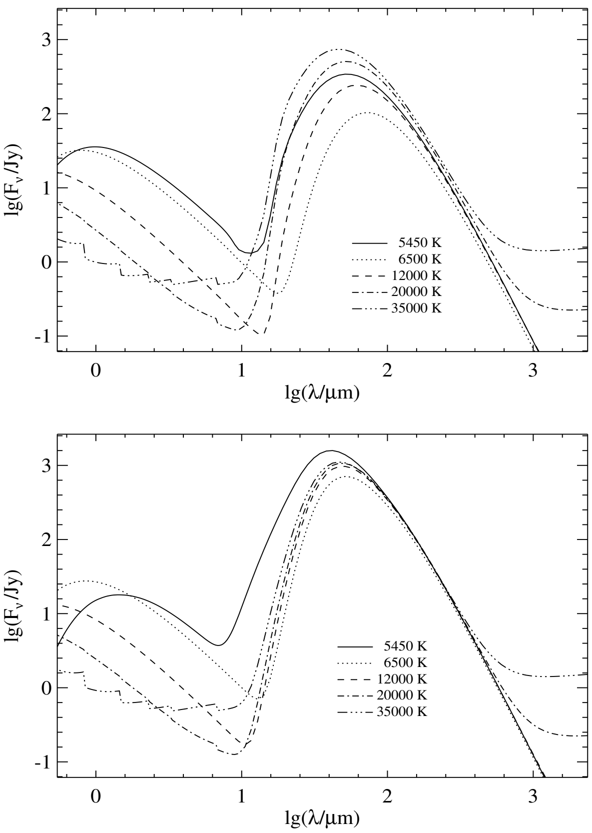

Figure 4.11 — *The spectral energy distribution at several stages during the post-AGB evolution for an earlier start of the transition phase (run 5). The upper panel shows the SED for silicate dust without post-AGB dust formation, the lower panel for graphite without post-AGB dust formation. The flux densities are calibrated for an assumed distance of 1 kpc. The temperatures are indicated.*

We will now look at the results for this run in the color-color diagram. It appears that the alternative end of the AGB entirely changes the path in the color-color diagram (Fig. 4.10). A selection of spectral energy distributions is presented in Fig. 4.11.

From the start, the silicate dust track moves strongly to the upper left, making a turn to the lower right, and finally a bend to the left. Since the star evolves slowly (it takes approximately 750 yr to go from 5450 K to 5500 K), the circumstellar shell cools rapidly, and only the stellar photosphere is visible at 12 μm (Fig. 4.11). This is reflected in an increasing [12]–[25] color temperature: the photospheric 12 μm flux remains approximately the same, while the 25 μm flux and the [25]–[60] temperature decrease due to the cooling of the shell. Subsequently the star starts to evolve more rapidly than the shell expands, and the [12]–[25] color temperature decreases. This is due to the fact that the

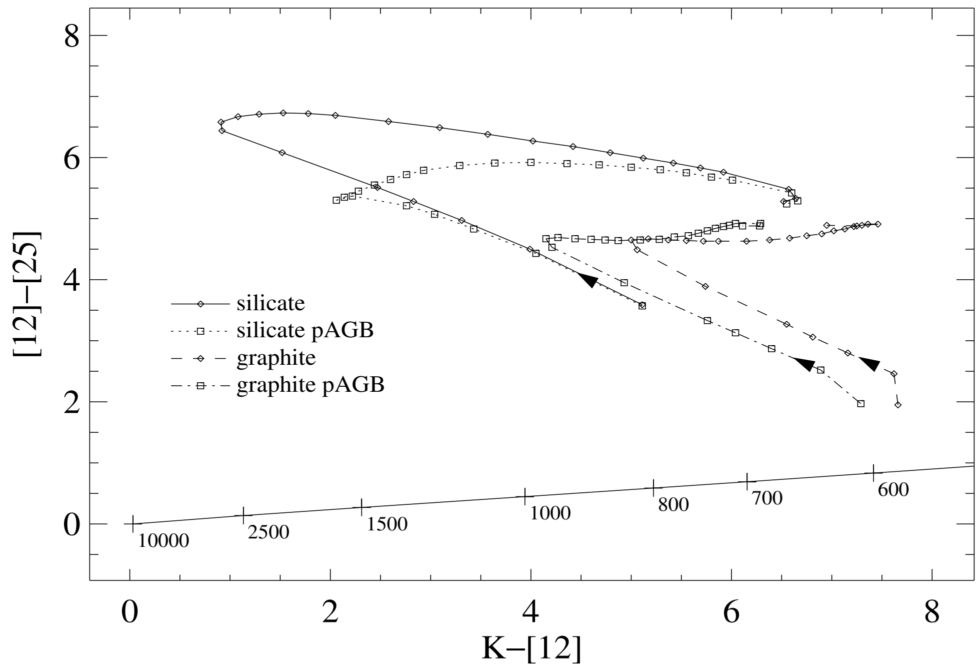

Figure 4.12 — *The near-IR color-color diagram at several stages during the post-AGB evolution for run 4. For reference a blackbody curve is also included in the diagram.*

shell now heats up, increasing the 25 μm flux and decreasing the [25]–[60] color, contrary to the 12 μm band which is still dominated by the decreasing photospheric emission of the evolving star. The shell continues to heat up, and the dust emission at 12 μm overtakes the decreasing photospheric flux density. The curve bends to higher [12]–[25] temperatures. The contribution of nebular bound-free emission at 12 μm for the hottest models increases the [12]–[25] color temperature even more, and the track makes the, now familiar, clockwise loop.

All effects outlined above appear less strong for the carbon-rich model. It initially starts on a cooling curve, and later bends to the clockwise loop. This is explained by the fact that the dust emission from the carbon grains still is present at 12 μm in the first points, so that the shell cools in all colors. For the remainder of the evolution there always remains some dust emission in the 12 μm band, making the loop to the left less pronounced.

4.4.5 A near-IR color-color diagram

In this section we present the evolution of a post-AGB star in a color-color diagram which uses colors at shorter wavelengths: the *K*–[12] vs. [12]–[25] diagram. This diagram gives a different view of the evolution since in all models the Johnson *K* band will be dominated either by the stellar continuum or the bound-free emission of the ionized part of the nebula. Only in the models containing hot graphite grains, part of the flux in this band will originate from the grains. So, contrary to the *IRAS* color-color diagram which we presented earlier, this diagram contains information both on the central star and the dust. The results for run 4 are shown in Fig. 4.12, giving both the tracks using silicate and graphite grains and both the tracks assuming AGB-only and post-AGB dust formation.

The first thing we notice is that all four tracks, at least in a qualitative sense, look quite similar. This suggests that this color-color diagram is less sensitive to particulars of the grain emission and thus that the information on the evolution of the central star and the nebula is less 'contaminated' when compared with the *IRAS* color-color diagram. We have only investigated this for the 3 $M_\odot$ track and it is not yet clear if this observation is valid in a more general context. In the past years the *IRAS* color-color diagram has proven to be a very useful tool for studying post-AGB evolution. Our knowledge has increased considerably since its introduction. However, when we try to understand the details of this evolution better, the information from the *IRAS* color-color diagram becomes more and more confusing. The *K*–[12] vs. [12]–[25] diagram may be a valuable additional tool for the study of post-AGB evolution.

We will only discuss the evolution of the *K*–[12] color in Fig. 4.12 since the evolution of the [12]–[25] color already has been discussed earlier. At first both the flux in the *K* band and the 12 μm band are decreasing. However the 12 μm flux decreases more rapidly and therefore *K*–[12] evolves towards hotter colors. This can be understood if we realize that the central star heats up relatively slowly while the circumstellar shell expands relatively rapidly. At a temperature of around 8000 K the central star evolution will speed up considerably, reversing the preceding argument.

The flux in the K band continues to drop, while the flux in the 12 μm band increases now, resulting in ever cooler K–[12] colors. This evolution continues until the central star starts to ionize a considerable part of the circumstellar shell and the K band flux will start to rise again due to nebular bound-free emission. This rise is so rapid that it reverses the evolution of the K–[12] color.

The tracks for silicate and graphite grains are qualitatively similar, but are offset with respect to each other. This is mainly due to the different absorption efficiency of silicate and graphite grains (see Sect. 4.4.2). The difference between the silicate track with and without post-AGB dust formation can be understood solely from the presence or absence of the 10 μm emission feature. The difference between the graphite tracks with and without post-AGB dust formation stems from the fact that the hot dust in the post-AGB section of the wind mainly radiates around 3 μm and thus contributes to the K band flux.

4.5 Discussion and conclusions

In this paper we have presented a new model to calculate the spectral evolution of a hydrogen burning post-AGB star. The main new ingredient of this model is the possibility of extracting timescales of the post-AGB central star evolution from the most recent evolutionary calculations. Hence, contrary to previous studies, it is possible now to investigate other AGB and/or post-AGB mass loss rates and different prescriptions for the start of the post-AGB phase. The use of a photo-ionization code in which a dust code is built in, gives us the opportunity to study the evolution of the infrared emission of the circumstellar material.

We have performed a parameter study on a typical post-AGB star with a core mass of 0.605 $M_\odot$ taken from Blöcker (1995b). By varying the parameters that govern the mass loss and the evolutionary timescales of the post-AGB phase by a reasonable amount we find that:

1. The influence of the evolving star on the infrared color evolution can not be neglected. In particular, the phase wherein the circumstellar shell can be considered as a stationary shell around a star that rapidly increases in temperature results in clockwise loops in the *IRAS* color-color diagram. This was not observed in many previous studies in which the temperature of the central star was taken to be constant. Instead, in these studies the evolutionary path followed a counter-clockwise loop in the color-color diagram because of the inevitable cooling of the shell.
   Only Szczerba & Marten (1993) who used a Blöcker track obtained a roughly similar result with their dust radiative transfer code. Volk (1992) found a slight deviation from the counter-clockwise loop in the color-color diagram. He used the coarse grid of evolutionary timescales from the 0.644 $M_\odot$ Schönberner (1983) track. The output of the photo-ionization code CLOUDY was used as input for a dust radiative transfer model. It is not clear to what extent that choice influenced the path followed in the *IRAS* color-color diagram.
   The crucial influence of the evolution of the central star warrants further parameter studies with other stellar models, where the increase in temperature as a function of time will be different. It is expected that the heating of the shell will be more important for more rapidly evolving (i.e. larger core mass) stars.
2. The tracks that are followed in the *IRAS* color-color diagram are very sensitive to the adopted dust opacity law and solid state features. Two main differences between the silicate and graphite models that were studied are evident. Firstly the *IRAS* colors of the silicate models are very sensitive to newly synthesized dust in the post-AGB wind because of the silicate 10 μm feature that contributes significantly to the 12 μm flux density. In contrast, hot graphite dust emits mainly shortward of the 12 μm pass band and thus post-AGB dust formation has less influence in this case. Secondly, the dependency of the absorption efficiency on the central star temperature is much stronger for silicates than for graphite in the temperature regime studied here. Therefore silicates react much stronger to the heating of the central star and thus give rise to much larger loops in the *IRAS* color-color diagram.
   Our knowledge of dust opacities, and certainly of solid state features in the mid- and far-infrared, will improve when the results of the *ISO* mission have been digested (Waters et al. 1996). For example, the well-known 21 μm and 30 μm features that have been observed in the infrared spectrum of carbon-rich post-AGB stars and planetary nebulae (e.g. Omont et al. 1995) have not been taken into account in this study. In addition, the wavelength coverage up to 200 μm will be of great help to determine the wavelength dependence of the dust opacities towards long wavelengths.
3. A third decisive factor that governs the evolution of the *IRAS* colors is the definition of the end of the AGB. The sooner an object enters the transition phase, i.e. the sooner the heavy AGB mass loss ceases, the longer the evolution to higher effective temperatures will last. This results in cool circumstellar dust shells, and consequently these models are on a location in the *IRAS* color-color diagram where not many post-AGB stars were expected previously. In this respect it is noteworthy to refer to Fig. 4.10 where oxygen-rich post-AGB stars are predicted to be present in the upper part of region VIII. A re-investigation of the sources in that region would be useful in testing whether this scenario is realistic.
4. Changing the mass loss prescription in the coolest part of the AGB evolution that we considered has little influence on the *IRAS* colors of the models.

In general we find that the variation of the parameters mentioned above, which are still not very well determined, result in a variety of different paths in the *IRAS* color-

color diagram. This is certainly part of the explanation why planetary nebulae do not occupy a well-structured region in the *IRAS* color-color diagram (cf. Volk 1992). As a by-product of this investigation we find that the same location in the *IRAS* color-color diagram can be occupied by objects with an entirely different evolutionary past. Apparently, the location in the *IRAS* color-color diagram can not *a priori* give a unique determination of the evolutionary status of an object.

As an alternative to the *IRAS* color-color diagram, the *K*–[12] vs. [12]–[25] color diagram is presented. The tracks in this diagram seem less affected by particulars of the grain emission. Hence this diagram might prove to be a valuable additional tool for studying post-AGB evolution.

The feedback of observational work, after a sufficient number of parameter studies, will be of help to assess the selection effects in our post-AGB sample selection criteria, and will give constraints on the assumptions that now have to be made on the central star and nebular evolution.

Acknowledgments. We are very grateful to Thomas Blöcker who has kindly provided us with the tables from which the evolutionary timescales could be reconstructed. The photo-ionization code CLOUDY was used. The code is written by Gary Ferland and obtained from the University of Kentucky, USA. We would like to thank the referee Ryszard Szczerba and Thomas Blöcker for critically reading the manuscript. PvH and RDO were supported by NFRA grants 782–372–033 and 782–372–031.

4.6 References

Aller L.H., Czyzak S.J., 1983, ApJS 51, 211
Blöcker T., 1995a, A&A 297, 727
Blöcker T., 1995b, A&A 299, 755
Blöcker T., Schönberner D., 1991, A&A 244, L43
Bowen G.H., 1988, ApJ 329, 299
Ferland G.J., 1993, University of Kentucky Physics Department Internal Report
Fernie J.D., 1995, AJ 110, 3010
Fernie J.D., Sasselov D.D., 1989, PASP 101, 513
Frank A., Balick B., Icke V., Mellema G., 1993, ApJ 404, L25
Górny S.K., Tylenda R., Szczerba R., 1994, A&A 284, 949
Groenewegen M.A.T., de Jong T., 1993, A&A 267, 410
Groenewegen M.A.T., de Jong T., 1994, A&A 283, 463
Hrivnak B.J., Kwok S., Volk K.M., 1989, ApJ 346, 265
Lèbre A., Mauron N., Gillet D., Barthès D., 1996, A&A 310, 923
Loup C., 1991, PhD Thesis, University of Grenoble
Marten H., Schönberner D., 1991, A&A 248, 590
Marten H., Szczerba R., Blöcker T., 1993, in Weinberger R., Acker A., eds, IAU Symp. 155: Planetary Nebulae. Kluwer Academic Publishers, Dordrecht, p.363
Martin P.G., Rouleau F., 1991, in Malina R.F., Bowyer S., eds, Extreme Ultraviolet Astronomy. Pergamon Press, Oxford, p.341
Mathis J.S., Rumpl W., Nordsieck K.H., 1977, ApJ 217, 425
Mellema G., 1993, PhD Thesis, University of Leiden
Olofsson H., 1993, in Schwarz H.E., ed., Second ESO/CTIO workshop, Mass loss on the AGB and beyond. ESO Conference and Workshop Proceedings No. 46, Garching, p.330
Omont A., Moseley S.H., Cox P. et al., 1995, ApJ 454, 819
Ostlie D.A., Cox A.N., 1986, ApJ 311, 864
Oudmaijer R.D., 1996, A&A 306, 823
Oudmaijer R.D., Bakker E.J., 1994, MNRAS 271, 615
Oudmaijer R.D., van der Veen W.E.C.J., Waters L.B.F.M., Trams N.R., Waelkens C., Engelsman E., 1992, A&AS 96, 625
Oudmaijer R.D., Waters L.B.F.M., Pottasch S.R., 1993, in Schwarz H.E., ed., Second ESO/CTIO workshop, Mass loss on the AGB and beyond. ESO Conference and Workshop Proceedings No. 46, Garching, p.122
Oudmaijer R.D., Waters L.B.F.M., van der Veen W.E.C.J., Geballe T.R., 1995, A&A 299, 69
Pauldrach A., Puls J., Kudritzki R.P., Méndez R.H., Heap S.R., 1988, A&A 207, 123
Pottasch S.R., 1984, Planetary Nebulae. Reidel Publishing Company, Dordrecht
Reimers D., 1975, Mem. Soc. Sci. Liège 8, 369
Schönberner D., 1979, A&A 79, 108
Schönberner D., 1981, A&A 103, 119
Schönberner D., 1983, ApJ 272, 708
Schönberner D., Blöcker T., 1993, in Sasselov D.D., ed., Luminous High-Latitude Stars. A.S.P. Conference Series Vol. 45, p.337
Siebenmorgen R., Zijlstra A.A., Krügel E., 1994, MNRAS 271, 449
Slijkhuis S., 1992, PhD Thesis, University of Amsterdam
Slijkhuis S., Groenewegen M.A.T., 1992, in Slijkhuis S., PhD Thesis, University of Amsterdam, Chapter 6
Straižys V., Kuriliene G., 1981, Ap&SS 80, 353
Szczerba R., 1993, in Weinberger R., Acker A., eds, IAU Symp. 155: Planetary Nebulae. Kluwer Academic Publishers, Dordrecht, p.350
Szczerba R., Marten H., 1993, in Schwarz H.E., ed., Second ESO/CTIO workshop, Mass loss on the AGB and beyond. ESO Conference and Workshop Proceedings No. 46, Garching, p.90
Trams N.R., Waters L.B.F.M., Waelkens C., Lamers H.J.G.L.M. van der Veen W.E.C.J., 1989, A&A 218, L1
Trams N.R., Waters L.B.F.M., Lamers H.J.G.L.M., Waelkens C., Geballe T.R., Thé P.S., 1991, A&AS 87, 361
van der Veen W.E.C.J., Habing H.J., 1988, A&A 194, 125
van der Veen W.E.C.J., Habing H.J., Geballe T.R., 1989, A&A 226, 108
Van de Steene G.C., van Hoof P.A.M., 1995, in Van de Steene G.C., PhD Thesis, University of Groningen, Chapter 7
Van de Steene G.C., Jacoby G.H., Pottasch S.R., 1996, A&AS 118, 243
van Hoof P.A.M., Trams N.R., Waelkens C., Cassatella A., 1991, in Trams N.R., PhD thesis, University of Utrecht, Chapter 7
Vassiliadis E., Wood P.R., 1993, ApJ 413, 641
Vassiliadis E., Wood P.R., 1994, ApJS 92, 125
Volk K., 1992, ApJS 80, 347
Volk K.M., Kwok S., 1989, ApJ 342, 345
Waelkens C., Van Winckel H., Bogaert E., Trams N.R., 1991, A&A 251, 495
Waelkens C., Van Winckel H., Trams N.R., Waters L.B.F.M., 1992, A&A 256, L15
Waters L.B.F.M., Molster F.J., de Jong T. et al., 1996, A&A 315, L361
Wood P.R. 1990, in Mennessier M.O., Omont A., eds, From Miras to Planetary Nebulae: Which Path for Stellar Evolution?. Editions Frontières, Gif sur Yvette, p.67

5 Radio and infrared emission from a [WC] type planetary nebula in the LMC†

A.A. Zijlstra, P.A.M. van Hoof, J.M. Chapman, C. Loup

Abstract — Radio continuum emission has been detected from a planetary nebula in the Large Magellanic Cloud: this is the first radio continuum detection for any planetary nebula outside our galaxy. The radio flux density is a factor of two lower than predicted from the Hβ flux. This could be due either to a two-component morphology or to a stellar contribution to the Hβ emission. We have modeled the optical and infrared spectrum using the photoionization code CLOUDY: a very good fit is obtained if we assume the nebula is carbon rich. The derived diameter implies an evolutionary age of the nebula of < 1000 yr, similar to what is derived from the *IRAS* colors alone. The central star, which is of [WC] type, has a much higher stellar temperature than galactic [WC] stars showing similar circumstellar *IRAS* colors. An explanation could be that the expansion velocity of the nebula is lower than those of its galactic counterparts. This radio detection indicates that accurate nebular luminosities could be determined from their radio emission for many LMC planetary nebulae.

5.1 Introduction

Radio and infrared observations have become important tools in the study of galactic planetary nebulae (PN). Radio continuum emission has the advantage over optical emission that it is not affected by atmospheric or interstellar extinction. The radio continuum emission can be used to detect PN in obscured galactic regions (e.g. Van de Steene & Pottasch 1993) and to determine accurate nebular luminosities. The infrared (*IRAS*) region contains the dust emission which can contribute up to 80 % of the total PN energy budget. From the *IRAS* colors the dust temperature can be derived, giving an indication of the nebula's physical size.

The study of galactic PN is severely hampered by the lack of accurate distances. Only the bulge provides a sample at a well-known distance, but it contains only low-mass planetary nebulae with old progenitors (e.g. Pottasch & Acker 1989). More luminous, high-mass PN with young progenitors are not found in the bulge and, for such objects, the Magellanic clouds have become the testing ground.

Radio observations of LMC PN have not yet been attempted due to the need for a sufficiently sensitive instrument. *IRAS* data have been available (Schwering 1989) but have not been used, mainly because until recently the optical positions for LMC PN were too inaccurate to establish reliable associations. Also, the flux densities are at the limit of *IRAS* detectability and require special processing. As a result, the study of LMC PN has exclusively been based on optical and, in a few cases, *IUE* observations. The optical measurements are not without problems: the observations must be done at significant air masses (> 1.2), requiring a correction for atmospheric dispersion. In addition, the fields are generally very crowded. The difficulty of obtaining reliable reddening corrections adds to the uncertainty: recent observations indicate reddening is significant for some objects (e.g. Vassiliadis et al. 1992a).

In this paper we present the first radio detection of a PN in the LMC. This PN (SMP 58) was also detected by *IRAS*. We discuss its characteristics and compare it to other *IRAS*-detected PN in the LMC. SMP 58 contains a Wolf-Rayet type central star (one of four such objects known in the LMC), which makes it especially interesting. These low-mass stars show spectra similar to those of the mas-

† Published in A&A 290, 228.

sive WR stars, with strong carbon and helium emission lines. Following van der Hucht et al. (1981), they are denoted as [WC] stars, to distinguish them from their massive counterparts. [WC] stars occur in approximately 5 % of all galactic PN (taken from Acker et al. 1992); the four LMC [WC] stars constitute a similar percentage of spectroscopically observed PN in the LMC. They are generally assumed to be helium-burners with little or no hydrogen envelope: at present there are no theoretical model calculations available for the evolution of such stars. We show that SMP 58 has bluer *IRAS* colors than galactic [WC] stars of similar temperature, indicating a more compact nebula. This conclusion is confirmed by modeling of the spectrum, and possibly indicates lower nebular expansion velocities.

5.2 Observations

We observed the LMC planetary nebula SMP 58 with the compact array of the Australia Telescope on two occasions. The array consists of six 22-meter antennas: five are movable on a 3 km east-west baseline and the sixth antenna has a fixed position 3 km further west. During the first observations, the five antennas were placed in a highly compact configuration. The sixth antenna was not used in the final analysis because of the uneven UV coverage it would create. There were problems with the amplitude calibration and we re-observed the source in June, using a more extended configuration which gave higher resolution and allowed use of all antennas. All observations were done simultaneously at 3 cm and 6 cm, in blocks at several different hour angles to improve the UV coverage. The pointing was offset from the PN to avoid problems with DC offsets which can cause artifacts at the field center. The observations are summarized in Table 5.1.

Data reduction was done using the AIPS software package. The central 75 % of the band was averaged in frequency to obtain a continuum database. A large map was made in order to find confusing sources, which were subsequently removed through the CLEAN procedure. The flux was determined as the average between the peak in the cleaned map, and the value obtained from a gaussian fit to the source. The flux determinations of the June data are expected to be accurate to better than 10 %, in addition to the uncertainty introduced by the the rms noise of the data. The uncertainty is primarily due to the poor UV coverage and the low signal to noise of the detections. In addition, the flux density of the primary calibrator is uncertain by a few percent: this introduces a systematic uncertainty in the derived flux densities.

5.3 The radio–Hβ discrepancy

We detected radio emission from SMP 58 at a level of about 0.8 mJy at 3 cm and 6 cm. The 3 cm image is shown in Fig. 5.1. The optical position (Meatheringham & Dopita 1991a) of $\alpha = 05^{\rm h}24^{\rm m}20^{\rm s}$, $\delta = -70°05'03''$ (J2000) agrees to within $2''$ with the more accurate radio position, leaving no doubt that the detected radio emission originates from the planetary nebula. The fact that the radio flux densities at 3 cm and 6 cm are identical within the uncertainties indicates that the radio emission is optically thin at these wavelengths. In this case the radio flux density and the Hβ flux should be related by a simple relation (Pottasch 1984, eq. IV-26) that only requires knowledge of the electron temperature and the amount of singly and doubly ionized helium; these parameters are given by Monk et al. (1988), Meatheringham et al. (1988) and Meatheringham and Dopita (1991a): $T_{\rm e} = 11\,200$ K, $n({\rm He}^+)/n({\rm He}^0) = 0.072$, $n({\rm He}^{++}) = 0$. The Hβ flux predicted from this relation and our radio flux is $\lg[F({\rm H}\beta)/({\rm W\,m^{-2}})] = -15.63$. This is considerably smaller than the observed value of $\lg[F({\rm H}\beta)/({\rm W\,m^{-2}})] = -15.20$, where we have corrected for the reddening: $c = 0.28$, derived from the $F({\rm H}\alpha)/F({\rm H}\beta)$ ratio (Meatheringham and Dopita 1991a). Conversely, the observed Hβ flux with the $F({\rm H}\alpha)/F({\rm H}\beta)$ reddening would predict a radio flux density of 1.9 mJy.

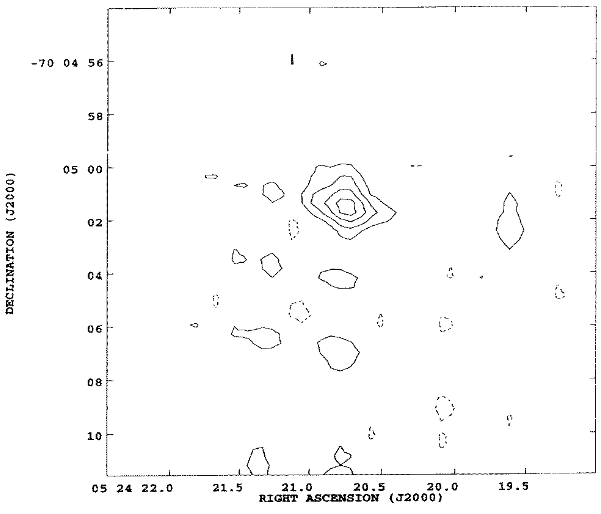

Figure 5.1 — *The 3cm radio image of SMP 58, from the June 1993 observations (Table 5.1). Contour levels are at −0.4, −0.2, 0.2, 0.4, 0.6, 0.8 mJy beam^{-1}.*

The reason for this large discrepancy is not clear. Obviously both the radio and optical measurements should be repeated: if the 3 cm flux density were found to be be less than 0.5 mJy, it would change our conclusion that the nebula is optically thin. This error is larger than the estimated uncertainty on the flux, but the possibility makes additional observations desirable. A smaller optical extinction would also lessen, but not remove, the discrepancy.

A possible explanation for the discrepancy could be that the nebula has a very compact core which is highly optically

Table 5.1 — *AT observations of SMP 58.*

	May 1993		June 1993	
AT configuration	375		6A	
wavelength (cm)	3	6	3	6
frequency (MHz)	8640	4800	8640	4800
bandwidth (MHz)	128	128	128	128
T_{sys} (K)	50	50	50	50
flux calibrator	1934−638	1934−638	1934−638	1934−638
calibrator flux (Jy)	2.59	6.34	2.59	6.34
phase calibrator	0454−810	0454−810	0522−611	0522−611
int. time (min)	90	90	100	100
resolution (arcsec)	35×12	72×22	2.2×1.6	5.3×3.7
rms noise (mJy beam^{-1})	0.16	0.20	0.10	0.10
PN flux (mJy)	0.6:	1.1:	0.84	0.79
uncertainty (mJy)			0.13	0.13
radio position (J2000)	$\alpha = 05^h24^m20\overset{s}{.}7$		$\delta = -70°05'01\overset{''}{.}5$	

thick to radio continuum emission. A galactic example of such an object is the planetary nebula M2-9 where the core is so optically thick that it contributes very little flux at 5 GHz: most of the detected radio flux comes from more extended emission (Zijlstra et al. 1989). The optically thick component only becomes apparent at higher frequencies. Our present results do not allow us to confirm such a core–halo morphology for SMP 58. An alternative explanation could be that the observed Hβ flux is contaminated by line emission from the central star. This can be tested through measurements of other Balmer lines, which in such a case would yield different values for the reddening.

The observed flux density can be used to obtain limits to the size of the nebula. The fact that the radio brightness temperature cannot exceed the electron temperature allows us to derive a lower limit to the diameter of the full nebula of $0.08''$ (e.g. Kwok 1986). If an optically thick core is present we can similarly put limits on the core size, using the fact that for optically thick emission the brightness temperature is equal to the electron temperature. Assuming that such a core contributes less than approximately 0.1 mJy at 6 cm, we derive an upper limit to its diameter of $0.03''$. Using optical measurements, Dopita & Meatheringham (1991) model the nebula as a very thin shell with an inner radius of 0.019 pc and an outer radius of 0.022 pc. The corresponding predicted angular diameter is $0.15''$. This diameter, though possibly not the density structure, is in agreement with our limit on the size of the full nebula of $> 0.08''$.

In the following section we will discuss *IRAS* data on PN in the LMC. Using the *IRAS* data for SMP 58, we will then model the optical and infrared spectrum to show that the nebula is possibly more compact than found by Dopita & Meatheringham.

5.4 IRAS detections of LMC planetary nebulae

The *IRAS* detection of SMP 58 is given in Schwering's catalogue (1989, hereafter S89) of *IRAS* sources in the LMC, with flux densities of 0.15 Jy at 12 μm and 0.22 Jy at 25 μm. The *IRAS* and radio positions agree within $11''$, leaving little doubt about their association. The flux densities are reasonable: the infrared excess (IRE, defined as the ratio of the infrared flux over the Lyα flux) is about 1.4. Here we determine the IRE by simply summing the emission in the *IRAS* bands. Strictly speaking this should be interpreted as a lower limit, since (especially for young objects) significant dust emission arises shortward of the 12 μm band. We use this value, however, because it can be compared to determinations for galactic PN. In the Galaxy the IRE shows a radial gradient coincident with the galactic metallicity gradient. The value of 1.4 coincides with the average for galactic PN outside the solar circle and is about a factor of two below PN in the inner disk (Zijlstra 1990).

S89 lists in total 29 LMC PN with possible *IRAS* associations. This listing can now be significantly improved because of (1) the much more accurate positions for PN now available, and (2) the availability of the Faint Source Catalogue (FSC) which covers the full LMC (S89 only covers the inner regions). We have correlated both the FSC and S89 catalogues with the list of LMC PN and selected all sources where the *IRAS* and PN position agree to within $15''$: in total 12 associations were found, with *IRAS* flux levels between 0.1 Jy and 0.5 Jy. These sources are listed in Table 5.2. Several of the associated *IRAS* sources appear in both the FSC and S89. In such cases the two catalogues show generally good agreement in flux densities and positions; the flux densities given in Table 5.2 are those from

Table 5.2 — *IRAS sources associated with LMC PN.*

	F_{12} Jy	F_{25} Jy	F_{60} Jy	lg $F(\mathrm{H}\beta)^a$ W m^{-2}	c	lg n_e cm^{-3}	ref	lg $L_\star^b$ L$_\odot$	IRE
SMP 1	0.06	0.24	0.14	−15.46	0.17	3.56	1,2	3.8	1.3
SMP 6	<0.06	0.11	<0.16	−15.67	0.50	4.25	1,2,3,7	3.9	0.3
SMP 8	0.21	0.50	–	−16.74	0.23	3.74	1,2,10	2.5	56
SMP 11	0.18	0.30	–	−16.15	–	–	5	–	–
SMP 28	<0.24	0.44	–	−16.35	–	–	5	–	–
SMP 31	0.13	0.45	<0.12	−15.91	<0.88	4.0	1,2,9	<4.0	>1.3
SMP 58	0.15	0.22	–	−15.48	0.28	4.82	1,2	3.9	1.5
MG 45	0.15	0.32	0.16	–	0.90	–	2,6	–	–
SMP 61	0.08	0.13	<0.16	−15.48	0.20	4.52	1,2,3	3.8	1.0
SMP 85	0.10	0.38	<0.75	−15.42	0.25	>5.0	2,4	3.9	1.4
SMP 98	0.16	0.23	0.14	−15.52	0.39	3.86	4	3.9	1.3
MA 18	0.08	0.12	<0.14	−15.67	0.07	>5.0	4,8	3.4	2.0

[a] Hβ fluxes are not corrected for reddening.
[b] The stellar luminosities are calculated as $150 \times L(\mathrm{H}\beta)$.
[c] The IRE is derived by simply summing over the *IRAS* bands and should therefore be considered a lower limit, especially for young objects.
references: 1. Meatheringham et al. 1988; 2. Meatheringham & Dopita 1991a; 3. Meatheringham & Dopita 1991b; 4. Vassiliadis et al. 1992a; 5. Wood et al. 1987; 6. Morgan & Good 1992; 7. The position in Meatheringham & Dopita (1991b) is wrong. The correct position is given in Meatheringham & Dopita (1991a); 8. Vassiliadis et al. 1992b; 9. Extinction from Monk et al. (1988) is considered as upper limit. 10. The Hβ flux may be in error.

the FSC. Of the 12 sources in Table 5.2, only SMP 58 is not listed in the FSC. The large fraction of sources from the FSC is possibly caused by the fact that in confused regions, where the S89 catalogue is better, the positional accuracy is lower.

The *IRAS* colors indicate that the *IRAS*-detected nebulae are very young objects. The F_{12}/F_{25} ratios are in the range 0.25 to 0.7 and are significantly bluer than the majority of galactic PN (Pottasch et al. 1988). This indicates that we have selected objects which have evolved rapidly towards the PN phase: the F_{12}/F_{25} ratio drops rapidly during the early evolution after the end of the AGB mass loss as a result of the decreasing dust temperature. At later phases the peak of the dust emission occurs longward of 25 μm, and the F_{12}/F_{25} ratio is less affected by further evolution; most of the galactic PN are in this phase. The blue *IRAS* colors in the LMC are the results of a selection effect, in the sense that a 12 μm detection is in general necessary in order to get a sufficiently accurate *IRAS* position, combined with the fact that at the distance of the LMC the peak of the PN luminosity function is not far above the detection limit of *IRAS*. However, it is interesting that such rapidly evolving objects exist at all in the LMC. The short post-AGB time scales are consistent with the high electron densities of most of the objects.

The objects SMP 58 and SMP 61 have [WC] central stars (Monk et al. 1988; Meatheringham & Dopita 1991a), based on the presence of the C IV λ5806 line. Meatheringham & Dopita also suggest that SMP 31 may have a [WC] central star, because the individual Balmer lines give inconsistent values for the extinction. Interestingly, these objects are among the high-luminosity PN in Table 5.2. As only four [WC] stars are known in the LMC (Monk et al. 1988), not including SMP 31, it appears that an unexpectedly high fraction of those have been detected by *IRAS*. It is noteworthy that one non-detected source (SMP 38) has a somewhat lower nebular density than the detected two, while the other (LM 1-64; Peña et al. 1994), is probably more evolved because of its higher stellar temperature.

5.5 A model for the optical, IRAS and radio data of SMP 58

An optical spectrum of SMP 58 is given by Meatheringham & Dopita (1991a). We have attempted to model this spectrum using a modified version of the photo-ionization code CLOUDY 84.06 (Ferland 1993). The following parameters were kept free in the modeling: the stellar temperature and luminosity, the inner and outer radius of the shell, the density, chemical composition and dust-to-gas ratio of the shell and the distance to the nebula. The distance is used as an independent check on the model, since the distance to the LMC is very well known. A detailed discussion of the method is given in van Hoof & Van de Steene (1997).

The shell is assumed to be spherical and to have uniform density. For the star we assumed a blackbody spectrum. As input to the model we use line ratios from the optical spectrum, the *IRAS* flux densities and the radio fluxes. The He II λ4686 line could not be reproduced by the fit. It is probably contaminated by line emission from the central star, since [WC] stars are expected to show this line in emission. Possible contamination of the H I, He I and C II

Table 5.3 — *Observed and predicted quantities for SMP 58.*

λ (Å)	id	observed	CLOUDY	Siebenmorgen
3727	[O II]	8.2	9.6	
3869	[Ne III]	33.9	34.2	
4102	Hδ	25.8	29.8	
4267	C II	1.4	1.4	
4340	Hγ	47.2	50.6	
4363	[O III]	9.0	11.6	
4472	He I	6.2	4.2	
4686	He II	1.8	0.6	
4861	Hβ	100.0	100.0	
4959	[O III]	244.7	247.9	
5007	[O III]	saturated	743.7	
5876	He I	13.1	14.7	
6300	[O I]	2.4	1.6	
6312	[S III]	1.9	1.9	
6364	[O I]	1.0	0.5	
6548	[N II]	2.0	2.0	
6563	Hα	saturated	272.3	
6583	[N II]	5.8	5.9	
7065	He I	11.1	11.2	
7136	[Ar III]	7.7	7.7	
7320	[O II]	6.5	7.5	
7330	[O II]	6.8	6.1	
12 μm	*IRAS*	0.15 Jy	0.10 Jy	0.13 Jy
25 μm	*IRAS*	0.22 Jy	0.29 Jy	0.24 Jy
60 μm	*IRAS*	—	0.12 Jy	0.12 Jy
3 cm	radio	0.84 mJy	0.86 mJy	
6 cm	radio	0.79 mJy	0.84 mJy	

Table 5.4 — *model parameters for SMP 58.*

parameter	value	element	abundance
T_*/kK	57.3	ϵ(He)	10.94
$L_*/L_\odot$	5330	ϵ(C)	9.22:
r_{in}/mpc	5.9	ϵ(N)	7.14
r_{out}/mpc	23.7	ϵ(O)	8.29
$\lg(n_H/cm^{-3})$	4.95	ϵ(Ne)	7.12:
D/kpc	50.7	ϵ(S)	6.39
		ϵ(Ar)	5.78
T_e/kK	12.0		
$M_{sh}/M_\odot$	0.164:		
r_{ion}/mpc	10.1		
Θ_{rad}/arcsec	0.041		
$M_{ion}/M_\odot$	0.011		
IRE[a]	5.5		
$\lg[F(H\beta)/(W\,m^{-2})]$	−15.54		

[a] Here the IRE is calculated as the integral over the dust emission spectrum; the value can therefore not be directly compared with those in Table 5.2.

lines was not considered. We also ignored possible N III contamination of the Hδ line.

A comparison of the observed and predicted quantities can be found in Table 5.3. The resulting parameters for the optimum fit are given in the Table 5.4. The abundances are logarithmic number densities with respect to hydrogen ($\epsilon(H) \equiv 12$). As additional information we also give the mean electron temperature, the total shell mass, the ionization radius, the angular radius, the ionized mass, the infrared excess and the (non-reddened) Hβ flux.

The observed line ratios and the radio flux densities are well reproduced by the fit. The outer radius is determined exclusively from the *IRAS* fluxes and is therefore not well determined. However, the model does not reproduce the *IRAS* colors particularly well. The reason for this is that the dust mixture used in CLOUDY is not appropriate for carbon-rich planetary nebulae. We have therefore used the final model as input to the Siebenmorgen dust model, which includes stochastically heated small grains and PAH's in a radiative-transfer calculation (Siebenmorgen & Krügel 1992). Both components are expected to give a significant (or even dominant) contribution to the 12 μm continuum flux in carbon-rich planetary nebulae (Siebenmorgen et al. 1993). This model predicts *IRAS* fluxes in much better agreement with observations, as shown in the table. However, we note that no total dust mass can be derived unless measurements at much longer wavelengths are available. The shell mass given in the table should be viewed with caution.

When we compare our results with those from Dopita & Meatheringham (1991) (hereafter DM) significant differences in the shell radius and density are apparent. The main reason is probably our use of the radio flux density rather than the Hβ flux as measure for the recombination rate: clearly the discrepancy between these two values needs to be resolved. Smaller differences can be caused by our exclusion of the He II λ4686 line, resulting in a slightly lower stellar temperature. The stellar temperature is in agreement with the spectral type and with the Zanstra temperature. The stellar luminosity agrees very well with DM. The hydrogen density is somewhat higher than determined from the [O II] line ratio (the value DM used), but the line-ratio method shows large uncertainties at high densities. Also the mean electron temperature is a little higher than determined from the [O III] line ratio. The abundances are in good agreement with the values determined by DM and indicate a non-type I PN (Clegg 1993). The nitrogen abundance seems very low. Also the carbon and neon abundances seem to deviate, but these values are very uncertain. The high (but uncertain) carbon abundance and the agreement of the Siebenmorgen model with the observed *IRAS* fluxes indicate that the nebula is carbon rich.

The derived inner radius is very small for a planetary nebula, and indicates that the nebula is very young. The ionization radius implies an angular *diameter* of 0.08″. Comparing this with the predictions from the radio emission shows that the radio emission is marginally affected by optical-depth effects; the optically thin radio flux would

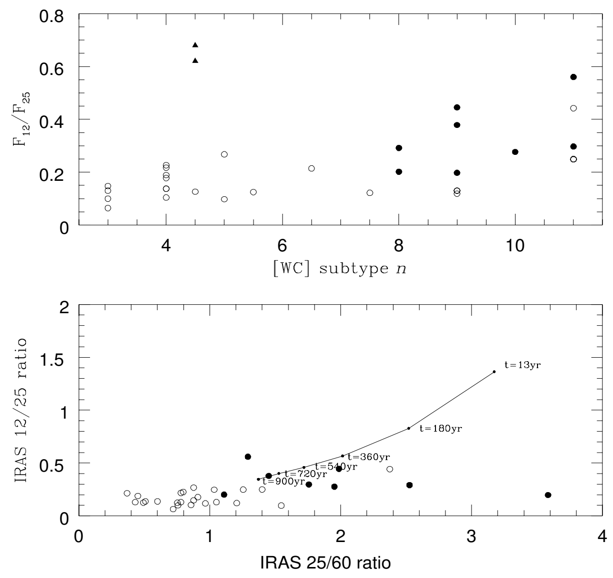

Figure 5.2 — **a** *Excitation class versus IRAS 12 μm over 25 μm flux ratio for [WC] stars. Open circles: galactic stars with $F_{12} <$ 10 Jy; filled circles: galactic stars with $F_{12} >$ 10 Jy; triangles: LMC [WC] stars.* **b** *IRAS color evolution of the galactic [WC9] star BD+30° 3639. Labels designate elapsed time after the end of the AGB mass loss. Open and filled circles as in upper panel.*

be about 1.0 mJy. This effect is insufficient to explain the discrepancy between the predicted and observed Hβ flux.

We conclude that a very good fit to the observed parameters can be obtained using the radio and *IRAS* flux densities.

5.6 Comparison with galactic [WC] stars

Although few [WC] stars are known in the LMC, they are not uncommon among galactic PN. The *IRAS* detections allow us to compare SMP 58 and SMP 61 with their galactic counterparts. [WC] stars are commonly classified as [WCn] where n indicates the degree of excitation of the star: it ranges from $n = 2$ for the hottest ($T_* \approx$ 100 000 K) to $n = 11$ for the coolest stars ($T_* \approx$ 20 000 K). SMP 58 and SMP 61 both are classified as [WC4/5] (Monk et al. 1988), with $T_* \simeq$ 60 000 K. The Zanstra temperatures of SMP 58 and SMP 61 are in reasonable agreement with this, at 67 500 K and 48 000 K respectively (Meatheringham & Dopita 1991a). The model temperature derived above for SMP 58 also agrees well with the excitation temperature.

Fig. 5.2a shows the distribution of F_{12}/F_{25} flux ratios as a function of subtype, for the two LMC [WC] stars and for all known galactic [WC] stars listed in the ESO–Strasbourg Catalogue of Planetary Nebulae (Acker et al. 1992). We only include reliable (quality 3) *IRAS* detections within 15″. The color distribution of the [WC] stars is similar to that of the general PN population (e.g. Pottasch et al. 1988). However, the higher subtypes (cooler stars) show a tendency toward higher ratios. This agrees qualitatively with the expected evolution: during the post-AGB evolution the stars become hotter with time (corresponding to decreasing n), while the envelope expands and cools (decreasing F_{12}/F_{25} flux ratio). Thus, an evolutionary sequence can be envisaged connecting the cool to the hot [WC] stars.

In Fig. 5.2a, the filled circles indicate sources with $F_{12} >$ 10 Jy, which roughly corresponds to the *IRAS* sensitivity for the LMC scaled to the distance of the bulge: all sources represented by the open circles would not be detectable in the LMC. The colors of the two LMC [WC] stars are reasonably similar to those of galactic [WC] stars of similar flux. However, the subtype of the LMC stars is much earlier: n = 4 to 5, where their galactic counterparts have n = 8 to 11. In terms of stellar temperature, the two LMC objects are about twice as hot as their galactic counterparts with similar *IRAS* colors.

We can assign time scales to the *IRAS* colors by using the calculated post-AGB evolution for the galactic [WC9] planetary nebula BD+30° 3639 (Siebenmorgen et al. 1993). Fig. 5.2b shows this track in the full color-color diagram, where the LMC stars are not plotted as they were not detected at 60 μm. The time scales assume a constant expansion velocity of 22 km s^{-1}. The observed range of F_{12}/F_{25} flux ratios for the cool [WC] stars correspond to t = 200 yr to 1000 yr after the end of the AGB. These short time scales are confirmed by the fact that, of the 15 known [WC8–11] stars, 7 show evidence for dust emission at *K* (IR-type D; Whitelock 1985). In contrast, of the 21 earlier [WC] stars, none are D-type (using data from Acker et al. 1992 and Zijlstra et al. 1991). *K*-band dust emission is only expected in objects where the mass loss has ended $\lesssim$ 300 yr to 500 yr ago (Siebenmorgen et al. 1993). This conclusion takes into account stochastic heating of small grains.

The *IRAS* flux ratios of both SMP 58 and SMP 61 also correspond to such young objects, unlike their galactic counterparts of similar stellar temperature. This indicates that both LMC objects have more compact dust shells than galactic [WC] stars of the same temperature. The model fit for SMP 58 discussed above confirms its compactness. Either the stars have evolved quicker, or the nebulae have expanded more slowly than their galactic counterparts. Support for the latter comes from Wood et al. (1992), who argue that AGB stars in the LMC have lower expansion velocities by about a factor of two than galactic AGB stars, due to the lower metallicity of the LMC. This effect could naturally explain the observed difference between galactic and LMC [WC] stars.

5.7 Other possible causes for blue IRAS colors

We derive a picture above in which SMP 58 contains a very compact nebula which has expanded slowly. However, before making this conclusion too strong, we should warn the reader that, if the blue *IRAS* colors could be explained in any other way than a compact nebula, the reason to prefer our ionization model over the more extended nebula derived by Dopita & Meatheringham (1991) would disappear. The compactness of the nebula would then purely depend on whether one accepts the radio flux density or the Hβ flux. It is therefore necessary to mention a few ways in which the low metallicity of the LMC could cause bluer *IRAS* colors, other than causing lower expansion velocities.

First, line blanketing in the far-UV could be lower for the LMC central stars. The importance of this is very difficult to estimate, since the atmosphere of [WC] stars is highly self-enriched in some elements (arising from the s-process) but not in others. However, if the line blanketing is significantly lower it would cause both the Zanstra temperature and the [WC] excitation temperature to be somewhat overestimated, which would reduce the discrepancy in *IRAS* colors between the LMC and galactic [WC] stars. This points requires detailed calculations which are not yet available.

Second, the *IRAS* bands contain contributions both from the dust continuum and a number of forbidden lines. If the dust content is lower, the lines could become more dominant; this would make the 12 μm flux relatively stronger since it contains more emission lines, where especially the [S IV] 10.51 μm line and the [Ne II] 12.81 μm line can be strong. However, the emission lines are significant for the total flux only in old, evolved nebulae. For SMP 58, CLOUDY gives an emission line contribution of 0.16 % in the 12 μm band and 0.02 % in the 25 μm band.

Finally, the dust composition could be significantly different from the composition in galactic PN. To explain the blue *IRAS* colors, one would need a larger contribution of the smallest grains, especially PAH's. It is not clear why a lower dust content would lead to smaller grains – the grain composition is probably largely determined by destruction mechanisms, both for galactic and LMC PN.

Of these four effects, a lower expansion velocity seems to give the more likely explanation for the observed blue *IRAS* colors. However, the other effects deserve further investigation.

5.8 Conclusions and future prospects

We have presented the first radio continuum detection of a PN in the LMC. The radio flux density is considerably lower than expected from the observed Hβ flux. The object, which contains a [WC] star, was also detected by *IRAS*. We show that all *IRAS*-detected PN, are likely to be young objects. We also compare the PN to [WC]-type objects in the galaxy, and find that the LMC PN has much bluer *IRAS* colors than its galactic counterparts. Our preferred explanation is that its circumstellar envelope is more compact due to a lower expansion velocity, caused by lower metallicity. This is supported by a photo-ionization model fitting of the spectrum of SMP 58 However, other possible causes also deserve further study.

Our radio continuum detection indicates that many PN in the LMC could be detected in the radio, since SMP 58 is not particularly luminous. This raises the possibility of obtaining accurate stellar luminosities for luminous, high-mass PN. Such a study has not been possible in our Galaxy because of the lack of such objects with known distances; as a consequence, at present it is not known what fraction of PN have massive central stars (e.g. Pottasch 1992; Dopita et al. 1993). This discussion also has implications for the mass distribution of white dwarfs, which originate from PN central stars. A radio survey of LMC PN appears the best way to resolve this controversy.

Acknowledgments. We thank the staff at the Australia telescope, especially Wilfred Walsh and Neil Killeen, for their support and advice during the observations and data reduction. We also thank Helen Pongracic of Sydney University for assisting with the data reduction. Rens Waters is acknowledged for several suggestions regarding the effects of low metallicity. Rene Oudmaijer helped us with accessing the *IRAS* data base. Tim Bedding, Griet Van de Steene and Stuart Pottasch are thanked for critical reading of the manuscript. Peter van Hoof receives financial support under grant no. 782-372-033 from the Netherlands Foundation for Research in Astronomy (ASTRON). This research has made use of the SIMBAD database, operated by CDS, Strasbourg, France, and of the CLOUDY program, obtained from the University of Kentucky, USA.

5.9 References

Acker A., Ochsenbein F., Stenholm B., Tylenda R., Marcout J., Schon C., 1992, Strasbourg–ESO catalogue of galactic planetary nebulae. European Southern Observatory, Garching

Clegg R.E.S., 1993, in: Weinberger R. and Acker A. (eds.), Proc. IAU Symp. 155, Planetary Nebulae (Kluwer, Dordrecht), p.549

Dopita M.A., Meatheringham S.J., 1991, ApJ 367, 115

Dopita M.A., Ford H.C., Bohlin R., Evans I.N., Meatheringham S.J., 1993, ApJ 418, 804

Ferland G.J., 1993, University of Kentucky, Physics Department, Internal Report

Kwok S., 1986, ApJ 290, 568

Meatheringham S.J., Dopita M.A., Morgan D.H., 1988, ApJ 329, 166

Meatheringham S.J., Dopita M.A., 1991a, ApJS 75, 407

Meatheringham S.J., Dopita M.A., 1991b, ApJS 76, 1085

Monk D.J., Barlow M.J., Clegg R.E.S., 1988, MNRAS 234, 583

Morgan D.H., Good A.R., 1992, A&AS 92, 571

Peña M., Olguin L., Ruiz M.T., Torres-Peimbert S., 1994, Rev. Mex. Astron. Astrofís. 28, 27

Pottasch S.R., 1984, Planetary Nebulae (Reidel, Dordrecht)

Pottasch S.R., 1992, A&AR 4, 215

Pottasch S.R., Acker A., 1989, A&A 221, 123

Pottasch S.R., Bignell C., Olling R., Zijlstra A.A., 1988, A&A 205, 248

Schwering P.B.W., 1989, A&AS 79, 105

Siebenmorgen R., Krügel E., 1992, A&A 259, 614
Siebenmorgen R., Zijlstra A.A., Krügel E., 1994, MNRAS 271, 449
Van de Steene G.C., Pottasch S.R., 1993, A&A 274, 895
van Hoof P.A.M., Van de Steene G.C., 1997, A&A, submitted (Chapter 2)
Vassiliadis E., Dopita M.A., Morgan D.H., Bell F.J., 1992a, ApJS 83, 87
Vassiliadis E., Meatheringham S.J., Dopita M.A., 1992b, ApJ 394, 489
Whitelock P.A., 1985, MNRAS 213, 59
Wood P.R., Faulkner D.J., 1986, ApJ 307, 659
Wood P.R., Meatheringham S.J., Dopita M.A., Morgan D.H., 1987, ApJ 320, 178
Wood P.R., Whiteoak J.B., Hughes S.M.G., Bessell M.S., Gardner F.F., Hyland A.R., 1992, ApJ 397, 552
Zijlstra A.A., 1990, A&A 234, 387
Zijlstra A.A., Pottasch S.R., Bignell C., 1989, A&AS 79, 329
Zijlstra A.A., Gaylard M.J., te Lintel Hekkert P., Menzies J.W., Nyman L.-Å, Schwarz H.E., 1992, A&A 243, L9

6 The central stars of the planetary nebulae NGC 7027 and NGC 6543[†,‡]

P.A.M. van Hoof, D.A. Beintema, F. Lahuis, S.R. Pottasch

Abstract — Infrared spectra of NGC 7027 and NGC 6543 ranging from 2.4 μm to 45 μm were obtained with the Short Wavelength Spectrometer on board the Infrared Space Observatory. A first analysis of these spectra, with the aid of photo-ionization models, is presented. We report the first detection of the [Ar VI] 4.53 μm and [Ne VI] 7.65 μm lines in the spectrum of NGC 7027. When compared with older observations it is clear that the [Ar VI] line and possibly also other lines have increased in strength since 1981. We argue that a likely explanation for this variability is a change in the spectral energy distribution of the central star, possibly an increase in effective temperature. However, this result needs to be confirmed by further observations.
We also report a non-detection of the [O IV] 25.9 μm line and the first detection of the [Na III] 7.32 μm line in the spectrum of NGC 6543. The non-detection is not expected based on a blackbody approximation to the spectrum of the central star. The ionization threshold for O^{3+} is just beyond the He II limit, and the absence of this line shows that the stellar flux drops at least by a factor 350 at the He II limit. Modeling the [O IV] line may prove to be a valuable test for atmosphere models.

6.1 Introduction

Both the planetary nebulae NGC 7027 and NGC 6543 are very well studied nebulae. However, a complete study of the infrared spectrum of these sources has not been possible until now. In view of their scientific interest and their brightness they were obvious candidates for early targets to be observed by the Short Wavelength Spectrometer (SWS) on board the Infrared Space Observatory (*ISO*). In this paper we will present selected ionic emission lines of both SWS spectra. We will also present preliminary photo-ionization models and we will discuss possible interpretations of the reported features.

† Based on observations with ISO, an ESA project with instruments funded by ESA Member States (especially the PI countries: France Germany, the Netherlands and the United Kingdom) and with the participation of ISAS and NASA.
‡ Published in A&A 315, L253.

6.2 The ISO SWS observations

The SWS spectra of NGC 7027 and NGC 6543 were obtained during the Performance Verification phase, in the 24th revolution of the *ISO* satellite on 11 December 1995. The *ISO* satellite is described by Kessler et al. (1996). SWS and its observing templates are described by de Graauw et al. (1996). The observations used the SWS01 template: a spectral scan from 2.4 μm to 45 μm. The observations were done at the slowest speed, which reduces the spectral resolution to roughly half the nominal resolution of SWS. The spectra were reduced with the SWS Interactive Analysis software (pipeline V4.3) and were subsequently smoothed with a gaussian profile of a half-width corresponding to a resolving power of 800. The wavelength calibration and the flux calibration were done with the set of calibration files adopted as a standard for this issue of A&A letters. The wavelength calibration is discussed by Valentijn et al. (1996); the flux calibration by Schaeidt et al. (1996). The

Table 6.1 — *Comparison of the observed line fluxes in the SWS spectra of NGC 7027 and NGC 6543 with previous observations in the literature. Where appropriate 3σ upper limits are given.*

ion	λ	SWS	Lit.	ref
	(μm)	(10^{-14} W m^{-2})		
NGC 7027				
Brα	4.05	9.3	16.3	a
[Mg IV]	4.49	13.1	31.0	a
[Ar VI]	4.53	10.6	< 2.0	a
[Mg V]	5.61	34.3	56.0	a
Pfα	7.46	2.4	5.6	a
[Ne VI]	7.65	8.8	< 5.4	a
NGC 6543				
[Na III]	7.32	0.23		
[S IV]	10.51	29.3	43.0	b
[Ne III]	15.55	71.1	53.0	b
[O IV]	25.89	< 0.021	< 6.6	c

a) Beckwith et al. (1984), b) Pottasch et al. (1986), c) Shure et al. (1983).

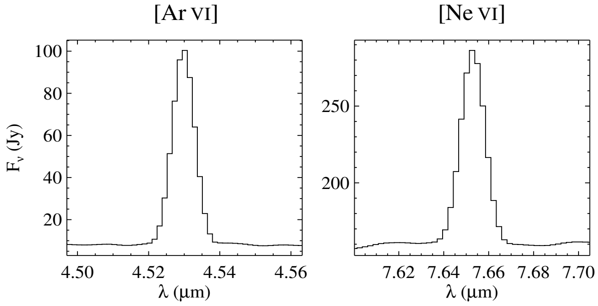

Figure 6.1 — *The observed [Ar VI] and [Ne VI] lines in the spectrum of NGC 7027.*

accuracy of the current flux calibration is estimated to be 30 %.

Especially the SWS spectrum of NGC 7027 is extremely rich. More than 100 emission lines were identified, down to a flux of 2×10^{-16} W m^{-2}. It is impossible to discuss or even present all these features. This will be postponed to a later publication. In this paper we report the first detection of the [Ar VI] 4.53 μm and the [Ne VI] 7.65 μm lines in the spectrum of NGC 7027. This makes Ne^{5+} the ion with the highest ionization potential observed in NGC 7027. In Table 6.1 the fluxes for these lines are compared with the 3σ upper limits determined by Beckwith et al. (1984; hereafter B84) based on KAO spectra obtained in June 1981. The SWS spectra are shown in Fig. 6.1. We can see that the SWS detections yield a higher flux than the upper limits given by B84. The first question to ask is whether flux could have been missed outside the aperture or if this discrepancy could be due to problems in the flux calibration in either of the spectra. The ionized part of NGC 7027 measures $9'' \times 13.5''$ based on the VLA 6 cm radio image of Masson (1989). This area fits completely in the aperture used by B84 (28$''$ circular) and the smallest SWS aperture ($14'' \times 20''$). However, in SWS observations pointing errors of up to 4$''$ may occur. The absence of wavelength shifts indicates that any errors larger than about 2$''$ could only have occurred along the slit (20$''$) and we estimate that signal losses due to mispointing are less than 5 %.

We also compared the fluxes of the four lines that were detected by B84 with the SWS fluxes (Table 6.1). The average ratio of the B84 fluxes over the SWS fluxes is 2.0$\pm$0.3. This might indicate a difference in flux calibration between the spectra. However, if anything, this would only exacerbate the discrepancy between the upper limits derived in 1981 and the detections in 1996. We therefore feel confident that at least the [Ar VI] line and probably also the [Ne VI] line have increased in strength over this period. We will discuss this further in Sect. 6.4.

We also report the non-detection of the [O IV] 25.9 μm line and the first detection of the [Na III] 7.32 μm line in the spectrum of NGC 6543. The upper limit for the [O IV] line derived from the SWS spectrum is much lower than was previously measured by Shure et al. (1983), as is shown in Table 6.1. The implications of this non-detection are discussed in Sect. 6.5.

6.3 The photo-ionization models

To model the planetary nebulae we used a modified version of the photo-ionization code CLOUDY 84.12a (Ferland 1993). We assumed that the central star has a blackbody spectrum; that the nebula is spherically symmetric; that the density is constant inside the Strömgren sphere of the nebula, and varies as $1/r^2$ outside; that the dust grains are intermixed with the gas at a constant dust-to-gas ratio and that the filling factor, describing the small scale clumpiness, is unity.

For NGC 7027 the following observations were added to the SWS spectrum to constrain the modeling. The ultraviolet and optical spectrum of NGC 7027 were taken from Middlemass (1990) together with the absolute Hβ flux. The distance to the nebula was taken from Pottasch (1996). The SWS spectrum of NGC 6543 was augmented with the ultraviolet spectrum from Middlemass et al. (1989) and the optical spectrum from Aller & Czyzak (1979). The absolute Hβ flux was taken from Acker et al. (1992) and the distance to the nebula from Van de Steene & Zijlstra (1994). Additionally also infrared continuum fluxes, radio fluxes and an angular diameter were used to constrain the models for both nebulae.

To derive the physical parameters of the planetary nebulae from these observables, we adjust the model parameters until an optimal fit to the observables is found. For this we calculate a goodness-of-fit estimator χ^2, which is minimized. A detailed discussion of the method is given in van Hoof & Van de Steene (1997).

Given the fact that in NGC 7027 the [Ar VI] and likely also the [Ne VI] line have increased in strength since 1981 one might expect that the optical and ultraviolet spectra have changed as well. To minimize the inconsistency we decided to omit the highest ionization levels from the older optical and UV spectra, because these are expected to be influenced most by an increase in stellar temperature.

For NGC 6543 we made two models. The input for both models was identical except that in model 2b a modified blackbody spectrum was used. This is discussed further in Sect. 6.5. It is well known that NGC 6543 has a very extended halo which contains most of the mass (Middlemass et al. 1989; Manchado & Pottasch 1989). However, the assumption of constant density inside the Strömgren sphere does not permit us to model this halo. Since the line flux is expected to be completely dominated by the core region, this poses no problem.

The results of the modeling are shown in Table 6.2. Most symbols have a commonly accepted meaning. Γ denotes the dust-to-gas mass ratio and ϵ the logarithmic abundance of an element (ϵ(H) $\equiv$ 12). The quoted number density of hydrogen is the value inside the Strömgren sphere. The electron temperature and density are averaged over the nebula.

Table 6.2 — *Parameters for the CLOUDY models of NGC 7027 and NGC 6543. Model 1 is for NGC 7027. Models 2a and 2b are for NGC 6543; these are identical except that different central star spectra were assumed. Abundances based on only one line are marked uncertain.*

	model 1	model 2a	model 2b
$T_{\rm eff}$/kK	161.4	42.3	58.1
L_*/L$_\odot$	6894.	5023.	3172.
$r_{\rm in}$/mpc	2.4	27.	26.
$r_{\rm str}$/mpc	22.	55.	52.
$r_{\rm out}$/mpc	345.	55.	52.
lg($n_{\rm H}$/cm^{-3})	4.49	3.56	3.60
$T_{\rm e}$/kK	16.13	9.36	7.57
lg($n_{\rm e}$/cm^{-3})	4.55	3.61	3.64
lg(Γ)	−2.52	−2.20	−2.06
$M_{\rm ion}$/M$_\odot$	0.058	0.085	0.070
$M_{\rm sh}$/M$_\odot$	2.10	0.085	0.070
ϵ(He)	10.98	11.11	10.94
ϵ(C)	8.87	8.50	8.96
ϵ(N)	8.12	7.65	8.10
ϵ(O)	8.65	8.44	9.09
ϵ(Ne)	7.79	7.81	8.13
ϵ(Na)	5.94	6.31:	5.82:
ϵ(Mg)	6.82		
ϵ(Al)	4.87:		
ϵ(Si)	6.90:	6.71:	6.39:
ϵ(S)	6.76	6.91	7.04
ϵ(Ar)	6.34	6.41	6.49
ϵ(Ca)	4.64:		
ϵ(Fe)	5.87		
D/pc	790.	1080.	1080.
χ^2	5.4	29.8	8.6

6.4 Discussion of the NGC 7027 results

Since infrared fine-structure lines are rather insensitive to electron temperature, the increase in strength of the [Ar VI] line must stem from a change in the ionization structure of the nebula. The ionization structure is the result of photoionization by the stellar radiation field and possibly also from shock heating due to the fast wind from the central star. Such a wind has never been observed for NGC 7027, therefore the presence of very strong shocks can be ruled out. Our model predicts that the [Ar VI] line is formed in a region ranging roughly from 6 mpc to 16 mpc from the central star. Based on the [Ar VI] line strength, an Einstein A coefficient of A = 0.0966 s^{-1} (Mendoza 1983) and assuming a relative upper level population of 1 % we can derive the minimum width of the line emitting region to be 1.7 mpc. Assuming 20 kK for the average electron temperature, the sonic travel time through the line emitting region would be > 70 yr, considerably longer than the 15 yr over which the spectrum changed. The electron temperature only enters as the square root in the sonic velocity, therefore it would have to be much higher than 20 kK to account for the discrepancy. This can be ruled out based on our models. Adding extra heating to the nebula (due to energy deposition by the stellar wind) equivalent to 10 % of all energy radiated by the central star would only double the electron temperature. Therefore we think that shocks are ruled out as the source of the variability in the spectrum.

By changing the parameters in our photo-ionization model we could assess that changes in the nebular density, inner radius and dust-to-gas ratio have little effect on the line-strength of the [Ar VI] line. An increase in the luminosity of the central star would increase the strength of all lines, which is not observed. Therefore the increased strength of the [Ar VI] line must in all likelihood be attributed to a change in the spectral energy distribution of the central star, possibly an increase in effective temperature. The nebula reacts rapidly to a hardening of the stellar spectrum. We calculated the typical timescale needed to ionize Ar^{4+} to be 0.2 yr.

When we change the stellar temperature in our photoionization model, we see that the strength of the [Ar VI] line indeed is sensitive to this parameter. However, in order to account for the large rise in strength of the [Ar VI] line an unrealistic large increase in the stellar temperature of roughly 60 kK to 100 kK is needed. Other lines show an increase in strength which is consistent with a more moderate increase in stellar temperature, or even with a decrease. These mixed results might be caused by calibration problems since the changes for these lines are much more moderate. The evidence gathered so far does favor a change in the spectral energy distribution of the central star, possibly an increase in the stellar temperature. However, more observations are needed to confirm this result.

6.5 Discussion of the NGC 6543 results

In Table 6.1 we reported a stringent upper limit for the strength of the [O IV] line in NGC 6543. This is not in contradiction with the detection of O IV 1342 Å P Cygni profile in the *IUE* spectrum of NGC 6543 since this UV line is formed in the wind coming from the central star, i.e. is formed much closer to the central star (Castor et al. 1981; hereafter CLS). We also report the detection of [S IV], [Ne III] and [Na III] emission. These detections, together with the upper limit, allow us to derive clear constraints on the shape of the central star spectrum. We will discuss this by starting off with a blackbody approximation, an assumption still often made in planetary nebula modeling.

The ionization threshold is 34.8 eV for S^{3+}, 41.0 eV for Ne^{2+}, 47.3 eV for Na^{2+} and 54.9 eV for O^{3+}. The presence of the [Na III] line indicates that sufficient photons with energies above 47.3 eV are present to produce appreciable amounts of Na^{2+}. When using a blackbody spectrum this makes it very likely that there are also enough photons to produce a significant amount of O^{3+}. The [O IV] line is expected to be a more sensitive tracer than the [Na III] line since the oxygen abundance is so much higher that, in all probability, it would more than make up for the lower transition probability of the [O IV] line. Therefore, if significant amounts of O^{3+} were present in the nebula, the [O IV] line should be clearly detectable. From its absence we conclude that the blackbody approximation can not be valid; the stellar flux must make a considerable drop at the He II limit.

This is also confirmed by our modeling. When we force the model to obey the upper limit on the [O IV] line when using a blackbody spectrum (model 2a), we see that the excitation of the model spectrum is much lower than what is observed (see Table 6.3). In general the fit is bad as is expressed by the high χ^2. The effective temperature is in good agreement with the measured H I Zanstra temperature of 47.0 kK (Kaler & Jacoby 1991). However, the predicted H I Zanstra temperature based on the model spectrum is 31.0 kK, much lower than observed.

We decided to test our hypothesis by modifying the blackbody spectrum such that beyond the H I limit the flux would be multiplied by a constant factor 0.40 and beyond the He II limit by an additional factor 10^{-5}. This resulted in model 2b. We can see that the overall fit of model 2b is much better and also that it has the right degree of excitation. The high oxygen abundance we find does not invalidate our model since the oxygen abundance in NGC 6543 is known to be high (Middlemass et al. 1989; Manchado & Pottasch 1989).

The effective temperature we find is higher than the upper limit for the stellar temperature derived by CLS. However, we argue that this upper limit is not valid. It is based on the He II Zanstra temperature derived from an upper limit for the nebular He II λ4686 emission. The Zanstra method makes the assumption of a blackbody stellar radiation field, which is clearly not valid. A stellar radiation field of any given effective temperature can satisfy the constraint on the nebular He II emission, provided that the flux in the He II Lyman continuum is low enough. This is also confirmed by our model. The predicted nebular He II λ1640 and λ4686 emission is 2.25×10^{-16} W m^{-2} and 2.46×10^{-17} W m^{-2} respectively, well within the restrictions imposed by CLS. The predicted H I Zanstra temperature based on the model spectrum is 41.6 kK, in agreement with the observations. The stellar temperature has also been derived by Lucy & Perinotto (1987). Their preferred value of 51.6 kK is higher than the value adopted by CLS, but still lower than the value we find. Our data point would fall to the left of the curve in their Fig. 2. The effective temperature is sensitive to the adopted multiplication factor at the H I limit. Since the nebular spectrum is not particularly sensitive to this factor, we decided to fix the value such that the predicted stellar *V* magnitude would coincide with the value from Castor et al. (1981).

Table 6.3 — *Comparison of the observed fluxes in NGC 6543 with model predictions.*

ion	λ	SWS	model 2a	model 2b
	(μm)	(10^{-14} W m^{-2})		
[S IV]	10.51	29.3	5.0	21.0
[Ne III]	15.55	71.1	26.0	71.2
[O IV]	25.89	< 0.021	0.027	0.0040

Photo-ionization modeling of the [O IV] line can prove to be a valuable test for predictions of stellar atmosphere models, since the results appear to be sensitive rather directly to the magnitude of the drop at the He II limit. This line is more suitable than the He II lines since there can be no ambiguity between stellar and nebular emission.

Using the parameters of model 2b we determined that the stellar flux drops at least by a factor 350 at the He II limit in order to obey the upper limit on the [O IV] line. In a future paper we hope to present a more stringent upper limit.

6.6 Conclusions

In this letter we reported the first detection of the [Ar VI] 4.53 μm and [Ne VI] 7.65 μm lines in the spectrum of NGC 7027. The strength of the [Ar VI] line and likely also the [Ne VI] line have increased since 1981. The most likely explanation for this variability is a change in the spectral energy distribution of the central star, possibly an increase in effective temperature. However, further observations are needed to confirm this result.

We also reported a non-detection of the [O IV] 25.9 μm line, and the first detection of the [Na III] 7.32 μm line in the spectrum of NGC 6543. The ionization energy needed to produce O^{3+} is just beyond the He II limit, and the absence of this line shows that the stellar flux drops at least by a factor 350 at the He II limit. Modeling the [O IV] line may prove to be a valuable test for atmosphere models.

Acknowledgments. We thank J.M. van der Hulst, P.R. Wesselius, G.C. Van de Steene and the referee M.J. Barlow for critically reading the manuscript. For this paper the photo-ionization code CLOUDY has been used, obtained from the University of Kentucky. PvH is supported by NFRA grant 782–372–033.

6.7 References

Acker A., Ochsenbein F., Stenholm B. et al., 1992, Strasbourg-ESO Catalogue of Galactic Planetary Nebulae, ESO, Garching
Aller L.H., Czyzak S.J., 1979, Ap&SS 62, 397
Beckwith S., Evans N.J. II, Natta A., Russell R.W., Wyant J., 1984, ApJ 277, 207 (B84)
Castor J.I., Lutz J.H., Seaton M.J., 1981, MNRAS 194, 547 (CLS)
de Graauw Th., Haser L.N., Beintema D.A. et al., 1996, A&A 315, L49
Ferland G.J., 1993, University of Kentucky Physics Department Internal Report
Kaler J.B., Jacoby G.H., 1991, ApJ 372, 215
Kessler M.F., Steinz J.A., Anderegg M.E. et al., 1996, A&A 315, L27
Lucy L.B., Perinotto M., 1987, A&A 188, 125
Manchado A., Pottasch S.R., 1989, A&A 222, 219
Masson C.R., 1989, ApJ 336, 294
Mendoza C., 1983, IAU Symp. 103, Ed. Flower D.R., Reidel, Dordrecht, p. 143
Middlemass D., 1990, MNRAS 244, 294
Middlemass D., Clegg R.E.S., Walsh J.R., 1989 MNRAS 239, 1
Pottasch S.R., 1996, A&A 307, 561
Pottasch S.R., Preite-Martinez A., Olnon F.M., Mo J.-E., Kingma S., 1986 A&A 161, 363
Schaeidt S.G., Morris P.W., Salama A. et al., 1996, A&A 315, L55
Shure M.A., Herter T., Houck J.R. et al., 1983, ApJ 270, 645
Valentijn E.A., Feuchtgruber H., Kester D.J.M. et al., 1996, A&A 315, L60
Van de Steene G.C., Zijlstra A.A., 1994, A&AS 108, 485
van Hoof P.A.M., Van de Steene G.C., 1997, submitted to A&A (Chapter 2)

7 Conclusions and outlook

7.1 Conclusions

In this thesis a new method is presented to determine the physical parameters of an emission line nebula in a fully self-consistent way. This method is based on the photo-ionization code CLOUDY, which was altered for this purpose. Part of these alterations were aimed at making the code more suitable for infrared predictions. This was done so that the method could be used for analyzing infrared spectra taken with *ISO*, although use of the method is not limited to analyzing only these spectra. In Chapter 2 the details of the method are presented, while the alterations to the code are described in Chapter 8.

Before the method could be applied to any real data, several tests had to be performed to assess the correctness of the method and the accuracy of its results. First, a formal convergence test was performed on an artificial set of 'observations' and it is shown that it is possible to reproduce all physical parameters with this method. Next, the effect of observational uncertainties on the derived physical parameters was studied. This way it could be shown that all the important physical parameters could be reproduced with good accuracy, i.e. their determination was stable against observational error. It could also be shown that photo-ionization models are less sensitive to noise in the optical spectrum than classical line diagnostics when determining the electron temperature, electron density and the abundances.

The biggest disadvantage of photo-ionization modeling is that various assumptions have to be made for the physical model of the nebula. These assumptions, by necessity, are sometimes very simplistic and involve parameters which are difficult or even impossible to measure. Inevitably, the model assumptions will have an effect on the derived physical parameters, and an attempt was made to investigate these effects. They were found to be different from what is commonly expected. The most critical are the assumed stellar spectrum and the assumption that the inner radius of the dust is the same as the inner radius of the gas. Modeling bipolar nebulae can also lead to less accurate results, especially if the polar regions are optically thin in the Lyman continuum. Also important, but only for the distance dependent parameters, is the assumed distance itself. Deviations from the density structure used in the modeling were not found to be very influential, provided that the real density structure still is spherically symmetric. The determination of the stellar and electron temperature by our method was found to be very robust in all circumstances. Line diagnostics assume only constant electron temperature and density. The dependency on the electron density of these methods is usually quite weak and hence they suffer much less from the effects described above. The major uncertainties in determining abundances with line diagnostics are the lesser accuracy of the electron temperature derived from line diagnostics and the uncertainty in correcting ionic abundances for unobserved ionization stages. In favorable circumstances, the correction factors can be very small and it is thus not *a priori* clear that photo-ionization modeling yields more accurate abundances than line diagnostics. This can only be the case when care is taken that the model assumptions are appropriate for the nebula being modeled.

In an early phase of this work an experiment was conducted where the distance was kept as a free parameter. This resulted in models where the accuracy depended very critically on the angular diameter. This dependence was considered unacceptable and this way of modeling data was later abandoned. From this we can learn that the modeling assumptions, the number of free parameters and the set of observables have to be carefully tuned to get the most stable method. More investigation into this is certainly needed. Minimization algorithms which yield a covariance matrix might prove very helpful in this respect.

The method has been applied to a sample of five galactic bulge planetary nebulae (PNe). Comparison of these and other, published, results shows that the stellar temperatures are generally in fair agreement but that there is a large spread in the electron temperatures, electron densities and the nebular abundances, even when the same method was applied. This clearly shows the need for more accurate methods.

Our conclusion is that our method for making photo-ionization models works, provided that ample observational data of good quality are available and that sufficient emission lines of various ionization stages are observed in the spectrum. Where possible, particular care should be taken to make the model assumptions as realistic as possible.

In view of the importance of an accurate determination of the angular diameter, an investigation has been conducted into one of the methods used for this purpose. When the observed nebula is only partly resolved, often a technique called 'gaussian deconvolution' is used. It was found that this technique was only weakly founded in theory. The technique uses a conversion factor to convert the deconvolved FWHM of the nebula into the true diameter. In Chapter 3 a complete description is given of the necessary theory to calculate conversion factors for the case where both the nebula and the beam are circularly symmetric. It was already known that this conversion factor depends on the (assumed) intrinsic surface brightness profile and on the beam size of the observation when gaussian fits are used. In this thesis the following additional conclusions were reached. First, in the case when second moments are used, the conversion factor is different from the conversion factor when gaussian fits are used. When second moments are used, the conversion factor is *independent* of beam size, but does depend on the assumed surface brightness profile. Second, the conversion factor is very sensitive to optical depth effects, so care should be taken when comparing angular diameters determined at different wavelengths. Also, for optical observations the conversion factor depends on the chosen emission line. In all cases differences of several tens of percent are possible. Third, nebulae which have a power law drop-off in their density distribution usually have a 'fuzzy' edge and the Strömgren radius will be situated in the faint surface brightness regions of the nebula. For such nebulae the conversion factor can become very large and is a very sensitive function of the assumed geometry of the nebula. Since this geometry can not be assessed accurately in general, it is not meaningful to apply a conversion factor in such cases.

The method to analyze nebular spectra presented in Chapter 2 has been applied several times. Three of these applications are described in this thesis. First, in Chapter 5 the first radio continuum detection of a planetary nebula in the LMC is presented. The object, which contains a [WC] star, was also detected by *IRAS*. It is shown that all *IRAS*-detected PNe in the LMC are likely to be young objects. The PN was also compared to [WC]-type objects in the galaxy, and it is found that the LMC object has much bluer *IRAS* colors than its galactic counterparts. The preferred explanation is that its circumstellar envelope is more compact due to a lower expansion velocity, caused by a lower metallicity. This is supported by photo-ionization modeling of the spectrum of SMP 58. Other possible explanations however can not be ruled out completely.

In Chapter 6 we report the first detection of the [Ar VI] 4.53 μm and [Ne VI] 7.65 μm lines in the *SWS* spectrum of NGC 7027. The strengths of the [Ar VI] line and probably also the [Ne VI] line have increased since 1981. The most likely explanation for this variability is a change in the spectral energy distribution of the central star, possibly due to an increase in effective temperature. However, further observations are needed to confirm this result.

In Chapter 6 the non-detection of the [O IV] 25.9 μm line is reported in the *SWS* spectrum of NGC 6543. The ionization energy needed to produce O^{3+} is just beyond the He II Lyman limit, and the absence of this line shows that the stellar flux drops at least by a factor 350 at the He II limit. Hence modeling the [O IV] line may prove to be a valuable test for atmosphere models.

These three examples show how photo-ionization models can be useful for individual studies of nebulae. They allow new insights into the various physical processes that operate in the nebulae. Hence photo-ionization modeling can be instrumental in deepening our knowledge of post-AGB evolution. CLOUDY can also be used for a different approach of the same problem, where theoretical predictions for post-AGB evolution are used as the starting point, instead of observations. In Chapter 4 such an approach is taken and new calculations of the spectral evolution of a hydrogen burning post-AGB star are presented. The intention of these calculations is to deepen our understanding of the implications that the assumptions in the theoretical predictions have on the observed infrared spectra of the nebulae. Hopefully this will lead to a better understanding of the observations, which in turn can lead to more realistic assumptions for the theoretical predictions. The main new ingredient of the calculations in Chapter 4 was the possibility of extracting timescales for the post-AGB central star evolution from the most recent evolutionary calculations. Contrary to previous studies, this allowed the investigation of other AGB and/or post-AGB mass loss rates and different prescriptions for the start of the post-AGB phase. The fact that a dust code is built into CLOUDY, gave the opportunity to study the evolution of the infrared emission of the circumstellar material.

The evolutionary calculations for hydrogen burning post-AGB stars show that the evolutionary rate is very dependent on the assumed mass loss rate as a function of time. This effect was investigated by modifying the mass loss prescription. The newly calculated evolutionary rates and density distributions were used to model the spectral evolution of a post-AGB star, where dust absorption and emission were included in the radiative transfer. Different assumptions for the dust properties and dust formation were considered. It was shown that by varying these parameters in a reasonable way, entirely different paths were followed in the *IRAS* color-color diagram. First of all, the effects of the evolution of the central star on the expanding dust shell could not be neglected. Also the dust properties and the definition of the end of the AGB phase had an important effect. The possible presence of hot dust due to dust formation in the post-AGB wind could have considerable influence on the *IRAS* colors as well. The model tracks showed that objects occupying the same location in the *IRAS* color-color diagram can have a different evolutionary past, and therefore the position in the *IRAS* color-color diagram alone can not *a priori* give a unique determination of the evolutionary status of an object. This is certainly part of the explanation why planetary nebulae do not occupy a well-structured region in the *IRAS* color-color diagram. An alternative color-color diagram, the *K*–[12] vs. [12]–[25] diagram, was introduced. The tracks in this diagram appear to be less affected by the particulars of the grain emission. This diagram may be a valuable additional tool for studying post-AGB evolution, e.g. it may provide additional selection criteria which would make the search for new post-AGB stars more efficient.

7.2 Outlook

In this thesis several studies have been presented which are aimed at giving a more solid foundation to certain aspects of the analysis and interpretation of observations of emission line nebulae. Ultimately, all studies presented here, either directly or indirectly, intend to increase our knowledge of post-AGB evolution. This is a vast field of study and this thesis can only be viewed as a small step towards achieving the goal of understanding this evolution. Many groups around the world are currently working on this problem and it would be simply too much to try and describe all the work they are currently undertaking. So in this outlook I will limit myself to the work in which I am involved, be it in the center or in the periphery.

In Chapter 2 a new method has been presented to analyze spectra of emission line nebulae. This method was subsequently used to study the propagation of errors from the observations to the model parameters. In principle this study is only valid for the particular set of artificial 'observations' that was used. Although it can be expected that these results are valid in a more general context, it is also clear that there must be certain limits to that validity. This needs to be studied further. However, an analysis of the type presented in Chapter 2 is very cumbersome and certainly not suitable for routine application. Hence new ways of studying the error propagation are needed. In Chapter 8, the new optimization algorithm PHYMIR was briefly mentioned, which was primarily developed for making optimum use of the computing power on parallel computers. This algorithm might also be extended in order to yield the Hessian matrix and ultimately the covariance matrix of the χ^2 function. These matrices can be used to speed up the convergence and, more importantly, to study the error propagation. Currently no optimizing algorithm is available which is able to yield a covariance matrix when the derivatives of the fitting function are *not* available, as is the case when fitting a numerical model to observed data. Hence, developing such an algorithm would have an impact far beyond the scope described here.

Another fundamental problem hampering the interpretation of observations is the alleged presence of electron temperature fluctuations in the ionized regions of both PN and H II regions. In PN research this problem is commonly known as the t^2-problem and it can severely affect e.g. abundance determinations. Theory does not predict the presence of such fluctuations, but certain observations indicate the possibility that they exist. An observational programme has been started to search for the possible presence of these fluctuations. Where possible, this programme should be combined with a search for the explanation of the discrepancy between abundances derived from recombination lines and collisionally excited lines. Most planetary nebulae are point sources for *ISO*, hence also an H II region was chosen to be studied. This nebula has an extent which is large enough that even with *ISO* spatially resolved spectroscopy can be obtained.

In a research proposed by Dr. S.R. Pottasch an investigation has been started to study the central star temperatures of high excitation PN by observing specific lines, belonging to high ionization stages, with *SWS*. These data will hopefully yield more accurate stellar temperatures for the hottest, and therefore probably also the most massive central stars.

A line of research which is very much related has been proposed by Dr. G.J. Ferland. In certain nebulae, especially bipolar type I nebulae, high velocity outflows are observed. These outflows produce shocks and heat certain parts of the nebula to X-ray temperatures. Interaction of this X-ray emitting gas with cooler parts of the nebula could raise the level of excitation beyond what would be expected based on the stellar spectrum alone. Identification of this mechanism would be important to study the t^2-problem mentioned above, but would also be important to obtain more accurate central star temperatures for these objects and to find their true place in the HR diagram.

In Chapter 1 it has already been argued that the AGB mass loss history can best be traced in very young post-AGB stars, before the fast post-AGB wind alters the structure of the nebula. Only few genuine post-AGB stars and very young PN are known to date and more need to be identified to get a better sample to study these processes. In a collaboration with Dr. G.C. Van de Steene we think that we have identified such a sample. We are currently observing this sample to establish the exact evolutionary status of the objects. In the future we want to give high priority to further study of this very interesting sample. Our first priority will be to establish the stellar temperature and luminosity class of all objects. After their post-AGB nature has been established, we wish to start studying the AGB ejecta, first of all the dust characteristics and the morphology. Also we would like to reconstruct the evolutionary past of the objects and establish whether there is an evolutionary connection between the various types of objects in our sample.

Additionally, we want to monitor our sample for possible evolutionary changes.

In Chapter 4 we proposed a new near-infrared color-color diagram to study post-AGB stars: the K–[12] vs. [12]–[25] diagram. We would like to investigate this diagram further and see how the post-AGB sample described above fits into this diagram.

In the phase prior to the launch of *ISO*, a comprehensive list of infrared allowed and forbidden atomic transitions has been compiled. Hopefully, in the near future this list will be updated, enlarged and combined with transition probabilities to make it even more versatile.

Hopefully these projects will lead to more accurate determinations of basic stellar and nebular parameters, a better understanding of their accuracy and ultimately to a better understanding of post-AGB evolution, post-AGB mass loss and the formation and shaping of planetary nebulae. These new insights will be needed for studies of galaxies and galaxy evolution. Post-AGB objects are important for understanding the chemical evolution of galaxies, especially of the lighter elements like carbon, nitrogen and oxygen. Furthermore, the luminosity function of planetary nebulae is used as a distance indicator for galaxies. Planetary nebulae are also important for understanding the ultraviolet spectrum of galaxies. They might even be useful in constraining the initial mass function at earlier epochs of the evolution of a galaxy, although this possibility seems very remote at the moment.

Appendix

8 Changes to cloudy

Implementation

P.A.M. van Hoof

Abstract — In this chapter a full description of the new or changed commands in CLOUDY will be given. Also the changes to the output will be described and a full list of the emission lines that were added will be given. It is assumed that the reader is familiar with HAZY, the original documentation of CLOUDY written by Gary Ferland.

8.1 New and changed cloudy commands

In the following sections a structure will be used which adheres as much as possible to the structure of the original documentation HAZY, i.e. first the new and changed commands will be described, then the changes to the output of CLOUDY will be described and finally all the emission lines that have been added to the code will be listed.

distance 21.85 [linear; parsec; vary]

You can supply the distance between the object and the observer to CLOUDY. This distance is used to normalize the flux emitted by the object at the earth's distance and to calculate the angular diameter. The number supplied should be the logarithm of the distance in centimeter. If the keyword PARSEC appears on the line, the number will be interpreted as the logarithm of the distance in parsec. If the keyword LINEAR appears, the number will be taken to be linear. The default distance is 1 kpc.

The distance can be varied by the optimizer if the keyword VARY appears on the line. Note that this only makes sense if distant dependent observables are supplied (like absolute fluxes or the angular diameter).

dlaw 3.80 −2 [vary]

This command allows you to define a special density law: the density is assumed to be constant inside the Strömgren radius, and the density will change according to an r^{α}-law outside the Strömgren radius. You need to supply two numbers: the logarithm of the number density per centimeter cubed in the constant density part, and the exponent α. Note that the two sections of the density law will be joined continuously at the Strömgren radius.

An optional keyword can be supplied to vary the density (i.e. the first number on the input line).

dtable [use full range]

This command allows you to supply an arbitrary density law in a separate file. This file should have the name `dens_law`. It should consist of an arbitrary number of lines (not more than 1000) each containing two numbers: the logarithm of the radius in centimeter and the logarithm of the number density per centimeter cubed. CLOUDY will determine the density at each radius by linear interpolation in this array. If an attempt is made to use a radius which is outside the range supplied in `dens_law`, a caution will be given in the output. The density at the nearest edge of the supplied range will be used. The radii supplied in `dens_law` should be strictly monotonically increasing.

If the keyword FULL appears on the line, the inner and outer radius of the nebula will be set to the complete range for which the density law is defined. This keyword can be used instead of the RADIUS command. A RADIUS command given further on in the input file will overrule the settings from this keyword.

element helium, carbon, . . . 11.02 [vary]

This command allows you to set the abundance of a single element, by giving it's usual name and the standard logarithmic notation for the abundance ($\epsilon(\mathrm{H}) \equiv 12$). This command also allows you to vary the abundances for each element separately.

flunit herz, jansky, nuFnu, . . . [at earth distance].

With this command you can change the unit and the normalization of the continuum flux in the PLOT CONTINUUM and the PLOT EXTENDED SPECTRUM commands.

If the keyword EARTH appears on the line then the fluxes will be normalized at the earth's distance (or the default 1 kpc), otherwise at the inner radius of the nebula. If one of the keywords HERZ, HZ, CM-1 or JANSKY appears on the line, F_ν will be given in units of $\mathrm{erg\,cm^{-2}\,s^{-1}\,Hz^{-1}}$, $\mathrm{erg\,cm^{-2}\,s^{-1}\,(cm^{-1})^{-1}}$ or in jansky. Default is to give F_ν in units of $\mathrm{erg\,cm^{-2}\,s^{-1}\,Ryd^{-1}}$. If one of the keywords MICRON or ANGSTROM appears on the line, F_λ will be given in units of $\mathrm{erg\,cm^{-2}\,s^{-1}\,\mu m^{-1}}$ or $\mathrm{erg\,cm^{-2}\,s^{-1}\,Å^{-1}}$. If the keyword NUFNU or LAFLA appears on the line, νF_ν or λF_λ will be plotted in units of $\mathrm{erg\,cm^{-2}\,s^{-1}}$.

frunit Rydberg, Hz, micron, . . .

If you use the plot command to plot some quantity as a function of energy (or wavelength, or frequency) you can choose your preferred axis unit with this command. The possibilities are: RYDBERG, HZ or HERZ, CM–1, EV, ERG, MICRON, NM or NANOMETER and ANGSTROM.

grains [0.2; planetary, . . . ; _log; vary; . . .]

It is now possible to optimize the dust to gas ratio by adding the keyword VARY on the input line. For this the syntax of the command had to be extended slightly. If somewhere on the line the keyword _LOG appears, the number will always be interpreted as a logarithm no matter what the sign of this number is. The rest of the syntax of this command is kept fully compatible with the original command.

minimum electron temperature [10 K]

If you want to calculate a model of a nebula containing dust, and you want to get the far-IR continuum right, you need to integrate deep into the neutral zone of the nebula. Only there will the temperature of the dust drop to low enough values (say less than roughly 25 K), that the contribution of the dust emission to the total continuum will be negligible. The dust and the electron gas are usually not in temperature equilibrium in these regions. The electron gas will have lower temperatures than the dust, and the electron temperature can drop well below 10 K. For such low temperatures CLOUDY is not numerically stable anymore and can easily crash. You can solve this problem by using the MINIMUM ELECTRON TEMPERATURE command. This will cause the code to force the electron temperature to the prescribed minimum value, once it tries to drop below this. A value of 10 K is probably a good choice and is also the standard value.

Since the electron temperature will be forced to a higher than equilibrium value, there will be a heating-cooling mismatch in each zone were this command is effective. If there are sufficient of such zones present in the model, this will cause the overall heating and cooling for the model to be mismatched as well. CLOUDY will inform you about this. Usually this will not be a problem, you should however check if the discrepancy between heating and cooling is small with respect to the total energy emitted.

optimize amoeba

This command already existed in the original version of CLOUDY. However, since AMOEBA was the standard optimizing algorithm in the original version, it had no effect. In the modified version of CLOUDY however, the standard optimizing algorithm is PHYMIR. Hence, if one wants to use the AMOEBA algorithm, this command is compulsory now.

optimize angular diameter [<] 12′′ [error 0.20]

It is possible to add an angular diameter in arcseconds to the list of observables. The program can try to optimize the distance and/or the radius of the nebula to reproduce this angular diameter. The radius of the nebula is defined as the Strömgren radius (i.e. this method is valid for diameters observed in radiation coming from the ionized part of the gas such as radio emission). The Strömgren radius is defined as the radius where the electron density drops below 10 % of the hydrogen density, or the outer edge of the nebula for density bounded nebulae. The error in the angular diameter is a linear relative fraction. It is also possible to supply an upper limit for the angular diameter.

optimize color temperature [<] 173 K [error 0.10]

With this command you can supply the color temperature of the dust continuum (e.g. obtained from a blackbody fit to the *IRAS* fluxes). The value needs to be a linear number in kelvin. The error is a linear relative fraction. It is also possible to supply an upper limit for the color temperature.

optimize continue

When using AMOEBA to optimize certain parameters, every couple of iterations the code will write a continue file which contains all information needed to restart from where the code is at that moment. When an optimization run stops this file can be used to restart the optimization process. All you need to do is:

1. include the command OPTIMIZE CONTINUE in the input file
2. edit other lines in the input file as needed, e.g. increase the maximum number of iterations in the OPTIMIZE ITERATIONS command. The initial values for the parameters to be varied in the input file need not be changed, they are ignored
3. make sure the continue file `fort.9` or `ftn09` is in place
4. start the run like any other run

As an alternative you can also use the macro CNTCL to execute these steps.

optimize far-infrared flux [<] 53.2 [error 0.10]

This command allows you to optimize the total infrared flux, normalized at the earth's distance, e.g. as determined from a blackbody fit to the *IRAS* fluxes. The distance to the earth is set by the DISTANCE command. The value should be entered as a linear number in units of 10^{-13} W m^{-2}. The error is a linear relative fraction. The total infrared flux is calculated as the integral from 1 μm to 300 μm over the emitted continuum of the nebula and includes internal extinction effects. Line emission in this wavelength region is not included in the integral. It is also possible to supply an upper limit for the total infrared flux.

This command, combined with the OPTIMIZE COLOR TEMPERATURE command, allows you to use an alternative for fitting the individual *IRAS* fluxes. Optimizing the latter sometimes causes problems when the abundances are varied. Since line contribution is included in the individual *IRAS* bands, the optimizing routine has two ways to achieve a better fit to the *IRAS* fluxes: by changing the continuum and by changing the line contribution through changing the abundances. The latter approach can lead to unrealistically high abundances. There is no way to control this behavior except by putting a stringent upper limit to the abundances, which is probably not what you want. In such cases, this command can be used as an alternative. Another alternative is to use the OPTIMIZE FLUX command. In this case the quoted fluxes in the *IRAS* bands should be converted into continuum fluxes using the appropriate color correction factors. This way the implicit assumption is made that the contribution of the line emission to these fluxes is negligible. At this moment it is not clear which approach is the best one.

optimize flux 3 _cm_ [<] 0.84 _mJy [error 0.15]

It is possible to optimize continuum fluxes at any wavelength within the extended range that is computed by CLOUDY (i.e. radio wavelengths are allowed). The wavelength should be linear and can be given in the units _CM_, MICRON, _NM_ or ANGSTROM. The fluxes should also be linear and can be given in _MJY, _JY_ or JANSKY. They are always assumed to be normalized at the earth's distance. The error is a linear relative fraction. It is also possible to supply an upper limit for the flux.

optimize intensity – 12.20 [error 0.15]

This optimize command now computes and compares the flux of the reference line (usually Hβ) at the earth's distance instead of the inner radius of the nebula. The value should be the logarithm of the flux in units of erg cm^{-2} s^{-1}. The flux should be dereddened. The error is a linear relative fraction.

optimize lines
IRAS 60 [<] 23.00 linear jansky [error 0.10]

The limit on the maximum number of lines that you can supply has been increased from 100 to 200.

It is possible to add broadband photometry to the list of observed line intensities. You can supply the photometric flux in magnitudes (if the keyword _MAG appears on the line) or in jansky (if the keyword JANSKY appears). If the keyword JANSKY is used the number will be interpreted as a logarithm unless the keyword LINEAR is used. The syntax of the input line, apart from the keywords _MAG, JANSKY and LINEAR, is identical to the syntax for supplying an observed emission line ratio. The conversion between magnitudes and fluxes is defined such that the flux will be equal to the monochromatic flux at the effective wavelength of the filter pass band for a spectrum $F_\nu \sim \nu^{-1}$. The error is a linear relative fraction. It is also possible to supply an upper limit for the flux.

The list of supported photometric bands can be found in Table 8.1. Note that the fluxes are normalized at the earth's distance (or the default 1 kpc).

Table 8.1 — *List of the supported photometric systems.*

name		description	name		description
gnU	3464	Geneva *U*	JoL1	354	Johnson *L1*
gnB	4227	Geneva *B*	JoL2	344	Johnson *L2*
gnV	5488	Geneva *V*	Jo M	503	Johnson *M*
gnB1	4015	Geneva *B1*	Jo N	1067	Johnson *N*
gnB2	4476	Geneva *B2*			
gnV1	5395	Geneva *V1*	Be U	3764	Bessell *U*
gnG	5807	Geneva *G*	Be B	4416	Bessell *B*
			Be V	5505	Bessell *V*
st u	3451	Strömgren *u*	Be R	6395	Bessell *R*
st v	4108	Strömgren *v*	Be I	7854	Bessell *I*
st b	4671	Strömgren *b*	esJ	129	ESO *J*
st y	5477	Strömgren *y*	esH	165	ESO *H*
			esK	220	ESO *K*
Jo U	3574	Johnson *U*	esL'	381	ESO *L'*
Jo B	4466	Johnson *B*			
Jo V	5553	Johnson *V*	IRAS	12	*IRAS* 12 μm
Jo R	6939	Johnson *R*	IRAS	25	*IRAS* 25 μm
Jo I	8780	Johnson *I*	IRAS	60	*IRAS* 60 μm
Jo J	125	Johnson *J*	IRAS	100	*IRAS* 100 μm
Jo K	220	Johnson *K*			

optimize phymir

With this command you can use the new parallel optimization algorithm, especially designed for the Cray or other multi-processor computers. This algorithm is currently the standard, so this command does not have any real effect.

optimize tolerance 0.02

With this command it is possible to set the accuracy with which you want to determine the model parameters when optimizing. The number entered is the accuracy in dex in the logarithm of the parameter.

The algorithm will try to find a minimum within the requested accuracy (which is reached when the biggest dimension of the search area is smaller than the requested accuracy). It will then try to check if this minimum really is the correct minimum. If it fails this test, the search process will be restarted, otherwise the final model will be printed.

plot opacity, . . .

The plot commands present in the standard release of CLOUDY (which give lineprinter plots) have been deleted. Instead a whole series of new plot commands aimed for use with the IDL routine PLC have been added. The total list of possible plot commands follows closely the list of punch commands. Some punch commands have no equivalent plot command because it would not be useful and some punch commands have been slightly altered (most notably the PLOT *element* OPACITY command will not terminate the program). The total list of plot keywords can be found in Table 8.2. For a description of the new plot command PLOT EXTENDED SPECTRUM, see below under the header PUNCH EXTENDED SPECTRUM. A combined maximum of ten plot and/or punch commands is permitted for each run.

print verbose, punch continuum verbose

When CLOUDY calculates a single model, it usually requires several iterations to reach the final model (see the ITERATE command). In the standard release of CLOUDY, printing, punching and plotting is done on each of these iterations, unless specified differently (e.g. with the PRINT LAST command).

In the current installation this situation has been reversed. The default is to give output only for the final iteration. You can change this by giving the command PRINT VERBOSE. You can combine this command with other print commands (e.g. PRINT EVERY 10 VERBOSE). For punching you must combine the keyword VERBOSE with some command, e.g. PUNCH CONTINUUM VERBOSE. Note that this keyword acts for punching and plotting commands simultaneously. It should also be noted that with this keyword the resulting output for plot commands can not be processed with the standard macros to produce a plot file.

punch emissivity unit=20 freq=0.00452 Ryd

This command will write the volume emissivity j_ν and the absorption coefficient κ_ν as a function of radius for the computed model. The frequency should be a linear number in Rydberg, and can take any value within the extended frequency range of CLOUDY (i.e. it may also be in the radio continuum). At the moment it is unfortunately mandatory that the logical unit number is specified before the frequency. This requirement may be relieved in the future. The output of this command can be used for any external code solving the radiative transport equation, e.g. to obtain a two-dimensional solution.

The first line in the punch file is a comment line, stating the requested frequency. The second line gives the inner radius of the nebula in cm and the stellar flux in Ryd $\mathrm{cm^{-2}\,s^{-1}\,Ryd^{-1}}$ normalized at the inner radius. From the third line onwards each line gives the radius of the center of the zone in centimeter, the volume emissivity in Ryd $\mathrm{cm^{-3}\,s^{-1}\,Ryd^{-1}}$ and the absorption coefficient in $\mathrm{cm^{-1}}$ for each zone of the model. The last line of the punch file gives the Strömgren radius in centimeter, the total optical depth at the requested frequency (from the center of the nebula to the outer edge), and the distance of the nebula in centimeter.

punch extended spectrum [jansky]

This additional punch command will punch the flux of the extended continuum in erg $\mathrm{cm^{-2}\,s^{-1}\,Hz^{-1}}$ normalized at the inner radius of the cloud. The frequency will be given in Rydberg. When the corresponding plot command is used, the flux unit can be chosen with the FLUNIT command, and the frequency unit with the FRUNIT command. Additionally, the volume emissivity (in photons $\mathrm{cm^{-3}\,Ryd^{-1}}$), the absorption coefficients (in $\mathrm{cm^{-1}}$) and the source function (in photons $\mathrm{cm^{-2}\,Ryd^{-1}}$) will be given. These quantities pertain to the outermost zone. The fifth quantity that will be given is the total optical depth as function of frequency (from the center of the nebula to the outer edge). The extended continuum is the normal continuum calculated by CLOUDY combined with the radio continuum. It extends out to a wavelength of 3.04 m, instead of the 0.911 cm used in the standard release.

rfac 3. vary

This command is an addition to the RADIUS command. The number on the line is the ratio of the outer to the inner radius. The number is interpreted as a logarithm when ≤ 1 or when the keyword _LOG is present, else as a linear quantity. Values ≤ 0 are illegal.

The ratio can be varied if the keyword VARY appears on the line. This then gives you the possibility to optimize both the inner and outer radius of a shell, if you use this command together with the RADIUS . . . VARY command. Other combinations are also possible, e.g. to vary the inner radius while keeping the ratio of the outer to inner radius fixed.

runit parsec, cm, A_V

With this command you can set the unit for the radius in a plot. Default is to use centimeters. If the keyword PARSEC or PC occurs on the line, then parsecs will be used. If the keyword ARCSEC occurs on the line, then arcseconds will be used. This is only meaningful when the distance is set with the DISTANCE command. If the keyword A_V is used, then $A_{\rm V}$ will be used instead of the radius. This choice has the additional side-effect that the radius will be plotted against $A_{\rm V}$, instead of the reverse in the PLOT _PDR command.

set drmax 0.01 relative

This command is a variation of the standard SET DRMAX command. It allows you to specify the maximum zone thickness as a fraction of the current radius. This makes

Table 8.2 — *List of the plot commands. The first column gives the name of the plot command. The second column gives the quantities that are being plotted.*

keyword	plotted quantities
opacity	albedo; total, absorption and scattering opacity
grain opacity	albedo; total, absorption and scattering opacity (grains only)
carbon,... opacity	photo-ionization cross section for an arbitrary element heavier than helium
hydrogen,...	ionization structure for an arbitrary element
compton	Compton heating and cooling
continuum	incident, attenuated incident, diffuse, transmitted, reflected
extended spectrum	continuum, emis. & abs. coefficient, source function, opt. depth
gaunt factors	free-free Gaunt factors for hydrogen and helium
grain physics	temperature, potential, drift velocity per species; tot. heating, cooling
line structure	volume emissivity for requested lines
line cumulative [relative]	integrated line strength [relative to norm line] for requested lines
Lyman alpha	optical depth, level population, excitation temp, electron temp
_map	total heating and cooling as function of electron temperature
molecules	relative molecule density
optical depths	total, absorption, reflection optical depths
_ots continua	flux, otscon, otslin, outcon
_pdr	photo-dissociation region physics
physical conditions	electron temp, hydrogen dens, electron dens, heating, acceleration
pressure	gas, line, continuum pressure
_qs	absorption and scattering efficiency for grains
radius	radius, zone thickness as function of zone number
recombination efficiency	τ_{912}, recombination efficiency to H(n=1), loss probability
source function	emission, absorption coefficient, source function, Planck ratio
temperature	electron temperature, gradient of electron temperature
wind structure	velocity, acceleration, force multiplier

the command also useful for very thick nebulae, since the maximum zone thickness will increase as the code moves through the nebula. The fraction should be given as a linear number. Values ≤ 0 and ≥ 1 are forbidden. This command is recommended when doing optimizer runs. The value of 0.01 given above should normally be a good choice.

silent

With this command all intermediate output of the optimizer is disabled, i.e. only the initial messages and the final model are displayed. This is useful for preventing very large output files which might not fit on your disk.

single iteration

If you are doing optimizer runs, you are sometimes interested in doing single iterations by hand. If this command appears somewhere in the input file, the run will be started just like a normal optimizer run but will be stopped after just one iteration. It differs from the NO VARY command in that the χ^2 section of the output will be printed.

stop flux at 5.9 _cm_ 93 _mJy

This command will cause the model to stop once a prescribed continuum flux is reached. The syntax for supplying the wavelength and flux is identical to the syntax for the OPTIMIZE FLUX command. See also the comments given under the header STOP PHOTOMETRY.

stop [ionized] mass 0.2 [solar]

This command will cause the model to stop once a prescribed ionized or total shell mass is reached. If the keyword SOLAR is present the mass should be given as a linear number in solar units, else the mass should be given as a logarithmic number in atomic units.

stop photometry IRAS 60 23.56 Jy [−2.32 magnitude]

This command will cause the model to stop once a prescribed flux in a certain photometric band is reached. You need to supply the flux as a linear number in jansky or, if the keyword MAGN is present, as a magnitude. You can use this command to determine the extent of the neutral zone, which usually can't be obtained directly from observations. Since the far-IR flux predominantly comes from the neutral region, a photometric band in this wavelength region like *IRAS* 60 μm or 100 μm would be suitable.

sublimation radius 17.25

When you calculate a model where the gas and dust is situated very close to the central star, this can result in the dust temperature to be unphysically high at the inner edge of the nebula. The code will complain about this, but will nevertheless include the emission from that dust in the emitted spectrum. You can prevent this by setting a separate inner radius for the dust shell. The number you give should be the logarithm of the radius in centimeter. You can combine this command with the command SUBLIMATION TEMPERATURE. In this case, the resulting inner radius for the dust shell will be such that both conditions will be fulfilled there.

sublimation temperature [1000 K]

When you calculate a model where the gas and dust is situated very close to the central star, this can result in the dust temperature to be unphysically high at the inner edge of the nebula. To prevent this, the command SUBLIMATION TEMPERATURE can be used. This will cause the code to incorporate dust in the model only in those zones where an approximation to the dust temperature is below a prescribed equilibrium value. In the zones closer to the star, the dust is assumed to be absent, i.e. either no dust or the complete amount of dust is assumed to be present in any particular zone. The default value for the sublimation temperature is 1500 K, but this value can be changed by giving an alternative value on the command line. This sublimation temperature is valid for all requested grain species, i.e. it is not possible to request different temperatures for different species. You can combine this command with the command SUBLIMATION RADIUS. The resulting inner radius for the dust shell will be such that both conditions will be fulfilled there.

8.2 Changes to the output

8.2.1 Compilation identifier

The first line of the CLOUDY output section which repeats the input lines now contains a unique compilation identifier which looks something like `940331a`. Using this identifier the exact CLOUDY version and the machine it was compiled on can be reconstructed. You can check this in the file `$CLD_DOC/cloudy.log` where a log of all compilations and modifications to CLOUDY is kept.

8.2.2 Output units

In CLOUDY the default logical unit for the final optimizer output as well as the default starting number for the punch logical units is 7. However under HP/UX logical unit 7 is reserved as standard error output. Therefore in the current installation the default logical unit for the optimizer output has been changed to unit 2 and the default starting number for the punch logical units is now unit 10.

It should be noted that, in addition to the logical unit numbers already reserved in CLOUDY (units 5,6 as standard input & output units, 0 or 7 as standard error output and units 90 thru 99 for internal use), the logical units 1,3 and 80 thru 89 are reserved for the plot commands. This assignment can *not* be changed by giving an explicit unit number on the plot command line. Logical unit 9 is reserved for the continuation file written during an optimizer run. Logical units 4 and 8 are reserved for future use.

8.2.3 Output frequency

When CLOUDY calculates a single model, it usually requires several iterations to reach the final model (see the ITERATE command). In the standard release of CLOUDY, lineprinter output as well as punch output is produced on each of these iterations, unless stated otherwise (e.g. with PRINT LAST). In the current installation this situation has been reversed. The standard is to give output only in the last iteration, unless the keyword VERBOSE is given (see also Sect. 8.1).

It is possible now to give punch and/or plot commands in optimizer runs. Output will be generated only for the final model.

8.2.4 Additional model output

At the end of the lineprinter output (if the command PRINT SHORT was given), or just in front of the `Contin Optical Depths` section otherwise, the current installation of CLOUDY will generate some extra lines of output which are described here.

Line 1: nebular radii

On this line the inner and outer radius of the nebula are given, both logarithmic (in centimeter) and linear (in parsec). Also the linear ratio of the outer to inner radius is given.

Line 2: Strömgren radius, distance, nebular mass

On this line the Strömgren radius and the distance of the nebula are given, both logarithmic (in centimeter) and linear (in parsec or kiloparsec respectively). Subsequently the angular Strömgren diameter is given in arcsecond. Last, the total and ionized shell mass are given in solar units.

Line 3: mean atomic weight, dust/gas ratio, stellar magnitudes

On this line first the mean atomic weight per hydrogen nucleus in atomic units is given. Then the linear dust-to-gas mass ratio is given. Subsequently are listed the internal extinction $A_{\rm V}$ and the stellar magnitude m_V as seen through the nebula (i.e. reddened by internal extinction). Both numbers are in magnitudes. Last, the corresponding numbers for the Johnson B band are given.

Line 4: Zanstra temperature, excitation class

On this line both the hydrogen and helium Zanstra temperature are given. If no solution for the temperature could be found, zero will be given. Subsequently the excitation class for the nebula is given, using the formula given by Dopita & Meatheringham (1990).

Line 5: average Ne, emission measure

This line gives the average electron density for the model in cm^{-3}. The value is computed as

$$\overline{n_e} = \int n_e^3 \mathrm{d}V \Big/ \int n_e^2 \mathrm{d}V.$$

The second number gives

$$\left(\overline{n_e^2}\right)^{1/2} = \left(\int n_e^4 \mathrm{d}V \Big/ \int n_e^2 \mathrm{d}V\right)^{1/2}.$$

The third number gives the n^2 parameter, which is defined as

$$n^2 = \frac{\overline{n_e^2} - \overline{n_e}^2}{\overline{n_e}^2}.$$

The last number is the logarithm of the emission measure $\int n_e^2 \mathrm{d}V$ in cm^{-3}.

Line 6: average Te, absolute Hβ flux

This line gives the average electron temperature of the model in kelvin. The value is computed as

$$\overline{T_e} = \int n_e^2 T_e \mathrm{d}V \Big/ \int n_e^2 \mathrm{d}V.$$

The second number gives

$$\left(\overline{T_e^2}\right)^{1/2} = \left(\int n_e^2 T_e^2 \mathrm{d}V \Big/ \int n_e^2 \mathrm{d}V\right)^{1/2}.$$

The third number gives the t^2 parameter, which is defined as

$$t^2 = \frac{\overline{T_e^2} - \overline{T_e}^2}{\overline{T_e}^2}.$$

The last number gives the logarithm of the absolute Hβ flux in $\mathrm{erg\,cm^{-2}\,s^{-1}}$ at the earth's distance. This flux is *not* reddened by internal extinction.

Line 7: far infrared flux, total flux in spectrum

On this line the total far infrared flux is given, defined as the integrated continuum flux from 1 μm to 300 μm, both as a logarithmic intensity (in erg per second) and a linear flux at the earth's distance (in 10^{-13} $\mathrm{W\,m^{-2}}$). Subsequently the total intensity of the nebular continuum, the nebular lines and the sum of these two is given as a logarithm in erg per second.

Line 8: fitted far infrared flux

A blackbody fit to the computed *IRAS* fluxes is made, if dust is included in the model. From this fit the following parameters are calculated: the logarithm of the total intensity of the blackbody integrated over all wavelengths (in erg per second), the color temperature (in kelvin) and the blackbody fluxes at the *IRAS* central wavelengths (in jansky).

Line 9: infrared excess

On this line six numbers are given: the infrared excess computed from the total Lyα flux, the logarithm of the total Lyα flux, the infrared excess computed from the 6 cm radio flux by using a simple approximation and by using the full formula, the Y factor used in this formula and last, the infrared excess computed from the Hβ flux. The flux value is the logarithm of the flux in $\mathrm{erg\,s^{-1}}$ (closed geometry) or $\mathrm{erg\,cm^{-2}\,s^{-1}}$ (open geometry).

Note that both the 6 cm and the Hβ infrared excess use the Case B ratio of Lyα to Hβ. In CLOUDY this ratio is only valid at high densities ($> 10^4$ $\mathrm{cm^{-3}}$).

Line 10 thru 13: radio fluxes

In four lines information is given about the radio free-free emission at the wavelengths of 2 cm, 3 cm, 6 cm and 20 cm. Each line gives the flux in milli-jansky, the optical depth τ of the nebula measured from the center of the nebula to the outer edge and the brightness temperature defined as $T_b = \overline{T_e}[1 - \exp(-\tau)]$. This last number will be wrong if the nebula is very optically thick at that wavelength ($\tau > 100$). This is because the continuum forming region then lies outside the Strömgren sphere, where the electron temperature is considerably lower than $\overline{T_e}$. Under normal circumstances this will only happen for wavelengths longer than 1 m.

Line 14 etc: photometric bands

The next block gives one output line for each photometric band. A list of all supported photometric bands can be found in Table 8.1. The first two numbers on the line are the quoted magnitude and flux in jansky, the next two numbers are the actual magnitude and flux. The meaning of the words quoted and actual is the same as in the *IRAS* Explanatory Supplement. The quoted flux is computed from the continuum and the emission line contribution; it is the flux as it would be observed. The actual flux is the monochromatic flux at the effective wavelength of the photometric band; it is included for information only, since it is not an observable. It is useful however to assess the magnitude of the color correction factor and the line contribution for each photometric band. The conversion between magnitudes and fluxes is defined by the requirement that the quoted and actual flux are equal for a $F_\nu \sim \nu^{-1}$ spectrum with no line contribution.

The next number on the line is the contribution in percent of the line emission to the total in-band flux. Then follow the most important single emission lines that contribute to the in-band flux (up to three, only those contributing more than 0.5 % are given). For each emission line three things are given: the ionic species, the wavelength in Ångstrom ($\lambda < 10$ μm) or tenths of a micron ($\lambda \geq 10$ μm) and the contribution of this line in percent.

8.2.5 Additional optimizer output

The definition of the χ^2 of a model has been changed with respect to the original code and is now calculated in a non-standard manner. All the observables that are fitted in a model run are separated into five distinct categories. These categories are labeled 'spectrum' (sp), 'photometry' (ph), 'column dens' (cd), 'abs flux' (af) and 'ang diameter' (ad). We will now explain how the total χ^2 is calculated. First, the contribution χ_i^2 of the i-th observable to the total χ^2 is calculated as

$$\chi_i^2 = \left(\frac{F_i^{\mathrm{m}} - F_i^{\mathrm{o}}}{\min(F_i^{\mathrm{m}}, F_i^{\mathrm{o}})\, \sigma_i} \right)^2 ,$$

where F_i^{o} is the observed value for the i-th observable, F_i^{m} the model value for this observable and σ_i the relative error in the observed value. If the observable could only be observed as an upper limit, the following alternative formulation is used

$$\chi_i^2 = \left(\frac{\max(F_i^{\mathrm{m}}, F_i^{\mathrm{o}}) - F_i^{\mathrm{o}}}{F_i^{\mathrm{o}}\, \sigma_i} \right)^2$$

where F_i^{o} now stands for the upper limit. Second, for each of the five categories the *average* χ_{c}^2 is calculated using

$$\chi_{\mathrm{c}}^2 = \frac{\sum_{i=1}^{N} \chi_i^2}{N} \quad \text{for } \mathrm{c} = \mathrm{sp, ph, cd, af, ad}$$

Where N is the number of observables in that category. If a certain category is empty, the value for χ_{c}^2 is taken to be zero. Third, the total χ^2 of the model is calculated by adding all the averaged χ_{c}^2-values for each of the categories. We can write this as

$$\chi^2 = \chi_{\mathrm{sp}}^2 + \chi_{\mathrm{ph}}^2 + \chi_{\mathrm{cd}}^2 + \chi_{\mathrm{af}}^2 + \chi_{\mathrm{ad}}^2.$$

For each of the categories which is not empty a line of output is generated which gives the name of the category, the number of observables contained in it, the total χ^2 of all these observables and the average χ_{c}^2 computed from that. Finally, in Table 8.3 a summary is given of which observables belong to which category.

This is approach is chosen because normally many more line ratios are given than other types of observables. If no precautions would be taken, the fitting proces would be completely dominated by the line ratios and virtually no weight would be given to the other observations. Averaging over each of the categaries ensures that the dominance of the line ratios is diminished.

Table 8.3 — *Definition of the five optimizing categories used in* CLOUDY.

category	optimization command
spectrum	OPTIMIZE LINES (line ratios)
photometry	OPTIMIZE LINES (photometry)
	OPTIMIZE COLOR TEMPERATURE
	OPTIMIZE FAR-INFRARED FLUX
	OPTIMIZE FLUX (1 μm $\leq \lambda \leq$ 300 μm)
column dens	OPTIMIZE COLUMN DENSITY
abs flux	OPTIMIZE LUMINOSITY
	OPTIMIZE INTENSITY
	OPTIMIZE FLUX ($\lambda <$ 1 μm or $\lambda >$ 300 μm)
ang diameter	OPTIMIZE DIAMETER

8.3 Additional emission lines

In the course of developing CLOUDY, many emission lines have been added to the code. These are mainly infrared lines of hydrogen and helium, but also some fine-structure lines of heavier elements have been added. A complete list of the lines is given in Table 8.4. This list however should be extended in the future. Probably the most important lines that still have to be added, are the infrared lines of He I.

8.4 References

Dopita M.A., Meatheringham S.J., 1990, ApJ 357, 140

Table 8.4 — *List of all the lines added to* CLOUDY*. The first two columns give the identifier used by* CLOUDY*, the third and fourth column give the standard spectroscopic notation and the last column the vacuum wavelength in micrometer.*

Cloudy identifier		Spectroscopic identification		λ μm	Cloudy identifier		Spectroscopic identification		λ μm
H 1f	930	H I	1–7	0.09307482	H 1f	382	H I	6–16	3.8194511
H 1f	926	H I	1–8	0.09262256	H 1f	1906	H I	7–8	19.061898
H 1f	3970	H I	2–7	0.39711950	H 1f	1131	H I	7–9	11.3086954
H 1f	3889	H I	2–8	0.38901506	H 1f	876	H I	7–10	8.7600641
H 1f	3835	H I	2–9	0.38364719	H 1f	751	H I	7–11	7.5081049
H 1f	3798	H I	2–10	0.37989757	H 1f	677	H I	7–12	6.7719905
H 1f	3771	H I	2–11	0.37717012	H 1f	629	H I	7–13	6.2919159
H 1f	3750	H I	2–12	0.37512174	H 1f	596	H I	7–14	5.9568435
H 1f	3734	H I	2–13	0.37354296	H 1f	571	H I	7–15	5.7114622
H 1f	3722	H I	2–14	0.37229966	H 1f	552	H I	7–16	5.5251882
H 1f	3712	H I	2–15	0.37130265	H 1f	2780	H I	8–9	27.803379
H 1f	3704	H I	2–16	0.37049064	H 1f	1620	H I	8–10	16.2091041
H 1f	10049	H I	3–7	1.00521281	H 1f	1238	H I	8–11	12.3871678
H 1f	9546	H I	3–8	0.95485899	H 1f	1050	H I	8–12	10.5034991
H 1f	9229	H I	3–9	0.92315474	H 1f	939	H I	8–13	9.3920177
H 1f	9015	H I	3–10	0.90173849	H 1f	866	H I	8–14	8.6645025
H 1f	8863	H I	3–11	0.88652168	H 1f	815	H I	8–15	8.1548905
H 1f	8750	H I	3–12	0.87528755	H 1f	778	H I	8–16	7.7803696
H 1f	8665	H I	3–13	0.86673983	H 1f	3886	H I	9–10	38.869866
H 1f	8598	H I	3–14	0.86007536	H 1f	2234	H I	9–11	22.340456
H 1f	8545	H I	3–15	0.85477304	H 1f	1688	H I	9–12	16.8806281
H 1f	8502	H I	3–16	0.85048188	H 1f	1418	H I	9–13	14.1830843
H 1f	217	H I	4–7	2.1661196	H 1f	1258	H I	9–14	12.5870767
H 1f	19445	H I	4–8	1.9450871	H 1f	1154	H I	9–15	11.5394914
H 1f	18174	H I	4–9	1.81790841	H 1f	1080	H I	9–16	10.8036015
H 1f	17362	H I	4–10	1.73668503	H 1f	5252	H I	10–11	52.534886
H 1f	16806	H I	4–11	1.68111115	H 1f	2983	H I	10–12	29.839500
H 1f	16407	H I	4–12	1.64116742	H 1f	2233	H I	10–13	22.3315740
H 1f	16109	H I	4–13	1.61137138	H 1f	1861	H I	10–14	18.6151505
H 1f	15880	H I	4–14	1.58848802	H 1f	1641	H I	10–15	16.4117243
H 1f	15700	H I	4–15	1.57049520	H 1f	1496	H I	10–16	14.9622556
H 1f	15556	H I	4–16	1.55606993	H 1f	6905	H I	11–12	69.071965
H 1f	465	H I	5–7	4.6537781	H 1f	3883	H I	11–13	38.842987
H 1f	374	H I	5–8	3.7405565	H 1f	2882	H I	11–14	28.8311497
H 1f	330	H I	5–9	3.2969916	H 1f	2386	H I	11–15	23.8680162
H 1f	304	H I	5–10	3.0392022	H 1f	2091	H I	11–16	20.9205615
H 1f	287	H I	5–11	2.8729959	H 1f	8873	H I	12–13	88.754631
H 1f	276	H I	5–12	2.7582676	H 1f	4947	H I	12–14	49.487676
H 1f	267	H I	5–13	2.67513124	H 1f	3646	H I	12–15	36.470508
H 1f	261	H I	5–14	2.61264766	H 1f	3000	H I	12–16	30.0100182
H 1f	256	H I	5–15	2.56432703	H 1f	11182	H I	13–14	111.856413
H 1f	253	H I	5–16	2.52609033	H 1f	6189	H I	13–15	61.910323
H 1f	1237	H I	6–7	12.371897	H 1f	4533	H I	13–16	45.340811
H 1f	750	H I	6–8	7.5024931	H 1f	13861	H I	14–15	138.65083
H 1f	591	H I	6–9	5.9082134	H 1f	7623	H I	14–16	76.247691
H 1f	513	H I	6–10	5.1286574	H 1f	16936	H I	15–16	169.41143
H 1f	467	H I	6–11	4.6725086	He2f	1085	He II	2–5	0.10849437
H 1f	438	H I	6–12	4.3764544	He2f	1025	He II	2–6	0.10252729
H 1f	417	H I	6–13	4.1707939	He2f	992	He II	2–7	0.09923635
H 1f	402	H I	6–14	4.0208675	He2f	972	He II	2–8	0.09721116
H 1f	391	H I	6–15	3.9075486	He2f	3203	He II	3–5	0.3204027

Table 8.4 — *Continued.*

Cloudy identifier		Spectroscopic identification		λ μm	Cloudy identifier		Spectroscopic identification		λ μm
He2f	2733	He II	3–6	0.27341061	He2f	558	He II	10–13	5.5806039
He2f	2511	He II	3–7	0.25119612	He2f	465	He II	10–14	4.6518788
He2f	2386	He II	3–8	0.23861309	He2f	410	He II	10–15	4.1012480
He2f	2306	He II	3–9	0.23069044	He2f	374	He II	10–16	3.7390294
He2f	10124	He II	4–5	1.0126385	He2f	1726	He II	11–12	17.260917
He2f	6560	He II	4–6	0.6561909	He2f	970	He II	11–13	9.706769
He2f	5412	He II	4–7	0.5413025	He2f	720	He II	11–14	7.2048345
He2f	4859	He II	4–8	0.4860676	He2f	596	He II	11–15	5.9645591
He2f	4542	He II	4–9	0.45428640	He2f	523	He II	11–16	5.2279972
He2f	4339	He II	4–10	0.43398911	He2f	2217	He II	12–13	22.179575
He2f	18637	He II	5–6	1.8641866	He2f	1236	He II	12–14	12.366855
He2f	11626	He II	5–7	1.1629601	He2f	911	He II	12–15	9.113894
He2f	9345	He II	5–8	0.9347499	He2f	750	He II	12–16	7.4994330
He2f	8237	He II	5–9	0.8239049	He2f	2794	He II	13–14	27.952665
He2f	7593	He II	5–10	0.7594844	He2f	1547	He II	13–15	15.471250
He2f	7178	He II	5–11	0.7179501	He2f	1133	He II	13–16	11.330565
He2f	309	He II	6–7	3.091692	He2f	3464	He II	14–15	34.64853
He2f	18743	He II	6–8	1.8748468	He2f	1905	He II	14–16	19.054130
He2f	14760	He II	6–9	1.4764419	He2f	4232	He II	15–16	42.33555
He2f	12813	He II	6–10	1.2816336	Na 3	73	[Na III]	$^2P^o_{3/2}$–$^2P^o_{1/2}$	7.3190
He2f	11673	He II	6–11	1.1676436	Na 4	90	[Na IV]	$^3P_2$–$^3P_1$	9.0391
He2f	10934	He II	6–12	1.0936607	Na 4	213	[Na IV]	$^3P_1$–$^3P_0$	21.290
He2f	476	He II	7–8	4.763507	Na 6	86	[Na VI]	$^3P_1$–$^3P_2$	8.613
He2f	283	He II	7–9	2.8260078	Na 6	143	[Na VI]	$^3P_0$–$^3P_1$	14.33
He2f	219	He II	7–10	2.1891127	Na 7	47	[Na VII]	$^2P^o_{1/2}$–$^2P^o_{3/2}$	4.675
He2f	18757	He II	7–11	1.8762520	Mg 7	55	[Mg VII]	$^3P_1$–$^3P_2$	5.504
He2f	16918	He II	7–12	1.6922992	Mg 7	90	[Mg VII]	$^3P_0$–$^3P_1$	9.033
He2f	15719	He II	7–13	1.5723301	Al 5	29	[Al V]	$^2P^o_{3/2}$–$^2P^o_{1/2}$	2.905
He2f	695	He II	8–9	6.947984	Al 6	36	[Al VI]	$^3P_2$–$^3P_1$	3.660
He2f	405	He II	8–10	4.0506090	Al 6	91	[Al VI]	$^3P_1$–$^3P_0$	9.116
He2f	310	He II	8–11	3.0955178	Al 8	37	[Al VIII]	$^3P_1$–$^3P_2$	3.69
He2f	262	He II	8–12	2.6247943	Al 8	58	[Al VIII]	$^3P_0$–$^3P_1$	5.85
He2f	235	He II	8–13	2.3470382	Al 9	20	[Al IX]	$^2P^o_{1/2}$–$^2P^o_{3/2}$	2.045
He2f	216	He II	8–14	2.1652342	S 9	13	[S IX]	$^3P_2$–$^3P_1$	1.2523
He2f	971	He II	9–10	9.713475	S 9	38	[S IX]	$^3P_1$–$^3P_0$	3.755
He2f	559	He II	9–11	5.582820	S 11	14	[S XI]	$^3P_1$–$^3P_2$	1.39274
He2f	422	He II	9–12	4.2184239	S 11	19	[S XI]	$^3P_0$–$^3P_1$	1.92012
He2f	354	He II	9–13	3.5443147	Ar11	6918	[Ar XI]	$^3P_2$–$^3P_1$	0.69175
He2f	314	He II	9–14	3.1454766	Ar11	26	[Ar XI]	$^3P_1$–$^3P_0$	2.619
He2f	288	He II	9–15	2.8836878	Ca 8	23	[Ca VIII]	$^2P^o_{1/2}$–$^2P^o_{3/2}$	2.3211
He2f	1312	He II	10–11	13.128335	Fe13	107	[Fe XIII]	$^3P_0$–$^3P_1$	1.07498
He2f	745	He II	10–12	7.456816	Fe13	108	[Fe XIII]	$^3P_1$–$^3P_2$	1.08009